TESIS DOCTORAL

INTEGRACIÓN Y DESARROLLO DE TÉCNICAS GEOMÁTICAS PARA EL SEGUIMIENTO DE LA EVOLUCIÓN Y VULNERABILIDAD DE ÁREAS COSTERAS. APLIACIÓN A UNA ZONA DEL LEVANTE DE ALMERÍA, ESPAÑA.

INTEGRATION AND DEVELOPMENT OF GEOMATICS TECHNIQUES FOR COASTAL AREAS EVOLUTION AND VULNERABILITY MONITORING. APPLICATION ON A ZONE OF LEVANTE DE ALMERÍA, SPAIN.

ISMAEL FERNÁNDEZ LUQUE

Memoria presentada para optar al Grado de Doctor en Tecnología de Invernaderos e Ingeniería Industrial y Ambiental, por la Universidad de Almería

Thesis submitted for the Degree of Doctor of Philosophy by the University of Almería, Spain.

Esta tesis ha sido dirigida por los doctores Fernando José Aguilar Torres y Manuel Ángel Aguilar Torres, profesores titulares del Departamento de Ingeniería de la Universidad de Almería.

This Thesis has been supervised by the doctors Fernando José Aguilar Torres and Manuel Ángel Aguilar Torres, professors at the Engineering Department of the University of Almería.

UNIVERSIDAD DE ALMERÍA, JULIO 2013

Departamento de Ingeniería. Escuela Politécnica Superior y Facultad de Ciencias Experimentales.

TESIS DOCTORAL

INTEGRACIÓN Y DESARROLLO DE TÉCNICAS GEOMÁTICAS PARA EL SEGUIMIENTO DE LA EVOLUCIÓN Y VULNERABILIDAD DE ÁREAS COSTERAS. APLIACIÓN A UNA ZONA DEL LEVANTE DE ALMERÍA, ESPAÑA.

AUTOR

ISMAEL FERNÁNDEZ LUQUE

V°B° Director Tesis

Fernando J. Aguilar Torres

V°B° Director Tesis

Manuel Á. Aguilar Torres

UNIVERSIDAD DE ALMERÍA, JULIO 2013

Departamento de Ingeniería. Escuela Politécnica Superior y Facultad de Ciencias Experimentales.

El trabajo que finalmente ha derivado en la publicación de esta Tesis Doctoral ha sido posible gracias a los fondos del proyecto de excelencia subvencionado por la Junta de Andalucía denominado *"Integración y análisis exploratorio de datos geoespaciales multifuente para el seguimiento y modelado de la evolución y vulnerabilidad de áreas costeras. Aplicación a una zona del Levante de Almería"*, con referencia RNM-3575, cofinanciado por la Unión Europea y que fue concedido en 2008, por el que fue concedida una beca predoctoral en 2009.

Además, es de agradecer el apoyo concedido por el proyecto titulado *"Generación de datos gerreferenciados de muy alta resolución a partir de imágenes de los satélites GeoEye-1 y WorldView-2"*, con referencia CTM2010-16573 y subvencionado por el Ministerio de Innovación y Ciencia del Gobierno de España.

This Thesis has been published thanks to the Junta de Andalucía regional government support through the excellence research project called "Integration and analysis for coastal evolution and vulnerability monitoring and modeling. Application to a zone of Levante de Almería", with reference RNM-3575, co-financed by the European Union and granted in 2008. By this project, a pre-doctoral grant was awarded by the author in 2009.

Moreover, it is appreciated the support given by the project titled "Generation of very high resolution georeferenced data from GeoEye-1 and WorldView-2 satellite images", with reference CTM2010-16573 and financed by the Innovation and Science Ministry of the Spanish Government.

AGRADECIMIENTOS

Llegado este momento, tras cuatro años de intenso trabajo, se hace difícil resumir todos los agradecimientos. Pero ha llegado el momento y espero no dejarme a nadie por el camino desde lo profesional a lo más personal, aunque claro está, en muchas ocasiones resultan muy difícil de separar estas dos facetas.

En primer lugar, merece un agradecimiento especial mi principal tutor y director, Fernando Aguilar, por su apoyo permanente en los malos y buenos momentos que tiene esto de la investigación, por enseñarme tanto durante este tiempo sobre lo académico y lo que no es académico (pero que también es preciso conocer), por haberme dado la oportunidad de convertirme en profesor novel, toda una experiencia, y sobre todo por transmitirme que tanto trabajo obtiene finalmente su recompensa. No he tenido la ocasión de encontrarme con otra persona tan trabajadora y perseverante. Siempre recordaré sus correcciones de madrugada o su disponibilidad continua, su capacidad para pasar de la docencia a la investigación puntera, de la Geomática a la ingeniería del diseño, de las tareas administrativas más arduas a la organización de congresos científicos o formando comités de expertos para corregir decenas de trabajos. Esta faceta multitarea que siempre le destaco, precisamente por lo que sé que cuesta. Sobre todo, he de agradecerle la oportunidad que en su día me ofreció, y que espero que valore positiva, ahora que se ven los frutos finales de aquella decisión.

Mención similar merece mi cotutor de este trabajo, Manuel Ángel Aguilar. Similar a su hermano en la capacidad de trabajo y cuya mirada crítica siempre ha resultado en una mejora continua del trabajo hecho, siempre atento que no dejar cabos sueltos y a que el resultado final sea lo más impecable posible. Es difícil también encontrarse con persona más productiva y seria en lo profesional.

Especial mención merece para mí la profesora y doctora Flor Álvarez, con la que realicé mi primera estancia de investigación, hecha en un lugar tan especial con Ponferrada y El Bierzo, en la Universidad de León. Su colaboración en el último capítulo de esta tesis así como en diversas publicaciones, me ha enseñado muchísimo en lo que a colaboración en investigación se refiere.

También tengo que agradecer aquí a mis tutores de mi primera estancia internacional en la *Newcastle University*, toda una experiencia tanto en lo profesional como en lo personal. John Mills y Pauline Miller estuvieron siempre a mi disposición y me enseñaron mucho, sobre todo en la dificultad de entender lo complicado de llevar a cabo trabajos multidisciplinarios desde el conocimiento de una ciencia como la cartográfica o la geomática. Además, tengo que agradecer en este punto a Fanar M. Abed, Ayaz, Brian y compañía que me hicieron sentir como en casa en tierras tan lejanas y frías.

También me gustaría tener un espacio aquí para mis profesores de la Universidad de Jaén, donde cursé mis estudios y donde me dieron la primera

oportunidad de adentrarme en esto de la investigación allá por 2007 y 2008. A Jorge Delgado y especialmente a José Luis Pérez, que me llevaron por el buen camino en el método científico y con los que luego he mantenido relación profesional en la investigación gracias a su colaboración en el proyecto de investigación por el cual fui becado. Especial mención he de realizar a José Luis, que fue un pilar fundamental en el desarrollo del capítulo 3 de esta Tesis, del que emanó mi primer artículo científico publicado.

Especial agradecimiento merece en este punto mi compañero de fatigas Andrés López. Primero compañero en las clases de Topografía y Cartografía, y después en el desarrollo de los dos primeros años de este proyecto de investigación. Su trabajo de obtención de los datos georrefereniados históricos de 1956, 1977, 1989 y 2001 es único y la calidad de los mismos ha permitido que los resultados de esta Tesis sean perfectamente confiables en cuanto a la información geográfica de la que parten. Hemos compartido mucho en esos dos años entre Jaén y Almería, tanto virtual, como presencialmente y estoy seguro de que nos volveremos a encontrar.

Tampoco me voy a dejar a mi "compi" de grupo María del Mar Saldaña. Desde el momento en que entró a formar parte del equipo de investigación, todo rodó mucho más fácil y ha sido un pilar fundamental en cuanto a la estancia en Almería se refiere. Creo que hemos aprendido mucho el uno del otro en este tiempo.

También es justo agradecer a los miembros del grupo de investigación, especialmente al Dr. Alfonso Viciana, cuyos datos aportados resultaron imprescindibles para la realización del capítulo cuarto de esta tesis.

A mis compañeros y amigos de la Universidad de Almería, especialmente a José Luis Torres, compañero de piso durante dos años y apoyo fundamental y a Emilio Rodríguez, que no sé todavía bien sobre qué tema no controla en cuanto a investigación se refiere. No me gustaría dejarme a aquéllos compañeros de la Universidad que me han hecho ver que en la Universidad hay algo más aparte del trabajo y que tiene que ver con sentirse parte de un entorno y de un grupo de compañeros, especialmente a Pablo Sayans y Daniel García.

Por supuesto, gracias a mi familia. Por estar ahí siempre, en las buenas y en las malas, por todo su apoyo y por todo el orgullo inmerecido que sienten por su hijo y por su hermano. Sin ellos, no hubiese sido posible emprender esta aventura.

Por último, tengo que agradecer enormemente esta Tesis a Mamme, que ha mitad de redacción de este documento se convirtió en mi mujer. Por todo el apoyo que me ha dado, por todo lo que ha aguantado y sufrido, por todo lo que me aporta cada día y por hacerme feliz.

A mi mujer Mamme, y a mis padres Inma y Donato

"¿Qué era lo que nos identificaba como geógrafos encubiertos, tal vez ya de niños, mucho antes de ser capaces de poner nombre a nuestra pasión secreta?

La primera razón, el amor visceral por los mapas. La segunda, común a todos nosotros, es la topofilia, una pasión igualmente visceral por la Tierra; más concretamente por algún lugar mágico o adorado en la superficie de la Tierra"

Peirce Lewis, citado en *Un mapa en la cabeza*, de Ken Jennings.

CONTENTS

LIST OF FIGURES

LIST OF TABLES

CHAPTER 0.

Introduction, study site and datasets

INTRODUCTION

General background

The coastal fringe constitutes the most changing and dynamic natural environment (Woodroffe 2002) and, therefore, it is one of the most fragile and valuable natural habitats according to the environmental equilibrium. Moreover, it comprises the most pressured area due to human activities such as the excess of urbanizations and the establishment of means of communication, ports and different industrial infrastructures. More than half of the total world population is settled on the first 60 km from the coastline, so those areas support a high economic development, mainly derived from tourist activities (Suárez de Vivero, Rodríguez Mateos 2005). With three-quarters of the world population expected to reside in the coastal zone by 2025, human activities originating from this small land area will keep representing a disproportionate amount of pressures on the global system.

Focusing in Spain, and mainly in the Andalusia region (where is placed the study site of this Thesis), the development of the coastal areas regarding investments, urbanization and economic dynamization can be considered as quite intense along the second half of the twentieth century. According to the report of the regional administration in charge of environmental affairs (Junta de Andalucía, Consejería de Medio Ambiente), the increase in the population living in coastal areas between 1991 and 2009 took a value of 34.06%. Notice that this littoral zone bears up to 40% of the Andalusia population which offers a clear view about the environmental pressure suffered by coastal areas. Furthermore, and turning to a country scale, it should be highlighted the Strategy for Coastal Sustainability (Estrategia para la Sostenibilidad de la Costa) driven by the Environment Ministry (MMA 2007) which indicated that the 44% of Spanish population live in coastal municipalities representing only the 7% of the territory. This document also reports that around 48 million of tourists are visiting our coastal areas every year. That situation has led to a gradual and steady degradation of our coastal natural resources since about the 75% of the nearest Sea terrain has been urbanized or targeted as suitable for urbanization and the 25% of the coastal areas have been already artificially developed. Finally, the 32% of the coastline is estimated as requiring environmental restoration (MMA 2007).

Vulnerability of coasts

Generally, the main threats in relation to the coastal zone are the coastal dynamic alteration due to human infrastructures, the natural habitats modification and transformation, the high level of pressure on the natural resources, the residues discharges, the degradation of the beaches, and the loss of water quality.

In Spain, although some regions might be considered vulnerable to both flooding and erosion, water stress poses the greatest threat (European-Commission 2009). An additional factor that should be taken into account for coastal management is the climate change phenomenon which could lead to a probable sea level rise (SLR) close to 0.5 m (reasonable scenario) by 2100 and the corresponding change of coastal dynamic owing to the alteration of control factors such as the wave height or the currents direction (Uceda, Sánchez-Arcilla & Cardeña 2005). In the same way, Rahmstorf (2006) used a simple regression model to suggest that SLR could reach 0.5 to 1.4 m above 1990 levels by 2100, but this work did not consider individual processes like dynamic ice sheet changes, being only based on how global sea level has been linked to global warming over the past 120 years. As it is discussed in that paper, any non-linear or threshold behaviour of ice sheets could lead to sea level rising faster than this estimate. Furthermore, climate change may aggravate the problem of water scarcity and therefore the sediment supply. In fact, south-east regions of Spain (included the study site of this Thesis) have been recognized as "particularly vulnerable to water shortages due to the hot weather and intensive urbanization of the coastline by the tourism industry and holiday homes" (European Commission 2009).

The erosion problem

One of the main indicators of coastal degradation is the shoreline erosion which is mainly occurring in sand beach areas because of their higher erodibility. In fact, shoreline erosion constitutes an important environmental and socioeconomic risk. Moreover, it increases the risk of flooding since the surface which protects the urbanized area may be reduced or removed for the most extreme cases. According to the European Commission, one fifth of the UE littoral has been eroded between 0.5 and 2.0 meters (European Commission 2005). For instance, in Spain the 11.5% of the coastline is subject to significant erosion, being more intense along the Mediterranean coast. Thus, it estimated that nearly 41% of the Andalusia Mediterranean coast is currently undergoing erosive processes (European Commission 2009). This erosion has rapidly increased because of the drastic reduction of solid sediment supply due to both the regulation and reforestation carried out on fluvial basins as well as the dam constructions (Uceda, Sánchez-Arcilla & Cardeña 2005).

The external factors which usually produce coastal erosion are the swell, the ocean currents, the tidal regime, and also the storm events. However, an additional issue has to be taken into account since it plays a key role especially for Mediterranean areas: the lack of sedimentary supply from the hydrologic basins, rivers, ravines, and so on, since anthropogenic interventions has led to changes in land-cover and land-use, besides the fact that the construction of dams has critically affected the final sediment supply to the coastal system (Uceda, Sánchez-Arcilla & Cardeña 2005). Furthermore, a probable SLR scenario provoked by the climate change would contribute with an added risk that should clearly justify a

comprehensive and rigorous study to achieve an appropriate and efficient coastal areas monitoring and management.

Coastal monitoring

The conservation actions are marked by the Integrated Coastal Zone Management (ICZM) regarding protection, restoration, control, and vigilance, apart from the management of the coastal environment.

The previously presented situation implies that the potential vulnerability of the coastal areas should be evaluated and monitored since the coastal dynamic characterizes the 'state of health' of coastal areas by indicating if the dynamic is balanced or what kind of processes, erosion or accretion, are gaining prevalence. This indicator will play a key role for general land-use management. Coastal dynamic can be quantitatively estimated by means of the evolution of the shoreline position through time, understanding the shoreline as the interface between the Sea water and the inner land. Monitoring of shoreline will enable to obtain the linear shoreline evolution (erosion or accretion), and so the estimation of eroded material volume, loss of beaches areas and so on.

According to some authors, coastal monitoring has to be combined with the space and time scales in which morphodynamic processes occur (Uceda, Sánchez-Arcilla & Cardeña 2005, Brommer, Bochev-Van Der Burgh 2009). For instance, while swell processes can be estimated in one-day changes, evolution produced by SLR needs a long-term study. Furthermore, an episodic scale is associated with extreme events with a return period of decades and they can modify the coast severely. In the Mediterranean areas, those episodes are the storms associated with meteorological high tides and highly energetic waves, and also the extreme floods related to a high and fast sediment supply. Furthermore, Mediterranean sandy coasts are usually controlled by the sediment supply in closed cells such as estuarine environments or deltas. Therefore, sediment budget assessment of the specific area may have a special importance (Rosati 2005).

Shoreline for coastal management

Shorelines, other than be essential for coastal evolution monitoring, constitutes a key element of information in geographical datasets (Consejería de Medio Ambiente de la Junta de Andalucía 2009), being a reference line for physiographic units representation, marine and terrestrial public domain management, flooding episodes simulation, and so on.

The position of the shoreline along ocean coasts varies over a broad spectrum of time scales in response to shoreline erosion (retreat) or accretion (advance), changes in water level, and land uplift or subsidence. Long-term trends in

shoreline position may be masked in the short term by variations over periods of 0.1-10 years or more, related, for example, to individual storms, changes in storminess, etc. Shoreline position reflects the coastal sediment budget, and changes may indicate natural or human-induced effects alongshore or in nearby river catchments. The detailed shape and sedimentary character of a beach (e.g. beach slope, cusp dimensions, bar position and morphology, barrier crest and berm elevation, sediment size and shape) are highly sensitive to oceanographic forcing, including deep-water wave energy, nearshore wave transformation, wave setup, storm surge, tides, and nearshore circulation: morphodynamic adjustments and feedbacks are common. Qualitative assessments of shoreline morphology can be used as a proxy for shore-zone processes, partially substituting for more quantitative measures of shoreline change where these are not available.

Historically, the shoreline has been used as the main indicator of the coastal dynamic (Moore 2000). Hence the geomatics techniques utilized for its extraction have been extended to a wide set of fields such as researching, engineering, management, land-use planning, or environmental issues. In fact, long coastlines and dynamic processes make the application of traditional surveying difficult, but recent advances made in the geomatics discipline allow for more effective methodologies to be investigated.

Among the coastal environments, the sandy beaches constitute the most dynamic natural system as well as the most exposed to morphological variations. Furthermore, they are usually under a large anthropic influence. Sandy beaches behave differently regarding the spatial and temporal scales. On one hand, seasonal changes in the way of the profile can be observed from winter to summer and for the different influence of atmospheric events (Ojeda 2000, Hernández et al. 2007). On the other hand, the general trend of coastal evolution can be assessed by means of a long-term evolution study (Douglas, Crowell 2000).

As previously indicated, the shoreline could be defined as the interaction between the Sea water and the inner land (Dolan, Fenster & Holme 1991). However, this interface does not correspond, obviously, with an invariant feature but with an instantaneous position depending on the tidal regime state and the meteorological conditions. Some researchers have preferred to define the shoreline in a more functional and practical way (Boak, Turner 2005) from which the shoreline can be established in a much more objective way. Moreover, the shoreline definition should be established in order to enable a proper extraction by means of the geomatics techniques for its integration in the long-term evolution studies. According to some authors, the best shoreline is that results less susceptible to the real physical changes of the own shoreline (Parker 2003). In that way, the most suitable technique to determine the shoreline will be that which can generate unbiased data that unambiguously define the shoreline, namely, an approach less sensitive to non-related variables regarding the phenomenon to measure.

At this point, the shoreline indicator concept emerges. That concept refers to any feature used as an approximation of the true shoreline (Gens 2010). That indicator will be utilized for all the shorelines included in the same evolution study. Historically, the most employed indicator has been the High Water Line (HWL), which is defined as the landward line in which recent position of water can be observed (border between dry and wet sand). So this indicator depends on the highest tidal and the runup (Pajak, Leatherman 2002). HWL indicator has been widely used since it results easy to interpret by means of aerial photographs or satellite imagery. However, the new data acquisition techniques have allowed the use of altimetric and tidal datums reducing the dependence on the interpretation. This kind of indicator has been established along the past decade. For instance, the Mean High Water (MHW) has been widely used in US, being estimated by means of a minimum of 19 years of tidal gauge measures. Some research has been done trying to relate both types of indicators (physical-based and tidal-based) in order to use old datasets together with contemporary tidal-based shorelines through observing the differences between both indicators and compensate them (Moore, Ruggiero & List 2006).

Shoreline evolution

As previously mentioned, shoreline is the main geo-indicator used in the coastal evolution monitoring. That is usually carried out by the erosion or accretion rates estimation, i.e. the shoreline change velocity in a historical way which is measured by the distance that is moved per year from a determined position (Ojeda 2000). Thus, large erosive rates areas can be identified in which the vulnerability of the coastal area is increased and future shoreline position can be estimated. Several approaches have been used for rate of change estimation (Douglas, Crowell 2000, Genz et al. 2007) taking into account a set of time spanned shorelines, probable errors or inaccuracies on them, acceleration of the rates, short-term variations, etc. Generally, those approaches try to quantify the long-term evolution so that the stationary variations keep out from the analysis.

Therefore, the more accurate shoreline extraction as well as the use of more robust rate of change estimations would be the basic tools for an appropriate coastal evolution study that, in the same way, would be the basis for the planning and monitoring activities in coastal areas.

Geomatics techniques on coastal areas

One of the main advantages of the tidal-based shoreline indicators is the possibility of being extracted by suitable data and methods. Here, geomatics techniques play a key role for the shoreline extraction. Historically, shoreline has been delimited in topographic maps and nautical charts by referring to a tidal

datum. Furthermore, physical indicators have been visually recognized by aerial images regardless they were previously orthorectified or not. Nowadays, and thanks to the spatial information technology development, the quasi-automatic shoreline extraction is a real possibility by using photogrammetric techniques (Ojeda et al. 2007), digital image processing (Li, Di & Ma 2003, Liu, Sherman & Gu 2007), and Airborne Laser Scanning based methods (Brock et al. 2002, Stockdon et al. 2002, Sallenger Jr. et al. 2003).

Airborne Laser Scanning (ALS)

ALS technique, developed mainly in the last decade, has opened a wide range of studies about shoreline detection since digital elevation models (DEMs) are able to be collected in a rapid, efficient, and accurate way (Sallenger Jr. et al. 2003, Brock, Purkis 2009). ALS, also called LiDAR (Light detection and ranging), enables the shoreline extraction by using tidal-based indicators which allowed the scientific community to adopt those indicators instead of physical ones. Several techniques have been developed by the researchers, e.g. the direct contour extraction of a determined elevation (Robertson V et al. 2004), the shoreline estimation by cross shore profile regression (Stockdon et al. 2002), or the altimetric datums transformation (White 2007).

Digital Photogrammetry for archival images

As previously mentioned, the new techniques such as ALS constitute an excellent data source for shoreline extraction. However, any evolutionary study of such shoreline along time requires for previous data that enable the extraction of the same type of shoreline. In this case, photogrammetry constitutes the set of techniques that have been more widely used for geographical information acquisition (Mills et al. 2005). From the first complete photogrammetric flight in Spain (carried out during the years 1956 and 1957), numerous image acquisitions have been done from which a valuable geographical information can be extracted. For instance, historical orthoimages and DEMs can be produced from historical photogrammetric flights by means of a proper methodology (Aguilar, Aguilar & Negreiros 2010).

However, the management and exploitation of those archival images can have some drawbacks, such as the lack of information about the employed cameras or their calibration certificates and the difficulty of obtaining an enough number of ground control points (GCPs) for the correct processing (Walstra, Dixon & Chandler 2007). Thus, when camera parameters are not completely known, self-calibration bundle adjustment techniques can be applied in order to mitigate the systematic errors produced by the lack of previous internal orientation parameters. Several bundle-adjustment methods have been developed such as the lens distortion model, the Bauer's simple model (Bauer, Müller 1972), the Jacobsen's simple model, the Ebner's orthogonal model (Ebner 1976), or the

Brown's physical model. Many of those methods have been widely tested in previous works (Grün 1978, Klein 1979, Ackermann 1981, Aguilar, Aguilar & Negreiros 2010).

Nevertheless, a need of a wide framework of GCPs constitutes a key disadvantage for the systematic application of self-calibration bundle adjustment techniques for historical flights since the land-use change may difficult the interpretation of those points nowadays. It is still challenging for the scientific community the search for more automatic and equally accurate techniques for the DEMs extraction from photogrammetric images. Hence, some proposals have been turned up such us GCPs extraction from LiDAR data (James et al. 2006) or DEMs coregistration by means of surface matching and image matching (Mills, Buckley & Mitchell 2003, Mills et al. 2005, Miller et al. 2008).

Robust matching techniques for DEM georeferencing

Coregistration-based techniques, in which one DEM is oriented or georeferenced by using another more accurate DEM, are particularly interesting. This kind of approaches seem to be truly suitable for DEMs change evolution studies since very high accurate DEM can be produced by the current techniques such as LiDAR. Thus, since grid DEMs can be treated as a raster images by means of, for instance, shaded-relief representation, an automatic approach for DEMs coregistration can be undertaken through image matching techniques (Aguilar et al. 2010). Other promising techniques are those based on surface matching coregistration. Those approaches are based on tridimensional transformation by using the elevation differences between both DEMs. An iterative weighting process is carried out by means of M-estimators such as Tukey's Biweight (Goodall 1983) to find an optimal solution. It is important to highlight that the real changes on terrain and the height differences regarding the misallocation between DEMs should be previously separated by means of techniques such as clustering analysis (Spath 1985).

Remote sensing and image classification

Additionally to shoreline extraction and shoreline evolution estimation, the assessing of other factors that might affect coastal evolution turn out to be highly relevant for a better understanding of all the processes which take place in the coastal area. In this sense, one of the most important factors affecting coastal evolution would be the percentage of impervious surface land cover along the coastal fringe. The impervious surface areas (ISAs) distribution provides a general vision of the land-use historical changes, affects the direct sediment exchanges between the sand beaches and landward areas, and may be a good indicator of the potential risk of flooding (Weng 2012). Historically, ISAs has been mapped by visual interpretation on orthoimages. However, the low effectiveness and efficiency of that approach have boosted the research and application of automatic

image classification methods for ISAs classification. Concretely, remote sensing have been playing a key role since very high resolution (VHR) satellite such as IKONOS (Hu, Weng 2011), Quickbird (Lu, Hetrick & Moran 2011), or more recently WorldView-2 and GeoEye-1, have been launched (Weng 2012).

VHR satellite images are not easy to analyse since the usual pixel-based classification methods usually lead to a salt-and-pepper effect which does not correspond with the reality. As a result, object-based image analysis (OBIA) -which uses homogeneous segments as a minimum classification unit instead of pixels- has been developed and widely used since it is able to remove or mitigate the spectral variability of the VHR image classification (Blaschke 2010).

For ISAs classification, the spectral resolution (the number of bands provided by satellite platforms) constitutes a basic parameter. Whereas most of the available VHR satellites offer four spectral bands (RGB visible spectrum plus near infrared band), some of the newest ones provide a higher spectral resolution. For instance, WorldView-2 satellite images include four additional bands (8 bands in total) and, consequently, the possibilities for the classification approaches are multiplied. However, if ISAs evolution along time is required, archival aerial images should be taken into account as a VHR historic data source. Unfortunately, this sort of images is available in colour (RGB visible spectrum) or, most of times, even only in panchromatic mode (PAN or black and white (B&W) images). Therefore, the ISAs classification from archival images keeps being a challenging issue to undertake.

Finally, estimating the performance of the most common classification methods in relation to ISAs classification will be crucial (Lu, Weng 2007). Generally, those classifiers can be labelled as parametric (e.g. maximum likelihood) or non-parametric. The latter kind of methods has been highly developed recently and, for instance, classification and regression trees (CART), neural networks, nearest neighbour (NN), or support vector machines (SVM) have been widely applied for image classification (Xu et al. 2005, Mas, Flores 2008, Samaniego, Bárdossy & Schulz 2008, Mountrakis, Im & Ogole 2011). Additionally, the most appropriate features (features vector) for ISAs classification should be explored. Thus, different ratios between bands, contextual information, or textural patterns could be tested (Agüera, Aguilar & Aguilar 2008).

JUSTIFICATION

The huge degradation of coastal areas as well as the high stress they bear makes this zones one of the most vulnerable environments. Determining the historical and contemporary shorelines as well as assessing the shoreline trend evolution over the years constitutes essential elements to evaluate the coastal area fragility. In this way, the development of suitable techniques for shoreline extraction and rate change estimation make up an indispensable tool for an efficient coastal areas monitoring.

Other important issue that may play a key role for coastal evolution management are the human interventions on the natural terrain of the coastal fringe since they alter the physic and chemist features of the land cover. Thus, the urbanization process entails an increase of runoff because of the sealing effect or imperviousness, provoking a lack of natural sedimentary processes of exchange between coastal areas and the inner land and the exclusive dependence of river sediment supply or alongshore sediment transport.

Taking into account the aforementioned considerations, the need of implementing efficient monitoring systems is greatly justified. The emerging and numerous multi-temporal data fusion and analysis techniques which geomatics engineering can provide (e.g. digital photogrammetry, high resolution satellite imagery, airborne laser scanning, automatic segmentation and classification of digital images, automatic DEM coregistration, and so on) enables the compilation of accurate and efficient geographically-oriented products such as DEMs or orthoimages. Those products can be properly utilized for shoreline extraction, change rate estimation or land-cover change assessment in the context of coastal monitoring and management research.

In short, efficient approaches should be established in order to evaluate what is the general trend in a specific coastal area as well as to determine what can be the causes of that trend in order to support the coastal policy and strategies followed by the decision makers in that area. The use of widespread geomatics techniques developed within the field of the scientific community, somehow adapted to the local conditions of a specific coastal area, should make possible to largely improve the monitoring and management of this kind of very sensitive and vulnerable coastal systems.

GOALS

The general purpose of this Thesis is the study and implementation of suitable geomatic techniques for coastal monitoring on a pilot area. Thus, a varied number of techniques such as photogrammetry, remote sensing, image classification, accurate coregistration of DEMs, shoreline extraction and shoreline evolution estimation are explored in this Thesis in order to provide a set of valuable tools for the coastal areas management and monitoring. Those different geomatics techniques have been tested and integrated on a coastal area located at the southeast of Spain, in the Almeria province. However, they have been developed to be easily extrapolated to any other coastal areas, mainly those situated in the Mediterranean Basin and so presenting a microtidal regime.

Therefore, the goals of this Thesis are numbered as follows:

1. On one hand, historical spatial data are extremely important for coastal evolution studies and aerial photography constitutes the main source of both historical orthoimages and DEMs. On the other hand, some of the older photogrammetric databases do not include specific essential information such as the camera calibration certificate. Therefore, self-calibrating bundle adjustment methods have to be explored in order to test which of them can improve the accuracy of the final triangulation. Additionally, the number of GCPs used for that adjustment could play an important role that should be examined. Thus, determining the most suitable combination of bundle adjustment method and the required number and distribution of GCPs for achieving the best possible exterior orientation of archival aerial images will be the first goal of this Thesis.
2. One of the main geomatics data source would be constituted by the DEMs. Those DEMs can be derived from old historical photogrammetric flights by means of a few number of GCPs. Therefore, the orientation of the resulting stereomatching-derived DEM may not be as suitable as required. Accurate archival DEM coregistration by means of a reference and more accurate DEM can become a valuable technique to take into account for historical-DEM georeferencing and terrain changes quantification. In this Thesis, shaded-relief DEMs image matching and surface matching by means of an approach based on a robust estimator will be explored in order to determine the accuracy of the final georeferentiation obtained. Both approaches will be tested both separately and jointly to refine the final DEM georeferencing.
3. The definition and delimitation of historical and contemporary shoreline constitutes the main data source for shoreline trend evolution analysis. Therefore, shoreline extraction from spatial data is one of the most important issues that a coastal evolution study should face. The typical shortcomings of the microtidal coastal areas and the geodetic and tidal gauges elevation origins largely limit the application of other pre-existing methods available in

literature to extract the shoreline in the study area of this Thesis. Therefore, a new approach to extract a tide-coordinated shoreline from very accurate LiDAR-derived DEM will be developed in order to establish a suitable and robust method especially thought to be applied in microtidal Mediterranean areas.

4. Once the definition and extraction of the shoreline for this kind of coastal areas have been established, the shoreline trend evolution will be estimated and erosion or accretion areas will be extracted according to the relative position of the different multitemporal shorelines. Here, all the historical and the contemporary data will be used to estimate long-term shoreline evolution. Some conclusions will be made in order to enable both suitable monitoring and management processes in the specific coastal area. Finally, the proposed approach is expected to serve as a reference for similar studies mainly along the Mediterranean coastal areas.

5. The impervious surface areas (ISAs) may constitute a key role for explaining coastal evolution. Furthermore, land cover data are essential for coastal monitoring in order to check the influence of the human intervention through coastal areas urbanization. Thus, remote sensing techniques and object-based image classification methods will be utilized to classify the corresponding ISAs. The aim of this work will be focused on the development of a routine to classify different data image sources ranging from colour archival orthoimage to multispectral very high resolution satellite imagery.

HYPOTHESES

The main hypotheses supporting this work highly rely on the aforementioned goals to achieve. Regarding the self-calibration bundle adjustment techniques applied to archival aerial images, it is expected that a high number of GCPs will be required, with no wide knowledge existing about what self-calibrating approach could be the most appropriate. Additionally, the developing of a new georeferentiation approach based on surface matching (i.e. coregistration between archival and reference DEMs) is expected to be more efficient, less time-consuming and more automatic than the traditional photogrammetric process. However, the final accuracy of the automatic surface matching technique is not supposed to be as fine as the one coming from the application of photogrammetric self-calibration method, although the efficiency of both approaches will have to be under consideration.

Regarding the shoreline extraction approach, it is expected that the most widespread method to extract the tide-derived shoreline from DEM, mostly used in other kind of coastal environments, will not suit well Mediterranean beaches since the tidal regime is quite different. Therefore, it is hypothesized that the developed technique could yield better results for shoreline extraction in the case of microtidal areas. Additionally, and with regard to the erosion and accretion rates estimation, a difficulty is expected since the time span used in this Thesis is not as large as that used in other similar studies, mainly due to the lack of historical data (in Spain 1956-57 is usually the oldest dataset while coastal charts dating from the nineteenth century are available in US, for instance). The main sources of the erosion process affecting this coastal area will be probably difficult to be established since a large number of sources should be taken into account (e.g., the lack of sediment, the sand mining, the human interaction, the sea level rise, some historical storm events, and so on). However, a suitable technique to control the process is expected to be achieved since different rate estimation methods will be tested.

Finally, and concerning the ISAs classification process, the use of object-based image analysis together with a proper sampling method and some non-parametric classification methods (e.g. nearest neighbour –NN- or support vector machine -SVM) is expected to yield accurate results after determining the most appropriate features vector to apply. It is also hypothesized that invariable feature sets, such as texture information, will play a key role on the classification accuracy. Additionally, VHR satellite imagery is expected to lead to more accurate results than those achieved from the archival aerial orthoimages since more spectral bands and better radiometric characteristics are contributed by the former.

STUDY SITE

The study site is located at the East of the Almeria province, south of Spain (Figure 0.1), between the localities of *Villaricos* (belonging to Cuevas de *Almanzora* township) and *Garrucha*, in North and South respectively (Figure 0.1). It comprises a coastal fringe approximately 11 km long and 770 m wide centred on WGS84 geographic coordinates of 37.2109° North and 1.8027° West. This area was chosen since a huge coastal erosion process have been carrying on throughout the twentieth century, especially in the so-called *Quitapellejos* beach and in areas close to the mouth of the *Almanzora* River, located just to the north of that beach. For instance, about 200 m of cross-shore beach erosion can be easily observed from 1957 to nowadays by having a quick look at the corresponding orthoimages (this means an estimated erosion rate close to 3.5 m/year). On the other hand, a steep front of erosion can be currently seen in *Punta de Hornicos* (just located south of the *Almanzora* river mouth) instead of the natural beach that was observed in the corresponding 1957 archival orthoimage (Figure 0.2).

At the North of the study site can be found the *Almagreda* coastal mountain chain (up to 368 m in the *Tenerife* peak), while at the South is situated the *Cabrera* mountain chain (almost 1.000 m in its maximum altitude). Therefore, non-sedimentary coastal environments are located outside this study site and natural or artificial embayed beaches and cliffs appear instead. Meanwhile, the study site can be considered entirely as a sandy coastal environment, mainly from the *Almanzora* River mouth to the *Garrucha's* Harbour.

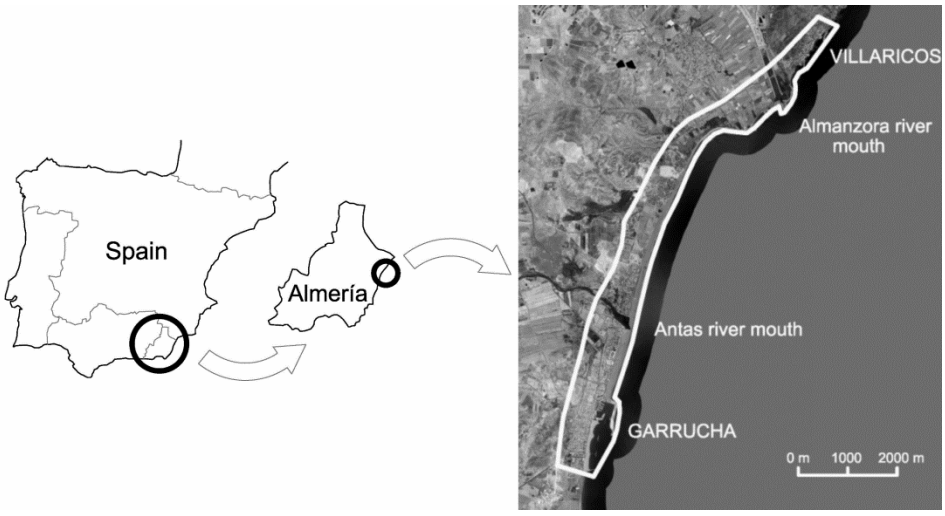

Figure 0.1. General location of the study site.

The study site contains two river mouths corresponding to the rivers *Almanzora* and *Antas*, situated in North and South respectively (Figure 0.1). Those drainage basins control the main sediment supply in that area although the *Almanzora* River can be considered as the main supplier since it is the largest river in the Almeria province. Furthermore, the *Almanzora* River can be classified as a non-permanent course while the *Antas* River can be considered as a dry-ravine or highly seasonal regime since its flow is mainly controlled by the rainfall. The construction of the 'Cuevas de *Almanzora'* dam (about 15.5 km upstream from the mouth) and the artificial canalization of the river channel from the dam to the mouth implied the reduction of the sediment catchment and transport, affecting the supply of these materials into the surrounding beaches (Viciana 2007). In this area can be found two Sites of Community Importance (SCI) such as the *Antas* channel and the marshes located at the *Antas*' mouth, so the environmental importance of the area is also crucial. The *Antas*' mouth is additionally considered as in a 'very serious flood risk' and, in fact, a really harmful flood happened on 28th September 2012, affecting some of the newest areas of urbanization and brutally modifying the temporal shoreline geometry (Figure 0.3).

Figure 0.2. Front of erosion in Quitapellejos beach. May 2011.

Figure 0.3. Mouth of the Antas River. This picture was taken from one margin of the Antas' mouth towards the other one. Normally, this mouth is completely full of sand and the beach is continued between both margins of the river. The storm episode happened on September 28th, 2012 removed the entire sand bank. Picture taken in October 2012.

Regarding hydrologic and oceanographic features of this area, it should be indicated that the main drift of the ocean currents come from the North to the South, according to the official data (Puertos del Estado 2013). That means that the original sediment supply, mainly from the *Almanzora* River mouth, is expected to move towards the South being settled along the traversed beaches. Furthermore, the submerged relief has to be taken into account. According to the official bathymetric charts, a deep canyon is placed northern the *Garrucha's* harbour, just at the end of the beaches system placed southern the *Almanzora* River. It means a great channel through which a large quantity of sediments is removed from the local coastal physiographic unit following the general oceanographic currents and without any possibility of recovery.

It is also important to highlight the high level of human intervention on this area. The level of urban development has been increased from the 50s to nowadays so that only two little urban sites existed in 1957 (*Villaricos* and *Garrucha*), whereas a large and wide fringe of urbanization areas can be seen today occupying a high percentage of the study site. Thus, a high increase of the impervious surface has been registered which could play an important role regarding the local coastal evolution. For instance, the direct sediment supply from

the nearest inland areas towards the beaches can be actually considered as close to zero or negligible. Additionally, some specific anthropic actions, very concerning for the coastal management, have taken place in the area. In fact, the building of many coastal infrastructures such as harbours rebuilding, jetties or breakwaters, as well as sand mining from the delta of the *Almanzora* River and other beaches, and the beaches nourishments over the years, play a key role in the coastal evolution of the study site.

Therefore, the environmental importance, the flood mitigation and management, the evolution of the impervious areas (soil sealing effect), and other human interactions affecting this coastal area make the geomatics techniques extremely useful and important to monitor its evolution, constituting a valuable natural laboratory where testing and validating the different approaches proposed in this Thesis.

DATASETS

The datasets listed and described in this section have been used in the chapters which make up this Thesis. Since those datasets were employed for multitemporal analysis, some of them can be considered as 'historical' and they perfectly represent the evolution of geomatics techniques during the twentieth and the beginning of the twenty first century. Thus, the datasets used in this Thesis can be classified as photogrammetric flights (historical or recent), airborne laser scanner (ALS or airborne LiDAR), high resolution satellite imagery, and ancillary data (which include those data used to support the exploitation of the raw data and pre-existing official data to test and validate some approaches tested in this Thesis). The differences among the circumstances and technological level of the employed datasets implied a special treatment and management in many cases. For instance, two historical photogrammetric flights did not include suitable information about the utilized camera. Therefore, self-calibration techniques were explored in order to obtain the most accurate absolute orientation of photographs and stereo models to ensure the derivation of a good georeferenced DSM (Digital Surface Model) from which extracting high quality shorelines (Chapters 1 and 3).

Two main kind of derived data have been extracted from the original datasets: orthoimages and DEMs. Latter ones could have been extracted by means of stereo matching and edition (historical flights), or ALS data processing (LiDAR).

Photogrammetric flights

The photogrammetry has been the most widely utilized technology throughout the twentieth century to obtain cartographic data and products. Historically, this technique has been based on conical images taken from airborne platforms which are used to extract 3D information based on the bundles

intersection and the stereovision from, at least, two different points of view. This process has undergone a huge enlargement during the last century and it has been the main source of cartographic data of any country. Launched by the explosion of the computer technology, the different stages of photogrammetry have reached the current step: the digital photogrammetry. It has enabled an increase in the use of this technique by means of reducing the needs of special hardware such as analogical or analytical restitutors, providing a much more efficient method to produce orthorectified images. Therefore, a new way to extract information from old photogrammetric projects has been reached since high resolution photogrammetric scanners are able to properly digitize old photographs in such a way that digital photogrammetric can be applied and orthoimages and DEMs can be more easily derived.

The photogrammetric flights used in this Thesis can be classified as historical or digital. The main difference relies on whether previous digitization is needed or not. Thus, the analogical flights from 1956 to 2001 used in this work can be considered as historical flights, whilst the two latest flights would be classified as digital flights. A large effort to get a wide and time spanned representation of the main photogrammetric flights taken on the study site was carried out. In the case of Spain, the first historical and systematic flight was taken in 1945-46 (Fernández, Quirós 1997) at a scale of 1:45.000, but it did not cover the entire country and, moreover, the first flight undertaken in Almeria would have to wait till the arrival of the 1956-57 series. The details of every photogrammetric dataset are listed below and summarized in Table 0.1.

American Flight (1956-57)

Undertaken by the United States government, it is often referred to in Spain as the 'American flight' and it marks the start of metric aerial photography in most of the Spanish regions. Therefore, it constitutes a valuable national information source for photo interpretation and land use evolution, among other possibilities. However, problems with the metric capabilities of this flight exist since a proper conservation of the prints is not guaranteed and there is an important lack of data with respect to the cameras employed (Cardenal et al 2006).

These photographs belonged to panchromatic photogrammetric flights at an approximate scale of 1:33 000, acquired using a 'standard' metric film camera of 230 x 230 mm with 60% forward overlap and 30% lateral overlap, providing a base to height (B/H) ratio of approximately 0.60. The original negatives were scanned using a photogrammetric scanner with a geometric resolution of 21 μm and a radiometric resolution of 8 bits; they were stored in TIFF format with a ground sample distance (GSD) of approximately 0.70 m. The digitized photographs were provided by the Network of Environmental Information of Andalusia (known as REDIAM).

The study site is covered by two stereo pairs (4 images in total) flown in different dates and had some different features since they belong to different strips of the flight plan. The southern stereo pair was captured on 30th October 1956, using a photogrammetric camera for which the principal distance (153.01 mm) appeared as marginal data in the photograph. The northern stereo pair was taken on 3rd September 1956 by using a different camera with an indicated principal distance of 154.19 mm. Full camera calibration details of these cameras were unknown. Moreover, these old cameras had no corner fiducial marks, as more recent cameras do. Instead they relied on only four marks in the middle of the edges of the photo frames to allow for interior orientation in the plate carriers of analogue stereoplotters of the time.

Agriculture or Interministerial flight (1977-1983)

This flight consisted of a panchromatic analogue photogrammetric flight carried out by some of the Spanish government ministries between 1977 and 1983. The photographs used in this research were taken on 15th July 1977 and they are composed by four stereo pairs with a B/H ratio of 0.55, presenting a 60% forward overlap and a 30% lateral overlap respectively. This flight presents an approximate scale of 1:18.000 and a principal distance, printed as a marginal data in the photographs, of 152.77m. The camera calibration certificate was unavailable. The eight photographs were scanned into a TIFF format from the original negatives using a photogrammetric scanner with a geometric resolution of 15 μm and a radiometric resolution of 8 bits, thus presenting a GSD of approximately 0.27 m. The photography from this flight had four fiducial marks in the corners of the frame.

Coastal Flight I (1989-1990)

This flight was carried out by the General Coastal Management (*Dirección General de Costas*, DGC, in Spanish) depending on the Spanish Ministry of Environment. This was one of the first colour flights taken over Spain. The date of the 13 original photograms used to cover the whole working area was the 15th September 1989, presenting a scale of 1:10.000 approximately. The final GSD was 0.16 m since the images were scanned at 16 μm spatial resolution. The conservation of these photographs was really poor as it can be appreciated in Figure 0.4.

Coastal Flight II (2001)

This flight was undertaken by the same administration of the Coastal Flight I. For this study site, 26 colour photographs were needed since the scale was larger in this case (1:5.000). The date of this flight was the 9th April 2001, being taken by means of a RC30 (focal distance = 152.92 mm) analogical camera. The relatively poorly-preserved positives which had poor radiometry and many artefacts

(scratches, fingerprints, etc.) were digitized by a photogrammetric scanner resulting in a GSD close to 0.10 m., with a resolution of 20 μm in the RGB channels.

Figure 0.4. Example of the scratches existing in the original images of the Coastal Flight I.

Table 0.1. Summary of the main characteristics for four historical photogrammetric flights used along this Thesis.

Flight	No. photos	Scale	Scanned resolution	GSD	Camera certificate	Colour
1956	4	1:33.000	21 μm	0.70 m	No available	PAN
1977	8	1:18.000	15 μm	0.30 m	No available	PAN
1989	13	1:10.000	16 μm	0.16 m	No available	RGB
2001	26	1:5.000	20 μm	0.10 m	Available	RGB

First digital flight (2009)

This digital dataset was specifically acquired for this research project covering the whole study site and being carried out on 28th August 2009. This flight was coupled with ALS data at a flying height of approximately 1000 m. Digital images were obtained using an Intergraph Digital Mapping Camera (DMC) and counting on the support of a ground GPS reference station. 86 high-resolution panchromatic images were captured simultaneously with multispectral images in 4 bands (red, green, blue and near infrared), presenting a composite GSD of approximately 0.10

m. Image orientation was directly measured using a GPS/INS (inertial navigation system) on board the aircraft which was used to aid in the calculation of the corresponding photogrammetric block triangulation. The images were only used for obtaining the orthoimages while the DEM was extracted from the ALS raw data (see below).

Second digital flight (2011)

This flight was undertaken by means of a helicopter-mounted LiDAR and camera integration system. The flying height was close to 350 m, employing a digital camera Hasselblad H3D-22. RGB visible images and Nir images were provided. The photogrammetric and orthorectification processes were carried out by the provider company (Aerolaser®) so no additional GCPs were surveyed.

LiDAR data

First digital flight (2009)

The Leica ALS60 system was utilized to acquire the LiDAR data of the study site in this flight. 4 strips were needed to cover the entire area using a FOV (field of view) of 35°. The average point density was close to 1.61 points/m^2, capturing more than 36 million points. The DEM extraction was derived from the original data by means of TerraScan® software. The DEM compilation was based on an automatic classification and a later manual editing process. Additionally, the good matching between the strips in the overlap areas indicated that no significant differences existed. However, an overall altimetric disagreement was estimated by comparing the extracted DEM with 62 ground-surveyed Differential Global Positioning System (DGPS) high accuracy check points. That offset reached -0.165 m, meaning that the LiDAR data were slightly below the reference coordinate system. This offset was easily corrected by adding that difference and no other systematic or planimetric inaccuracies were detected. The final vertical accuracy of the LiDAR-derived DEM took a value of ±0.089 m, estimated as the standard deviation of the final vertical differences between the LiDAR-derived DEM and the same set of ground check points.

Second digital flight (2011)

The LiDAR data from this flight were captured by the AeroLaser System airborne laser scanning platform (see www.aerolaser.es/), based on a Q240i Riegl LMS laser scanner with a FOV of 30º. It was mounted on helicopter at a flying height above ground around 350 m, which yielded an average point density close to 2 points/m^2, although the final LiDAR-derived DEM was resampled to 1 point/m^2 (extracted by the provider company). A systematic error of -0.08 m was found and corrected by means of an appropriate set of GCPs. The vertical accuracy,

given by the standard deviation estimated from the vertical differences between the LiDAR-derived DEM and the GCPs, took a value of ±0.066 m.

Satellite imagery

Two satellite images from GeoEye-1 and WorldView-2 VHR satellites were used in this Thesis to classify impervious surface areas (ISAs) by means of an object-based image analysis (OBIA) approach. The purpose was to compare the accuracy classification results from satellite imagery against those previously obtained through a similar approach applied on the 'Coastal Flight II (2001)' archival orthoimages. These satellite images were previously oriented and orthorectified (see Aguilar, Saldaña & Aguilar 2013) so they were used only as an input data for this work. Both images were collected with a narrow time span so they were able to be compared with no significant land use changes being expected.

GeoEye-1

This image was taken on 27th August 2011 as a part of a stereo pair product (GeoStereo product of GeoEye Company), although it was used as a single image in this work. This satellite is characterized by having one VHR panchromatic band (PAN) and four multispectral bands (MS) which include Blue (450-510 nm), Green (510-580 nm), Red (655-690 nm), and Near-infrared (Nir, 780-920 nm) bands. The original spatial resolution is 0.41 and 1.65 m for PAN and MS bands respectively, although they are resampled to 0.50 and 2.00 m because of a USA government restriction. It was ordered with a dynamic range of 11 bits per pixel and without any adjustment (i.e. maintaining absolute radiometric accuracy and full dynamic range for scientific applications).

The GeoEye-1 image used in this work was captured with a sensor elevation of 81.5° which implied an off-nadir angle of 8.5°. The PAN image orientation was carried out by means of the rational polynomial coefficients (RPCs) refined through zero-order transformation in image space with the support of 7 GCPs. The image orthorectification was undertaken by using as ancillary data the LiDAR-derived DEM of the 'First digital flight (2009)'. The corresponding pan-sharpened image, with 0.5 m GSD and containing the spectral information gathered from the MS image (four bands), was attained by using the PANSHARP module included in Geomatica v. 12 (PCI Geomatics, Richmond Hill, ON, Canada).

WorldView-2

In this case, a basic image of a stereo pair taken on 18th August 2011 by *DigitalGlobe*© Company was used in this Thesis. Again, the coupled image was not taken into account in this work, and the image which had the larger sensor elevation was chosen (80.0° that implied an off-nadir angle of 10.0°). Similar

characteristics than those described for the case of GeoEye-1 can be found, sharing the same radiometric resolution (11 bits/pixel), whereas the original spatial resolution for WorldView-2 imagery is 0.46 and 1.84 m for PAN and MS bands respectively, although the final resolution is again 0.50 and 2.00 m because of the same aforementioned official restriction.

The main difference between both satellites relies on the spectral resolution, since four additional bands are included in WorldView-2 such as Coastal Blue (400-450 nm), Yellow (585-625 nm), Red Edge (705-745 nm), and second Near-infrared (860-1040 nm). Finally, the methodology to produce the final orthoimage was the same than that used for GeoEye-1.

Ancillary data

Field data

Several surveying campaigns were perform in order to collect a total amount of 150 ground surveyed points to be used both as GCPs or check points (CPs). Ground points were obtained by DGPS using a Topcon HiPer PRO GOS receiver working in real time kinematic (RTK) mode. The reference system was the European Terrestrial Reference System 1989 (ETRS89), while the chosen projection was the Universal Transverse Mercator (UTM) in the zone 30. Moreover, the vertical datum was based on the geoid as the reference surface, adopting the mean sea level in the calm seas of Alicante, Spain, as the null orthometric height datum (official Spanish height origin). The DGPS observations were supported by eleven survey points: four belonging to the national geodetic network, one obtained from using high precision GPS techniques (Spanish REGENTE network), and six survey points provided by REDIAM. The resulting root mean square errors (RMSE) took values of 56 mm, 33 mm and 76 mm in the *X*, *Y* and *Z* axes respectively.

Those points were collected in order to carry out the orientations of the photogrammetric projects and the satellite imagery, and also to compute the corresponding LiDAR data correction. Furthermore, independent CPs were used to check the previously mentioned orientations, the orthoimagery derived (whether airborne or satellite captured imagery), and the accuracy of the derived DEMs or DEMs. In order to identify GCPs for historical flights, man-made and natural points located within the study site were unambiguously identified, which made much more difficult the data collection.

Additionally, a specific surveying campaign was designed in order to check the shoreline position derived from the digital flight of 2011, which consisted in a systematic beach profiling in some sample areas of the coastal zone. 6 different beach areas with a number of profiles from 10 to 21 were surveyed. The coordinate system and measuring method of this set of ground points was the

same as the previous ones, but they were collected in a different way. Since a datum-referred shoreline was extracted (see Chapter 3 of this Thesis), a subsequent interpolation process was carried out. Thus, a ground truth shoreline was available to be compared against the tested shoreline extraction methods and enough points could be used for LiDAR-derived DEM in the beach zone.

Pre-existing DEM

In order to validate a developed approach to automatically orientate stereomatching-derived DEMs, a pre-existing DEM was used (see Chapter 2). This DEM was obtained by a LiDAR dataset taken during August and September 2004 by the Cartographic Institute of Catalonia (Spain) in the area of the Antas ravine. An Optech ALTM 3025 LiDAR sensor was utilized on a flight height of 2300 m, yielding a point density of around 1 point/m^2 and an estimated vertical accuracy between 6 and 15 cm depending on the land cover.

REFERENCES

Ackermann, F. 1981, "Block adjustment with additional parameters", *Photogrammetria,* vol. 36, no. 6, pp. 217-227.

Agüera, F., Aguilar, F.J. & Aguilar, M.A. 2008, "Using texture analysis to improve per-pixel classification of very high resolution images for mapping plastic greenhouses", *ISPRS Journal of Photogrammetry and Remote Sensing,* vol. 63, no. 6, pp. 635-646.

Aguilar, M.A., Saldaña, M.D.M. & Aguilar, F.J. 2013, "Assessing geometric accuracy of the orthorectification process from GeoEye-1 and WorldView-2 panchromatic images", *International Journal of Applied Earth Observation and Geoinformation,* vol. 21, no. 1, pp. 427-435.

Aguilar, F.J., Fernández, I., Aguilar, M.A., Pérez, J.L., Delgado, J. & Negreiros, J.G. 2010, "Shaded-reliefs matching as an efficient technique for 3D geo-referencing of historical digital elevation models.", *International Archives of the Photogrammetry, Remote Sensing and Spatial Information Science, Volume XXXVIII, Part 8,* Kyoto, Japan, August, pp. 1002-1007.

Aguilar, M.A., Aguilar, F.J. & Negreiros, J.G. 2010, "Self-calibration methods for using historical aerial photographs with photogrammetric purposes", *Anales de Ingeniería Gráfica,* vol. 21, pp. 33-40.

Bauer, H. & Müller, J. 1972, "Height accuracy of blocks and bundle block adjustment with additional parameters", *12th Congress of the International Society for Photogrammetry and Remote Sensing (ISPRS),* Ottawa, Canada, 1972.

Blaschke, T. 2010, "Object based image analysis for remote sensing", *ISPRS Journal of Photogrammetry and Remote Sensing,* vol. 65, no. 1, pp. 2-16.

Boak, E.H. & Turner, I.L. 2005, "Shoreline definition and detection: A review", *Journal of Coastal Research,* vol. 21, no. 4, pp. 688-703.

Brock, J.C. & Purkis, S.J. 2009, "The emerging role of lidar remote sensing in coastal research and resource management", *Journal of Coastal Research,* SPECIAL ISSUE 53, pp. 1-5.

Brock, J.C., Wright, C.W., Sallenger, A.H., Krabill, W.B. & Swift, R.N. 2002, "Basis and methods of NASA Airborne Topographic Mapper lidar surveys for coastal studies", *Journal of Coastal Research,* vol. 18, no. 1, pp. 1-13.

Brommer, M.B. & Bochev-Van Der Burgh, L.M. 2009, "Sustainable coastal zone management: A concept for forecasting long-term and large-scale coastal evolution", *Journal of Coastal Research,* vol. 25, no. 1, pp. 181-188.

Cardenal, J., Delgado, J., Mata, E., González, A. & Olague, I. 2006, "Use of historical flight for landslide monitoring", *Proceedings of the 7th International*

*Symposium on Spatial Accuracy Assessment in Natural Resources and Environmental Sciences*Lisbon, Portugal, 2006, pp. 129.

Consejería de Medio Ambiente de la Junta de Andalucía 2009, *Medio ambiente en Andalucía. Informe 2009.*, Consejería de Medio Ambiente, Sevilla.

Dolan, R., Fenster, M.S. & Holme, S.J. 1991, "Temporal Analysis of Shoreline Recession and Accretion", *Journal of Coastal Research,* vol. 7, no. 3, pp. pp. 723-744.

Douglas, B.C. & Crowell, M. 2000, "Long-term shoreline position prediction and error propagation", *Journal of Coastal Research,* vol. 16, no. 1, pp. 145-152.

Ebner, H. 1976, "Self-calibrating block adjustment", *Bildmessung und Luftbildwesen,* vol. 4, pp. 128-139.

European Commission, E. 2009, *The economics of climate change adaptation in EU coastal areas. Final report,* Directorate-General for Maritime Affarirs and Fisheries, Brussels.

European Commission, E. 2005, *Living with coastal erosion in Europe: Sediment and space of sustainability. Results of the EUROSION project*, European Commission official office of publications, Luxemburg.

Fernández, F., Quirós, F. 1997, "El vuelo fotográfico de la 'Serie A'", *Ería: Revista cuatrimestral de Geografía*, vol. 43, pp. 190-198.

Gens, R. 2010, "Remote sensing of coastlines: Detection, extraction and monitoring", *International Journal of Remote Sensing,* vol. 31, no. 7, pp. 1819-1836.

Genz, A.S., Fletcher, C.H., Dunn, R.A., Frazer, L.N. & Rooney, J.J. 2007, "The predictive accuracy of shoreline change rate methods and alongshore beach variation on Maui, Hawaii", *Journal of Coastal Research,* vol. 23, no. 1, pp. 87-105.

Goodall, C. 1983, "M-Estimators of location: An outline of the theory" in *Understanding Robust and Explanatory Data Analysis*, eds. D. Hoaglin, F. Mosteller & J.W. Tukey, John Willey & Sons, New York, pp. 339-403.

Grün, A. 1978, "Experiences with self-calibrating bundle adjustment", *American Congress on Surveying and Mapping/American Society of Photogrammetry (ACSM-ASP)* Washington, D.C.

Hernández, L., Alonso, I., Sánchez-Pérez, I., Alcántara-Carrió, J. & Montesdeoca, I. 2007, "Shortage of sediments in the Maspalomas dune field (Gran Canaria, Canary Islands) deduced from analysis of aerial photographs, foraminiferal content, and sediment transport trends", *Journal of Coastal Research,* vol. 23, no. 4, pp. 993-999.

Hu, X. & Weng, Q. 2011, "Impervious surface area extraction from IKONOS imagery using an object-based fuzzy method", *Geocarto International,* vol. 26, no. 1, pp. 3-20.

James, T.D., Murray, T., Barrand, N.E. & Barr, S.L. 2006, "Extracting photogrammetric ground control from lidar DEMs for change detection", *Photogrammetric Record,* vol. 21, no. 116, pp. 312-328.

Klein, H. 1979, "New results of bundle block adjustments with additional parameters", *Proceedings of 37thPhotogrammetric Week*Stuttgart, Germany.

Li, R., Di, K. & Ma, R. 2003, "3-D shoreline extraction from IKONOS satellite imagery", *Marine Geodesy,* vol. 26, no. 1-2, pp. 107-115.

Liu, H., Sherman, D. & Gu, S. 2007, "Automated extraction of shorelines from airborne light detection and ranging data and accuracy assessment based on Monte Carlo simulation", *Journal of Coastal Research,* vol. 23, no. 6, pp. 1359-1369.

Lu, D., Hetrick, S. & Moran, E. 2011, "Impervious surface mapping with quickbird imagery", *International Journal of Remote Sensing,* vol. 32, no. 9, pp. 2519-2533.

Lu, D. & Weng, Q. 2007, "A survey of image classification methods and techniques for improving classification performance", *International Journal of Remote Sensing,* vol. 28, no. 5, pp. 823-870.

Mas, J.F. & Flores, J.J. 2008, "The application of artificial neural networks to the analysis of remotely sensed data", *International Journal of Remote Sensing,* vol. 29, no. 3, pp. 617-663.

Miller, P., Mills, J., Edwards, S., Bryan, P., Marsh, S., Mitchell, H. & Hobbs, P. 2008, "A robust surface matching technique for coastal geohazard assessment and management", *ISPRS Journal of Photogrammetry and Remote Sensing,* vol. 63, no. 5, pp. 529-542.

Mills, J.P., Buckley, S.J. & Mitchell, H.L. 2003, "Synergistic fusion of GPS and photogrammetrically generated elevation models", *Photogrammetric Engineering and Remote Sensing,* vol. 69, no. 4, pp. 341-349.

Mills, J.P., Buckley, S.J., Mitchell, H.L., Clarke, P.J. & Edwards, S.J. 2005, "A geomatics data integration technique for coastal change monitoring", *Earth Surface Processes and Landforms,* vol. 30, no. 6, pp. 651-664.

MMA, G. 2007, *Estrategia de sostenibilidad de la costa. Documento de inicio*.

Moore, L.J. 2000, "Shoreline mapping techniques", *Journal of Coastal Research,* vol. 16, no. 1, pp. 111-124.

Moore, L.J., Ruggiero, P. & List, J.H. 2006, "Comparing mean high water and high water line shorelines: Should prosy-datum offsets be incorporated into shoreline change analysis?", *Journal of Coastal Research,* vol. 22, no. 4, pp. 894-905.

Mountrakis, G., Im, J. & Ogole, C. 2011, "Support vector machines in remote sensing: A review", *ISPRS Journal of Photogrammetry and Remote Sensing,* vol. 66, no. 3, pp. 247-259.

Ojeda, J. 2000, "Métodos para el cálculo de la erosión costera. Revisión, tendencias y propuesta.", *Boletín de la A.G.E.,* , no. 30, pp. 103-118.

Ojeda, J., Vallejo, I., Hernández, L. & Álvarez, J. 2007, "Fotogrametría y LIDAR como fuentes de información en geomorfología litoral (marismas mareales y sistemas dunares): El potencial de su análisis espacial a través de SIG", *Boletín de la A.G.E.,* vol. 44, pp. 215-233.

Pajak, M.J. & Leatherman, S. 2002, "The high water line as shoreline indicator", *Journal of Coastal Research,* vol. 18, no. 2, pp. 329-337.

Parker, B.B. 2003, "The Difficulties in Measuring a Consistently Defined Shoreline - The Problem of Vertical Referencing", *Journal of Coastal Research,* Special issue 38, pp. 44-56.

Puertos del Estado. Available: http://www.puertos.es/ [2013, 03/13].

Rahmstorf, S. (2007), "A semi-emprirical approach to projecting future sea-level rise", *Science,* vol. 315, no. 5810, pp. 368-370

Robertson V, W., Whitman, D., Zhang, K. & Leatherman, S.P. 2004, "Mapping shoreline position using airborne laser altimetry", *Journal of Coastal Research,* vol. 20, no. 3, pp. 884-892.

Rosati, J.D. 2005, "Concepts in sediment budgets", *Journal of Coastal Research,* vol. 21, no. 2, pp. 307-322.

Sallenger Jr., A.H., Krabill, W.B., Swift, R.N., Brock, J., List, J., Hansen, M., Holman, R.A., Manizade, S., Sontag, J., Meredith, A., Morgan, K., Yunkel, J.K., Frederick, E.B. & Stockdon, H. 2003, "Evaluation of airborne topographic lidar for quantifying beach changes", *Journal of Coastal Research,* vol. 19, no. 1, pp. 125-133.

Samaniego, L., Bárdossy, A. & Schulz, K. 2008, "Supervised classification of remotely sensed imagery using a modified k-NN technique", *IEEE Transactions on Geoscience and Remote Sensing,* vol. 46, no. 7, pp. 2112-2125.

Spath, H. 1985, *Cluster Dissection and Analysis: Theory, FORTRAN, Programs, Examples,* Halsted Press, New York.

Stockdon, H.F., Sallenger Jr., A.H., List, J.H. & Holman, R.A. 2002, "Estimation of shoreline position and change using airborne topographic lidar data", *Journal of Coastal Research,* vol. 18, no. 3, pp. 502-513.

Suárez de Vivero, J.L. & Rodríguez Mateos, J.C. 2005, "Coastal crisis: The failure of coastal management in the Spanish Mediteranean region", *Coastal Management,* vol. 33, no. 2, pp. 197-214.

Uceda, A.C., Sánchez-Arcilla, A. & Cardeña, Z. 2005, "Chapter 11. Impacts on coastal areas" in *Impacts of climate change in Spain*, ed. J.M. Moreno-Rodríguez, Centro de Publicaciones. Ministerio Medio Ambiente, Madrid, pp. 451-504.

Viciana, A., 2007, "La costa de Almería: Desarrollo socio-económico y degradación físico-ambiental (1957-2007)". *Paralelo 37º*, vol. 19, pp. 149-183

Walstra, J., Dixon, N. & Chandler, J.H. 2007, "Historical aerial photographs for landslide assessment: Two case histories", *Quarterly Journal of Engineering Geology and Hydrogeology,* vol. 40, no. 4, pp. 315-332.

Weng, Q. 2012, "Remote sensing of impervious surfaces in the urban areas: Requirements, methods, and trends", *Remote Sensing of Environment,* vol. 117, pp. 34-49.

White, S. 2007, "Utilization of LIDAR and NOAA's vertical datum transformation tool (VDatum) for shoreline delineation", *Oceans Conference Record (IEEE)*.

Woodroffe, C.D. 2002, *Coasts: form, process, and evolution.* 1st edn, Cambrigde University Press, New York.

Xu, M., Watanachaturaporn, P., Varshney, P.K. & Arora, M.K. 2005, "Decision tree regression for soft classification of remote sensing data", *Remote Sensing of Environment,* vol. 97, no. 3, pp. 322-336.

CHAPTER 1

Accuracy assessment of commercial self-calibrating bundle adjustment routines applied to archival aerial photography

ABSTRACT

The use of archival or historical photography for photogrammetric purposes often involves a lack of data concerning the aerial cameras employed, difficulties in identifying control points on the photos and inappropriate conservation of the photography. When camera calibration parameters are unknown, they should be estimated by means of a self-calibrating bundle adjustment. Several calibration models available in the Leica Photogrammetry Suite software have been tested on two archival datasets, captured in 1956 and 1977, covering the same working area. The accuracy of the dataset triangulation was found to depend significantly on the self-calibration method and the number of ground control points used; when the latter ranged from six to nine per stereo pair, self-calibrating bundle adjustment techniques were found to slightly, but not always significantly, improve the photogrammetric capability of archival aerial photography. Thus the adoption of self-calibration cannot guarantee the improvement of results when working on poorly-conserved imagery. Results from such datasets are very dependent on numerous local variables which cannot be extrapolated to other areas for the same camera since each dataset is unique and may present systematic errors of a different nature.

Keywords: self-calibration, bundle adjustment, mapping, triangulation, accuracy, archival photography

INTRODUCTION

Archived aerial photography is currently receiving the attention of many earth scientists, with such datasets representing a very important information source in order to evaluate the temporal spatial evolution of zones of interest. Aerial photographs are the earliest remote sensing data source, having being collected since the early 20th century, and photogrammetric and digital image processing techniques are now being extensively used to extract both qualitative and quantitative information from such datasets. Appropriate comparison of photogrammetric surveys of an area conducted in different years allows the identification of accurate geometric change over time. Such techniques have been successfully applied to detect changes in glaciated areas (Schiefer, Gilbert 2007), river bank erosion (Lane 2000), coastal evolution (Mills et al. 2005), gully erosion (Marzolff, Poesen 2009), forest canopy cover (Véga, St-Onge 2008) and landslides (Chadwick et al. 2005, Prokešová, Kardoš & Medveďová 2010).

Metric aerial photography has been routinely collected in North America and Europe for land surveying and topographic purposes over the past 50 years or so. However, significant problems can present themselves when attempting to make metrical use of archival aerial photography. For example, the proper conservation of the original film, derived diapositives or prints is not readily guaranteed, and there is often a critical lack of information with respect to the cameras employed, in particular the regular absence of a geometric calibration certificate. Another general problem when utilising archival photography for metric purposes is the difficulty in locating sufficient ground control points (GCPs), both in terms of quantity and quality, because often the suitable potential points that can be identified in the archival images can no longer be located on the ground at the present time (Zanutta et al. 2006, Walstra, Dixon & Chandler 2007).

When camera calibration parameters are unknown (the most usual case when working with archival photography), then they should be estimated using a self-calibrating bundle adjustment (Chandler, Cooper 1989, Kraus 1997). Self-calibration is a well-known method which has long been successfully and routinely applied in close range photogrammetric applications utilising non-metric cameras (Fraser 1997). In recent years self-calibration has also been increasingly applied in aerial photogrammetry. In fact, most current digital photogrammetric workstations incorporate triangulation software which offers self-calibration options. Among them are the self-calibration routines which use additional parameters (APs) in the triangulation process, as available in the advanced options within the aerial triangulation module of the Leica Photogrammetry Suite (LPS) software. Self-calibration methods were intensively researched and developed in the 1970s and 1980s, where it was confirmed that systematic image errors can be completely or partially compensated by additional parameters (Bauer, Müller 1972, Ebner 1976, Grün 1978, Klein 1979, Ackermann 1981). Nowadays, such

approaches are routinely used for improving the triangulation process with modern airborne digital sensors such as the ADS40/80 by Leica Geosystems, DMC by Z/I Imaging, or UltraCAM by Microsoft/Vexcel Imaging (Cramer 2009). Moreover, other applications are arising using these methods such as the calibration of panoramic cameras and laser scanners (Amiri Parian, Gruen 2010, Lichti 2010). The successful application of self-calibration depends on many factors which include: the strength of the block (fore-and-aft overlap, cross-strips); the number and distribution of GCPs and tie points; the magnitude of any systematic errors present; and the significance of, and correlation between, the additional parameters used. In order to extract high quality data from archival aerial photography, where there may be only a small number of images available and the redundancy may be low, GCPs should be of high quality and well distributed in the block. This is especially important if camera calibration information is incomplete or unavailable. However, the identification and quality of ground control in archival photography is often problematic. As a result, much research has been carried out in order to reduce the need for these costly and difficult to measure GCPs by means of surface matching (Li et al. 2001, Mills, Buckley & Mitchell 2003, Mills et al. 2005, Miller et al. 2008, Akca 2010, Aguilar et al. 2012), or extracting GCPs from LiDAR-derived digital elevation models (DEMs) (James et al. 2006).

Nowadays the results regarding the application of self-calibration to archival photography are extremely variable. Firstly, it cannot be assumed that systematic image errors are constant for the entire archive of photographs; every archival flight will present its own systematic errors depending on the camera used, the image scale, and so on. Secondly, due to a usual lack of existing ground points, accuracy reports are usually based on an insufficient number of independent check points (CPs), producing low reliability for the accuracy assessment. Finally, replication of the experiments (repetition of the experimental conditions so that the variability associated with the phenomenon can be estimated) is hardly ever undertaken.

The main objective of the work reported in this chapter was therefore to investigate the use of self-calibration models to try to improve the photogrammetric capabilities of two archival aerial flights captured in 1956 (1:33000 scale) and 1977 (1:18000) over our specific pilot coastal area. The underlying hypothesis supposes that self-calibrating bundle adjustment techniques will correct the difference between the mathematical model of perspective geometry and the true image geometry for archival aerial photography and so remove, at least partially, any systematic errors present. By using a large number of ground points, a statistical analysis to determine the influence of various factors on the accuracy of triangulating these specific archival photographic datasets was performed. The factors considered and reported herein were: (i) the different models utilised in self-calibrating bundle adjustment

available in the LPS 9.1® software (models of Bauer, Jacobsen, Ebner, Brown and lens distortion), and (ii) the number of GCPs used in the triangulation process.

DATASETS AND METHODOLOGY

For this study, the used dataset were: 1956 photographs, 1977 photographs, 2009 digital image survey, and the GCPs set as an auxiliary data. The reader is referred to the Datasets section of this Thesis to obtain additional information. Table 1.1 shows a summary of the main features of both flights.

1956 photogrammetric flight was the first of the two archival datasets; both acquired using a "standard" metric film camera format of 230 mm x 230 mm, used in this study. From a historic perspective, although the systematic flights from 1945-46 were apparently the first photogrammetric project covering most of Spanish territory (Fernández and Quirós, 1977), the 1956 dataset is probably the oldest covering Almeria. Undertaken by the United States government, it is often referred to in Spain as the "American flight" and in most regions of the country marks the start of the archival record of metric aerial photography. It is therefore regarded as a valuable national information source for photo interpretation and land use evolution. As shown in **Figure 1.1**, four photographs from this dataset were required to cover the entire study area.

As indicated in Datasets section, full camera calibration details of these cameras were unknown. Moreover, these old cameras had no corner fiducial marks, as more recent cameras do. Instead they relied on only four marks in the middle of the edges of the photo frames to allow for interior orientation in the plate carriers of analogue stereoplotters of the time.

The 1977 dataset consisted of a panchromatic analogue photogrammetric flight that is commonly referred to in Spain as the "agriculture photogrammetric flight". Four stereo pairs from this survey, with a B/H ratio of 0.55, were used to cover the study area (**Figure 1.1**). The camera calibration certificate was unavailable. The eight photographs were scanned into a TIFF format from the original negatives using a photogrammetric scanner with a geometric resolution of 15 μm and 8 bit radiometric resolution, presenting a GSD of approximately 0.27 m. The photography from this flight had four fiducial marks in the corners of the frame.

For the 2009 dataset, image orientation was directly measured using a GPS/INS system on board the aircraft which was used to aid the photogrammetric block triangulation. This flight was used to photogrammetrically generate new 3D ground points to be subsequently transferred to the older datasets.

Table 1.5. Main characteristics of the analyzed archival photogrammetric datasets. GSD: ground sample distance; DGPS: differential Global Positioning System; SP: stereophotogrammetry. Ground points: horizontal (h) and vertical (v).

Date	*No. of images*	*Scale*	*Flying height (m)*	*Principal distance (mm)*	*Scan resolution (μm)*	*GSD (m)*	*Image Type*	*DGPS/SP ground points*
1956	4	1/ 33 000	5650	154.19/ 153.01	21	0.70	B/W	86 h/ 84 v
1977	8	1/ 18 000	2980	152.77	15	0.27	B/W	89 h/ 77 v

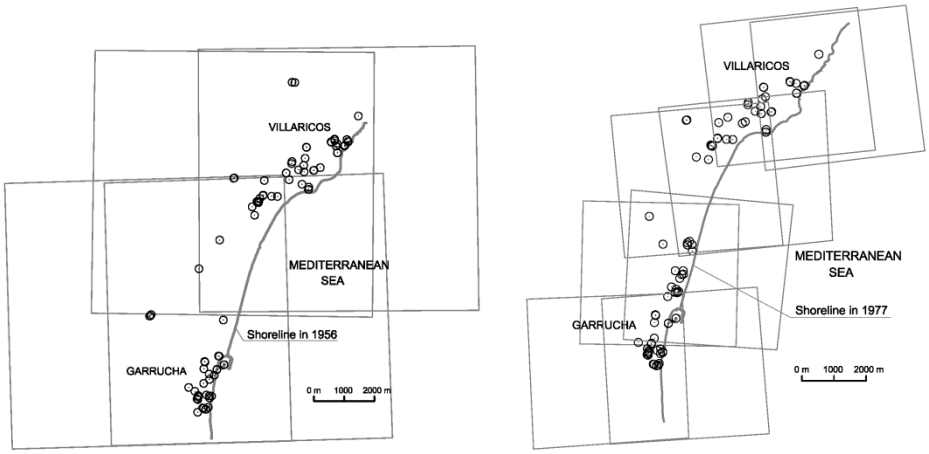

Figure 1.5. Configuration scheme for photography, ground points, and shoreline in the two archival datasets tested: 1956 (left) and 1977 (right). Note that the coastline position limits the collection or an optimal distribution of GCPs.

In conventional aerial surveys, the coordinates of ground points (both GCPs and CPs) are collected at the same time as the photogrammetric survey using topographic surveying techniques. In this case, due to the lack of any such data, man-made and natural points located inside the study area were unambiguously identified in the two archival datasets being assessed. Most ground points were obtained by a differential global positioning system (DGPS) using a Topcon HiPer PRO GOS receiver working in real time kinematic (RTK) mode. The coordinates of 150 ground points, located on well-defined features, were measured with reference to the European Terrestrial Reference System 1989 (ETRS89) and UTM projection. The vertical datum took the geoid as the reference surface, adopting the mean sea level in the calm seas of Alicante, Spain, as the null orthometric height datum. The DGPS observations were supported by eleven survey points: four

belonging to the national geodetic network, one obtained using high precision GPS techniques (Spanish REGENTE network), and six survey points provided by REDIAM (Red de Información Ambiental de Andalucía). The root mean square errors (RMSE) obtained were 56 mm, 33 mm and 76 mm in the X, Y and Z axes respectively.

The task of identifying ground points for the archival datasets was very difficult due to the significant changes in the coastal fringe during the last five decades. It proved especially difficult in the case of the 1956 dataset because of several reasons: it was the oldest photography, the original film was not well preserved, and the photographic scale was relatively small. These factors are exemplified in **Figure 1.2** and **Figure 1.3**. As a result of this, of the original 150 survey points, only 47 and 51 DGPS ground points could be used for 1956 and 1977 flights respectively. Furthermore, because of the coastal scenes and significant changes in its landscape, the spatial distribution of these ground points was poor. To improve this situation, 45 additional ground points, for which direct access with GPS was very difficult, were observed from the aforementioned 2009 photogrammetric dataset using a SOCET SET® v.5.3 digital photogrammetric workstation by BAE Systems. 39 and 38 of these points were finally used in the 1956 and 1977 triangulation projects, respectively. For a number of these points, typically corners of buildings where there was an apparent height change over time, only horizontal coordinates were utilised. The estimated accuracy of the 2009 photogrammetric project, calculated as the three-dimensional root mean square error ($RMSE_{3d}$) on 57 check points measured by DGPS, was 0.247 m ($RMSE_x$ 0.136 m; $RMSE_y$ 0.123 m and $RMSE_z$ 0.167 m).

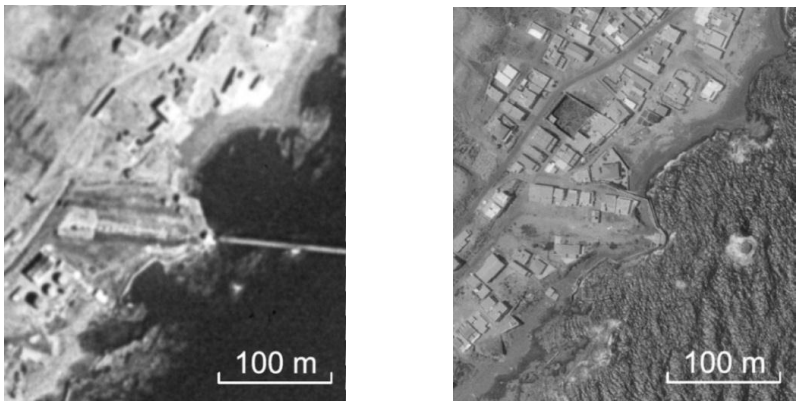

Figure 1.6. Coastal village of Villaricos on 1956 (left) and 1977 (right).

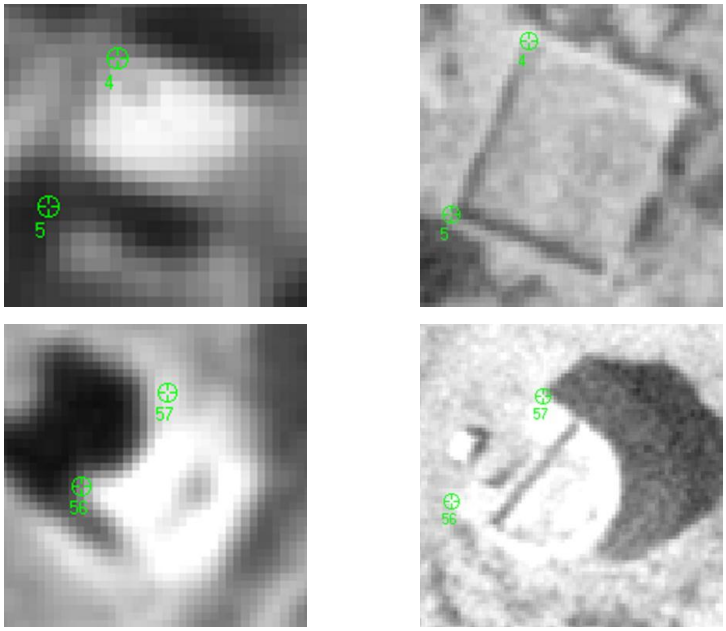

Figure 1.7. Ground points marked on the same features as they can be visualized in the 1956 (left) and 1977 (right) photogrammetric datasets tested.

Self-Calibrating Bundle Adjustment Models

Five self-calibrating bundle adjustment models were tested on the two historic flights using a variable number of GCPs. These models were compared with bundle adjustments conducted without self-calibration models (subsequently referred to as no self-calibration, NSC). All the photogrammetric projects were carried out using LPS 9.1® software, produced by Leica Geosystems.

The NSC bundle adjustment was applied to both historic datasets. The principal distance and principal point position were held fixed. The principal distance printed as marginal data in the aerial photography was used as the camera calibration information and the principal point was set to x_0=0 and y_0=0, so that no offset was assumed between the principal point and the fiducial centre. In order to solve the interior orientation, the photo-coordinates for the fiducial marks were required for each camera used. With no fiducial mark information available, the following steps were carried out: (i) a digital photograph at the correct scale was loaded into CAD software; (ii) a translation was computed such that the image coordinates of the point where the lines joining opposite fiducial marks intersected was assigned as the origin (zero) of the photo-coordinates; (iii) a rotation was applied to fix the angle between the principal point and the first fiducial mark to 0º (in cases where the fiducial marks were only available along the edges of the photo frame) or 45º (where the fiducial marks were placed in the

corners of the photo frame); (iv) the image coordinates of the fiducial marks were precisely measured on each digital image using the CAD software; (v) finally, the mean of the fiducial mark coordinates for all the photographs in every dataset were used to compute each camera's interior orientation. Note that for the 1956 dataset two cameras were used, thus two different sets of fiducial marks and principal distances were entered.

Besides the NSC bundle adjustment triangulation, five other self-calibrating bundle adjustment triangulations (advanced options in the aerial triangulation module of the LPS software) were undertaken. These models are incorporated in the collinearity equations, which allow for the modelling of various systematic errors associated with the camera/sensor model and atmospheric refraction. Five different self-calibrating models can be used in the triangulation process offered by LPS:

(1) *Lens distortion model*. This is designed to self-calibrate the lens distortion parameters automatically. This model has two APs (k_1 and k_2).

(2) *Bauer's simple model*. This has three APs, two parameters determine the extent of affine deformation (non-orthogonality and scale differential between the two axes in space image) and one parameter estimates symmetric lens distortion.

(3) *Jacobsen's simple model*. This has four APs, which compensate for the first and second order distortions associated with affine deformation and lens distortion.

(4) *Ebner's orthogonal model*. This model has twelve APs which compensate for various types of systematic error. It mathematically models and eliminates the systematic image errors in the location of the Von Gruber points, without any physical background. Since a greater number of parameters are estimated, an increased number of GCPs are required.

(5) *Brown's physical model*. This has fourteen APs which compensate for most of the linear and non-linear forms of film and lens distortion.

Further information regarding all models implemented in LPS can be found in the Leica Photogrammetry Suite Project Manager (Leica 2006).

Photogrammetric Projects from the 1956 and 1977 Datasets

90 individual photogrammetric experiments were performed using the 1956 dataset. Six triangulation models, both with and without self-calibration models, were tested (NSC, lens distortion, Bauer's, Jacobsen's, Ebner's and Brown's). Three different repetitions of 9, 18, 27, 36 and 45 GCPs, obtained either by DGPS or from the 2009 flight, were extracted from the initial 86 ground points. The 15 sets of GCPs extracted had the best possible distribution, although some weak areas were identified. Once the task of observing every ground point (GCPs and CPs) in image

space was complete (noting that the interior orientation and photo-coordinates for each ground point remained constant for every project), the LPS automatic tie point collection was performed. Thus, 44 tie points were automatically generated for the 1956 flight. These were visually checked and manually edited as required. The exterior orientation of each photogrammetric project was then computed. Because any aerial triangulation accuracy assessment should ideally be based upon CPs, in other words those ground points not used in the aerial triangulation process, the remaining ground points were used as CPs for computation of the $RMSE_{3d}$ for each photogrammetric project. The number of CPs therefore ranged from 41 to 77, depending on the number of GCPs employed.

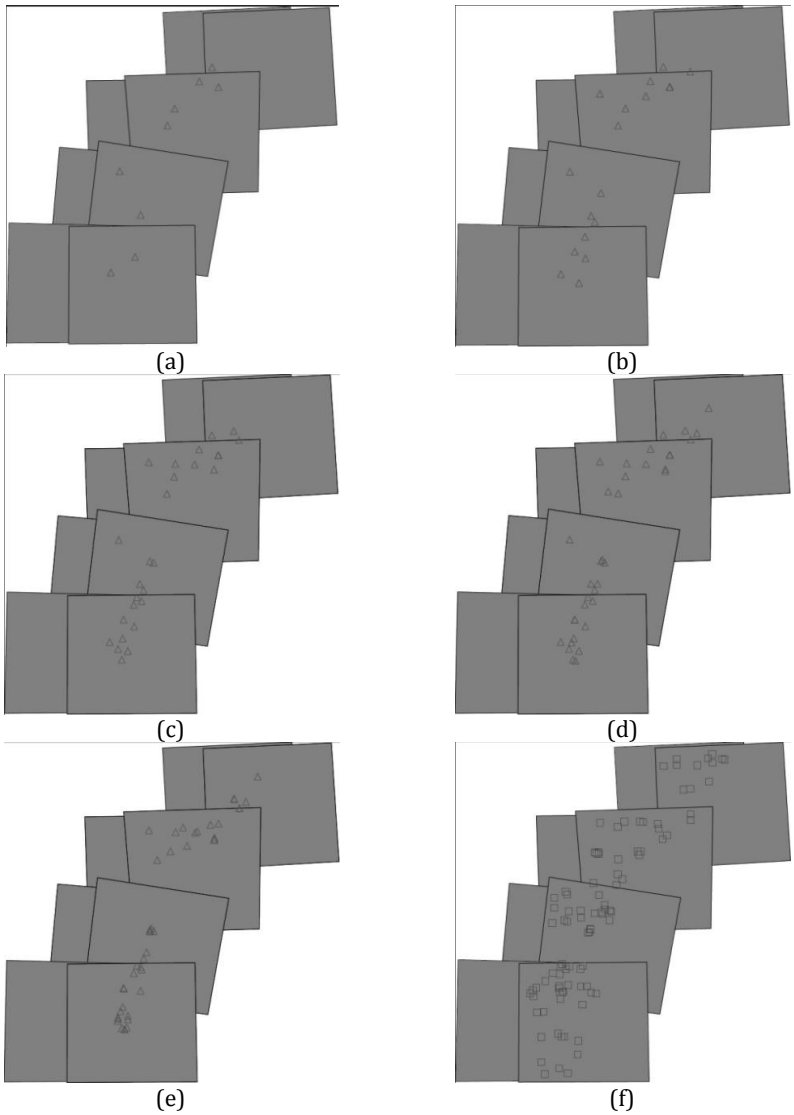

Figure 1.8. Distribution of one of the three sets of GCPs and tie points used in the 1977 dataset. (a) 9 GCPs; (b) 18 GCPs; (c) 27 GCPs; (d) 36 GCPs; (e) 45 GCPs; (f) tie points.

The same methodology was followed for the 1977 dataset. In this way, 90 photogrammetric cases were computed, but in this instance 89 ground points and 95 tie points were used to compute the bundle adjustment for every photogrammetric block. The 15 groups of GCPs showed a slightly better distribution than in the 1956 case, although there were still zones where new urbanisation meant new ground points could not be measured (**Figure 1.4**).

Statistical Analysis

In order to study the influence of different factors on aerial triangulation accuracy, analysis of variance (ANOVA) tests were utilised. ANOVA is a common statistical tool used to analyse datasets for which the importance of several factors is evaluated at once (Snedecor, Cochraw 1980). In this case, the observed variables in the ANOVA for the designed factorial model with three repetitions were the planimetric RMSE ($RMSE_p$), vertical RMSE ($RMSE_z$), and $RMSE_{3d}$, corresponding to 1956 and 1977 projects. The sources of variation, or factors, were the number of GCPs, the employed self-calibration method, and the cross-interactions between them all. When the results of the ANOVA turned out to be significant, the separation of means was carried out using Duncan's multiple range test at a 95% confidence level.

It is noteworthy that all the residual populations at the X, Y, and Z axes were tested for the normality of their distribution by means of the Kolmogorov–Smirnov test. Furthermore, no blunder errors were identified at the residual populations after applying the 3-sigma rule (Daniel, Tennant 2001).

RESULTS

Two independent statistical tests were developed using the accuracy estimates for the triangulations ($RMSE_p$, $RMSE_z$ and $RMSE_{3d}$ values obtained using CPs) as observed variables. They were carried out from the 90 photogrammetric cases generated with both 1956 and 1977 datasets respectively. Within these statistical tests, the observed variance was partitioned into components due to the different sources of variation which had been considered. The two main factors analysed (namely the number of GCPs and the method of self-calibration) were significant at the 95% level for both the 1956 and 1977 datasets. In both cases the number of GCPs had the most significant repercussion in the ANOVA model, followed by the method of self-calibration. However, the interaction between the self-calibration method and the number of GCPs was not found to be significant, indicating that there are no statistical differences among the performance of the six calibration methods regarding the number of GCPs required to perform the triangulation.

Table 1.6. Global comparison of mean values expressed in metres (m) of $RMSE_p$, $RMSE_z$, and $RMSE_{3d}$ from the 1956 and 1977 projects depending on the number of GCPs and self-calibration method. RMSE values given in planimetry (p), height (z) and 3D (3d). Values in the same column followed by different superscript letters (a, b, c) indicate significant differences at a 95% significance level (p < 0.05).

	1956			*1977*		
	$RMSE_p$	$RMSE_z$	$RMSE_{3d}$	$RMSE_p$	$RMSE_z$	$RMSE_{3d}$
No. of GCPs						
45	1.330^{ab}	1.438^{a}	1.961^{ab}	0.273^{a}	0.377^{a}	0.466^{a}
36	1.290^{a}	1.431^{a}	1.929^{a}	0.276^{a}	0.371^{a}	0.463^{a}
27	1.266^{a}	1.450^{a}	1.928^{a}	0.282^{a}	0.405^{a}	0.494^{a}
18	1.344^{ab}	1.555^{a}	2.058^{ab}	0.299^{b}	0.478^{b}	0.566^{b}
9	1.579^{b}	1.843^{b}	2.438^{b}	0.334^{c}	0.618^{c}	0.707^{c}
Self-Calibration Method						
Lens distortion	1.348^{ab}	1.415^{a}	1.958^{a}	0.287^{ab}	0.445^{ab}	0.530^{ab}
Brown	1.312^{a}	1.570^{b}	2.049^{ab}	0.277^{a}	0.411^{a}	0.496^{a}
Jacobsen	1.379^{ab}	1.562^{ab}	2.087^{b}	0.303^{c}	0.458^{ab}	0.551^{ab}
Bauer	1.374^{ab}	1.571^{b}	2.091^{b}	0.300^{c}	0.451^{ab}	0.544^{ab}
Ebner	1.341^{a}	1.600^{b}	2.091^{b}	0.297^{bc}	0.433^{ab}	0.528^{ab}
NSC	1.418^{b}	1.542^{ab}	2.103^{b}	0.294^{bc}	0.501^{b}	0.585^{b}

Influence of the Number of GCPs on Triangulation Accuracy

1956 Dataset. Table 1.2 shows the global comparison of mean values of $RMSE_p$, $RMSE_z$, and $RMSE_{3d}$ from 1956 and 1977 projects according to the number of GCPs and self-calibration methods. For example, 1.330 m is the $RMSE_p$ mean value obtained for all the photogrammetric projects carried out using the 1956 dataset and 45 GCPs for any self-calibration model, whereas 1.348 m is the $RMSE_p$ mean value for all 1956 dataset's projects using the model of lens distortion for any number of GCPs. For the 1956 flight, the worst accuracies were generated using 9 GCPs. In theory, of course, with more GCPs the accuracy should improve. Thus, the significant differences presented in Table 1.2 imply 27 GCPs would be optimal for this flight in terms of $RMSE_p$ and $RMSE_{3d}$ (i.e. for $RMSE_p$, 1.266 m using 27 and 1.290 m with 36 GCPs are the only values in this column which present significant differences with the mean value of 1.579 m attained using 9 GCPs because the 1.266 and 1.290 m values are the only ones without the letter "b", which accompanies the 9 GCPs value). However, 18 GCPs would be the ideal number of GCPs in the case of $RMSE_z$. Bearing in mind that GCPs were distributed across different numbers of stereo pairs for each flight, it is perhaps prudent to refer to the ratio of the number of GCPs per stereo pair. In this manner, the ideal ratio for the 1956 flight could range from 9 to 14 GCPs per stereo pair.

1977 Dataset. In the case of the 1977 flight and for $RMSE_p$, $RMSE_z$, and $RMSE_{3d}$, the best and significantly different ($p < 0.05$) accuracies were generated when 27, 36 or 45 GCPs were used (Table 1.2). Although the RMSE values for 36 and 45 GCPs were better than those attained using only 27 GCPs, no statistical differences were found. Thus, the optimal number of GCPs is around 7 per stereo pair for this flight.

Influence of Self-Calibration Method on Triangulation Accuracy

The general results regarding the tested self-calibration models are also depicted in Table 1.2. These results are provided in more detail in Table 1.3 and Table 1.4 for the 1956 and 1977 datasets respectively, comparing the accuracies attained by applying the different self-calibration methods and varying the number of GCPs. Furthermore, the standard deviations corresponding to three repetitions are shown in brackets as an indicator of the variability of the planimetric, vertical and three-dimensional RMSE mean values.

1956 Dataset. The results attained by the self-calibration models tested for the 1956 archival flight were very changeable depending on the RMSE analysed (Table 1.2). While the models of Brown and Ebner presented the best planimetric accuracies, the lens distortion model showed the best vertical results. In fact, when the number of GCPs was up to 27, only the lens distortion model could improve the vertical accuracies attained without self-calibration (Table 1.3). It is noteworthy that using 27 GCPs (Table 1.3), the $RMSE_p$ mean value for Brown's model was statistically better than those obtained using the lens distortion model or without self-calibration.

The best overall accuracy in terms of $RMSE_{3d}$ was achieved by means of the lens distortion model (Table 1.2), although very closely followed (and without significant differences at $p < 0.05$) by Brown's model. The models of Jacobsen, Bauer, Ebner and NSC presented values that were statistically different to the lens distortion model. Regarding the detailed results for the number of GCPs used, the lens distortion model always attained the best accuracies, though being significantly better against the models of Bauer, Jacobsen and Ebner only for the case of 36 GCPs (Table 1.3). The standard deviations from the three repetitions, presented in Table 1.3, were almost always higher for NSC than for any of the self-calibration models. That was true especially when the aerial triangulation was undertaken with a low number of GCPs. Hence the results from the self-calibration methods can be deemed as more reliable.

The accuracy improvements achieved in the 1956 dataset using the lens distortion model compared with NSC were very dependent on the number of GCPs used. Also it was very dependent on the RMSE type being analysed (planimetric or vertical). Thus, using 9 GCPs, $RMSE_p$ improved to approximately 0.15 m (a relative improvement of 9%), while $RMSE_z$ diminished to 0.22 m (11% degradation). On

the other hand, when 27 GCPs were used, $RMSE_p$ was only improved to around 0.05 m (a relative improvement of approximately 3.8%), while $RMSE_z$ decreased to about 0.12 m (8.3% degradation).

Table 1.7. 1956 archival flight. Mean values and standard deviations (in brackets), of accuracy estimates for the triangulations ($RMSE_p$, $RMSE_z$ and $RMSE_{3d}$) measured in CPs (horizontal, h, and vertical, v) regarding the number of GCPs and the self-calibration method. Values in the same row followed by different superscript letters (a, b, c) indicate significant differences at a significance level p < 0.05. Values in rows without superscripts indicate no significant differences.

No. of GCPs	No. of CPs	Accuracy (m)		Self-calibration method					
				NSC	Lens	Bauer	Jacobsen	Ebner	Brown
9	77 h 75 v	$RMSE_p$	Mean	1.647	1.499	1.598	1.613	1.593	1.526
			SD	0.081	0.048	0.222	0.208	0.037	0.113
		$RMSE_z$	Mean	1.987	1.769	1.926	1.882	1.748	1.748
			SD	0.738	0.219	0.192	0.181	0.218	0.235
		$RMSE_{3d}$	Mean	2.609	2.321	2.514	2.488	2.369	2.329
			SD	0.573	0.188	0.019	0.040	0.136	0.114
18	68 h 66 v	$RMSE_p$	Mean	1.372	1.309	1.363	1.383	1.339	1.300
			SD	0.083	0.099	0.097	0.113	0.066	0.071
		$RMSE_z$	Mean	1.585	1.433	1.568	1.555	1.622	1.567
			SD	0.300	0.206	0.131	0.082	0.126	0.076
		$RMSE_{3d}$	Mean	2.099	1.944	2.080	2.082	2.106	2.038
			SD	0.281	0.186	0.110	0.105	0.056	0.033
27	59 h 57 v	$RMSE_p$	Mean	1.346^{c}	1.295^{bc}	1.258^{ab}	1.254^{ab}	1.234^{ab}	1.209^{a}
			SD	0.048	0.058	0.032	0.035	0.040	0.018
		$RMSE_z$	Mean	1.390	1.274	1.468	1.469	1.582	1.513
			SD	0.124	0.056	0.098	0.095	0.185	0.160
		$RMSE_{3d}$	Mean	1.936	1.818	1.933	1.932	2.010	1.939
			SD	0.108	0.037	0.091	0.087	0.132	0.117
36	50 h 48 v	$RMSE_p$	Mean	1.351	1.309	1.300	1.296	1.250	1.236
			SD	0.111	0.112	0.022	0.022	0.031	0.035
		$RMSE_z$	Mean	1.374	1.279	1.459	1.464	1.527	1.484
			SD	0.055	0.033	0.087	0.089	0.040	0.027
		$RMSE_{3d}$	Mean	1.928^{ab}	1.832^{a}	1.955^{b}	1.957^{b}	1.973^{b}	1.932^{ab}
			SD	0.101	0.067	0.053	0.055	0.030	0.020
45	41 h 39 v	$RMSE_p$	Mean	1.372	1.327	1.353	1.350	1.291	1.289
			SD	0.110	0.114	0.049	0.050	0.053	0.061
		$RMSE_z$	Mean	1.375	1.321	1.434	1.440	1.524	1.536
			SD	0.077	0.037	0.095	0.093	0.107	0.075
		$RMSE_{3d}$	Mean	1.943	1.874	1.972	1.975	1.998	2.005
			SD	0.115	0.088	0.077	0.079	0.086	0.084

Table 1.8. 1977 archival flight. Mean values and standard deviations (in brackets), of accuracy estimates for the triangulations ($RMSE_p$, $RMSE_z$ and $RMSE_{3d}$) measured in CPs (horizontal; h and vertical; v) regarding the number of GCPs and the self-calibration method. Values in the same row followed by different superscript letters indicate significant differences at a significance level $p < 0.05$. Values in rows without superscripts do not present significant differences.

No. GCPs	No. CPs	Accuracy (m)		Self-calibration method					
				NSC	Lens	Bauer	Jacobsen	Ebner	Brown
9	80 h 68 v	$RMSE_p$	Mean	0.328	0.334	0.333	0.339	0.338	0.331
			SD	0.018	0.014	0.011	0.014	0.014	0.021
		$RMSE_z$	Mean	0.778	0.570	0.587	0.609	0.638	0.524
			SD	0.260	0.162	0.161	0.199	0.162	0.043
		$RMSE_{3d}$	Mean	0.849	0.665	0.678	0.702	0.725	0.621
			SD	0.235	0.135	0.138	0.176	0.140	0.034
18	71 h 59 v	$RMSE_p$	Mean	0.297	0.293	0.309	0.312	0.304	0.281
			SD	0.021	0.030	0.021	0.022	0.036	0.030
		$RMSE_z$	Mean	0.563	0.465	0.469	0.472	0.468	0.432
			SD	0.137	0.075	0.082	0.077	0.085	0.032
		$RMSE_{3d}$	Mean	0.638	0.549	0.563	0.567	0.561	0.516
			SD	0.127	0.079	0.070	0.063	0.070	0.040
27	62 h 50 v	$RMSE_p$	Mean	0.286^{b}	0.278^{b}	0.290^{b}	0.292^{b}	0.285^{b}	0.261^{a}
			SD	0.006	0.010	0.003	0.005	0.011	0.010
		$RMSE_z$	Mean	0.446	0.415	0.410	0.417	0.377	0.367
			SD	0.063	0.036	0.041	0.042	0.048	0.042
		$RMSE_{3d}$	Mean	0.530^{b}	0.499^{ab}	0.503^{ab}	0.509^{ab}	0.474^{ab}	0.450^{a}
			SD	0.057	0.035	0.032	0.033	0.037	0.036
36	53 h 41 v	$RMSE_p$	Mean	0.281^{c}	0.268^{b}	0.285^{c}	0.287^{c}	0.280^{c}	0.258^{a}
			SD	0.004	0.005	0.003	0.004	0.006	0.005
		$RMSE_z$	Mean	0.372^{ab}	0.390^{b}	0.390^{b}	0.394^{b}	0.333^{a}	0.351^{ab}
			SD	0.031	0.020	0.020	0.022	0.029	0.028
		$RMSE_{3d}$	Mean	0.466^{ab}	0.473^{ab}	0.483^{b}	0.487^{b}	0.435^{a}	0.435^{a}
			SD	0.027	0.019	0.015	0.017	0.023	0.025
45	44 h 32 v	$RMSE_p$	Mean	0.277^{b}	0.262^{a}	0.284^{b}	0.284^{b}	0.277^{b}	0.253^{a}
			SD	0.007	0.006	0.003	0.003	0.009	0.007
		$RMSE_z$	Mean	0.346	0.385	0.400	0.400	0.347	0.382
			SD	0.029	0.034	0.045	0.044	0.036	0.065
		$RMSE_{3d}$	Mean	0.444	0.466	0.491	0.491	0.445	0.459
			SD	0.022	0.031	0.039	0.037	0.033	0.058

1977 Dataset. For the 1977 flight, Brown's model could be considered as the optimal method overall, presenting significant differences ($p < 0.05$) with respect to the NSC approach for planimetric, vertical and three-dimensional RMSE mean values (Table 1.2). However, when the results were qualified by the number of GCPs (Table 1.4), Brown's model was only statistically better than using NSC in the case of 27 GCPs. The 1977 imagery had better radiometric quality and a larger scale than the 1956 dataset (**Figure 1.2**), reducing the pointing error when measuring GCP positions in image space. Furthermore, the photography was acquired more recently and so the available GCP distribution was slightly better than for the 1956 dataset. In this sense, it is noteworthy that the standard deviations for the accuracy values in 1977 presented in Table 1.4 were smaller than those for the 1956 flight.

Regarding accuracy improvements achieved in the 1977 dataset using Brown's model, $RMSE_p$ did not change when the 9 GCPs scheme was applied, whereas $RMSE_z$ diminished to around 0.25 m (a 33% relative improvement). However, when 36 GCPs were used, the $RMSE_p$ and $RMSE_z$ values only improved to around 0.02 m (a relative improvement of approximately 8% and 5.6% respectively). As in the 1956 dataset, a relatively small accuracy improvement was attained by self-calibration when a high number of very accurate GCPs were used.

DISCUSSION

Regarding the number of GCPs, in previous work Aguilar, Aguilar & Negreiros (2010) attained similar accuracies when applying the self-calibration models included in the LPS software with 24 GCPs and 12 GCPs, using only one stereo pair at a scale of 1:5 000 for a flight taken in 2001 with a Zeiss RMK TOP 15 camera. On the other hand, Walstra (2006) estimated the interior orientation of five vertical archival photographs without a calibration certificate in a self-calibrating bundle adjustment using between four and nine GCPs per stereo pair. In this case, the self-calibration was performed using GAP (General Adjustment Program) software developed by Chandler, Clark (1992). Considering these results, a suitable number of GCPs per stereo pair to perform self-calibrating bundle adjustment could be placed at between six and nine. However, in the case of very old flights where the prints or negatives have not been appropriately conserved, are very hazy, or are taken at small scales, it could be necessary to increase this ratio up to values closer to 14 GCPs per stereo pair.

With regard to the self-calibration models tested, previous works carried out upon photogrammetric datasets acquired with film or digital cameras have reported the successful use of self-calibrating bundle adjustment methods with additional parameters (Ackermann 1981, Cramer 2009). According to Kraus (1997), the proper use of self-calibration might improve the accuracy of conventional aerial triangulation by 50%.

With regard to which self-calibration model is best applied, the recommendations from other works are very variable. For example, Ebner's model was presented as the best self-calibration approach for analogue photogrammetric datasets by both Cardenal et al. (2006) and Aguilar, Aguilar & Negreiros (2010). Silva et al. (2008) identified the lens distortion model as the best self-calibration method included in the LPS software for correcting systematic errors in imagery taken with a Hasselblad digital camera. Alamús, Kornus & Talaya (2006) considered four independent sets of Ebner's self-calibration parameters (one for each image quadrant) in the block adjustments to model Intergraph DMC systematic errors detected in adjustments. Moreover, working with a stereo pair of conventional colour aerial photographs at a scale of 1:5 000, but scanned from negatives and using 24 GCPs, Aguilar, Aguilar & Agüera (2005) reported $RMSE_{3d}$ values of 0.252 m after the self-calibrating bundle adjustment was carried out using a low-cost close range software package. In this case, the principal point coordinates, affine image parameters (A, B) to correct for scale difference and non-perpendicularity of the x and y image coordinates, radial lens distortion parameters (k_1, k_2) and decentring lens distortion parameters (p_1, p_2) were calculated. Working on the same stereo pair and with the same aforementioned number of GCPs, Aguilar, Aguilar & Negreiros (2010) attained $RMSE_{3d}$ values of 0.153 and 0.157 m using the models of Ebner and Brown respectively.

All the works mentioned above point to the underlying hypothesis constituting the basis of the current work, namely that self-calibration techniques should be able to remove, at least partially, the presence of systematic errors. This was found to be true in many cases where certain conditions were fulfilled, such as: no correlation among additional parameters; good distribution of GCPs in three dimensions; highly redundant photographic coverage; low pointing errors in image space (pre-marked points); preferably highly convergent photography; and, maybe the most relevant constraint, where systematic deformations were similar for all images in the block. In other words, the additional parameters are treated as block invariant. Unfortunately this supposition is only correct in cases of homogeneous projects (such as one camera, one roll of film, same flight direction, and so on) where any significant random errors due to poor conservation of the images are absent. Indeed, the assumption of systematic image errors which are constant for a whole set of photography cannot always account for the total error budget, which would also include correlation and variation of image deformations within a series of photographs. As already demonstrated by other authors, sometimes it may even be recommend to apply alternative additional parameters to different strips or groups of photographs belonging to a certain area. In this sense it is necessary to clarify that any extrapolation of the results from a locally computed self-calibration bundle adjustment to those areas outside the area bounded by the GCPs (even in the same stereoscopic model) should definitely be avoided. In this project, it should be taken into account that the quality of the self-calibration will be compromised by the poor planimetric and vertical distribution

of GCPs due to the age of the imagery (and hence the difficulty in surveying proper GCPs), by the typical low relief of coastal areas (small vertical range) and by the presence of the sea occupying a high percentage of some photographs. However, all these characteristics are very common in archival photogrammetric imagery over coastal areas and, therefore, the approach is justified when working under real operational conditions.

Examining the 1956 dataset investigated here, it is noteworthy that $RMSE_{3d}$ attained using 9 GCPs and without self-calibration was about 3.7 times higher than the GSD, whereas using the lens distortion model with 27 GCPs this value decreased to 2.6 times the GSD. These low accuracies might be expected since the photography was very old and in poor condition. Furthermore, the photography had a low resolution and poor radiometric quality, which made it difficult to precisely measure the corresponding GCPs in image space (see **Figure 1.3** and **Figure 1.4**). Subsequently, the GCP pointing error arising from this dataset may be deemed as excessively large, thereby contributing to somehow masking the possible improvements derived from the application of the tested self-calibration models. In summary, there is an underlying masking effect due to higher degree sources of error as compared to the sort of systematic errors that can be properly modelled by self-calibration, which is very typical for archival photogrammetric imagery. Besides, the distribution of GCPs and tie points could be considered quite poor. As a reference, it should be noted that Cardenal et al. (2006) reported an accuracy of 3.86 m (measured as $RMSE_{3d}$ on CPs) working with imagery from the "American flight".

In the case of 1977 dataset, using 9 GCPs and without self-calibration, the $RMSE_{3d}$ was around 3.1 times higher than the image GSD. On the other hand, with 36 GCPs and applying the Brown's model, the $RMSE_{3d}$ value decreased to 1.6 times the image GSD. Walstra (2006) reported $RMSE_{3d}$ accuracies within the range of 1.31 m (4.8 GSD) and 0.63 m (2.3 GSD) for archival datasets acquired in 1971 and 1995 respectively, displaying a GSD similar to that of the 1977 flight investigated here.

Finally, a further reason which may explain why it is very difficult to highlight a single self-calibration method as optimal for all cases encountered in this work, could be related to the fact that the blocks are well-controlled. In this case, the standard bundle block adjustment (NSC case) could already be expected to compensate well for systematic errors. In that case additional parameters would only produce, at best, a relatively moderate improvement on the accuracy of adjusted coordinates. Given the low standard deviations computed when working with more than 18 GCPs (1956) or even only 9 GCPs in the case of the 1977 data, both blocks could be deemed as relatively well-controlled.

CONCLUSIONS

This chapter has addressed the important issue of adopting self-calibrating bundle adjustment models, as included in commercial software, to try to improve the accuracy of results attained from the photogrammetric triangulation of historic aerial imagery taken at different scales and times on a specific pilot area. The underlying hypothesis of this work proposes that self-calibration with additional parameters might model the difference between the theoretical perspective geometry and the real image geometry for archival aerial photography and so remove, at least partially, the presence of systematic errors. The research has involved extensive fieldwork that provided a large number of very accurate ground points (GCPs and CPs). The use of accuracy estimations based on a large number of CPs makes the findings of the study reliable. Moreover, repetitively undertaking each experiment has allowed the realisation of a full statistical analysis which enables the following conclusions to be drawn.

(1) *Number of GCPs used in triangulation*. The recommended number of accurate GCPs for performing a self-calibrating bundle adjustment with archival photography could be placed within the range of six to nine GCPs per stereo pair. However, when working with very old photography at small scales it could be necessary to increase this number to somewhere between 12 and 16 GCPs per stereo pair.

(2) *Self-calibrating bundle adjustment.* The best three-dimensional accuracies were achieved for the 1956 dataset using the lens distortion model, although this was very closely followed by Brown's model (without statistically significant differences). For the 1977 dataset, Brown's model was found to be the best self-calibration method. The recommendation should always be to test other models since each flight can present systematic errors of a different nature. In fact, the scale and special characteristics of each archival photogrammetric flight are, probably, the most important factor affecting the choice of self-calibration model. Therefore, every archival dataset should be treated in an independent and empirical way depending on its own particular characteristics. Furthermore, it may sometimes be recommended to apply alternative additional parameters to different strips or groups of photographs belonging to a certain spatial area. In this sense, it is necessary to clarify that any extrapolation of the results from a locally computed self-calibration bundle adjustment to those areas outside the area delimited by the GCPs (even within the same stereoscopic model) should definitely be avoided.

(3) *Accuracy improvement by applying self-calibration models.* Low relative three-dimensional accuracy improvements were achieved using self-calibration models when a high number of very accurate GCPs were available. $RMSE_p$ and $RMSE_z$ improved by around 4% to 8% with respect to NSC for the two archival datasets. However, the accuracy improvement for $RMSE_p$ ranged from 0% to 9%

when using only 9 GCPs, whereas $RMSE_z$ diminished by between 11% and 33%. Hence, self-calibration techniques included in LPS software would be especially interesting when the number of GCPs is small. There are two main reasons which could explain the relatively poor performance of the self-calibration applied in this work. Firstly, there is an underlying masking effect due to higher degree sources of error, as compared to the sort of systematic errors that can be properly modelled by self-calibration, which is very typical for archival photogrammetric imagery. The magnitude of such non-systematic errors could be much higher than systematic errors which can be solved by self-calibration. Thus the results are more heavily influenced by the number of GCPs used in the bundle adjustment than the self-calibration model employed. Furthermore the APs are computed as an average for the whole block, but each photograph could have its own systematic errors which would explain the reason why it is very difficult to point out a method as optimal for all the cases examined. The second reason relates to the fact that the blocks were relatively well-controlled. In these cases, the standard bundle adjustment of the block (NSC case) usually compensates well for systematic errors and additional parameters would only produce, at best, a moderate improvement on the accuracy of adjusted coordinates.

As further research, it would be useful to compare the optimised accuracies achieved here using a high number of very accurate GCPs with the results obtained by other approaches such as those based on surface matching. Such approaches, which will be faced in the next chapter, would avoid the costly and time-consuming necessity of collecting GCPs, which may be almost impossible to identify in archival photography.

REFERENCES

Ackermann, F. 1981, "Block adjustment with additional parameters", *Photogrammetria,* vol. 36, no. 6, pp. 217-227.

Aguilar, F.J., Aguilar, M.A., Fernández, I., Negreiros, J.G., Delgado, J. & Pérez, J.L. 2012, "A new two-step robust surface matching approach for three-dimensional georeferencing of historical digital elevation models", *IEEE Geoscience and Remote Sensing Letters,* vol. 9, no. 4, pp. 589-593.

Aguilar, M.A., Aguilar, F.J. & Agüera, F. 2005, "Mapping small areas using a low-cost close range photogrammetric software package with aerial photography", *Photogrammetric Record,* vol. 20, no. 112, pp. 335-350.

Aguilar, M.A., Aguilar, F.J. & Negreiros, J.G. 2010, "Self-calibration methods for using historical aerial photographs with photogrammetric purposes", *Anales de Ingeniería Gráfica,* vol. 21, pp. 33-40.

Akca, D. 2010, "Co-registration of Surfaces by 3D Least Squares Matching", *Photogrammetric Engineering and Remote Sensing,* vol. 76, no. 3, pp. 307-318.

Alamús, R., Kornus, W. & Talaya, J. 2006, "Studies on DMC geometry", *ISPRS Journal of Photogrammetry and Remote Sensing,* vol. 60, no. 6, pp. 375-386.

Amiri Parian, J. & Gruen, A. 2010, "Sensor modeling, self-calibration and accuracy testing of panoramic cameras and laser scanners", *ISPRS Journal of Photogrammetry and Remote Sensing,* vol. 65, no. 1, pp. 60-76.

Bauer, H. & Müller, J. 1972, "Height accuracy of blocks and bundle block adjustment with additional parameters", *12th Congress of the International Society for Photogrammetry and Remote Sensing (ISPRS),* Ottawa, Canada, 1972.

Cardenal, J., Delgado, J., Mata, E., González, A. & Olague, I. 2006, "Use of historical flight for landslide monitoring", *Proceedings of the 7th International Symposium on Spatial Accuracy Assessment in Natural Resources and Environmental Sciences*Lisbon, Portugal, 2006, pp. 129.

Chadwick, J., Dorsch, S., Glenn, N., Thackray, G. & Shilling, K. 2005, "Application of multi-temporal high-resolution imagery and GPS in a study of the motion of a canyon rim landslide", *ISPRS Journal of Photogrammetry and Remote Sensing,* vol. 59, no. 4, pp. 212-221.

Chandler, J.H. & Clark, J.S. 1992, "The archival photogrammetric technique: Further application and development ", *The Photogrammetric Record,* vol. 14, no. 80, pp. 241-247.

Chandler, J.H. & Cooper, M.A.R. 1989, "The extraction of positional data from historical photographs and their application to geomorphology", *Photogrammetric Record,* vol. 13, no. 73, pp. 69-78.

Cramer, M. 2009, *Digital Camera Calibration*, European Spatial Data Research (EuroSDR), Official Publication No. 55, Amsterdam, The Netherlands.

Daniel, C. & Tennant, K. 2001, "DEM quality assessment" in *Digital elevation model technologies and applications: the DEM users manual* , ed. D.F. Maune, American Society for Photogrammetry and Remote Sensing, Bethesda, Maryland, pp. 395-440.

Ebner, H. 1976, "Self-calibrating block adjustment", *Bildmessung und Luftbildwesen,* vol. 4, pp. 128-139.

Fernández, F., Quirós, F. 1997, "El vuelo fotográfico de la 'Serie A'", *Ería: Revista cuatrimestral de Geografía*, vol. 43, pp. 190-198.

Fraser, C.S. 1997, "Digital camera self-calibration", *ISPRS Journal of Photogrammetry and Remote Sensing,* vol. 52, no. 4, pp. 149-159.

Grün, A. 1978, "Experiences with self-calibrating bundle adjustment", *American Congress on Surveying and Mapping/American Society of Photogrammetry (ACSM-ASP),* Washington, D.C.

James, T.D., Murray, T., Barrand, N.E. & Barr, S.L. 2006, "Extracting photogrammetric ground control from lidar DEMs for change detection", *Photogrammetric Record,* vol. 21, no. 116, pp. 312-328.

Klein, H. 1979, "New results of bundle block adjustments with additional parameters", *Proceedings of 37th Photogrammetric Week,* Stuttgart, Germany.

Kraus, K. 1997, *Photogrammetry. Volume 2. Advanced methods and applications,* 4th edn, Dummler, Bonn, Germany.

Lane, S.N. 2000, "The measurement of river channel morphology using digital photogrammetry", *Photogrammetric Record,* vol. 16, no. 96, pp. 937-961.

Leica, G. 2006, *Leica Photogrammetry Suite Project Manager*, Leica Geosystems Geospatial Imaging, LLC, Norcross, Georgia, USA.

Li, Z., Xu, Z., Cen, M. & Ding, X. 2001, "Robust surface matching for automated detection of local deformations using least-median-of-squares estimator", *Photogrammetric Engineering and Remote Sensing,* vol. 67, no. 11, pp. 1283-1292.

Lichti, D.D. 2010, "Terrestrial laser scanner self-calibration: Correlation sources and their mitigation", *ISPRS Journal of Photogrammetry and Remote Sensing,* vol. 65, no. 1, pp. 93-102.

Marzolff, I. & Poesen, J. 2009, "The potential of 3D gully monitoring with GIS using high-resolution aerial photography and a digital photogrammetry system", *Geomorphology,* vol. 111, no. 1-2, pp. 48-60.

Miller, P., Mills, J., Edwards, S., Bryan, P., Marsh, S., Mitchell, H. & Hobbs, P. 2008, "A robust surface matching technique for coastal geohazard assessment and management", *ISPRS Journal of Photogrammetry and Remote Sensing,* vol. 63, no. 5, pp. 529-542.

Mills, J.P., Buckley, S.J. & Mitchell, H.L. 2003, "Synergistic fusion of GPS and photogrammetrically generated elevation models", *Photogrammetric Engineering and Remote Sensing,* vol. 69, no. 4, pp. 341-349.

Mills, J.P., Buckley, S.J., Mitchell, H.L., Clarke, P.J. & Edwards, S.J. 2005, "A geomatics data integration technique for coastal change monitoring", *Earth Surface Processes and Landforms,* vol. 30, no. 6, pp. 651-664.

Prokešová, R., Kardoš, M. & Medveďová, A. 2010, "Landslide dynamics from high-resolution aerial photographs: A case study from the Western Carpathians, Slovakia", *Geomorphology,* vol. 115, no. 1-2, pp. 90-101.

Schiefer, E. & Gilbert, R. 2007, "Reconstructing morphometric change in a proglacial landscape using historical aerial photography and automated DEM generation", *Geomorphology,* vol. 88, no. 1-2, pp. 167-178.

Silva, R.D., García, A.M., Galo, M., Kiyoshi, J. & Cesar, R. 2008, "Fototriangulação com parâmetros adicionais para câmaras digitais: uma avaliação experimental", *Boletim de Ciências Geodésicas,* vol. 14, no. 4, pp. 571-587.

Snedecor, G.W. & Cochraw, W.G. 1980, *Statistical Methods,* Seventh edn, The Iowa State University Press, Ames, Iowa, USA.

Véga, C. & St-Onge, B. 2008, "Height growth reconstruction of a boreal forest canopy over a period of 58 years using a combination of photogrammetric and lidar models", *Remote Sensing of Environment,* vol. 112, no. 4, pp. 1784-1794.

Walstra, J. 2006, *Historical aerial photographs and digital photogrammetry for landslide assessment.* Ph.D. thesis , Loughborough University, UK.

Walstra, J., Dixon, N. & Chandler, J.H. 2007, "Historical aerial photographs for landslide assessment: Two case histories", *Quarterly Journal of Engineering Geology and Hydrogeology,* vol. 40, no. 4, pp. 315-332.

Zanutta, A., Baldi, P., Bitelli, G., Cardinali, M. & Carrara, A. 2006, "Qualitative and quantitative photogrammetric techniques for multi-temporal landslide analysis", *Annals of Geophysics,* vol. 49, no. 4-5, pp. 1067-1080.

CHAPTER 2

A new two-step robust surface matching approach for 3D georeferencing of historical digital elevation models

ABSTRACT

3D surface matching techniques have been used for multi-date DEMs co-registration to help the quantification of terrain changes. In this chapter a new approach based on a two-step robust surface matching for DEM 3D georeferencing is proposed to avoid the costly and time-consuming GCPs acquisition. The procedure starts from a coarse orientation of the historical DEM where the stereo model y-parallax is removed by means of a traditional Automatic Relative Orientation. Additionally, it is recommendable to manually mark three GCPs (only approximated coordinates) just to apply a coarse Helmert 3D transformation, obtaining a preoriented stereo pair which turned out to be helpful to improve and speed up the subsequent surface matching process. The first step consists of an automatically process called shaded-relief image matching, basically headed up to improve the previous aforementioned coarse orientation. The second step starts from the absolute z-differences between reference and historical DEMs, allowing for the application of the widely known K-means algorithm to cluster up to four groups of homogeneous absolute z-differences. The two clusters showing the highest values are, thus, considered as areas where terrain has significantly changed. The remaining areas are deemed as potentially matching areas where the robust surface matching may be applied using the widely known Tukey's Biweight (TB) M-estimator. In this way the diagonal weight matrix, regarding the TB function, is introduced in an iterative least-square routine to compute the Helmert 3D transformation parameters to finely georeference the historical DEM.

The proposed methodology was tested for georeferencing a historical grid format DEM (1977 photogrammetric flight). A 10 m grid-spacing DEM generated from a higher scale photogrammetric flight taken in 2001 was used as the reference surface. Two accurate DEMs based on LiDAR technology taken in 2004 and 2009 were also employed to validate the final georeferenced product.

The results obtained from this work may be deemed as very promising, showing a high efficiency and accuracy for historical DEM 3D georeferencing. The first step, i.e. shaded-relief image matching, was not always needed, mainly depending on the quality of the preorientation stage. The vertical accuracy for the finally co-registered DEM was computed over a validation dataset, presenting relatively non-altered or stable areas and yielding a computed uncertainty (standard deviation of the z-differences) close to 1.09 m. That is fairly similar to the estimated uncertainty for the reference DEM.

Keywords: Matching; DEM/DTM; georeferencing; monitoring; change detection

INTRODUCTION

Spatial registration of multi-date data is required for many applications in remote sensing, such as change detection, the construction of image mosaics, DEMs generation from stereo pairs, and orthorectification. Focusing on coastal area, it is widely recognized that it is one of the greatest environmental and economic assets for a nation. In fact, coastal vulnerability studies are experimenting a growing demand because of the threatening tourism and construction development joined to the future scenario of widely predicted sea level rise (SLR) and coastal flooding due to climate change (Titus et al. 2009). Indeed, DEMs are usually used to model SLR vulnerability (Cowell, Zeng 2003) and coastal flood risk (Webster et al. 2006). Furthermore, DEM change detection within a certain time period may be also used to automatically quantify terrain changes owing, for instance, to urban development.

The geometric correction for spatial registration of multi-date data must be accurate enough, because misalignments of features at the same location could render useless results. In this sense, many researchers have adopted 3D surface matching techniques without control points to automatically co-register multi-temporal DEMs, usually using the newer DEM as the reference surface to achieve the 3D registration of an older and generally less accurate DEM (Rosenholm, Torlegard 1988, Pilgrim 1996, Li et al. 2001, Miller et al. 2008, Zhang, Cen 2008). Regarding surface matching, it is based on three-dimensional conformal transformations, requiring the computation of three rotations, three translations and a global scale parameter, so that the un-oriented DEM is transformed to the coordinate system of the reference DEM (Mills et al. 2005).

On the other hand, nowadays DEM production is efficiently accomplished by means of LiDAR technology which is contributing, often coupled with passive optical imaging, to a wide range of coastal scientific investigations (Brock, Purkis 2009). Nonetheless, as LiDAR is a relatively new technology, historical data beyond the past decade are practically unavailable (James et al. 2006). This is the reason why most of the studies headed up to extract shoreline position and evolution along a certain period of time (i.e. monitoring studies) are mainly based on rectified aerial photographs, beach profiles from surveying techniques and topographic maps.

Despite DEMs are deemed as the best choice to extract accurate shoreline position (Aguilar et al. 2010a), few attempts have involved stereo-photography and, thus, 3D information extraction to monitor shoreline evolution. Taking into account that the accuracy of DEMs is clearly bound to the accuracy of the derived variables via error propagation (Aguilar et al. 2010b), it is crucial to start from the best possible DEM, both for newly-made DEMs and for historical DEMs (mostly compiled from historic stereo photogrammetric flights).

The same could be said about terrain change detection from multi-date stereo-photogrammetric flights, where it is necessary to count on a precise and well distributed set of GCPs to attain the georeferenced DEM. So, taking the idea a bit further, the latter approach requires a number of GCPs to compute the absolute orientation of every stereo pair, a survey task that usually becomes inefficient and costly because of the difficulty to accurately identify and survey a suitable set of ground points which could be pointed on the corresponding historic photographs. In fact, those GCPs are cumbersome to obtain in remote areas or from relatively old flights, simply because historical features are difficult to be currently localized, measured and even pointed out onto the digital images (**Figure 2.1**), depending on their scale, resolution and radiometric quality. Additionally, the current process of manual GCP measurement may be prohibitively labour-intensive for large projects under operational conditions, and it does not enforce sub-pixel level correlation between images due to the limitation of human visual interpretation. Finally, and with regard to extract high quality topographic data from historical imagery, GCPs should also be of high quality and well distributed over the photographs (Aguilar et al. 2013). This is especially important when camera calibration information is incomplete or unavailable (James et al. 2006).

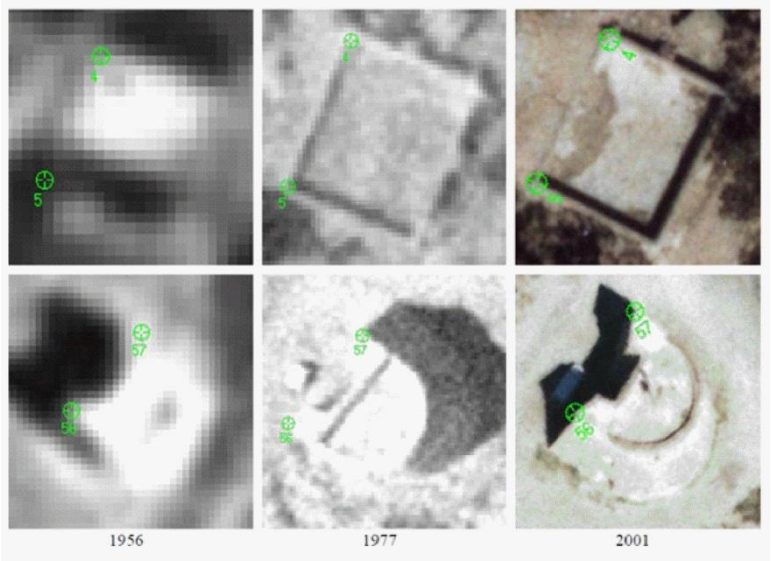

Figure 2.12. Example with regard to typical troubles on ground points location working on historical photogrammetric images (approximated scales: 1956-1:33000, 1977-1:18000, 2001-1:5000).

Given the aforementioned shortcomings of historical DEMs co-registration, the main goal of this work is to develop, test and validate a new rapid, efficient and robust surface matching procedure, non-sensitive to actually true terrain changes (considered as outliers in the surface matching jargon) and able to georeference

very-coarsely-oriented historical DEMs using a newer DEM as the reference surface without the need of GCPs.

SURFACE MATCHING APPROACH

The basic flow chart diagram regarding the new two-step robust surface matching fundamentals is shown in **Figure 2.2** (step 1) and **Figure 2.3** (step 2). Briefly, the proposed method starts from a pre-processing stage of the historical DEM applied onto previously digitized photographs, where the stereo model y-parallax is removed by means of the Automatic Relative Orientation (ARO), a widely known photogrammetric procedure.

Subsequently, suitable photogrammetric software must be utilised to carry out the interior orientation and the ARO process. In this case, ImageStation Digital Mensuration software (ISDM 4.0® by Z/I Imaging) was employed. ARO is the procedure that determines the relationship between two overlapping images, providing the position and attitude of one image with respect to another image by automatically matching tie points. Thus, it is an unattended process. Nonetheless it is worthy to manually mark three control points (two full points XYZ and one only Z point) to apply a coarse three-dimensional conformal transformation (seven-parameters Helmert 3D), so obtaining a preoriented stereo pair which will be very helpful to improve and speed up the convergence of the subsequent robust surface matching process. It is noteworthy that those ground points only have to present approximated coordinates, both horizontal and vertical, so they can be easily extracted from available orthophotos (horizontal) and supposing a common Z coordinate (e.g. an average ground height for the whole working area).

In this way, a DSM or, after applying a filtering process, a Digital Terrain Model (DTM), may be obtained by means of digital stereo image matching techniques (Aguilar et al. 2007). ImageStation Automatic Elevations (ISAE 4.0® by Z/I Imaging) was the software utilised to automatically generate a large number of elevation points.

Shaded-Relief Image Matching stage (step 1)

Within this stage, a 2D shaded-relief is generated for both the historical DEM (model to georeference) and the reference DEM (a more recently obtained and already georeferenced DEM). In this regard, different shaded-reliefs may be tested, only changing the solar elevation and azimuth to optimize the final 3D matching between the historical and reference DEMs. In this sense, the algorithm could be repeated till obtaining the best solution (**Figure 2.2**).

An automatic matching algorithm, based on the Scale Invariant Feature Transform (SIFT), has been implemented to identify conjugated points in image

space (pixel coordinates) belonging to the reference and historical DEM shaded-relief images. This algorithm is able to extract features invariant to image scale and rotation. Moreover, these features are shown to provide robust matching across a substantial range of affine distortion, change in 3D viewpoint, noise addition and illumination change, so it can be deemed as very suitable to our practical application. The reader can find an in-depth description of SIFT method in (Lowe 2004).

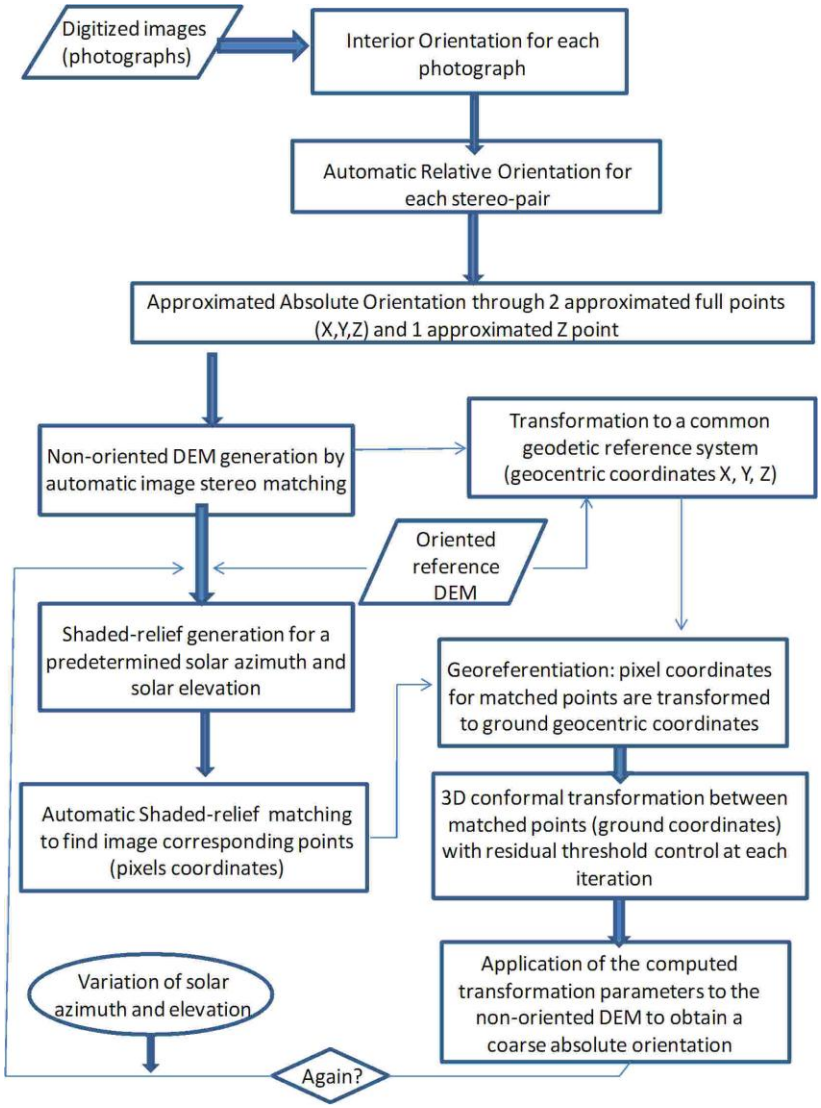

Figure 2.13. Flow chart diagram showing the algorithm framework for obtaining the coarse absolute orientation (Step 1: Shaded-Relief Image Matching stage).

Finally, the 3D coordinates for every pair of conjugated points were automatically extracted from the reference shaded-relief (UTM ETRS89 East and North) and reference DEM (bilinearly interpolated heights above GRS80 ellipsoid in our particular case). Those pairs of 3D points, previously transformed to geocentric coordinates, allowed computing an iterative least squares registration between both DEMs by means of a 3D conformal transformation (eq. 2.1):

$$\begin{bmatrix} X \\ Y \\ Z \end{bmatrix} = \lambda \begin{bmatrix} a_{11} & a_{12} & a_{13} \\ a_{21} & a_{22} & a_{23} \\ a_{31} & a_{32} & a_{33} \end{bmatrix} \begin{bmatrix} x \\ y \\ z \end{bmatrix} + \begin{bmatrix} \Delta X \\ \Delta Y \\ \Delta Z \end{bmatrix} \quad (2.1)$$

where the orthonormal rotation matrix is represented by 3x3 elements which are trigonometric functions of the rotation angles Ω, Φ and K. On the other hand, X, Y and Z are the transformed coordinates regarding the reference system (reference DEM), being x, y and z the original coordinates for the DEM to be georeferenced. Equally, ΔX, ΔY and ΔZ are the corresponding three translations and λ is a global scale parameter.

It is relevant to notice that the gross errors among the geocentric coordinates of the conjugated points (reference and historical matching points after applying the computed transformation) found after each iteration were discarded and not taken into account in the next one by establishing a threshold value to avoid possible outliers due to both landscape changes (e.g. cut and fill earthworks, new buildings, etc.) and false matching points. Based on our experience, that threshold should be set up to around ten times of the approximated uncertainty measure of the reference DEM, but sometimes had to be increased because, at least, three points were needed to compute the 3D Transformation.

By estimating the previous seven transformation parameters, the computed 3D transformation was applied to the historical DEM to georeference it. All this process making up the basis framework, except for ARO and DEM generation, was programmed by using MATLAB®.

Robust Surface Matching stage (step 2)

This second step consists of using the reference DEM as a reference topographic surface to robustly register the historical DEM previously oriented by means of shaded-relief image matching (step 1). Thus, this second stage may be considered as a refine process to improve, whether it is possible, the georeferentiation results achieved through the first step.

In this way, the conjugated points were extracted by overlapping both DEMs (e.g. map projection UTM ETRS89 and heights above GRS80 ellipsoid) and using bilinear interpolation over the reference DEM to obtain two different and planimetrically corresponding elevations (one for each DEM). At this time, those non-overlapping DEM points detected have to be pointed out and excluded from

the matching process from here onwards (i.e. each observation is assigned a zero weight). In this way, a very dense dataset of z-differences (dz_i) between historical and reference DEM for every grid point can be computed.

The widely known K-means clustering method (Spath 1985) was employed to take into account potential divergences between new and old DEM elevations due to true terrain change. Those true changes are considered here as outliers, and thus they should be excluded from the surface matching process. With K-means clustering, we are given a large dataset of N absolute Z-differences data points in a two-dimensional space and an integer of K. The problem is to separate the N observations into K clusters by means of an iterative algorithm that minimizes the sum of distances from each object to its cluster centroid over the remaining clusters. This algorithm moves points between clusters until the sum cannot be decreased any further. The result is a set of K clusters that are as compact and well-separated as possible.

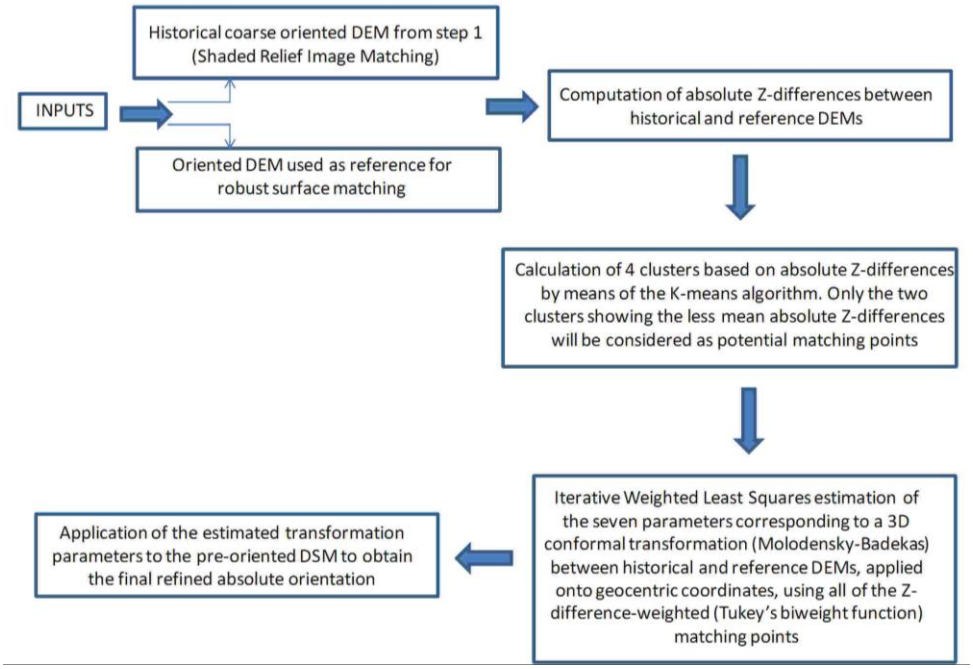

Figure 2.14. Flow chart diagram showing the algorithm framework for obtaining the final refined absolute orientation of the historical DEM (Step 2: Robust Surface Matching stage).

Based on our experience, K was set to four in our particular application. In this sense, once the four absolute z-differences clusters are computed, the two clusters presenting the highest mean absolute z-differences are to be considered as potentially revised areas and so discarded to be applied in the subsequent surface matching process. The remaining two clusters are considered as potentially

matching areas where the robust surface matching can be applied using the M-estimator called Tukey's Biweight (TB). TB function is one of the most commonly-utilised M-estimators, and as noted by Goodall (1983), is difficult to surpass in terms of delivering good performance in most situations. The weight function is defined as follows:

$$w(u_i) = \begin{cases} (1-u_i)^2 \; if \; |u_i| \leq 1 \\ 0 \quad if \; |u_i| > 1 \end{cases} \tag{2.2}$$

being u_i the standardised least-squares residuals (dz_i/σ), where σ is the standard deviation of all the Z-differences potentially selected to be involved in the surface matching process. In this way, the diagonal weight matrix regarding the TB function, that is $w(u_i)$ in eq. 2.2, is introduced in an iterative and massive least-square weighted solution (Pilgrim 1996, Allan 2004) to compute the so-called Molodensky-Badekas 3D conformal transformation which works on geocentric coordinates (eq. 2.1).

After the estimation of the seven transformation parameters, the resulting 3D transformation was applied to the historical DEM to refine its previous georeferentation that was achieved from step 1. This two stage procedure was also programmed with MATLAB® (**Figure 2.3**).

DATASETS

Datasets corresponding to 1977 (Historical DEM to georeference)

Because this historical flight lacked of camera calibration certificate, which is very usual by the way, the corner coordinates for each photograph (fiducial marks) were established using the same methodology explained in Chapter 1. The principal point coordinates were fixed at zero, i.e. no offset existed between the principal point and the fiducial centre. Focal length was included because it usually appears as marginal data in aerial photographs. The reader is referred to the Datasets section of this Thesis for further information.

A 10 m grid-spacing DEM was extracted by means of stereo matching techniques (ISAE 4.0® from Z/I Imaging), ranking over previously digitised images (15 μm per pixel ≈ 30 cm ground sample distance) with a radiometric resolution of 8 bits. ISDM 4.0®, from Z/I Imaging® was used to carry out the preliminary and approximate absolute orientation as it was depicted in the previous section.

To test the capability of the developed method to deal with highly deformed DEMs (i.e. badly preoriented), different rotations, translations and scale changes were applied to the original preoriented DEM to obtain three synthetic deformed DEMs, as it is expressed in Table 2.1.

Table 2.10. Translations, rotations and scale change applied to the preoriented 1977 DEM to produce three different versions of synthetic deformations.

Parameters	Version 1	Version 2	Version 3
ΔX	10 m	50 m	100 m
ΔY	10 m	50 m	100 m
ΔZ	10 m	50 m	100 m
ΔΩ	10º	30º	45º
ΔΦ	10º	30º	45º
ΔK	10º	30º	45º
Δλ	0.9	0.7	0.5

Additionally, ISAE 4.0® software from Z/I Imaging was employed to extract a 10 m grid-spacing DEM through similar stereo matching techniques but, in this case, by using a robust exterior orientation computed from the support of 45 evenly distributed and accurate GCPs without applying self-calibrating additional parameters or APs (please see Chapter 1) due to the fact that ISAE 4.0® software does not allow their implementation. This configuration based on a large number of GCPs and no APs was proved to provide an absolute orientation with similar accuracy to that achieved from self-calibrating models supported by APs and with the same number of GCPs. The corresponding RMSE was 0.277, 0.346, and 0.444 m for planimetric, vertical and tridimensional accuracy respectively (see further information in Chapter 1 of this Thesis). Therefore, this configuration can be considered as the most accurate as possible, and so the collected DEM can be directly compared with the reference DEM. In this sense, the traditional photogrammetric techniques can be tested against robust surface matching techniques in order to check if GCPs collection effort can be someway replaced.

Reference dataset corresponding to 2001

The reference DEM corresponding to 2001 consisted of a 10 m grid-spacing DTM produced by the Andalusia Regional Government (Spain) throughout a photogrammetric flight taken in 2001 (scale ≈ 1:20000). This original DTM was transformed from the UTM European Datum (1950) and orthometric heights to the new Spanish official geodetic system called the European Terrestrial Reference System (ETRS89) and ellipsoidal heights (based on the GRS80 ellipsoid). The corresponding DTM accuracy was estimated upon 62 DGPS check points located at open terrain, yielding a mean vertical error of 0.88 m (underestimated elevations), a vertical RMSE close to 1.34 m, and a standard deviation of 1.03 m. The 1977 historical DEM to georeference and the 2001 reference DEM are illustrated in **Figure 2.4**4 as 3D surface maps.

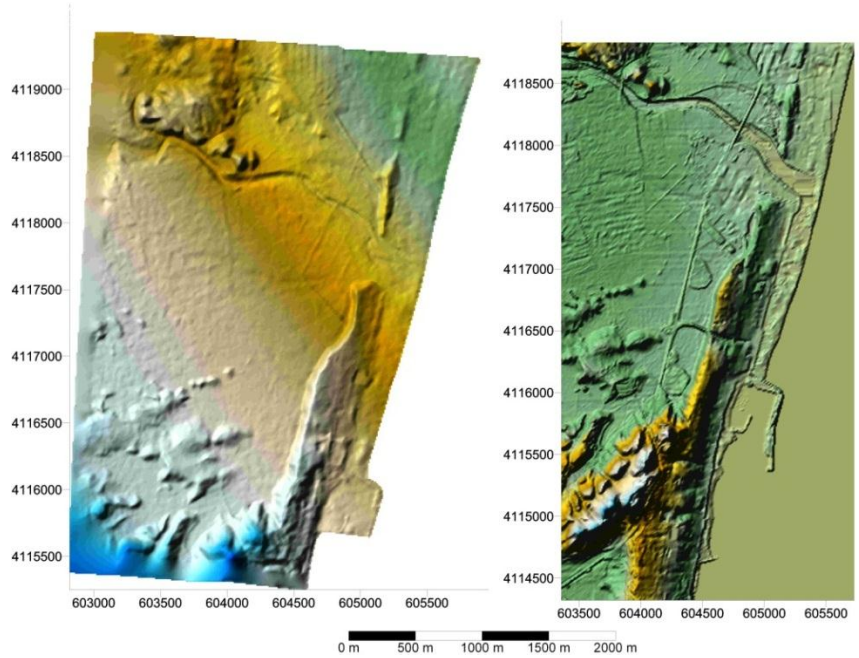

Figure 2.15. Photogrammetrically-derived DEMs corresponding to 1977 (left) and 2001 (right). Reference system UTM-ETRS89.

Validation datasets

Two different validation datasets were used in this work to test the accuracy of the proposed two-step robust surface matching to register historical DEMs. The first one consisted of a LiDAR dataset taken during August and September 2004, based on a flood risk mapping study in Andalusia and led by the Water Government Agency of Spain. The LiDAR data capture was handled by the Cartographic Institute of Calalunya (Spain) by means of an Optech ALTM 3025 LiDAR sensor. Among its main operational parameters, we highlighted the following ones: flight height 2300 m, point density around 1 point/m^2 and computed vertical accuracy between 6 and 15 cm depending on the land cover. The accurate and high resolution (1 m grid-spacing) raw DSM was filtered and decimated using TerraScan® software to produce a more suitable to handle 3 m grid-spacing DTM within the working area, comprising a non-urbanised and, thus, relatively stable area along the Antas dry-ravine bed (**Figure 2.9**).

The second validation dataset was a very recent DEM taken in 2009 (**Figure 2.10**). It means a heavily developed coastal area relatively prone to be altered along time. This second DEM was a high accuracy (standard deviation estimated in 8.9 cm) and resolution LiDAR-derived DEM. The initial very high resolution DEM was resampled to an easier to handle 5 m grid-spacing DEM. The reader is referred to the Datasets section of this Thesis for further information.

RESULTS AND DISCUSSION

Starting point. 1977 preoriented DEM

The initial preoriented historical DEM (coarse-oriented using ARO) presented a clearly diagonal-rotated N-W to S-E direction leaning as compared with the 2001 reference DEM. It originated a sparse histogram of signed vertical residuals as can be observed in **Figure 2.5**.

The mean error took a value of 16.18 m (Table 2.5), indicating a notable overall bias or systematic error from the preorientation process, as could be expected given the approximated coordinates of the ground points utilised to compute the absolute orientation. Meanwhile, random errors were also quite large as can be deduced from the high standard deviation of the whole z-differences within the overlap area (Table 2.5). Thus, the starting preorientation should be improved to allow an acceptable terrain change detection analysis. In this case, it is necessary to cope with these high local deformations by treating them as outliers while the designed algorithm, as a robust estimator technique, should be less sensitive to the existence of outliers. It is a non-easy problem to solve because there will be coexisting matching points, gross errors (significant surface differences due to the passage of time) and boundary outliers (i.e. points within the transition area). In the remaining sections, the two-step proposed algorithm will be tested to check its ability to afford this intriguing challenge.

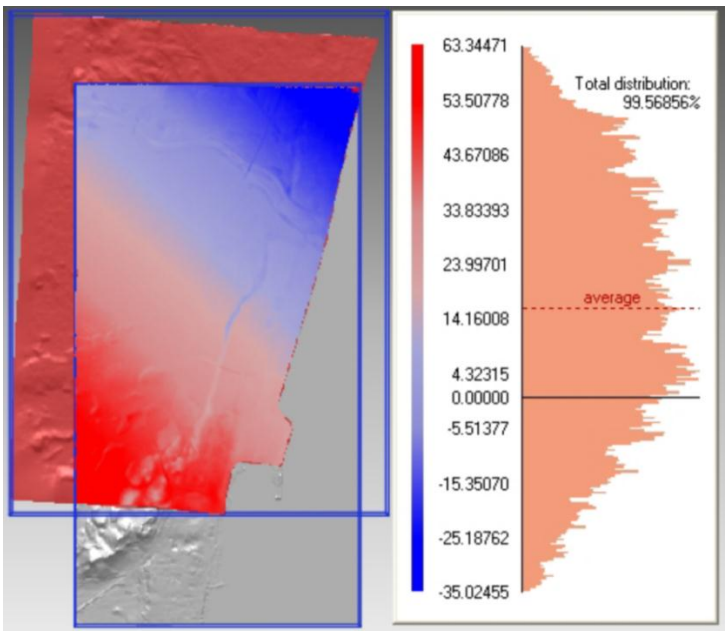

Figure 2.16. Map of signed z-differences (1977 ARO preoriented DEM – 2001 reference DEM within the overlap area) and the corresponding histogram.

Shaded-Relief Image Matching (step 1)

As it was previously commented, the process called Shaded-Relief Image Matching (SRIM) makes up the first step of the proposed two-step robust surface matching approach.

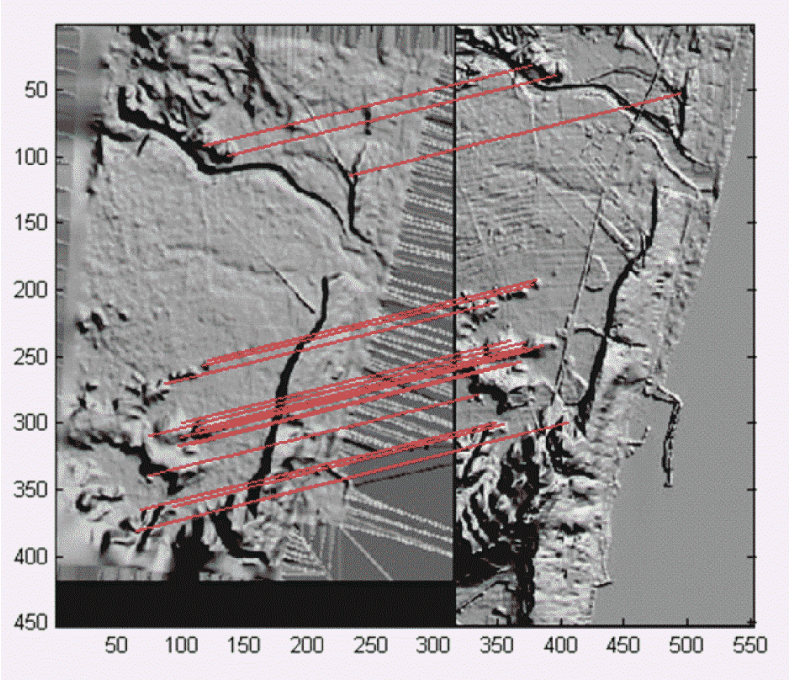

Figure 2.17. Results regarding Shaded-Relief Image Matching (image space) for a 45º solar azimuth and a 45º solar elevation. 1977 DEM (left) and 2001 DEM (right).

First of all, it is important to point out that the matching results may be quite variable depending on the solar position from which the shaded-relief images were generated. In fact, automated GCP location in two images consists of two stages. The first one extracts spatial features from each image. Then the features are paired by correspondence matching. The success of the process depends, partially, on the similarity of the features in the two images, which is clearly related to the solar position. This is the reason why the proposed algorithm attempts to iteratively search for an optimal solution changing both solar azimuth and solar elevation. Just as an example, the matching results coming from different solar positions are depicted in **Figure 2.6** and **Figure 2.7**. With the 45º solar azimuth case, 22 conjugated points were successfully matched out of 2784 and 1722 key points found in 1977 and 2001 shaded-relief images, respectively. Likewise, with the 90º solar azimuth situation, 21 conjugated points were finally extracted out of 2172 and 1380 key points detected in 1977 and 2001 shaded-

relief images, respectively. At this point, it is imperative to state that the most important is not only the number of pairs achieved but the matching precision and even distribution of those points on the working area.

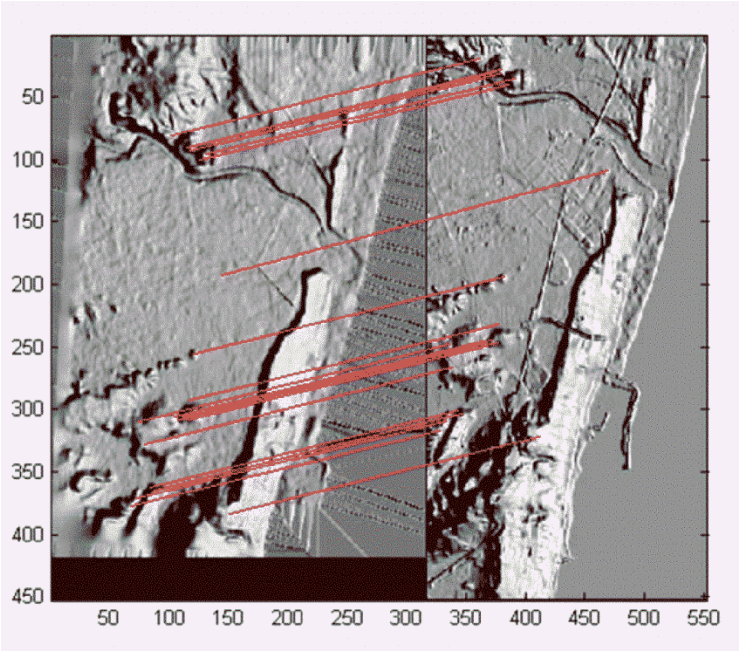

Figure 2.18. Results regarding Shaded-Relief Image Matching (image space) for a 90º solar azimuth and a 45º solar elevation. 1977 DEM (left) and 2001 DEM (right).

Table 2.2 shows the estimated transformation parameters for the iteratively computed 3D conformal transformation. It is important to underline that the number of automatically detected GCPs, already included in the adjustment (robust least-squares adjustment iteratively discarding poorly matched points), has been notably lower in the case of 90º solar azimuth shaded-relief situation (Table 2.3 and Table 2.4). It is also worth reporting that the used threshold to discard GCPs along the iterative adjustment took a value of 10 m since the final results are highly depending of this variable. In this way, the accuracies obtained from the least-squares variance-covariance matrix turned out to be better with the 45º solar azimuth case (Table 2.2), indicating a more robust and reliable solution. In short, the higher the number of ground points included in the least-squares adjustment, the better to achieve an even distribution over the complete working area. So, we strongly recommend computing the 3D conformal transformation with no less than 10 ground points, particularly if the two matching DEMs correspond to a highly dynamic area where landscape change probability may be considered as very high.

Table 2.11. Estimated parameters and accuracies for the computed 3D conformal transformation (based on geocentric coordinates with regard to GRS80 reference ellipsoid).

Parameter	Solar azimuth 45º Solar elevation 45º		Solar azimuth 90º Solar elevation 45º	
	Value	Accuracy	Value	Accuracy
ΔX	-30.10 m	0.24 m	-43.01 m	1.21 m
ΔY	-7.78 m	0.25 m	-4.60 m	1.21 m
ΔZ	-21.64 m	0.24 m	-31.07 m	1.22 m
ΔΩ	0.454º	0.072º	0.373º	0.217º
ΔΦ	0.990º	0.028º	1.104º	0.310º
ΔK	-0.856º	0.092º	-0.750º	0.229º
λ	1.00007	0.0003	1.00629	0.0032

Table 2.12. Residuals in X, Y and Z from the 3D conformal transformation adjustment computed on the five utilised (out of 21) GCPs and automatically obtained by shaded-relief image matching (azimuth 90º, elevation 45º).

Matched GCPs	X (m)	Y (m)	Z (m)
1	-2.02	3.61	2.91
2	0.27	-3.20	-0.04
3	-0.19	-1.72	0.02
4	-0.29	-2.12	0.02
5	2.52	5.55	-2.94

Table 2.13. Residuals in X, Y and Z from the 3D conformal transformation adjustment computed on the 15 utilised (out of 22) GCPs and automatically obtained by shaded-relief image matching (azimuth 45º, elevation 45º).

Matched GCPs	X (m)	Y (m)	Z (m)
1	-0.40	-0.27	0.14
2	0.34	-0.31	0.12
3	0.74	1.65	-0.03
4	-0.74	0.01	-0.46
5	-0.66	-1.29	-1.26
6	0.69	1.67	0.20
7	0.64	0.05	0.37
8	0.10	-0.28	0.30
9	-1.16	-1.98	-0.44
10	0.06	-0.33	0.89
11	-0.01	-0.35	0.19
12	-0.24	-2.04	0.33
13	0.70	2.68	0.47
14	0.62	1.03	-0.66
15	-0.68	-0.23	-0.15

Table 2.14. Signed z-differences statistics within the overlap area corresponding to the comparison between 1977 historical DEM and 2001 reference DEM.

1977 DEM - 2001 DEM comparison	Mean	Maximum	Minimum	Standard deviation
1977 Initial preoriented DEM 2001 DEM	16.18	63.34	-35.02	22.12
1977 SRIM-oriented DEM (90º-45º) 2001 DEM	-1.78	10.40	-18.66	3.17
1977 SRIM-oriented DEM (45º-45º) 2001 DEM	-0.14	10.14	-16.28	2.03

The initial position of the 1977 historical DEM has been notably corrected and the matching results have been clearly improved after applying the SRIM algorithm (**Figure 2.8**). Because the algorithm checks through different solar positions (previously selected by the user), it is possible to obtain dissimilar solutions and, later on, to check which is the best option. In this sense, the 45º solar azimuth solution would be preferred. Indeed, some signed statistical results are shown in Table 2.5. It is worthy of note that the standard deviation of the 45º solar azimuth case is still almost twice higher than the one estimated for the 2001 reference DEM (1.03 m). Since outliers were not removed from the SRIM-oriented DEM and reference DEM comparison, the final matching from SRIM process may be considered as highly accurate.

By judging numerical data and qualitative maps depicted in Table 2.5 and **Figure 2.8**, SRIM stage can be used to automatically and coarsely co-register multi-temporal DEMs without GCPs. It is necessary to take into account that some of the gross errors detected (**Figure 2.8**) may be actually considered no error but landscape change due to earthworks projects (e.g. cut and fills). In this way, the proposed methodology seems to be very robust because localised shaded-relief features supporting the robust 3D conformal transformation are usually geomorphological features that remain relatively stable along time.

When registering multi-temporal DEMs, the most important problem is associated to the intensity of temporal deformation or change occurred between the periods of the study. In most surface matching algorithms the deformation area is restricted, at most, 50% by introducing the so-called differential model and improving the classic least z-difference or LZD algorithm. It is rather complex and needs a previous rough co-registration or knowing about the approximated transformation to carry out (Zhang, Cen 2008). This SRIM stage has been used as a first step to later apply our robust surface matching algorithm to refine the initial matching as much as possible. The outcomes from the application of this second step will be presented along the next section.

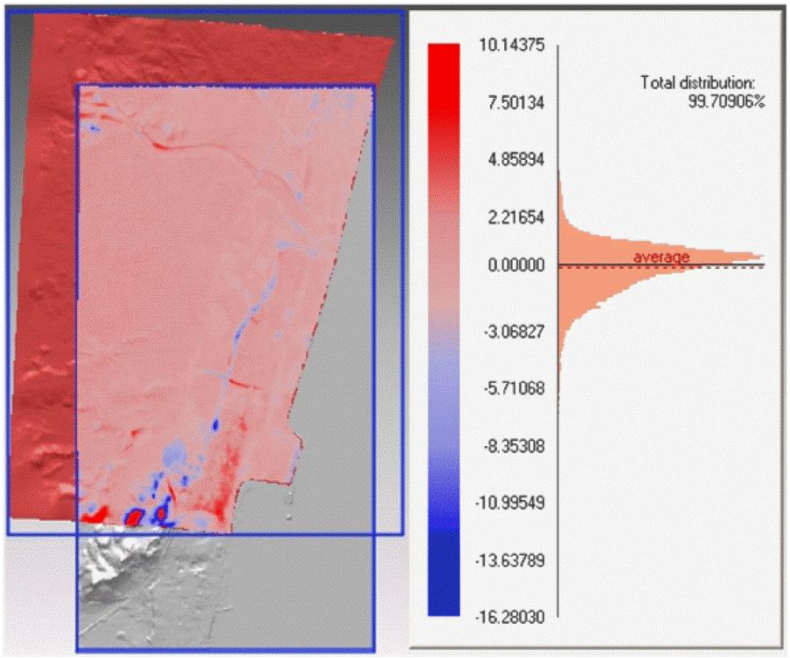

Figure 2.19. Map of signed z-differences (1977 SRIM-oriented DEM – 2001 reference DEM within the overlap area) and the corresponding histogram after applying the computed 3D conformal transformation (45º solar azimuth and 45º solar elevation shaded-relief).

Robust Surface Matching (step 2)

Once step 1 (SRIM) has been concluded about the approximated best coarse-orientation (45º solar azimuth in our case), it is time to refine the computed orientation by means of the aforementioned Robust Surface Matching (RSM) approach. According to the RSM results depicted in **Figure 2.6**, it can be noticed that the computed translation and rotations at this stage can be considered as very small, an expected situation given the good coarse orientation coming from the first step. The accuracy for the estimated parameters, calculated through the dispersion matrix, was very high. It was mainly due to the huge number of available matching points what confers to this process an important soundness and robustness.

After applying this second step (RSM algorithm), the SRIM-oriented 1977 historical DEM has been slightly refined to improve on its co-registration with respect to the 2001 reference DEM, yielding the accuracy results shown in Table 2.7. As can be checked, the results may be deemed as fairly similar to those obtained after applying only the SRIM first step. Regarding this issue, it is essential to point out that the RSM second step has been designed to correct, whether needed, the approximation carried out through the SRIM first step. In this sense, the poorer is the SRIM performance the better is the added value from RSM stage.

Regarding the LiDAR-derived validation DEMs, the Antas dry-ravine can be supposed as a mainly non-altered area during the last decades and so reasonably free of change. In this sense, the maximum and minimum errors were the lowest, while the matching accuracy worked the best (Table 2.7), presenting an uncertainty (measured as standard deviation) almost equal to that one estimated for the 2001 reference DEM. In the same way, the z-differences analysis, with regard to the comparison between the 2001 reference DEM and the 2004 Antas DEM, showed similar results (Table 2.7), demonstrating the great efficiency of this method to obtain excellent multi-date surface registrations without costly and time-consuming surveyed ground points. Furthermore, the spatial error distribution turned out to be quite stable and evenly distributed all over the working area, indicating a good performance of the proposed matching algorithm to correct the poor preorientation of the original historical DEM (**Figure 2.9**).

Table 2.15. Estimated parameters and corresponding accuracies from the Robust Surface Matching application.

Parameters	value	Accuracy
ΔX (m)	-0.0159	0.0018
ΔY (m)	0.0005	0.0018
ΔZ (m)	-0.0757	0.0028
ΔΩ (º)	0.030	$1.70\ 10^{-4}$
ΔΦ (º)	-0.004	$1.37\ 10^{-4}$
ΔK (º)	-0.043	$1.72\ 10^{-4}$
λ	0.99998	$2.06\ 10^{-6}$

Table 2.16. Signed z-differences statistics within the overlap area corresponding to the comparison between the oriented 1977 historical DEM and several reference DEMs (for the presented cases, a 45º solar azimuth and elevation was applied to the SRIM orientation).

Compared DEM	Reference	Mean	Standard deviation	Maximum	Minimum
1977 SRIM oriented DEM	2001 reference DEM	-0.14	2.03	10.14	-16.28
	2004 Antas dry-ravine DEM	-0.58	1.27	3.63	-6.00
	2009 coastal DEM	-1.29	1.48	6.35	-11.91
1977 SRIM+RSM oriented DEM	2001 reference DEM	-0.20	1.95	9.38	-15.57
	2004 Antas dry-ravine DEM	-0.55	1.09	3.32	-7.31
	2009 coastal DEM	-0.81	1.44	6.09	-11.75
2001 reference DEM	2004 Antas dry-ravine DEM	-0.50	0.93	3.87	-5.37
2001 reference DEM	2009 coastal DEM	-0.68	1.40	7.39	-7.02

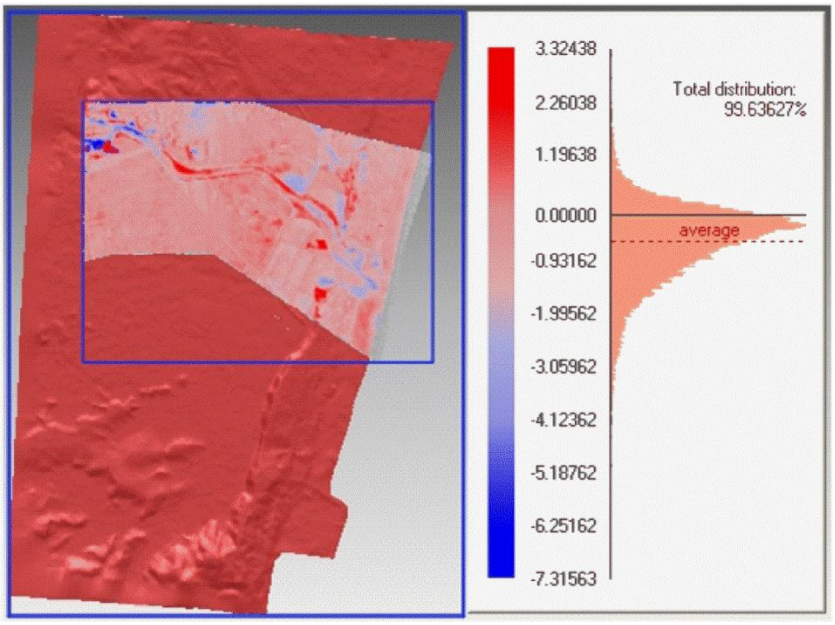

Figure 2.20. Spatial distribution of signed z-differences (1977 SRIM-45º-45º+RSM oriented DEM – 2004 Antas dry-ravine DEM within the overlap area) and the corresponding histogram.

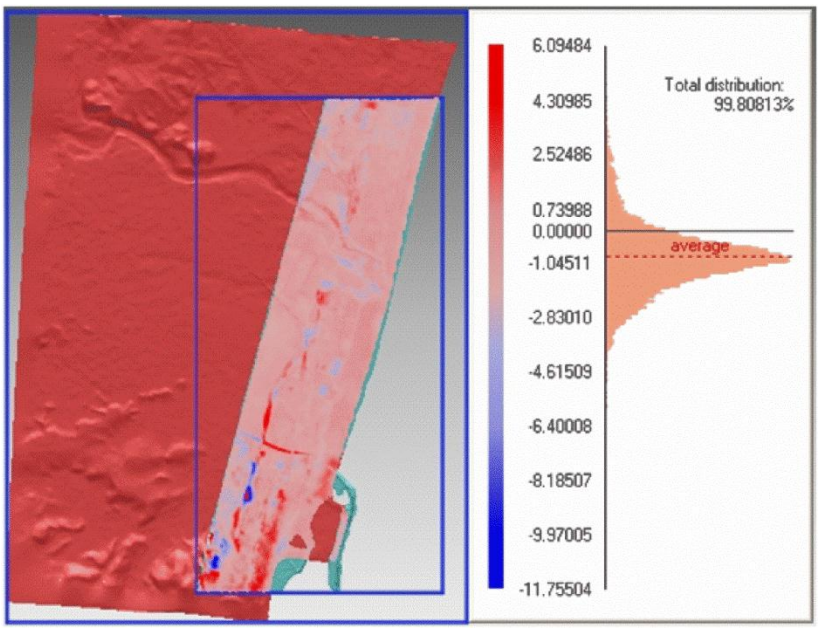

Figure 2.21. Spatial distribution of signed z-differences (1977 SRIM-45º-45º+RSM oriented DEM – 2009 coastal DEM within the overlap area) and the corresponding histogram.

Notice that the validation matching results coming from the 2009 LiDAR-derived DEM were slightly poorer than those achieved in the case of the Antas dry-ravine (Table 2.7). It was likely due to the larger number of years passed (since 1977) and, above all, the presence of new urbanisations in this heavily developed coastal area what, somehow, means a lesser correspondence between the 1977 and 2009 DEMs. Shortly, this area can be deemed as more contaminated and fully modified and, as expected, the number of potential matching points has decreased (**Figure 2.10**).

In other words, the height changes between multi-date DEMs contain three main parts: random errors, terrain deformations and matching errors. Random errors come from DEM generation while terrain deformations are mainly caused by anthropogenic activities (constructions, land use changes, etc.). Obviously, the area embraced by the 2009 coastal DEM is more tending to suffer terrain deformations than the 2004 Antas DEM.

Again, the statistical results coming from the z-differences analysis between the 2001 reference DEM and the 2009 coastal DEM turned out to be very similar to those offered by the SRIM+RSM oriented historical DEM (Table 2.7), confirming the goodness of 1977 DEM registration.

Highly deformed DEMs

One of the most important problems when registering multi-date DEMs is closely related to the quality of the previous preorientation issue because, somehow, a bad preorientation accentuates the problems due to the presence of local deformations. Summing up, it is needed a relatively well preoriented historical DEM to obtain accurate results. In fact, our second step of the RSM approach was not able to fully register any type of the synthetic deformations applied to the original preoriented 1977 DEM, as it can be observed in Table 2.8 (though it is worth noting that those deformations are not usual under operational conditions).

Therefore, and for those cases, it was needed to apply a first step process, the so-called SRIM algorithm, to get ready the preoriented DEM to be refined by the second step and based on the RSM algorithm. In this sense, the obtained results may be believed as fairly accurate, taking into account the extreme deformations, likely far away from real datasets, applied to the original 1977 historical DEM to test the robustness and soundness of the proposed two-step methodology.

Table 2.17. Signed z-differences statistics for the overlap area corresponding to the comparison between different versions of deformed 1977 DEM and 2001 reference DEM (for the presented cases, a 45º solar azimuth and elevation was applied to the SRIM orientation).

Version of 1977 DEM	Orientation phase	Reference DEM comparison results			
		Mean	Std. Dev.	Max.	Min.
1	Raw	-0.80	47.03	80.84	-81.48
	RSM oriented	-1.40	8.31	25.46	-36.88
	SRIM+RSM oriented	-0.94	1.99	5.68	-19.21
2	Raw	0.89	45.93	78.91	-79.51
	RSM oriented	-2.78	23.25	48.56	-49.68
	SRIM+RSM oriented	-0.45	2.05	7.11	-14.76
3	Raw	-0.10	30.10	51.59	-52.00
	RSM oriented	5.94	15.73	38.13	-28.30
	SRIM+RSM oriented	-0.25	2.54	12.33	-16.49

Traditionally extracted DEM

It is quite interesting to compare the results obtained from applying this automatic robust matching technique with the traditional way to acquire DEM by means of photogrammetric processes. Thus, the 1977 photogrammetrically oriented project was used to produce an accurate DEM (henceforth 1977 photo DEM) which was directly compared with the 2001 reference DEM and the 2004 lidar-derived DEM. The results are shown in the Table 2.9 revealing that no significant differences were observed between photo DEM and SRIM + RSM DEM (both for 1977).

Table 2.18. Signed z-differences statistics within the overlap area corresponding to the comparison between the 1977 no APs DEM and two reference DEMs.

	Mean	Sd. Dev.	Max.	Min.
1977 photo DEM - 2001 reference DEM	0.21	1.56	6.68	-8.76
1977 photo DEM - 2004 Antas dry-ravine DEM	-0.16	0.94	4.70	-9.06

The systematic bias for the 1977 photo DEM was opposite to the DEM obtained by the two-step robust matching (0.21 instead of -0.20, Table 2.7). These results were achieved since the georreferenced SRIM + RSM DEM was obtained by matching it with the 2001 reference DEM which presented a systematic vertical offset as it was previously mentioned (DGPS quality control). Furthermore, the 1977 photo DEM was extracted by a photogrammetric project directly referenced

by accurate GCPs so not including the vertical offset appreciated in the 2001 reference DEM. Moreover, the random error estimated from the standard deviation values was similar between both approaches, especially for the comparison with the 2004 lidar-derived DEM in which the traditional photogrammetric process was only 15 cm more accurate. When the two georreferenced DEMs were compared to the 2001 reference DEM, the difference between them regarding vertical accuracy was close to 39 cm, again being the classical process more accurate. However, and taking into account the larger cost of the ground support in the case of the traditional photogrammetric process (45 GCPs had to be surveyed in field to ensure the highest possible accuracy), the results obtained from robust matching (image and surface) can be considered as accurate enough and the proposed approach should be stated as much more efficient than the classical one.

Terrain change detection

One of the main advantages of the proposed method could be its immediate application to issues related to terrain change detection. Certainly, detecting regions of change in DEMs for the same area taken at different times is of widespread interest due to a large number of applications in land cover or land use studies (Coppin, Bauer 1996). Moreover, terrain changes could be relevant to studies such as shoreline evolution, soil sealing, flooding analysis and so on. The goal is to identify the set of points (pixels in a raster context) that are significantly different between the last DEM of the sequence and the previous DEMs (these pixels comprise the "change mask"). The traditional methods usually used in this discipline can be very sophisticated when they are applied to images, but are notably simplified working on DEMs because there is no need to apply pre-processing methods (radiometric/intensity adjustments, sudden changes in illumination, shadows, etc.) except for the crucial geometric adjustments, i.e. matching as best as possible all the compared DEMs just as it has been already done via the algorithm proposed along this chapter.

Several methodologies have been developed for change detection, from the simplest one (simple differencing), to the more sophisticated one such as those based on significance and hypothesis tests, predictive models, shading models, background modelling, etc. (Radke et al. 2005). In this case, and just as an approximation attempt, a mixed approach has been used involving simple differencing and significance tests supposing that the z-differences follow a Gaussian distribution. In fact, a 95% confidence interval has been computed from the reference DEM estimated uncertainty (Sd ≈ 1.03 m). Thus, the symmetric upper and lower limits would adopt the values ±1.96.Sd = ±2.02 m (presuming a zero mean of z-differences). This methodology has been applied to the working area highlighting a few and defined areas where there have been changes between

1977 (referenced by SRIM+RSM) and 2001 (**Figure 2.11**). Those areas were concentrated in high relief zones and, in some cases, may be partially due to the different quality of the compared DEMs (**Figure 2.5**), being the 1977 DEM smother and worse defined (e.g. without breaklines edition) than the 2001 counter partner. Actually, the results can be visually checked in a reliable way. Additionally, most of the working area presented z-differences within the computed confidence interval (see the corresponding histogram in **Figure 2.11**).

Summing up, the percentage of significant terrain change within the tested area from 1977 to 2001 (24 years) could be estimated as 9.53% as much while the fill earthworks (69.2%) clearly prevailed over cut earthworks (30.8%).

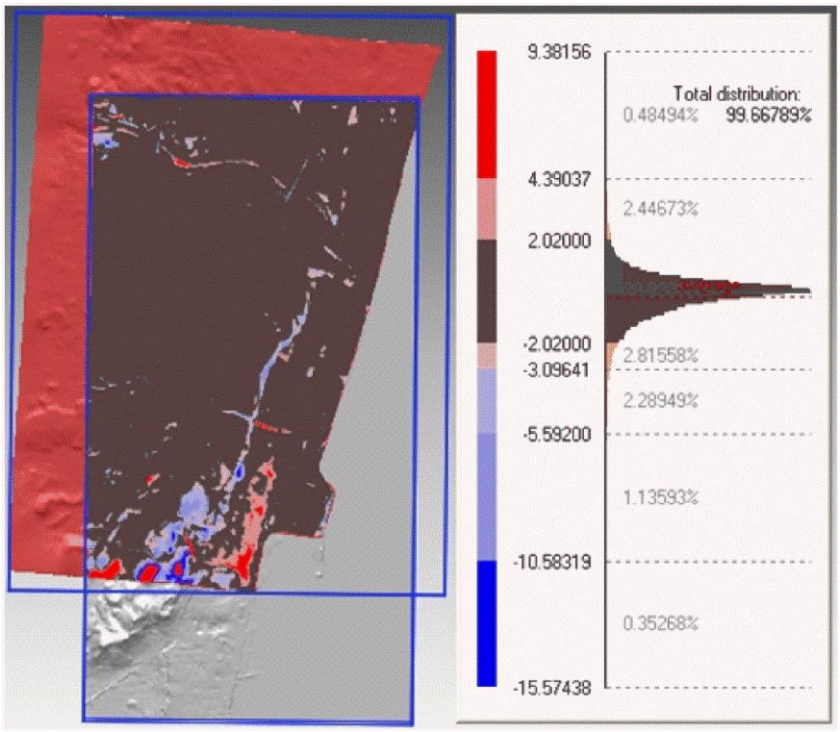

Figure 2.22. Discrete distribution of signed z-differences (1977 SRIM-45º-45º+RSM oriented DEM – 2001 reference DEM within the overlap area) where dark grey colour means areas within the tolerance of ±2.02 m (95% confidence interval).

CONCLUSIONS

The results obtained from this work can be regarding as very promising, showing a good co-registration between reference and historical DEMs in heavily developed coastal areas.

The second step process, based on a robust surface matching algorithm which needs a relatively good first approximation, can be applied successfully only whether the preoriented historical DEM turns out not to be excessively misaligned respect to the reference DEM. In the case of a very badly preoriented DEM, and likely also for intense temporal deformations or terrain changes, it is necessary to take into consideration a previous step headed up to correct such issues, which can be afforded by means of the proposed Shaded-Relief Image Matching. In such situations, the second step method proposed along this work could be applied as a refining method to polish subtle deficiencies coming from the first step.

Therefore, and just to widen the range of situations wherein our methodology could be suitable, it is always highly recommendable applying the Shaded-Relief Image Matching (first step), which makes up an integrated method comprising a two-step robust surface matching. The first step should render a well coarse-oriented historical DEM by means of the automatic and unattended shaded-relief image matching. On the other hand, the second step would refine the initial coarse orientation using the developed robust surface matching algorithm. In this way, it would be possible to deal even with very poor preoriented DEMs that present a high rate of change regarding the reference DEM.

Certainly, the point is the high efficiency and robustness demonstrated by our Robust Surface Matching approach for historical DEMs 3D georeferencing, especially when it is compared to the costly and time-consuming traditional methods such as photogrammetric absolute orientation based on surveyed GCPs and, very often, self-calibrating bundle adjustment techniques, which have been proved as similar in terms of accuracy even when a large number of GCPs have been utilised.

REFERENCES

Aguilar, F.J., Fernández, I., Pérez, J.L., López, A., Aguilar, M.A., Mozas, A. & Cardenal, J. 2010a, "Preliminary results on high accuracy estimation of shoreline change rate on coastal elevation models.", *International Archives of the Photogrammetry, Remote Sensing and Spatial Information Science,* Kyoto, Japan, 9-12 August 2010, pp. 986-991.

Aguilar, F.J., Carvajal, F., Aguilar, M.A. & Agüera, F. 2007, "Developing digital cartography in rural planning applications", *Computers and Electronics in Agriculture,* vol. 55, no. 2, pp. 89-106.

Aguilar, F.J., Mills, J.P., Delgado, J., Aguilar, M.A., Negreiros, J.G. & Pérez, J.L. 2010b, "Modelling vertical error in LiDAR-derived digital elevation models", *ISPRS Journal of Photogrammetry and Remote Sensing,* vol. 65, no. 1, pp. 103-110.

Aguilar, M.A., Aguilar, F.J., Fernández, I. & Mills, J.P. 2013, "Accuracy Assessment of Commercial Self-Calibrating Bundle Adjustment Routines Applied to Archival Aerial Photography", *The Photogrammetric Record,* vol. 28, no. 141, pp. 96-114.

Allan, A.L. 2004, *Maths for Map Makers,* Second edn, Whittles Publishing, Dunbeath, UK.

Brock, J.C. & Purkis, S.J. 2009, "The emerging role of lidar remote sensing in coastal research and resource management", *Journal of Coastal Research,* Special Issue 53, pp. 1-5.

Coppin, P.R. & Bauer, M.E. 1996, "Digital Change Detection in Forest Ecosystems with Remote Sensing Imagery", *Remote Sensing Reviews,* vol. 13, no. 3-4, pp. 207-234.

Cowell, P.J. & Zeng, T.Q. 2003, "Integrating uncertainty theories with GIS for modeling coastal hazards of climate change", *Marine Geodesy,* vol. 26, no. 1-2, pp. 5-18.

Goodall, C. 1983, "M-Estimators of location: An outline of the theory" in *Understanding Robust and Explanatory Data Analysis*, eds. D. Hoaglin, F. Mosteller & J.W. Tukey, John Willey & Sons, New York, pp. 339-403.

James, T.D., Murray, T., Barrand, N.E. & Barr, S.L. 2006, "Extracting photogrammetric ground control from lidar DEMs for change detection", *Photogrammetric Record,* vol. 21, no. 116, pp. 312-328.

Li, Z., Xu, Z., Cen, M. & Ding, X. 2001, "Robust surface matching for automated detection of local deformations using least-median-of-squares estimator", *Photogrammetric Engineering and Remote Sensing,* vol. 67, no. 11, pp. 1283-1292.

Lowe, D.G. 2004, "Distinctive image features from scale-invariant keypoints", *International Journal of Computer Vision,* vol. 60, no. 2, pp. 91-110.

Miller, P., Mills, J., Edwards, S., Bryan, P., Marsh, S., Mitchell, H. & Hobbs, P. 2008, "A robust surface matching technique for coastal geohazard assessment and management", *ISPRS Journal of Photogrammetry and Remote Sensing,* vol. 63, no. 5, pp. 529-542.

Mills, J.P., Buckley, S.J., Mitchell, H.L., Clarke, P.J. & Edwards, S.J. 2005, "A geomatics data integration technique for coastal change monitoring", *Earth Surface Processes and Landforms,* vol. 30, no. 6, pp. 651-664.

Pilgrim, L. 1996, "Robust estimation applied to surface matching", *ISPRS Journal of Photogrammetry and Remote Sensing,* vol. 51, no. 5, pp. 243-257.

Radke, R.J., Andra, S., Al-Kofahi, O. & Roysam, B. 2005, "Image change detection algorithms: A systematic survey", *IEEE Transactions on Image Processing,* vol. 14, no. 3, pp. 294-307.

Rosenholm, D. & Torlegard, K. 1988, "Three-dimensional absolute orientation of stereo models using digital elevation models", *Photogrammetric Engineering & Remote Sensing,* vol. 54, no. 10, pp. 1385-1389.

Spath, H. 1985, *Cluster Dissection and Analysis: Theory, FORTRAN, Programs, Examples,* Halsted Press, New York.

Titus, J.G., Anderson, K.E., Cahoon, D.R., Gesch, D.B., Gill, S.K., Gutierrez, B.T., Thieler, E.R. & Williams, S.J. 2009, *Coastal sensitivity to sea-level rise; a focus on the mid-Atlantic region*, U.S. Environmental Protection Agency, National Oceanic and Atmospheric Administration, U.S. Geological Survey.

Webster, T.L., Forbes, D.L., MacKinnon, E. & Roberts, D. 2006, "Flood-risk mapping for storm-surge events and sea-level rise using lidar for southeast New Brunswick", *Canadian Journal of Remote Sensing,* vol. 32, no. 2, pp. 194-211.

Zhang, T. & Cen, M. 2008, "Robust DEM co-registration method for terrain changes assessment using least trimmed squares estimator", *Advances in Space Research,* vol. 41, no. 11, pp. 1827-1835.

CHAPTER 3

A new, robust, and accurate method to extract tide-coordinated shorelines from coastal elevation models

ABSTRACT

The extraction of high accuracy shorelines is fundamental to carry out accurate and reliable studies headed up to understand coastal evolution and vulnerability. In our case, it was needed to develop a method based on extrapolation process since the most suitable height for datum-coordinated shoreline extraction along Spanish coastal areas turned out to be the orthometric datum origin, i.e., the origin of the vertical reference system in Spain. Due to the microtidal nature of the Mediterranean Sea, this vertical datum makes rather troublesome to remotely extract ground points under this reference vertical datum to apply traditional shoreline extraction methods based on interpolation procedures. In this sense, a new method for shoreline extraction based on an iterative digital elevation model extrapolation is presented in this work. The Elevation Gradient Trend Propagation method employs the local elevation gradient in order to estimate the shoreline position by extrapolating the slope until the zero-elevation contour, representing the modeled intersection of the vertical datum and beach profile, is reached.

The proposed methodology was tested on a LiDAR-derived digital elevation model, which comprised a coastal area of Almeria (Mediterranean Sea, South Spain). The results obtained from the new approach were compared with those provided by the widely known Cross-Shore Profile (CSP) method.

A validation process was carried out over both methods to bring out their advantages and shortcomings. An alternative contour level of 0.4 m was employed as ground truth since the zero-elevation contour was not available due to the lack of LiDAR returns under water surface. The validation pointed out that the proposed method turned out to be more robust and suitable than CSP method for microtidal coasts and when there was a need of extrapolation to reach the desired contour level. In addition, the influence of the starting point to apply the elevation extrapolation process was also proved.

Keywords: Shoreline change, shoreline detection, shoreline analysis, shoreline definition, coastal erosion-accretion, remote sensing, LiDAR, digital elevation model, extrapolation method, cross-shore profile

INTRODUCTION

Mediterranean coastal areas are being progressively degraded mainly due to they are withstanding a high dynamic economic activity that provides large profits from the tourist industry. Moreover, this process is causing the emergence of new infrastructures (harbors, roads, urbanizations, engineered structures, etc.) which are seriously affecting the coastal environment (Suárez de Vivero, Rodríguez Mateos 2005). In this sense, it is noteworthy that urban development on the coastal areas and resource use conflicts spawn environmental degradation and increasing hazard vulnerability (Mills et al. 2005). Indeed, they are one of the richest and changeable, but also fragile, systems (Woodroffe 2002). As a result, some specific programs have been developed for the Mediterranean Sea (e.g. United Nations Environment Program/Mediterranean Action Plan) in order to study the degradation and conservation processes along Mediterranean coastal areas.

The shoreline, as the reference of land-water interface, is one of the most important features on the Earth's surface, representing a critical indicator of coastal evolution and vulnerability for any Coastal Geographic Information System (Li, Ma & Di 2002). In this way, the development of monitoring techniques has become essential to improve the accuracy and efficiency of shoreline mapping, facilitating studies headed up to coastal evolution assessment by estimating the rate of coast erosion or accretion (Boak, Turner 2005, Genz et al. 2007, Aguilar et al. 2010a).

In order to extract the shoreline, a wide range of geomatics techniques have been employed (Gens 2010, Boak, Turner 2005). Since the 1920s, aerial photogrammetry has replaced more and more traditional ground surveys headed up to capture beach surface by means of topographic profiling. In recent decades, new technologies have arisen for coast and shoreline mapping, including high resolution satellite imagery, kinematic GPS vehicles and, above all, airborne LiDAR surveys (Brock, Purkis 2009). Until recently, the direct digitization over aerial image (orthorectified images are preferred) has been the most utilized method by identifying a physical shoreline indicator as the High Water Line (HWL) (Pajak, Leatherman 2002). However, since more accurate spatial data acquisition and analysis techniques have appeared, the set of methods for shoreline definition have been increased. The development of some techniques that make possible to efficiently obtain high accuracy DEMs, such as Digital Aerial Photogrammetry or airborne LiDAR technology, have pointed out to the datum-coordinated shorelines, based on either tidal or vertical reference datums, as the most suitable shoreline indicator. In fact, a shoreline that is defined based on a stable vertical datum can be treated as a reference shoreline and used to differentiate shoreline changes (Li, Ma & Di 2002). In this sense, LiDAR surveys are quite efficient as compared with

coastlines extracted from digital orthophotography or photo interpretation. That is because LiDAR-based shorelines are georeferenced to a certain tidal datum which avoids problems related to biases or horizontal shifts bound to the presence of different tidal levels when the images were taken, the disturbing effects of waves and runup, or even the possible misinterpretations of the wet-dry beach line. Hence using tidal datum indicators can be deemed as a more objective and robust way to identify the shoreline position.

Several methods have been employed in this decade in order to extract the desired tide-coordinated or datum-coordinated shoreline from LiDAR data. Li, Ma & Di (2002) described a method for mapping the shoreline by using instantaneous shorelines and other ancillary data; Liu, Sherman & Gu (2007) devised a method based on morphological operations over segmented LiDAR DEMs; White 2007, White et al. (2011) proposed a contouring method over LiDAR data by utilizing a datum transformation from geodetic to tidal datum. The latter method is being employed officially by the U.S. National Ocean Service. One of the most widespread method to extract the datum-based shoreline from altimetry data or DEMs is the Cross-Shore Profile (CSP) method (Stockdon et al. 2002), which is based on linear regression over foreshore altimetry profiles. This method has also been officially used by the U.S. Geological Survey (Morton, Miller & Moore 2004, Morton, Miller 2005, Hapke et al. 2006). The adjusted straight line is estimated over a vertical range of heights and it is intercepted with the desired datum in order to obtain the shoreline position for each specific profile by using linear interpolation. Tidal datums as Mean High Water (MHW) or Mean Lower Low Water (MLLW) are usually employed as the reference for high accuracy tide-coordinated shoreline extraction (NCR 2004, Monmonier 2008) since they correspond to the nautical charts depths reference (MLLW) or include legal boundary considerations (MHW in US) as well as the fact that the MHW shoreline provides mariners with a visually recognizable boundary between land and sea (Graham, Sault & Bailey 2003, Monmonier 2008). Furthermore, these tidal datums are averaged over a historical record of elevation water levels embracing a period of not less than 19 years, corresponding to a National Tidal Datum Epoch (NTDE) (Ruggiero, List 2009), and so they can be considered as robustly computed.

In contrast to the United States case, some areas of the Mediterranean coasts (e.g. Spanish coast) lack of a large enough network of historical tidal observations for the establishment of an accurate tidal datum. Moreover, the elevation of the MHW tidal datum may experience large variations along the coast as a function of the local tide range and mean tide level. This is the main reason why an open coast tide station very close to our working coastal area is needed to accurately estimate its MHW. And it is not always available in the case of Spanish coast. Therefore, an accurate enough and easy to define datum should be specified for shoreline extraction along Spanish coast. In this sense, we strongly recommend the use of the Spanish Vertical Reference System (orthometric heights). According to the

Spanish legislation, the vertical reference system in Spain is defined as the mean sea level in the city of Alicante (located at the East of Iberian Peninsula, Mediterranean Sea). Actually, it was the first tide gauge station in Spain. That mean sea level was recorded along the decade from 1870 to 1880. Nowadays, the Spanish vertical reference system is materialized by the Spanish High Precision Leveling Network ('Red de Nivelación de Alta Precisión', REDNAP; Instituto Geográfico Nacional). The EGM08 geoid model has been recently adapted to the Spanish Vertical Reference System (REDNAP) by means of a correction surface adjusted by applying the minimum curvature algorithm over around 13700 check points where both the orthometric and ellipsoid heights were known. Therefore, a reasonably dense geodetic network is currently available in Spain which allows to locally and accurately establish that EGM08-REDNAP vertical datum in everywhere along the Spanish coast. Furthermore, the observations of the national network of tide gauges are related to this vertical datum (Puertos del Estado 2013), and other geographical features such as cadastral or administrative information are also related to this vertical reference level. In fact, the Spanish Oceanography Institute (IEO 2013) defines the 0 m contour level (based on EGM08-REDNAP orthometric datum) as a required feature for the official geographical database, making up the cartographic element called "shoreline". That datum-coordinated shoreline could be also applied as a vertical reference for bathymetric works since the "hydrographic zero" (analogous to MLLW datum) is the reference datum for nautical charts in Spain and many Spanish tide gauges report a vertical relation between the EGM08-REDNAP datum and the "hydrographic zero" (IHM 2013).

However, the choosing of the EGM08-REDNAP vertical datum as the most suitable for datum-coordinated shoreline extraction makes difficult to apply interpolation methods since the instantaneous sea level is, most of the time, located over the corresponding 0 m contour level along the Mediterranean Spanish coast. Furthermore, the short tide level variation and the presence of waves and runup on flat beaches stand in the way of mapping negative elevation data. It means that it is very troublesome to count on a nearshore bathymetry. As a consequence, interpolation methods could be unsuitable in order to obtain an accurate zero-elevation shoreline position and, thus, extrapolation methods should be tested.

The main goal of this work is to look for a response to all the aforementioned shortcomings, outlining a new methodological proposal for high accuracy shoreline mapping based on DEMs processing and taking the EGM08-REDNAP orthometric datum as the vertical reference datum. In this way, a new approach for shoreline extraction, called Elevation Gradient Trend Propagation (EGTP), is introduced and tested along this work. This method has been based on the iterative extrapolation of the local gradient in order to obtain the desired zero-elevation contour level (Aguilar et al. 2010a). The new approach has been

compared with the widespread CSP method since this approach, based on straight line regression, allows for the application of an extrapolation process. A validation process was carried out on the results from both methods to check which one is more suitable to be applied on microtidal Mediterranean coastal areas.

DATASET AND STUDY AREA

The shoreline extraction methods tested over the study area were applied on a 1 m grid spacing LiDAR-derived DEM taken in August 2009. The flight height above ground was close to 1000 m, using a LeicaGeosystems® ALS60 airborne laser scanner with 35° FOV, 1.61 points/m^2 average point density and counting on one ground GPS reference station. These data were properly processed to their registration in ETRS89 geodetic system. The orthometric vertical datum was chosen based on the Spanish vertical reference system (REDNAP 2013). The estimated vertical accuracy, computed from 62 Differential Global Positioning System (DGPS) high accuracy check points distributed over the whole working area, took a value of 8.9 cm (measured as standard deviation). All the processes to filter the laser point cloud, adjusting the four flight-lines strips and managing LiDAR data were carried out by means of TerraMatch® and TerraScan® 010 software.

Additionally, Terrascan® software also allowed estimating the instantaneous sea level by plane-to-cloud adjustment at time when LiDAR data were taken. It was possible since the LiDAR-infrared echo was capable to return from the water surface in many occasions. In that way, the instantaneous mean sea level was extracted and vertically georeferenced to the Spanish vertical datum, turning out to be close to 18 cm average in open coast. That is nearly the locally corrected MHW estimated from historical data coming from the tide gauge station located at Almeria harbor (non-open coast station), which would take a value around 20 cm. After applying a contouring process to the LiDAR-derived DEM, the 0.4 m contour level was proved to be the lower one free of noise and outliers owing to waves and runup (i.e., it was a continuous contour). As a result, this contour was employed as reference in order to filter out LiDAR sea points and carry out the next extrapolation processes (as described further below).

SHORELINE EXTRAPOLATION METHODS

Cross-Shore Profile Method

As one of the most extended methods for shoreline extraction based on vertical datum indicators, the CSP method has been implemented as a proper reference for this work (Stockdon et al. 2002, Morton, Miller & Moore 2004, Hapke et al. 2006, Brock, Purkis 2009, Ruggiero, List 2009). Notice that, along this work,

CSP method has been employed as an extrapolation method, while it has been proved as suitable enough for interpolation processes. It implies that the shoreline position is estimated supposing that the computed slope from the available data is kept further below the data set range.

Firstly, and in order to attain the 0 m datum shoreline by means of this methodology, the horizontal cross-shore profiles were initially obtained. DSAS© software (Thieler et al. 2008) was employed to achieve an appropriate framework of cross-shore profiles or transects (5 m transect spacing) from which the final CSP shoreline was extracted.

Secondly, by means of a 2 m both sides buffer operation, the corresponding elevation data were included into every cross profile along the coast. As a result, distances to profile origin data (abscise) and elevation data (ordinate) were recorded for each transect. Then, a regression line was fitted for each profile data by means of least-squares method, the slope and intercept being the variables to compute. Finally, it was calculated the intersection between that adjusted line and the chosen water level or reference datum as it is shown in eq. 3.1. Moreover, the covariance matrix resulting from the least-squares adjustment was employed to estimate the uncertainty related to shoreline position for every transect (Wilcox 2003).

$$x_s = \frac{Z_{datum} - \bar{b}}{\bar{a}} \tag{3.1}$$

Being x_s the estimated shoreline position respect to the corresponding profile origin along cross-shore axis, Z_{datum} is the datum elevation, $\bar{a}$ is the regression-estimated slope, and $\bar{b}$ is the regression-estimated intercept. Additionally, the linear regression coefficient of determination (R^2) was also computed for each profile.

Shoreline uncertainty estimation for the CSP method

Briefly, the relationship between the foreshore slope, DEM vertical accuracy and extracted shoreline accuracy (Stockdon et al. 2002) can be explained by

$$\sigma_{XY\ DEM} = {}^{\sigma_Z}/_{\hat{a}} \tag{3.2}$$

Being $\sigma_{XY\ DEM}$ the shoreline uncertainty due to vertical uncertainty of the ancillary DEM (σ_Z = ± 0.089 m in our case) and $\hat{a}$ the foreshore least-squares estimated slope. However, in addition to the uncertainty proposed by (Stockdon et al. 2002), the overall uncertainty should also depend on the method employed for the shoreline position estimation (Aguilar et al. 2010b), as it is shown in eq. 3.3.

$$\sigma_{XY\ TOTAL} = \sqrt{\sigma^2_{XY\ DEM} + \sigma^2_{XY\ regression}} \tag{3.3}$$

Where $\sigma_{XY\ TOTAL}$ corresponds to the total shoreline uncertainty, and $\sigma_{XY\ regression}$ is the uncertainty owing to the own regression as a result of the application of the general error propagation law (Heuvelink, Burrough & Stein 1989), yielding:

$$\sigma^2_{XY\ regression} = \frac{\sigma_a^2\left(m-\hat{b}\right)^2}{\hat{a}^4} + \frac{\sigma_b^2}{\hat{a}^2} + 2\sigma^2_{ab}\frac{\left(m-\hat{b}\right)}{\hat{a}^3} \tag{3.4}$$

Where σ_a^2 and σ_b^2 are the variances of computed slope and intercept, respectively, and σ^2_{ab} represents the covariance between both parameters.

Looking for the best elevation range for applying the CSP method

An essential parameter for the shoreline position estimation by means of the CSP method is the proper elevation range to be used. Other authors (Stockdon et al. 2002) have proposed a general data range of ±0.5 m from the required datum (i.e., MHW). Since data below the chosen datum in this work were not available, a further study has been carried out in order to find out the most suitable elevation data range from which starting the linear extrapolation process. The 0.2 m and 0.4 m elevations were taken into account as the minimum heights whilst the tested maximum elevation ranged from 0.8 m up to 2.0 m stepping 0.2 m. The potential outliers derived from the CSP shoreline computing process were removed by applying the widely known 3-sigma rule (Maune 2001). The overall results were compared by means of a decision factor (DF) shown in eq. 3.5. The final chosen range was the range whose results yielded the largest value for the decision factor, which depends on the average for all the computed coefficients of determination ($R^2_{average}$), the percentage of remaining data after outliers removal ($\%_{remaining\ data}$), and the average estimated uncertainty ($\sigma_{XY\ average}$).

$$DF = \frac{R^2_{average} \cdot \%_{remaining\ data}}{\sigma_{XY\ average}} \tag{3.5}$$

In this way, the elevation range from 0.4 m to 0.8 m was found as the best-in-class range in our local conditions. Moreover, the 0.4 m level was proved as the optimum reference elevation level in order to apply the extrapolation methods to the DEM data employed in this work since it was perfectly distinguishable against those ranges where the lowest level was 0.2 m (Figure 3.1). In this last case waves and runup clearly disturbed the performance of the contouring process by introducing an unacceptable noise.

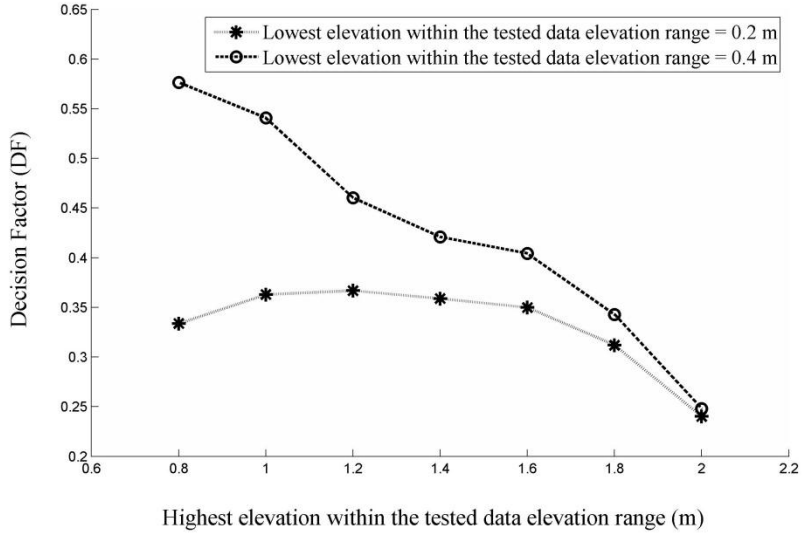

Figure 3.9. Decision Factor (DF) values for every tested elevation data range.

Elevation Gradient Trend Propagation method

In this work, EGTP method is proposed as a new approach for shoreline extraction especially thought to cope with data and operational conditions where extrapolation is needed. For example, it would be very useful to face those cases where a nearshore bathymetry is not available. It is based on an iterative grid-based data technique that expands the elevation gradient trend (norm and direction) computed for every grid point towards extrapolated grid points with unknown heights. The process is repeated till the new grid point reaches the level just below the chosen vertical datum. After that, it is easy to join the border which separates grid points situated above and below the reference height to map the corresponding datum-coordinated shoreline. Obviously, the datum-coordinated shoreline (e.g. EGM08-REDNAP in our case) can be extended to tidal-coordinated shoreline, whether a proper tidal datum was available, and should not affect the discussion in the remaining part of the article.

Firstly, elevations below a specific threshold (reference elevation) are removed. Then, the initial local gradients and their uncertainty are estimated in east-west direction (X-axis) and north-south direction (Y-axis) by means of a Sobel's filter (González, Woods 2008) from the non-removed elevations (eq. 3.6).

$$\frac{\partial z}{\partial x} = Gx \cong Z \otimes \begin{bmatrix} -1 & 0 & 1 \\ -2 & 0 & 2 \\ -1 & 0 & 1 \end{bmatrix}; \frac{\partial z}{\partial y} = Gy \cong Z \otimes \begin{bmatrix} -1 & -2 & -1 \\ 0 & 0 & 0 \\ 1 & 2 & 1 \end{bmatrix} \qquad (3.6)$$

Being Gx and Gy the local gradients for X and Y directions, respectively, Z is a 3x3 neighborhood within a grid DEM and $\otimes$ represents the convolution operation. Additionally, the estimated initial gradient uncertainty for both orthogonal directions is estimated ($\sigma^2_{initial_{Gx}}$, $\sigma^2_{initial_{Gy}}$) by applying the general error propagation law (eq. 3.7).

$$\sigma^2_{initial_{Gx}} = \sigma^2_{initial_{Gy}} = \frac{3}{16 \cdot \mathrm{r}^2}\sigma^2_Z \tag{3.7}$$

Being r the DEM grid spacing and assuming that it is the same along both axes X and Y.

It is worth to point out that, in every iteration, the elevation gradient for components X and Y is only computed for those central grid points which present a complete neighborhood (i.e., all the 8 neighbours have a height value). The elevation gradient for each component of those grid points located at the border was interpolated by means of the inverse distance weighting method, using a local support made up of the gradients really calculated on the nearest adjacent grid points (eq. 3.8).

$$Gx_0 = \frac{\sum_{i=1}^{n} Gx_i \cdot {}^1\!/_{d_i}}{\sum_{i=1}^{n} {}^1\!/_{d_i}} \; ; \; Gy_0 = \frac{\sum_{i=1}^{n} Gy_i \cdot {}^1\!/_{d_i}}{\sum_{i=1}^{n} {}^1\!/_{d_i}} \tag{3.8}$$

Being Gx_0 and Gy_0 the gradient to be interpolated, i represents each adjacent node where elevation data is known, d_i is the Euclidian distance from each known node to the node to be interpolated, and Gx_i and Gy_i are the gradient values for each adjacent node. Similarly to eq. 3.3, the total gradient uncertainty (given by eq. 3.10) is estimated by the initial gradient uncertainty (eq. 3.7) and the uncertainty due to the extrapolation process described in eq. 3.8. The application of the general error propagation law yields the following expression:

$$\sigma^2_{extr_{G_x}} = \frac{1}{\left(\sum_{i=1}^{n} {}^1\!/_{di}\right)^2}\left(\frac{1}{{d_1}^2}\sigma^2_{initial_{Gx1}} + \cdots + \frac{1}{{d_n}^2}\sigma^2_{initial_{Gxn}}\right) \tag{3.9}$$

$$\sigma^2_{total_{Gx}} = \sigma^2_{initial_{Gx}} + \sigma^2_{extr_{G_x}} \tag{3.10}$$

Where n is the total number of adjacent nodes containing elevation data. Again, the Y-axis expression results in an analogous way. Fort the next extrapolation iteration, $\sigma^2_{total_{Gx}}$ would be the initial component while $\sigma^2_{extr_{G_x}}$ would depend on the corresponding variances. In this sense, the actual variance $\sigma^2_{total_{Gx}}$ would be increased in each iteration.

An estimation process for extrapolated elevations is carried out once the gradients have been computed. The unknown elevations are extrapolated by

means of a weighted average onto a 3x3 kernel neighborhood. The previously extrapolated gradient results, adjacent node elevations and relative position regarding the central node are taking into account for the extrapolated elevation estimation (eq. 3.11).

$$Z_i = \frac{\sum Z + \sum G_x \Delta_i + \sum G_y \Delta_j}{N} \tag{3.11}$$

In eq. 3.11, Δ_i and Δ_j are the weighting indexes for the gradients, which make the local gradient additive or subtractive, depending on its relative position with regards to the central node (see eq. 3.12 where *r* represents the DEM grid spacing).

$$\Delta_i = \begin{bmatrix} r & r & r \\ 0 & 0 & 0 \\ -r & -r & -r \end{bmatrix};\ \Delta_j = \begin{bmatrix} r & 0 & -r \\ r & 0 & -r \\ r & 0 & -r \end{bmatrix} \tag{3.12}$$

Following the description of the elements of the eq. 3.11, $\sum Z$ is the summation of the adjacent elevations, G_x and G_y are the local gradients corresponding to the 3x3 kernel neighborhood, and *N* is the number of adjacent nodes containing known elevation data. The iterative process is locally stopped when the estimated elevation results are located just below the required vertical datum for shoreline extraction. In our case, the process was stopped when the extrapolated elevations resulted in negative numbers (i.e., below 0 m elevation level). Similarly to the gradient process, the elevation uncertainties were also estimated using the following expression:

$$\sigma^2_{total_Z} = \sigma^2_{initial_Z} + \sigma^2_{extr_Z} \tag{3.13}$$

In this case, $\sigma_{initial_Z}$ refers to the initial DEM uncertainty (±0.089 m for the first iteration) and $\sigma^2_{extr_Z}$ indicates the uncertainty caused by the own extrapolation process. Again, and as a result of applying the general error propagation law through eq. 3.11, $\sigma^2_{extr_Z}$ could be estimated by means of the next formula:

$$\sigma^2_{extr_Z} = {}^1/_{N^2} \cdot \sum_{\forall i,j} \left(\sigma^2_{initial_{Z\,ij}} + \sigma^2_{total_{Gx\,ij}}\, r^2 + \sigma^2_{total_{Gy\,ij}}\, r^2 \right) \tag{3.14}$$

Where *N* is the total number of adjacent nodes containing elevation data, $\sigma^2_{total_{Gx\,ij}}$ and $\sigma^2_{total_{Gy\,ij}}$ are the gradient variances at *i* and *j* positions (ranging from 1 to 3), and *r* takes the value of the DEM grid spacing. It is worth noting that grid spacing effectively affects the uncertainty of extrapolated height, so it is strongly recommended to use high resolution DEMs to limit somehow the extrapolation error. Also notice that the gradient error will be increased after each iteration because the growing uncertainties of extrapolated heights.

The last step in the EGTP approach deals with the shoreline contour level extraction from the final extrapolated DEM. In doing so, the norm and direction of the local elevation gradient are used in the immediately upper elevation of the required datum by means of the horizontal distance from those positions respect to the required datum. The uncertainty was estimated for both the slope (m) and the horizontal distance (D), as it is shown through the following equations:

$$m = \sqrt{G_x^2 + G_y^2};\ \sigma_m^2 = \frac{1}{m^2}\left(G_x^2\sigma_{G_x}^2 + G_y^2\sigma_{G_y}^2\right) \tag{3.15}$$

$$D = \frac{Z_{ref} - Z_{datum}}{m};\ \sigma_D^2 = \frac{1}{m^2}\left(\frac{(Z_{ref} - Z_{datum})^2}{m^2}\sigma_m^2 + \sigma_{Z_{ref}}^2\right) \tag{3.16}$$

In the last equations, G_x and G_y are the gradient in X and Y directions, respectively, $\sigma_{G_x}^2$ and $\sigma_{G_y}^2$ being their estimated uncertainties along the iterative process. Furthermore, σ_m^2 is the slope uncertainty, whereas Z_{ref} and $\sigma_{Z_{ref}}^2$ are just the upper elevation regarding the desired vertical datum elevation and its corresponding uncertainty. Finally, Z_{datum} refers to the shoreline vertical level (0 m in our case).

The final horizontal coordinates are obtained by means of the slope direction, the D distance and the horizontal coordinates of the starting node. Thus, a continuous shoreline can be extracted usually comprising a large set of shoreline points, one for each pair of contiguous heights vertically located at both sides of the shoreline. Therefore, the denser is the original DEM, the more points are drawing the extracted shoreline.

Finally, the shoreline extraction for each CSP transect was carried out in order to compare the EGTP and CSP methods. In this way, the intersection of each reference transect with the entire shoreline was computed and, moreover, the average uncertainty between the points A and B was estimated according to the next expression (Li 1993), where A and B are shoreline points lying on both sides of the resulting intersection point.

$$\sigma_{AB}^2 = \frac{1}{3}\sigma_A^2 + \frac{1}{3}\sigma_B^2 \tag{3.17}$$

RESULTS AND DISCUSSION

Cross-Shore Profile Method Results

As has been widely proved in other works (Stockdon et al. 2002, Ruggiero, List 2009), the foreshore slope has a crucial effect on the shoreline accuracy when CSP method is employed, as can be easily deduced from eq. 3.2. Furthermore, the employed data range to compute the linear regression has been proved as very

significant in this work. The accuracy is lower and outliers arise when estimated slope is too small or the elevation data range hardly fits to a straight line, so a further outlier removal process is required. When this sort of errors turns out to be frequent in a specific area, a dispersion effect appears and certain coastal areas are clearly bad-defined (e.g. Figure 3.2). Also bearing in mind that a relatively short elevation data range was employed (only from 0.4 m to 0.8 m), the data points used in the fitting procedure could be too small and, thus, the relative high weight apply to any outlier could get worse the computed least-squares adjustment.

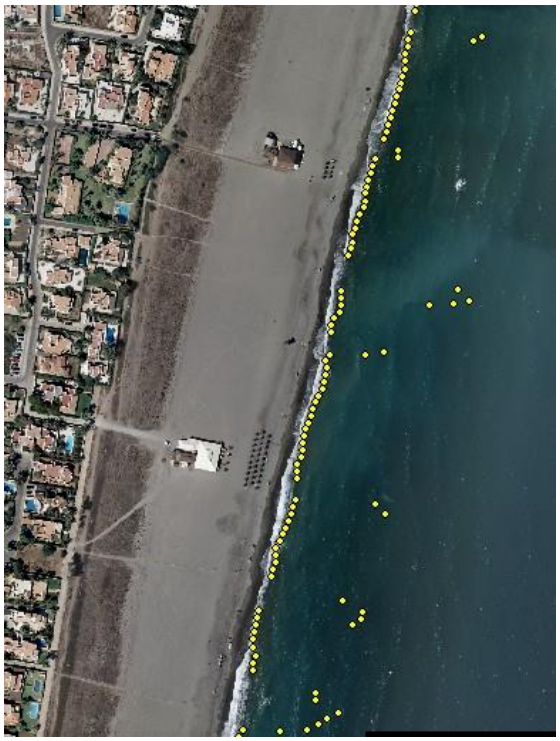

Figure 3.10. Dispersion effect for the computed shoreline position (yellow points) due to the presence of too flat areas (low slope estimation).

Finally, and after applying the outlier removal by means of the 3-sigma rule over the entire study area, the maximum uncertainty took a value of ±10.22 m, the median turned out to be ±1.00 m and the average was ±1.34 m. The number of lost transects was significant, representing the 15% of the initial ones. Additionally, it should be noticed that $\sigma^2_{XY\,regression}$, defined in eq. 3.4, contributed with 20% average over the whole $\sigma^2_{XY\,TOTAL}$, depicted in eq. 3.3. That is to say, DEM uncertainty ($\sigma^2_{XY\,DEM}$) was the most influent component on the total uncertainty, although the uncertainty due to the regression term made the model more complete.

Note that the computed theoretical uncertainty for the extracted shoreline seems to be high (average of ±1.34 m), although this value should be compared with a proper ground truth since the error owing to the extrapolation process has to be quantified. For example, the presence of an abrupt change in beach slope and curvature in the immediate vicinity of the datum-shore intersection would produce an additional uncertainty not taken into account by the theoretical model.

On the other hand, a clear influence on the final results was attributed to the lack of orthogonality between shoreline and transects. It was evaluated by using a simple test consisting on checking the effect on shoreline accuracy due to different rotations of the transect framework respect to the shoreline. In fact, CSP method was applied taking into account a synthetic required datum of 0.4 m and an elevation data range from 0.6 to 1.0 m in a steady-sloped beach close to 100 m long. The transects system was rotated regarding the local steepest line from 0° up to 75°, stepping 15°. The resulting shoreline for each set of transects was then compared with the ground truth, which was previously extracted as the 0.4 m contour level. The results are depicted in Table 3.1. It is shown that, as a rule of thumb, the less the alignment between transects and local steepest line, the greater the extracted shoreline error committed. Moreover, a systematic bias was found which was increased with the growing misalignment between transects and steepest line.

Table 3.14. Residuals average and residuals standard deviation regarding the ground truth for the different misalignments between transects and steepest line.

Applied misalignment	Average slope	Average R^2	Residual average (m)	Standard deviation (m)
0°	-0.117	0.981	0.390	± 0.287
30°	-0.104	0.956	0.337	± 0.407
45°	-0.05	0.572	-2.506	± 1.009
60°	-0.05	0.992	1.909	± 1.764
75°	-0.035	0.523	-4.889	± 1.797

Elevation Trend Propagation Method Results

The results obtained by means of EGTP method have been referred to the reference elevation of 0.4 m because it was previously proved as the most suitable lower contour level. For this iterative approach, the shoreline positions which presented the largest uncertainties did not correspond to any “dispersion effect”, but a high number of iterations needed to achieve the final position. Therefore, the outlier removal process was not applied in this case. It is worth noting that a little and limited error appeared as “shoreline gaps” where the local gradient turned out to be positive (landward direction), since the extrapolation process was not able to propagate elevations along seaward direction. Regarding the estimated uncertainty, a large influence of slope was also revealed for EGTP method.

Generally, the smaller the slope, the larger number of iterations was required and the greater uncertainties were estimated. An average uncertainty of ±2.08 m and a median of ±1.51 m were estimated over the entire study area, being a little bit larger than CSP one, although it should be taken into account that the outlier removal process was not applied in the EGTP case.

Qualitative comparison CSP vs. EGTP

For the study area, the EGTP method was able to represent the shoreline in a more continuous way than CSP method. CSP was affected in those areas where the elevation data profile was not alike to a linear trend. Moreover, complex and bended coast forms (engineered structures, rocks, little islands, sedimentary shapes, etc.) made the CSP method to yield irregular results. Finally, when the adjusted profiles included outlier data, i.e. wave and runup data, the linear regression was also affected. On the other hand, the EGTP method came out much more efficient than CSP one in order to represent the complex shapes, drawing the coast shape properly. In fact, around 14% more transects were available for EGTP method as compared with those available for CSP one. Furthermore, the EGTP method was able to identify little islands, achieving even more than one position for the same transect and later allowing to carry out a more suitable shoreline evolution analysis over these areas (Figure 3.3). Additionally, EGTP method can be deemed as much more automatic and unattended than CSP, since it is not needed to choose an appropriate elevation data range. In fact, the CSP method has offered inappropriate results when small or positive slopes were estimated (Figure 3.4 and Figure 3.5), producing a shoreline indetermination along certain coastal areas. Moreover, it is very sensitive to the elevation data range employed, so being the most affected for the local coast morphology (e.g. berm areas, Figure 3.6). In such cases, the fit straight line did not correspond to the morphological local variations. Thus, an important shortcoming attributable to the CSP method is that it would require a previous study of the altimetry profiles to find out the most suitable elevation data range, and even to check other sort of fits apart from the linear one (Huang, Jackson & Cooper 2010). Finally, EGTP method is more independent than CSP regarding the transect framework orientation.

Quantitative comparison CSP vs. EGTP

The high performances of the interpolation processes have been previously proved (Wilcox 2003). In order to test the performance of the extrapolation methods applied in this work, a numerical validation process has been developed. Since the true 0 m contour level (EGM08-REDNAP required vertical datum in this work) was not available due to the absence of a nearshore bathymetry, a synthetic elevation level of 0.4 m was employed as ground truth because it was the first contour level free of unacceptable noise. 14 sample areas were extracted from the

DEM, which represent different type of beaches along the working area. In addition, a mixed methodology was proposed in order to determine the potential negative effect of the transect-steepest line deviation for the CSP method. Therefore, the mixed method, called from here onwards CSP_EGTP method, was carried out in two steps: i) an iterative extrapolation of the DEM is applied, similarly to EGTP and ii) the shoreline is extracted by applying the CSP method over the previously EGTP extrapolated DEM.

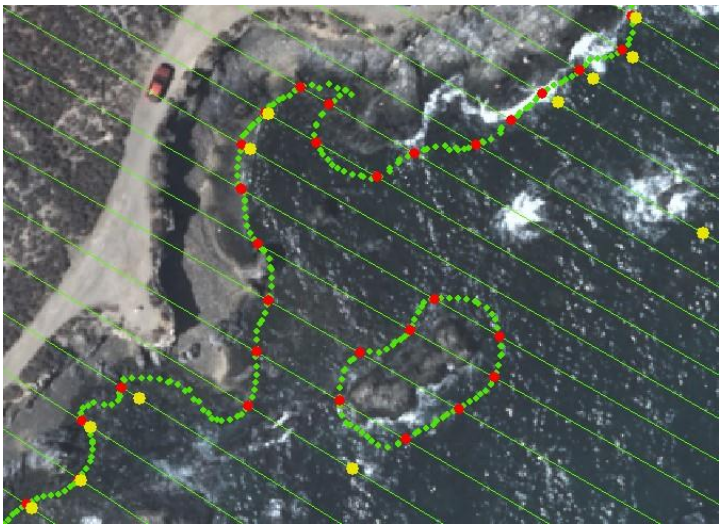

Figure 3.11. Example of the EGTP method performance for irregular coastal shapes and rocky coastal areas. Green points represent the 'continuous' EGTP-derived shoreline, whereas red points depict the EGTP-derived shoreline positions along the transect framework. Yellow points represent CSP-derived shoreline positions. Note that more than one position per transect could be captured the EGTP-derived shoreline. Notice the lack of data and the large errors committed along some transects in the case of the CSP-derived shoreline.

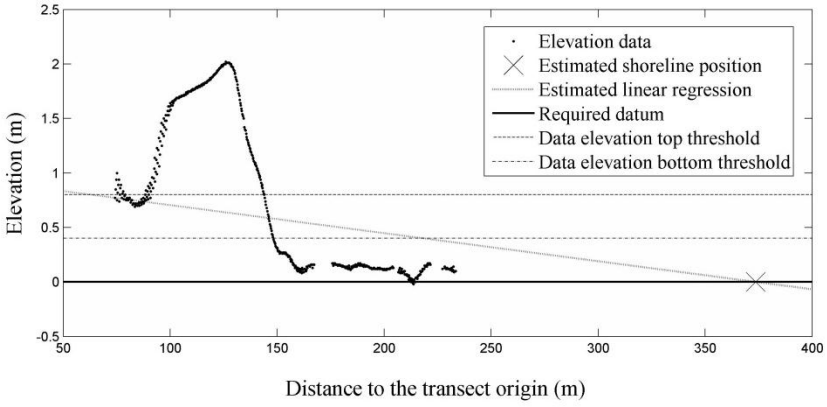

Figure 3.12. Example of the underestimation of foreshore slope because of the use of inadequate landward elevation data.

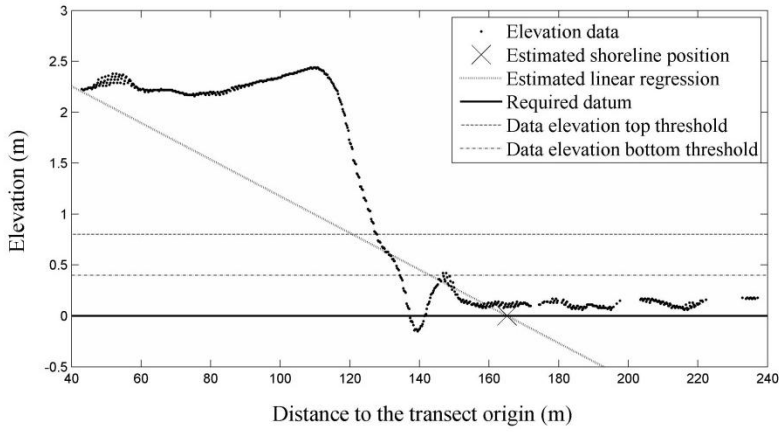

Figure 3.13. Example of the underestimation of foreshore slope because of the use of inadequate seaward elevation data.

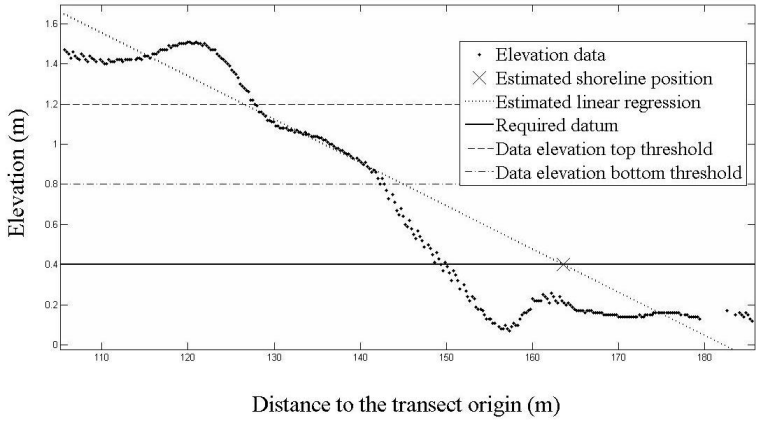

Figure 3.14. Example of the underestimation of foreshore slope because of the 'berm effect'. Note that the required shoreline vertical level is the synthetic 0.4 m one, instead of the 0.0 m level (both referred to EGM08-REDNAP vertical datum). The used data elevation in this case ranged from 0.8 m to 1.2 m.

This validation approach was intended to establish the main factors which significantly affect the shoreline accuracy. The standard deviation of the differences between the ground truth contour level and the extracted shorelines was employed as an accuracy indicator for each sample area. The tested variables were i) the applied method (CSP, EGTP and CSP_EGTP), ii) the reference elevation from which the DEM is extrapolated seaward, and iii) the extrapolated amplitude, i.e., the height difference between the required shoreline extraction level and the reference elevation. Moreover, the extrapolated data range, i.e., the height

difference between the minimum and maximum elevation used to compute the regression line in the case of the CSP method, took a value of 0.4 m in every case. The experimental design has been summed up in Table 3.2.

Table 3.15. Experimental design for the quantitative analysis carried out to compare the three tested methods.

Method	Reference elevation (m)	Extrapolated amplitude (m)	Elevation data range (m)	Alias
EGTP	0.6	0.2	-	EGTP06
EGTP	0.8	0.4	-	EGTP08
EGTP	1.0	0.6	-	EGTP10
CSP	0.6	0.2	1.0 – 0.6	CSP06
CSP	0.8	0.4	1.2 – 0.8	CSP08
CSP	1.0	0.6	1.4 – 1.0	CSP10
CSP-EGTP	0.6	0.2	0.7 – 0.0	CSP_EGTP06
CSP-EGTP	0.8	0.4	0.9 – 0.0	CSP_EGTP08
CSP-EGTP	1.0	0.6	1.1 – 0.0	CSP_EGTP10

The results of the standard deviation and the average of the shoreline position differences (random and systematic errors, respectively) for every sample area are shown in Table 3.3 and Table 3.4. Note that the 3-sigma rule for outlier removal was applied in order to obtain the results in a more suitable way to be analysed. It should be observed that certain residuals average values could be highly significant. That systematic error or offset could be likely due to the difference between the extrapolated gradient and the true one. This is a bias error inherent to the application of extrapolation approaches and, usually, is larger for the CSP method, since the EGTP method utilizes a local gradient which is closer to the true gradient than that estimated from the CSP method. In Table 3.3 and Table 3.4 may be underlined the large variability existing among the sample areas, which mainly depends on the beach morphology. Significant differences have been found between EGTP and CSP methods for rocky and high sloped areas and also for moderate sloped beaches, where EGTP method performed better. Furthermore, the transect orientation effect could be tested in some samples. The results from both methods were quite similar in steady-sloped beaches (sample areas 4 and 10). The largest error came out from the so-called “non-classified areas”, which corresponded to beach areas where typical berm shapes were present. These bended and irregular shapes negatively affected the results computed from the CSP method when they were embraced by the elevation data range. In this sense, the EGTP method was pointed out as more robust and so less affected by this kind of beach morphology. Meanwhile, the EGTP method resulted in failures and provided inappropriate results in part of the sample areas where the local gradient was positive or quite low.

*Table 3.16. Residuals Average results (m) for the extrapolated shoreline validation depending on the observed sample area. EGTP extrapolation failure due to non-extrapolation of positive gradients is indicated by *. Results supported by a low number of observations due to the 3-sigma outliers analysis are indicated by **.*

Sample data	Group	CSP06	CSP08	CSP10	EGTP06	EGTP08	EGTP10	CSP EGTP06	CSP EGTP08	CSP EGTP10
1	Rocky and high-sloped areas	-1.683	-1.518	-2.316	0.563	0.489	0.557	0.242	-0.246	-0.852
2		-0.713	-1.316	-1.397	0.013	-0.422	-0.488	-0.179	-0.904	-0.888
14		-0.273	-0.074	-0.339	0.125	0.48	0.797	0.04	0.343	0.552
3	Sandy and moderate-sloped beaches areas	-0.416	-0.766	-1.022	0.414	0.861	1.418	0.315	0.725	1.276
13		-1.643	-5.332	-7.838	-0.271	-1.567	-3.995	-0.358	-1.866	-4.698
4	Sandy and low-sloped beaches areas	0.175	-0.991	-0.335	0.418	-0.587	-0.945	0.38	-0.602	-0.142
10		0.782	0.858	0.307	0.643	1.077	0.348	0.609	1.071	0.378
5	Non-classified areas	-3.499	-2.894	-2.955	-0.645	-2.593*	0.091	-0.659	-2.986*	0.097
6		0.346	-5.07	-6.572	0.432	-0.392	-3.981*	0.407	-0.393	-8.58*
7		0.271	-13.946	-15.805	0.292	-0.812	-6.003*	0.277	-0.809	-5.655*
8		-15.945	-45.159	-13.936	0.436	-1.851	6.35*	0.415	-1.661	28.772*
9		0.563	-2.488	-152.581	0.459	0.905	-1.343	0.429	0.883	-1.591
11		-23.566	-46.553	-128.643	0.17	-0.327	3.079	0.054	-0.892	3.398**
12		-2.44**	-4.785**	-95.73	-1.63	-2.704	4.911*	-1.63	-2.631	-3.826**

*Table 3.17. Standard Deviation results (uncertainty in m) for the extrapolated shoreline validation depending on the observed sample area. EGTP extrapolation failure due to non-extrapolation of positive gradients is indicated by *. Results supported by a low number of observations due to the 3-sigma outliers analysis are indicated by **.*

Sample data	Group	CSP06	CSP08	CSP10	EGTP06	EGTP08	EGTP10	CSP EGTP06	CSP EGTP08	CSP EGTP10
1	Rocky and high-sloped areas	3.639	3.187	4.159	1.031	1.745	1.718	1.385	2.818	3.562
2		1.168	1.861	2.247	0.587	1.313	1.678	0.792	1.76	1.934
14		1.13	1.807	3.234	0.901	1.444	2.469	0.923	1.41	2.385
3	Sandy and moderate-sloped beaches areas	0.755	1.447	2.149	0.392	0.705	0.649	0.398	0.635	0.678
13		2.164	3.891	7.12	0.528	1.539	3.869	0.546	1.575	4.113
4	Sandy and low-sloped beaches areas	1.193	1.216	1.809	0.857	1.715	1.763	0.84	1.737	1.337
10		0.548	1.223	1.742	0.576	0.959	1.878	0.563	0.948	1.818
5	Non-classified areas	3.486	2.205	8.638	0.56	1.679*	1.856	0.542	2.034*	2.172
6		0.51	4.584	3.537	0.48	0.92	2.54*	0.466	0.897	7.998*
7		0.468	9.275	5.866	0.382	1.177	2.112*	0.375	1.174	1.893*
8		14.399	38.11	14.695	0.524	1.427	7.852*	0.519	1.434	88.534*
9		0.842	6.72	155.558	0.819	1.202	2.528	0.803	1.198	2.801
11		31.067	59.789	339.387	1.164	3.028	5.78	1.26	4.172	6.592**
12		1.352**	4.467**	101.547	0.805	1.74	16.414*	0.821	2.002	4.123**

Results by Reference Elevation

The influence of the reference elevation can be properly understood if the results for every tested method are separately analysed. Standard deviation results, or extracted shoreline uncertainty, highlighted the higher accuracy of the EGTP method and how it is affected by the reference elevation (Figure 3.7). At the reference elevation of 0.6 m (i.e., 0.2 m extrapolated amplitude), the shoreline accuracy is generally under 1 m and rather stable. At 0.8 m, or 0.4 m extrapolated amplitude, the accuracy results were located within around 1 and 2 m. Note that for 1.0 m reference level (the highest extrapolated amplitude), the sample areas number 8 and 12 have been removed since the extrapolation turned out to be erroneous (positive local gradient). It is shown that the EGTP values were similar until reaching the sample area 5, whereas the results from sample area 6 are usually worse. The offset value clearly grew with the reference elevation. According to these results, it can be concluded that the EGTP accuracy clearly depended on the extrapolated amplitude. In fact, the ground truth and the extracted shoreline were quite similar in the case of low amplitudes to extrapolate, whereas the deviations were greater for farther distances depending on the discrepancy between the modelled foreshore morphology and the true one. Thus, it is stated that the best reference elevation should be the nearest as possible to the chosen shoreline extraction level in order to minimize the difference between the true gradient and the extrapolated one.

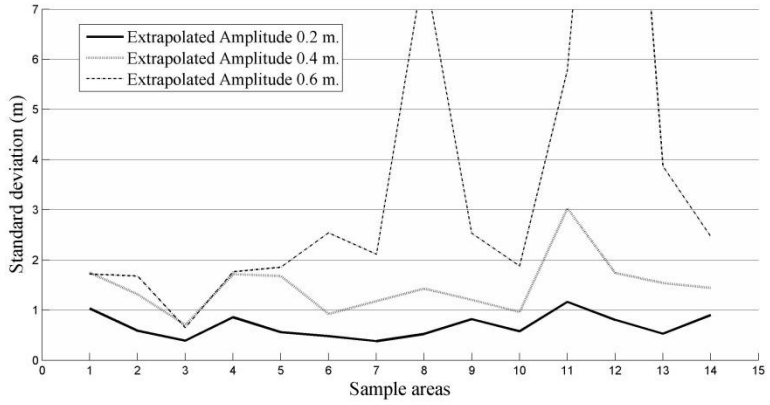

Figure 3.15. Uncertainty results (standard deviation) for the EGTP method according to the extrapolated amplitude along the different sample areas.

A better understanding about the performance of every method can be achieved by examining the accuracy results regarding the reference elevation. The

results of standard deviations for each reference elevation are shown through Figure 3.8. According to these results, the EGTP method has proved to be the more accurate for every reference elevation.

On the other hand, CSP seems to be much more dependent on the used data range since the results are, usually, less accurate than those from the EGTP method. However, it could be noted that the CSP results were still rather appropriate for the 0.6 m reference elevation because they have not been affected by the berm effect. In fact, the best accuracy for the CSP method is given by the lowest reference elevation (0.6 m) with a general standard deviation close to 2-2.5 m. On the contrary, the results became worse when higher reference levels were used, especially in berm sample areas. It could be explained because most of the foreshore is located within the data range from 0.6 to 1.0 m, whereas most of the berms arise from heights higher than 1.0 m. Indeed, that result is proved as compared with the other reference elevations, where the berm morphology clearly altered the linear foreshore morphology. This behaviour is also stepped up by the offset results. Therefore, the reference elevation has been underlined as the main parameter for the CSP method application, since beach areas have a significant variation in those elevation ranges.

Finally, the results for the EGTP and CSP_EGTP methods can be considered as quite similar, excepting for some sample areas where CSP_EGTP was less accurate. It was mainly due to a misalignment between the transect framework and the local steepest line.

Statistical Analysis of the Quantitative Results

In order to complete the analysis of the aforementioned results, a factorial experimental design was carried out. The differences between the estimated shorelines and the ground truth data for each transect were employed as observed or dependent variable. This experimental design allowed analysing the influence of different factors and their interactions on the shoreline extraction accuracy. The studied sources of variation were sample area, shoreline extraction method and reference elevation. Thus, a factorial univariate analysis of variance (ANOVA) was applied. It was performed onto two dependent variable grouping levels: i) individual observations (i.e., each transect constituted an independent observation) and ii) grouping observations which belonged to a given homogeneous sample area and computing their corresponding uncertainties or standard deviations (observed variable in this second case).

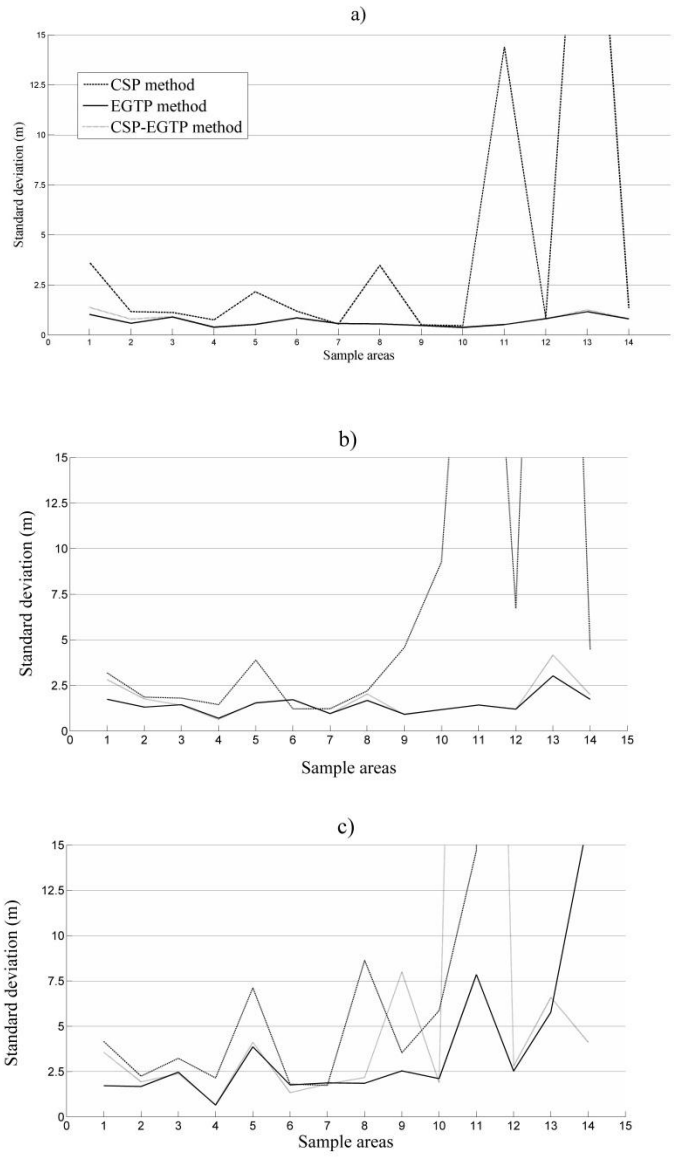

Figure 3.16. Uncertainty results (standard deviation) for every tested method. (a) Results for 0.6 m reference elevation or 0.2 m extrapolated amplitude; (b) results for 0.8 m reference elevation or 0.4 m extrapolated amplitude; (c) results for 1.0 m reference elevation or 0.6 m extrapolated amplitude. Note that several results have not been depicted in order to offer a more understandable representation. These results especially correspond to the CSP method for non-classified areas (i.e., the sample areas 12, 13, 14 in c). See Table 3.4 for further information.

ANOVA for the individual observations

As a summary, Table 3.5 depicts the number of observations for each source of variation: Sample Area, Computation Method and Reference Elevation. Note that the number of observations for each Computation Method is variable due to the 3-sigma outlier analysis, which removed less number of noisy observed data from the CSP method. It was mainly due to its high level of variability as compared with EGTP and CSP_EGTP methods. Additionally, it should be highlighted that the number of observations was also different for each Reference Elevation owing to the fact that a larger number of outliers was detected and removed in the case of the highest elevations.

Table 3.18. Number of observations for each source of variation.

Factor	Variation	Number of observations
Sample Area	1	914
	2	1527
	3	1327
	4	1035
	5	1106
	6	1459
	7	1953
	8	706
	9	1105
	10	2140
	11	826
	12	582
	13	999
	14	972
Computation Method	EGTP	5471
	CSP	5741
	CSP_EGTP	5439
Reference Elevation	0.6 m	5789
	0.8 m	5600
	1.0 m	5262

The final results from the ANOVA study are shown in Table 3.6. It is worth noting the high signification level for all the factors and their interactions ($p<0.001$). These results clearly bring out that every one of the tested explanatory variables presented a large and statistically significant influence on the final results, as it was initially expected. Therefore, it can be stated that the estimated shoreline accuracy greatly depends on the applied extrapolation method. In addition, and as was shown in previous sections by means of a qualitative approach, it has been proved that both the sample area and the reference elevation are also relevant to explain shoreline extraction accuracy. Meanwhile, the

interactions between all these variables were also statistically significant. For example, each method worked significantly different depending on the sample area where it was applied, likely due to the presence of different beach morphologies (Computation Method and Sample Area interaction). With regard to the Computation Method and Reference Elevation significant interaction, it should be noted that it is pointing out that each method yielded different results depending on the reference elevation. Finally, the significant results shown by the Sample Area and Reference Elevation interaction is clearly indicating that every homogeneous area considered, and so each beach typology, was sensitive to the different reference elevations tested. In this sense, more steady slopes allows increasing the reference elevation and vice versa.

Table 3.19. ANOVA table corresponding to the differences between the extracted shoreline and the ground truth along each transect (observed variable).

Source of variation	Degrees of freedom	Sum of squares	Mean square	F	Significance (p<0.05)
Model	126	6168051.49	48952.79	48.20	**<0.001**
Computation Method (A)	2	673802.05	336901.02	331.75	**<0.001**
Reference Elevation (B)	2	198285.40	99142.70	97.62	**<0.001**
Sample Area (C)	13	616843.00	47449.46	46.72	**<0.001**
A * C	26	1387091.31	53349.66	52.53	**<0.001**
B * C	26	838015.45	32231.36	31.73	**<0.001**
A * B	4	468609.08	117152.27	115.36	**<0.001**
A * B * C	52	1647466.52	31682.04	31.19	**<0.001**
Error	16525	16781593.46	1015.52		
Total	16651	22949644.95			

Once proved that the results were statistically significant, a Mean Separation Analysis (MSA) was applied to each factor. In this case, a Tukey's test for treatment differences (John 1998) was carried out. Tukey's test is a 'post hoc' test designed to perform a pairwise means comparison between the different levels or treatments corresponding to an analysed factor after ANOVA analysis.

The MSA results for the variable Sample Area are depicted in Table 3.7. Five clusters were statistically separated, the groups 1 and 2 being significantly different, while the groups 3, 4 and 5 are quite underhand. Obviously, the qualitative-based classification carried out for Table 3.3 and Table 3.4 does not match with this one because the 'post hoc' analysis was applied in order to differentiate the mean of each group, while the previous qualitative classification was made up attending to the standard deviation of each group, since it indicates the overall accuracy of the applied shoreline extraction method.

Table 3.20. Mean Separation Analysis for the 14 levels which make up the factor Sample Area. Different super indices indicates significant differences at level p<0.05.

Sample Area	Homogeneous groups regarding mean differences (m) for each sample area				
	1	2	3	4	5
11	-23.64[a]				
9		-18.00[b]			
12		-15.34[b]			
8			-6.56[c]		
7			-4.57[cd]	-4.57[cd]	
13			-3.13[cd]	-3.13[cd]	-3.14[cde]
6			-2.49[cd]	-2.49[cd]	-2.50[cde]
5				-1.72[de]	-1.73[de]
2				-0.69[de]	-0.69[de]
1				-0.49[de]	-0.49[de]
4				-0.29[de]	-0.29[de]
14					0.29[e]
3					0.35[e]
10					0.67[e]

The MSA results for the variable Computation Method are depicted in Table 3.8. This may be deemed as a very relevant result because it stated that the EGTP and CSP_EGTP methods were significantly more accurate than the CSP one. In fact, the overall accuracy for the CSP method turned out to be very poor, especially due to the *'berm effect'* over the profile data adjustment.

Finally, the 'post hoc' results for the variable Reference Elevation turned out to be very relevant as well, since they proved that the elevation from which the DEM is extrapolated highly affected the shoreline extraction accuracy. In fact, as it is shown in Table 3.9, there were three significantly different groups according to the observed variable and the factor Reference Elevation. That is, an increase of only 0.20 m in the reference height produced statistically different results regarding extracted shoreline accuracy, what arises the need of finding the most suitable reference elevation (i.e., as close as possible to the required shoreline extraction level) for starting the extrapolation process.

In order to check the influence of the CSP method observations on the previous analysis, a further factorial experimental design was carried out over the observed data after removing all the CSP ones. In this second case, all the factors and interactions were found significant ($p<0.05$) except the factor Computation Method and the Computation Method and Reference Elevation interaction. Therefore, the EGTP and CSP_EGTP methods seemed to perform quite similar shoreline accuracy. However, a very important finding can be observed in Table 3.10. The 'post hoc' results for the Reference Elevation variable points out how the

mean value for each level turns out to be much lower than those found in the previous results (Table 3.9), indicating a somehow polluting effect owing to the inclusion of the CSP data. On the other hand, it is worth to notice that a lesser dependence regarding the reference elevation was found since the two highest elevations rendered the same accuracy results.

Table 3.21. Mean Separation Analysis for the three levels which make up the factor Computation Method. Different super indices indicates significant differences at level p<0.05.

Computation Method	Mean values (m) for each method	
	1	2
CSP_EGTP		-0.225[a]
EGTP		-0.174[a]
CSP	-11.854[b]	

Table 3.22. Mean Separation Analysis for the three levels which make up the factor Reference Elevation. Different super indices indicates significant differences at level p<0.05.

Reference elevation	Mean values (m) for each level		
	1	2	3
0.6 m			-0.749[a]
0.8 m		-2.827[b]	
1.0 m	-9.514[c]		

Table 3.23. Mean Separation Analysis for the two levels which make up the factor Reference Elevation after excluding all the CSP observations. Different super indices indicates significant differences at level p<0.05.

Reference Elevation	Mean values (m) for each level	
	1	2
0.6 m.		0.12[a]
0.8 m.	-0.37[b]	
1.0 m.	-0.37[b]	

ANOVA for the uncertainty (standard deviation) estimated for each sample area

The ANOVA results regarding individual observations have proved that the variables Sample Area, Computation Method and Reference Elevation can be deemed as statistically significant to explain the variability of the differences between the estimated shoreline and the considered ground truth. However, and along this paper, the standard deviation of the aforementioned differences has been established as an adequate accuracy indicator for the extracted shorelines. Therefore, an additional factorial univariate ANOVA was carried out over the standard deviation results for each combination of Sample Area, Computation Method and Reference Elevation. In this case, the number of cases or observations was 146 (14 sample areas, three computation methods and three reference elevations).

In Table 3.11 are depicted the results of the computed standard deviation for the observed differences, where it is worth to underline that the factors Computation Method and Reference Elevation turned out to be statistically significant ($p<0.05$), whereas Sample Area only showed slightly significant differences ($p<0.10$). These results could be expected since the number of observations has been drastically reduced respect to those used in the first ANOVA headed up to analyse individual observations or transects.

Table 3.24. ANOVA table corresponding to the standard deviation (dependent variable) computed from the individual observed differences regarding the extracted sample areas.

Source of variation	Degrees of freedom	Sum of squares	Mean square	F	Significance ($p<0.05$)
Computation Method (A)	2	8549.05	4274.53	4.65	**0.0139**
Reference Elevation(B)	2	7931.15	3965.58	4.31	**0.0185**
Sample Area (C)	13	21876.20	1682.79	1.83	0.0628
A*B	4	7395.49	1848.87	2.01	0.1068
A*C	26	39324.9	1512.50	1.64	0.0636
B*C	26	22563.6	867.83	0.94	0.5530
Error	52	47852.00	920.23		
TOTAL	125	155492.00			

With regard to the 'post hoc' analysis for the ANOVA significant factors, a highly relevant finding has been obtained from the variables Computation Method and Reference Elevation. Two statistically homogeneous groups have been

separated according to Tukey's test in the case of the factor Computation Method (Table 3.12). The first group included the CSP method, which was clearly less accurate than the other two ones. In this way, there was no significant differences ($p<0.05$) between the EGTP and CSP_EGTP computation methods regarding the shoreline extraction accuracy.

Table 3.25. Mean Separation Analysis for the standard deviation within the three levels which make up the factor Computation Method. Different super indices indicates significant differences at level p<0.05.

Computation Method	Homogeneous groups regarding standard deviation (m)	
	1	2
EGTP		1.984[a]
CSP_EGTP		3.904[a]
CSP	20.338[b]	

Regarding the variable Reference Elevation (Table 3.13), the 'post hoc' analysis brought out two different subsets. The reference elevations of 1.0 m and 0.6 m were situated within different homogeneous groups, whilst the reference elevation of 0.8 m was not statistically different from the other two ones. Summing up, the reference elevation to start the extrapolation process significantly affected the shoreline extraction accuracy, being more pronounced when the height difference between the reference elevation and the desired shoreline extraction level was larger.

Table 3.26. Mean Separation Analysis for the standard deviation within the three levels which make up the factor Reference Elevation Method. Different super indices indicates significant differences at level p<0.05.

Reference Elevation	Homogeneous groups regarding standard deviation (m)	
	1	2
0.6 m.		1.966[a]
0.8 m.	4.385[ab]	4.385[ab]
1.0 m.	19.875[b]	

This quantitative analysis over the transect-by-transect shoreline differences between the extracted shoreline and the ground truth has highlighted the high influence contributed by every tested variable. The extrapolation method has turned out to be a highly significant factor affecting the variability of the shoreline differences, both considering individual observations and computing their accuracy by means of their standard deviation. The EGTP method could be pointed out as the most suitable method, although there were no significant differences with respect to the CSP_EGTP method. On the other hand, the CSP method was

found as an unsuitable method to extrapolate along typical microtidal beach profiles. In addition, the reference elevation has been established as a decisive parameter since at least two groups could be statistically separated. It is indicating the importance of a proper choice for the reference elevation. Shortly, the nearer is the reference elevation regarding the shoreline extraction level, the better will be the extracted shoreline accuracy. Finally, the influence of the data for every sample area could be proved through the individual transects study, underlining the existence of a close relationship between the extracted shoreline accuracy and the beach morphology.

CONCLUSIONS

A new methodology based on iterative gradient extrapolation, called EGTP method, has been presented in this work. It has been especially designed to be applied over coastal microtidal areas where the required shoreline vertical datum could not be interpolated because of the absence of data under that level. Moreover, the linear adjustment of altimetry profiles (CSP methodology) was developed in order to carry out the extrapolation process, being one of the most widespread DEM-derived shoreline extraction approaches. The EGTP method have usually headed up to a better drawing of the coastal shapes as compared with the results from the CSP method, above all when working on bended and complex coastal areas. The influence of transect orientation for an accurate shoreline extraction when using the CSP method has been also proved. Therefore, it is strongly recommended to apply an automatic profile extraction following the local direction of the steepest line.

Conversely to the CSP algorithm, the EGTP method is presented as a more robust and unattended method, i.e., less dependent on onshore data. Furthermore, this new methodology does not need an elevation data range, but a minimum elevation from which the original DEM is extrapolated. This elevation took a value of 0.40 m in this work after performing a careful DEM contouring inspection, although it could be also estimated as the maximum wave height or runup (Stockdon et al. 2006), or by removing LiDAR returns over water (Yates et al. 2008). This methodology also offers a high resolution shoreline, since it is extracted from an analogous way to a contour level. In this sense, the EGTP method does not need defining a transect framework to draw the extracted shoreline, although the transect system could be needed for carrying out a shoreline evolution assessment.

In addition, an exhaustive validation process based on a factorial experimental design was carried out to quantitatively test the performance of the CSP, EGTP and CSP_EGTP methods. The analysis was carried out using the 0.4 m contour level instead of the required zero-elevation contour (both referred to the Spanish EGM08-REDNAP vertical datum) since nearshore bathymetric data were

not available. Regarding further works, 'in situ' data will be collected (e.g. by means of DGPS profiles) in order to carry out a specific validation on the zero-elevation contour corresponding to the Spanish EGM08-REDNAP vertical datum. From this analysis, a systematic error or offset has been detected which is mainly attributed to the difference between the true gradient and the extrapolated one. Thus, those data which allow applying interpolation processes are strongly recommended. The reference elevation was proved as a statistically significant factor affecting the extracted shoreline accuracy, especially in the case of the CSP method. In this way, the inadequate performance of the CSP method in many areas was mostly due to the berm morphology effect, i.e., the captured foreshore profile did not match to a linear fit. This situation was frequent when the elevation data range was the highest one and so the likelihood to embrace a berm was relatively high. This results recommend that the ready-to-fit elevation range should be the nearest as possible to the required shoreline extraction height. The use of an elevation range below the berm morphology elevation is also recommended.

Summing up, along this work has been proved the satisfactory results yielded by the proposed local gradient extrapolation method in order to estimate datum-coordinated shorelines where the interpolation methods cannot be used. Based on the presented results, it can be drawn that, both quantitatively and qualitatively, the new grid-based approach can be strongly recommended because its precision, local slope acquisition, robustness regarding the presence of noise and outliers, and capability to deal with very curved and even closed coastal features.

REFERENCES

Aguilar, F.J., Fernández, I., Pérez, J.L., López, A., Aguilar, M.A., Mozas, A. & Cardenal, J. 2010a, "Preliminary results on high accuracy estimation of shoreline change rate on coastal elevation models.", *International Archives of the Photogrammetry, Remote Sensing and Spatial Information Science*Kyoto, Japan, 9-12 Augost 2010, pp. 986.

Aguilar, F.J., Mills, J.P., Delgado, J., Aguilar, M.A., Negreiros, J.G. & Pérez, J.L. 2010b, "Modelling vertical error in LiDAR-derived digital elevation models", *ISPRS Journal of Photogrammetry and Remote Sensing,* vol. 65, no. 1, pp. 103-110.

Boak, E.H. & Turner, I.L. 2005, "Shoreline definition and detection: A review", *Journal of Coastal Research,* vol. 21, no. 4, pp. 688-703.

Brock, J.C. & Purkis, S.J. 2009, "The emerging role of lidar remote sensing in coastal research and resource management", *Journal of Coastal Research,* , no. SPECIAL ISSUE 53, pp. 1-5.

Gens, R. 2010, "Remote sensing of coastlines: Detection, extraction and monitoring", *International Journal of Remote Sensing,* vol. 31, no. 7, pp. 1819-1836.

Genz, A.S., Fletcher, C.H., Dunn, R.A., Frazer, L.N. & Rooney, J.J. 2007, "The predictive accuracy of shoreline change rate methods and alongshore beach variation on Maui, Hawaii", *Journal of Coastal Research,* vol. 23, no. 1, pp. 87-105.

González, R.C. & Woods, R.E. 2008, *Digital Image Processing (3th Edition),* Pearson Prentice Hall, Upper Saddle River, New Jersey.

Graham, D., Sault, M. & Bailey, J. 2003, "National Ocean Service Shoreline - Past, Present, and Future", *Journal of Coastal Research,* , no. SPEC. ISS. 38, pp. 14-32.

Hapke, C.J., Reid, D., Richmond, B., Ruggiero, P. & List, J. 2006, *National assessment of shoreline change: Part 3: Historical shoreline changes and associated land loss along the sandy shorelines of the California coast*, U.S. Geological Survey Open-File Report.

Heuvelink, G.B.M., Burrough, P.A. & Stein, A. 1989, "Propagation of errors in spatial modelling with GIS", *International Journal of Geographical Information Systems,* vol. 3, no. 4, pp. 303-322.

Huang, J.D., Jackson, D.W.T. & Cooper, J.A. 2010, "Piecewise Polynomial Expression of Beach Profiles", *Journal of Coastal Research,* vol. 27, no. 1, pp. 851-859.

IEO, S. 2013, *Instituto Español de Oceanografía*. Available: www.ieo.es [2013, 03/15].

IHM, S. 2013, *Instituto Hidrográfico de la Marina*. Available: http://www.armada.mde.es/ArmadaPortal/page/Portal/ArmadaEspannola/ciencia_ihm_1/prefLang_es/ [2013, 03/13].

John, P.W.M. 1998, *Statistical design and analysis of experiments,* Society for Industrial and Applied Mathematics, New York.

Li, R., Ma, R. & Di, K. 2002, "Digital Tide-Coordinated Shoreline", *Marine Geodesy,* vol. 25, no. 1-2, pp. 27-36.

Li, Z. 1993, "Mathematical models of the accuracy of digital terrain model surfaces linearly constructed from square gridded data", *Photogrammetric Record,* vol. 14, no. 82, pp. 661-674.

Liu, H., Sherman, D. & Gu, S. 2007, "Automated extraction of shorelines from airborne light detection and ranging data and accuracy assessment based on Monte Carlo simulation", *Journal of Coastal Research,* vol. 23, no. 6, pp. 1359-1369.

Maune, D.F. 2001, *Digital Elevation Model Technologies and Applications,* American Society for Photogrammetry and Remote Sensing, Bethesda, Maryland.

Mills, J.P., Buckley, S.J., Mitchell, H.L., Clarke, P.J. & Edwards, S.J. 2005, "A geomatics data integration technique for coastal change monitoring", *Earth Surface Processes and Landforms,* vol. 30, no. 6, pp. 651-664.

Monmonier, M. 2008, *Coastlines: How Mapmakers frame the World and Chart Environmental Change,* The University of Chicago Press, Chicago.

Morton, R.A. & Miller, T.L. 2005, *National assessment of shoreline change: Part 2: Historical shoreline changes and associated coastal land loss along the U.S. Southeast Atlantic Coast.*, U.S. Geological Survey Open-file Report.

Morton, R.A., Miller, T.L. & Moore, L.J. 2004, *National assessment of shoreline change: Part 1: Historical shoreline changes and associated coastal land loss along the U.S. Gulf of Mexico.*, U.S. Geological Survey Open-file Report.

NCR, U.S. 2004, *A Geospatial Framework for the Coastal Zone: National Needs for Coastal Mapping and Charting,* National Academy Press, Washington, D.C.

Pajak, M.J. & Leatherman, S. 2002, "The high water line as shoreline indicator", *Journal of Coastal Research,* vol. 18, no. 2, pp. 329-337.

Puertos del Estado. Available: http://www.puertos.es/ [2013, 03/13].

REDNAP, S. 2013*, Red de Nivelación de Alta Precisión*. Available: http://www.ign.es/ign/layoutIn/actividadesGeodesiaRedn.do [2013, 03/13].

Ruggiero, P. & List, J.H. 2009, "Improving Accuracy and Statistical Reliability of Shoreline Position and Change Rate Estimates", *Journal of Coastal Research,* vol. 25, no. 5, pp. 1069-1081.

Stockdon, H.F., Holman, R.A., Howd, P.A. & Sallenger Jr., A.H. 2006, "Empirical parameterization of setup, swash, and runup", *Coastal Engineering,* vol. 53, no. 7, pp. 573-588.

Stockdon, H.F., Sallenger Jr., A.H., List, J.H. & Holman, R.A. 2002, "Estimation of shoreline position and change using airborne topographic lidar data", *Journal of Coastal Research,* vol. 18, no. 3, pp. 502-513.

Suárez de Vivero, J.L. & Rodríguez Mateos, J.C. 2005, "Coastal crisis: The failure of coastal management in the Spanish Mediteranean region", *Coastal Management,* vol. 33, no. 2, pp. 197-214.

Thieler, E.R., Himmelstoss, E.A., Zichichi, J.L. & Ergul, A. 2008, *Digital Shoreline Analysis System (DSAS) version 4.0—An ArcGIS extension for calculating shoreline change.*, U.S. Geological Survey Open-File Report.

White, S. 2007, "Utilization of LIDAR and NOAA's vertical datum transformation tool (VDatum) for shoreline delineation", *Oceans Conference Record (IEEE)*.

White, S.A., Parrish, C.E., Calder, B.R., Pe'Eri, S. & Rzhanov, Y. 2011, "LIDAR-derived national shoreline: Empirical and stochastic uncertainty analyses", *Journal of Coastal Research,* , no. SPEC. ISSUE 62, pp. 62-74.

Wilcox, R.R. 2003, "Least Squares regression and Pearson's correlation" in *Applying contemporary statistical techniques* Elsevier, The Netherlands, pp. 173-206.

Woodroffe, C.D. 2002, *Coasts: form, process, and evolution.* 1st edn, Cambrigde University Press, New York.

Yates, M.L., Guza, R.T., Gutierrez, R. & Seymour, R. 2008, "A technique for eliminating water returns from lidar beach elevation surveys", *Journal of Atmospheric and Oceanic Technology,* vol. 25, no. 9, pp. 1671-1682.

CHAPTER 4.

Assessing medium-term shoreline change rate along heavily developed Mediterranean coastal areas. A study case located at Almeria province, Spain.

ABSTRACT

The long-term shoreline change rate constitutes an essential parameter for coastal areas management and monitoring in order to estimate erosion areas and to be able to forecast the future shoreline position. Here, shoreline rates were assessed in a heavily human influenced coastal cell of the Mediterranean coast located at Almeria province, Spain, by using multisource and multitemporal shoreline positions from 1956 to 2011. Since no older data than 1956 was available, medium-term instead of long-term evolution could be yielded. Two kinds of sources were used in order to derive shoreline positions: digitizing the high water line through orthoimage interpretation and automatically extracting a contour level from coastal elevation models (CEMs). Moreover, two types of images were used: own-produced and existing spatial data infrastructure (SDI) orthoimages; while two types of CEMs were also utilized: high accurate LiDAR-derived and photogrammetrically-extracted own-produced CEMs.

The most appropriate proxy used for shoreline extraction was studied, comparing HWL and two datum-based contours, one extrapolated up to 0 m and the other interpolated at 0.75 m above mean sea level (Spanish altimetric datum), resulting the last one as the most accurate shoreline indicator and proving the effects of including the bias between HWL and datum-based shoreline. Moreover, a high variability of shoreline position could be tested when HWL was used as a proxy for shoreline, being HWL less accurate than CEM-derived shorelines except for the oldest dataset. The shoreline accuracy was estimated for both HWL and CEM-derived shorelines in order to apply weighted regression methods to estimate shoreline change rate. The rate of shoreline change was observed over the time in order to relate natural and artificial impacts with shoreline evolution. In this way, it was observed that the temporal distribution on flood events and the sediment reduction due to a dam construction into the main river basin presented a high relation with the erosion occurred over the years. Additionally, other human-induced factors such as jetties installation and sand nourishment had a large impact on shoreline evolution.

Finally, the effects of including SDI shorelines, using concentrated in-time shoreline positions, considering different time spans, performing estimation of outlier shoreline position, and considering shoreline position accuracy, were estimated by means of the assessment of medium-term shoreline change rate by means of several regression methods and different sets of shorelines. The most appropriate approach was proved to be the reweighted-weighted least squares (RWLS) when the entire time span was used by means of a confidence interval comparison.

Keywords: Shoreline change rate, shoreline accuracy, shoreline indicator, medium-term shoreline evolution.

INTRODUCTION

Coastal areas are one of the most populated and economic development areas in the world and this pressure in the coastal zone will increase during the last centuries (Brommer, Bochev-Van Der Burgh 2009). Shoreline evolution constitutes one of the most important issues for coastal scientists, engineers, and managers (Boak, Turner 2005). Determination of erosive coastal stretch and the erosion rate is highly important in order to estimate future positions of shoreline and to plan the needed actions. For instance, setback policies (buffer space where permanent constructions are not allowed) should take into account the possible effects of extreme storm events but also the most probable future position of the high water mark (Sánchez-Arcilla, Jiménez & Marchand 2011). Therefore, according to the Spanish coastal law the shoreline behaviour has strong implications for the position of the limit of the Maritime-Terrestrial Public Domain –MTPD- (Sanò et al. 2011).

Shoreline change rate assessment is only one part of the coastal zone management which comprises several disciplines such as stratigraphic, geomorphological, and coastal engineering communities (Brommer, Bochev-Van Der Burgh 2009). Coastal sediment cell (or just coastal cell) is delimited for coastal management and corresponds to a geographical area within the budget of sediment is determined and it is essential for analysing coastal erosion or accretion (Marchand et al. 2011). Therefore, a complete shoreline evolution assessment should be performed in an entire coastal cell. Sediment budget is also a highly important issue regarding the coastal management since it constitutes one of the main influent factors of shoreline behaviour related to long-term coastal evolution (Rosati 2005, Brommer, Bochev-Van Der Burgh 2009). Especially for Mediterranean coasts, the sediment supply reduction coupled with alongshore currents have been considered the main reason of shoreline erosion (Uceda, Sánchez-Arcilla & Cardeña 2005). Moreover, especially in the Spanish case, torrential-type meteorology makes quite difficult to properly assess the sediment input from very short rivers (Sánchez-Arcilla, Jiménez & Marchand 2011). The same authors also identified the shortage of space for coastal processes due to urbanization as an erosion problem source together with the lack of sediments.

For coastal management it is also important to define the scale of the framework and the relations among different processes occurred at different scales. Thus, long-term and medium-term shoreline change rates are related with mega and macro scales respectively representing from years to centuries time span (Cowell et al. 2003), although shoreline evolution studies usually include around 100 years. Temporal scale is a central issue and it can influence the perceptions of dynamics and conclusions regarding cause and effect relationships within them (Fenster, Dolan & Morton 2001) and, in fact, forecast should not be made for periods longer than half the period covered by the dataset (Bowman,

Pranzini 2008). Moreover, the geological framework should be taken into account to explain the erosional or accretion processes (Honeycutt, Krantz 2003) and some authors have recommended the sediment thickness mapping to explain the relationship between erosion and the underlying geology (Bowman, Pranzini 2008).

Regarding the methods used to estimate shoreline evolution and variability, the most used approach is based on transects (historical shoreline position are used for change rate estimation), although some other approaches such as surface variation analysis have been utilized (Pranzini, Daniela 2008). Moreover, although having as many transects as possible reduces the effects of noise, some binning methods have been developed to eliminate overparameterization (Frazer, Genz & Fletcher 2009). In order to estimate the shoreline evolution for every transect (or a group of them), it should be clear whether the aim is the assessment of long-term or short-term evolution. While different and varied regression methods are used for the former (Genz et al. 2007), some polynomial approaches have been developed for trying to describe the latter (Romine et al. 2009) and even acceleration on shoreline evolution has been tested (Frazer, Genz & Fletcher 2009). Furthermore, shorelines have to be defined by a physical shoreline indicator used as a proxy to represent the true shoreline position (HWL, wet/dry boundary, etc.) or by a tidal datum-based shoreline, e.g. MHW or mean sea level (MSL) (Boak, Turner 2005). The latter are being more commonly used during the last decade due to availability of high accurate LiDAR-DEMs, while physical shoreline indicators have been usually extracted from aerial (ortho)images or even more coarse satellite images (Maiti, Bhattacharya 2009). However, although accurate shoreline extraction is indispensable, it does not guarantee to define the long-term coastal evolution since oversampling can occur and severe oscillations must be cut off (Bowman, Pranzini 2008). Moreover, for the most of the shoreline evolution studies, the inherent variability of the shoreline position indicator (especially for physical ones) will remain a limitation on the final accuracy of the data (Douglas, Crowell 2000).

Shoreline evolution assessment on Mediterranean areas

Many of the most relevant literature on shoreline evolution assessment methods, shoreline indicators and accuracy, shoreline data source and extraction, and influent factors such as time span, influence of storm-events, etc., are based on very different types of coast but non-Mediterranean ones (Crowell, Leatherman & Buckley 1993, Crowell, Douglas & Leatherman 1997, Douglas, Crowell 2000, Fletcher et al. 2003, Morton, Miller & Moore 2004, Morton, Miller 2005, Hapke et al. 2006, Genz et al. 2007, Frazer, Genz & Fletcher 2009, Romine et al. 2009). For instance, beach morphology and shoreface are not equal for different tidal regime

coasts (Mediterranean can be considered entirely micro-tidal), so the shoreline indicator and accuracy can be different.

Other considerations should be done because the time span can significantly vary since accurate old data source are not widespread available for every coastal area. Thus, while in UK some charts exist from 1750, US T-sheets are available from mid-1800s in some areas. Latters have been widely used for shoreline evolution assessment constituting the warrantee for estimating long-term shoreline rates and their uncertainty has been also studied (Moore 2000, Boak, Turner 2005). However, for some Mediterranean areas such as Spain, it is difficult to have such an old dataset and the long-term evolution assessments are constrained and the first dataset used is normally the so-called *'American flight'* taken between 1956 and 1957 (Jiménez, Sánchez-Arcilla 1993, Viciana 1996, Ojeda et al. 2007, Espinosa, Rodríguez 2009). However, older maps (e.g. from 1870) have been used for other Mediterranean coastal areas (Alberico et al. 2012).

Regarding the shoreline definition in Mediterranean areas, there is not a unique proxy used for physical indicator but HWL or wet/dry boundaries are usually utilized (Bowman, Pranzini 2008, Virdis, Oggiano & Disperati 2012). Furthermore, there is not a Mediterranean regional tidal-datum used for shoreline definition in contrast with US, where MHW –average elevation of all high waters recorded locally over 19 years (Ruggiero, List 2009)- is officially used. It has been found that in Italy, the zero isobaths is generally used as reference shoreline in spite of it is invisible on beach but it is an objective geodetic element (Bowman, Pranzini 2008). Therefore, the definition of a stable datum-based reference should be a key issue in order to harmonize shoreline change rates at European or Mediterranean continental scale.

Shoreline change assessment has become an important issue in Mediterranean coasts in Europe. For instance, almost 41% of the Andalusia Mediterranean coast is currently undergoing erosive processes (European-Commission 2009). In Italian Tuscany beaches, the 45.7% of them experienced a shoreline retreat greater than 2 m/yr during the last 50 years (Bowman, Pranzini 2008). The most important factor for erosion in Mediterranean beaches has been the drastic reduction of sediment supply because fluvial basins regulation and dams construction (Senciales, Malvárez 2003, Uceda, Sánchez-Arcilla & Cardeña 2005). Thus, deltas and river mouths have experienced great retreats. For example, up to 10.7 m/yr erosion was found along the Tuscany river mouths (Bowman, Pranzini 2008). Additionally, the differences in climate conditions play a key role for sediment supply and have an effect on shoreline evolution when the rainfall rate changes (Alberico et al. 2012). The effects of wave currents were found to be highly significant for delta and river mouths erosion when coupled with sediment supply reduction (Jiménez, Sánchez-Arcilla 1993).

The aim of this Chapter is determining the medium-term shoreline change rate in a Mediterranean sediment cell of Almeria (Spain). In order to yield a

comprehensive explanation of shoreline change evolution, a more detailed description of the study site (as compared with *Study Site* section of this Thesis) will include geological background, the nearshore description, the oceanographic and climatic features, and the principal human impacts affecting this coastal area. Then, the different datasets from which shorelines were extracted will be described. Afterwards, the different shoreline indicators used, their extraction from the datasets, and the accuracy of every extracted shoreline will be discussed. Finally, shoreline change will be presented by discussing the short-term evolution of changes linked with climatic features and human interventions, and assessing the long- or medium-term shoreline change rate for the entire time span trying to find the most appropriate regression method.

STUDY SITE

General description of the area

As previously seen in the *'Study site'* section of this Thesis, the study area of this work was situated between the villages of *Villaricos* and *Garrucha*, in the East part of the Almeria province (South of Spain). Here, a much more detailed description of the study area is undertaken in order to help the understanding of the shoreline evolution results. Although the dataset extension comprises a wider area, only those coastal zones in which relevant changes are due to natural processes have been included. For instance, the *Garrucha*'s beach corresponds to an artificial embayed beach progressively installed at the south of the *Garrucha*'s harbour. The *Villaricos*' urban beaches do not depict any sensible evolution and they are also close embayed beaches located between rocky systems and harbour docks. Therefore, the remaining coastal area from the South of the *Villaricos* urban area to the North of the *Garrucha*'s harbour will be the study site of this work. It is worth noting that the finally chosen coastal area seems to fit the 'coastal sediment cell' concept perfectly since it *"defines a coastal compartment that contains a complete cycle of sedimentation including sources, transport paths and sinks"* (Marchand et al. 2011). The sources of sediment are clearly defined in this area by the *Almanzora* and *Antas* river mouths, although direct sediment exchange between sand beaches and open coastal areas cannot be discarded. Regarding transport processes, it seems to be clear that the main transport direction is alongshore from North-East to South-West (see climate features). The *Almanzora*'s mouth and delta, located at the north of the coastal cell, can be considered as the main sediments supplier of the studied coastal cell, delivering the sediments through the alongshore direction, the balance between erosion and accretion mainly depending on the relative position between the coast angle (given by the normal to the shoreline) and the dominant waves direction (Roelvink, Reniers 2012).

Geological background

It is important to know the geological background of the area and its evolution (Figure 4.1), in order to contextualize the coastal evolution under the low-order coastal change (geological time scale order, 10^3 years). The entire study site is located in the so-called 'Vera basin', one of a series of interconnected Neogene-Quaternary sedimentary basins located within the Internal Zone of the Betic Cordillera (Stokes, Mather 2003, Stokes 2008).

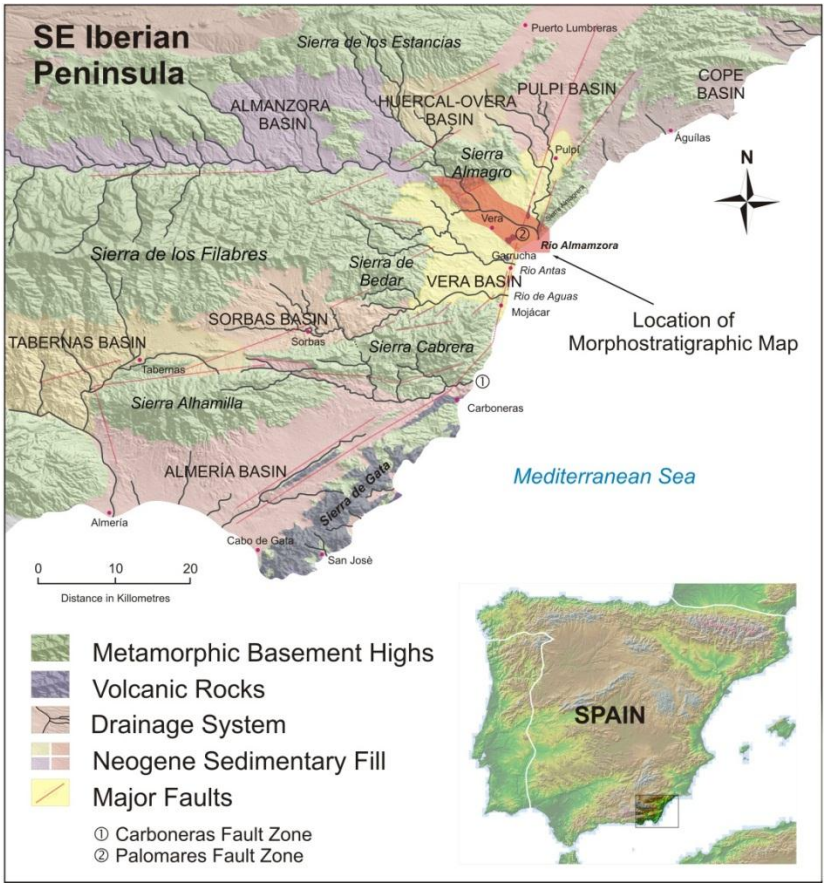

Figure 4.1. Representation of the geological background of the study site. Image courtesy of Dr. Chris Meikle (Meikle 2008).

This area is confined among the Paleozoic-Mesozoic metamorphic basement formed by four ranges of mountains: Sierra Almagrera, Sierra Almagro, Sierra de los Filabres, and Sierra Cabrera. Historically, Vera basin has been filled from the ancestral forms of the rivers *Almanzora*, Aguas and *Antas* which captured basins and mountain catchments from the north (Huercal-Overa basin), southwest (Sorbas basin) and west (Sierra de los Filabres range). Consecutively, the evolution

followed in this basin mainly consisted of three stages: first, a Pliocene marine sedimentation; second, a Plio-Pleistocene continental sedimentation; and finally, a Pleistocene fluvial incision (Stokes 2008). Moreover, the *Palomares* fault crosses the Vera basin near the shoreline and it would have acted as a shelf edge and also it would have induced to a narrow offshore shelf (Meikle, Stokes & Maddy 2010). Summing up, the study area has a sedimentary nature and the rivers which flow on it had a key role on the relief formation.

Nearshore description

The bathymetry of the study site indicates the great influence of the *Almanzora* River apart from the previously mentioned geological aspects (Figure 4.2). Examining the depth data up to 30 m below sea level, it is clear that the distance between the -30 m contour line and the shoreline is gradually narrower from the *Almanzora*'s mouth to the *Garruchas*' harbour. Moreover, the influence of the fan-delta sediment supplied by the *Almanzora*'s mouth seems to have much less influence towards North, being the -30 m contour line and the shoreline distance much rapidly narrower than towards South. That fact could strengthen the hypothesis that the overall historic sediment transport has been towards southwest from the *Almanzora*'s mouth. A key aspect of the nearshore area would be the *Palomares* canyon located at the study site south edge (just in front of *Garrucha*'s harbour), in which the previously indicated -30 m contour line is almost coincident with the harbour main dock. Geologically, the *Palomares* submarine canyon has influenced the near-shore morphology since it was connected with the *Almanzora* and *Antas* valleys varying the equilibrium profile of the rivers and increasing the eroded process during the sea-level lowstands (Meikle 2008). That canyon can play a key role since it constitutes a sediment sink from which sediment is removed far away from the coastal cell.

Coastal sub-areas

In order to discuss the results, different sub-areas can be defined. They do not have a clear edge between one each other but they present some geomorphologic distinction. However, this description can clarify the discussion of the shoreline evolution results. Following the guide of beaches from the Spanish Environmental Department (Ministerio de Agricultura, Alimentación y Medio Ambiente) these subareas would be the following (Figure 4.3):

- *Villaricos:* from *Villaricos* village to the *Almanzora*'s mouth. It comprises about 550 m of rocky sea bed beach. The northern part is formed by sand while the nearest part to the *Almanzora*'s mouth has a larger grain size.
- *Fábrica del Duro:* constitutes the shoreline on the *Almanzora*'s mouth and the surrounding areas. It is 600 m long and most of the material can be considered

as coarse soil. Here, the difference in grain size is also clear since the foreshore has a significant higher slope.

- *Punta Hornicos:* a cape located at the south of the *Almanzora*'s mouth which separates the *Fábrica del Duro* and *Quitapellejos* beaches.
- *Quitapellejos:* corresponds to a non-built coastal area with a length of 1400 m which includes the curved transition between *Punta Hornicos* and the main coastal orientation (northeast-southwest). It presents a clear erosion front starting in *Punta Hornicos* and gradually extending up to the end of this beach (Figure 4.4).
- *El Playazo:* sand beach located in a touristic built area with a length of 1200 m which has suffered an important erosive process that caused the construction of two transversal jetties to try to maintain an important and one-off sand nourishment effort carried out in the same area.
- *Puerto Rey:* a 2300 m length sand beach located at the north of the *Antas*' river mouth. It comprises an urbanized area which has been apparently in equilibrium over the years.
- *Las Marinas:* the portion of beach located between the *Antas*' mouth and the *Garrucha*'s harbour. It has a length of 1550 m and its evolution has been very changing since it constitutes the last part of the beach system, just adjacent to the dock of the harbour and, therefore, some sediment deposit has been tested. However, it is known that a sort of sand mining activities have been done in this beach in order to carry out several sand nourishments in the northern beaches.

As previously mentioned, the beaches located northern and southern the previous ones were not included since the evolution has been considered not interesting for this study because they are either no-evolution embayed beaches or totally artificially installed beaches. This is the case of *Garrucha*'s beach, just located at the south of the harbour of the same village.

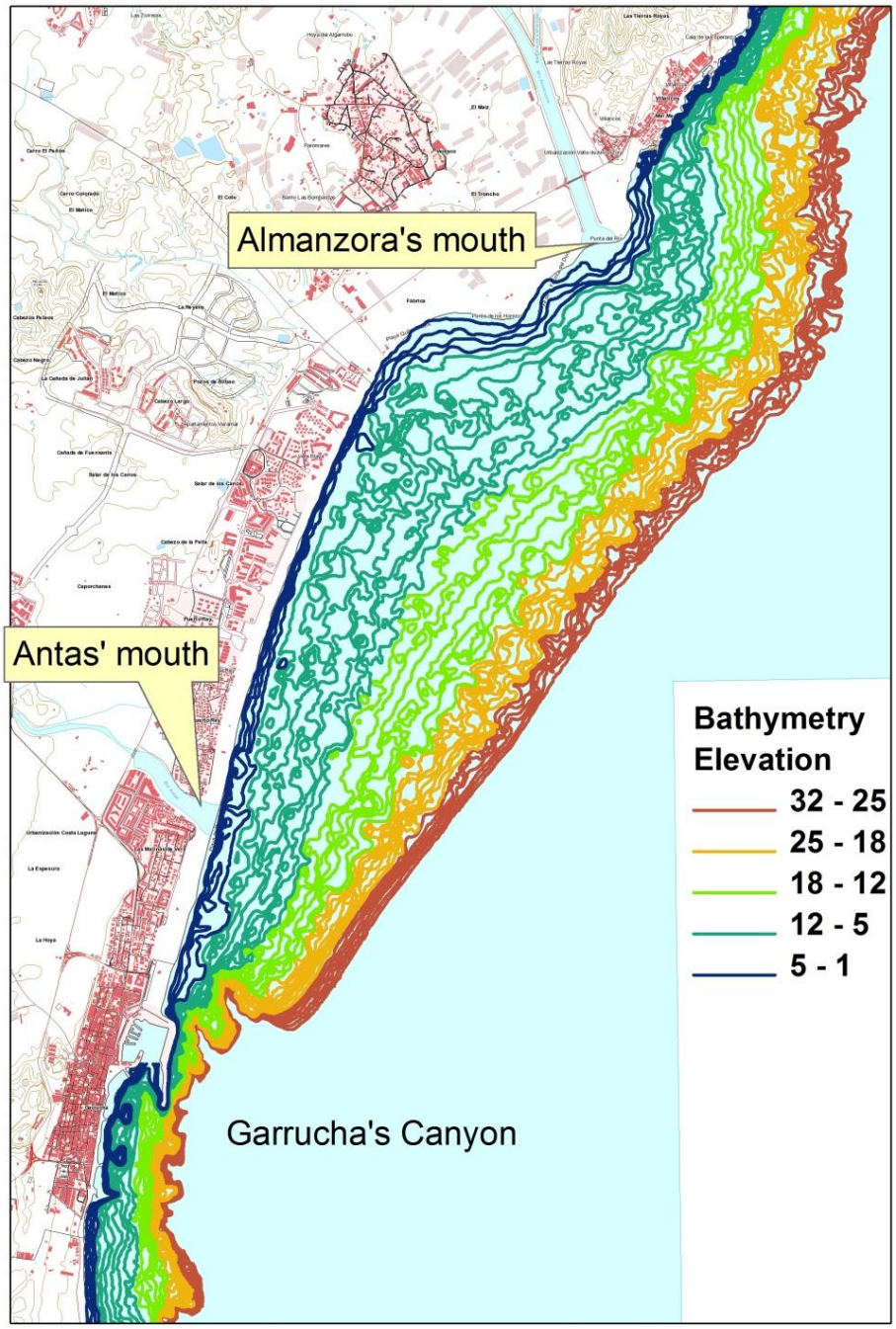

Figure 4.2. Bathymetric map of the study site nearshore area up to 32 m of depth.

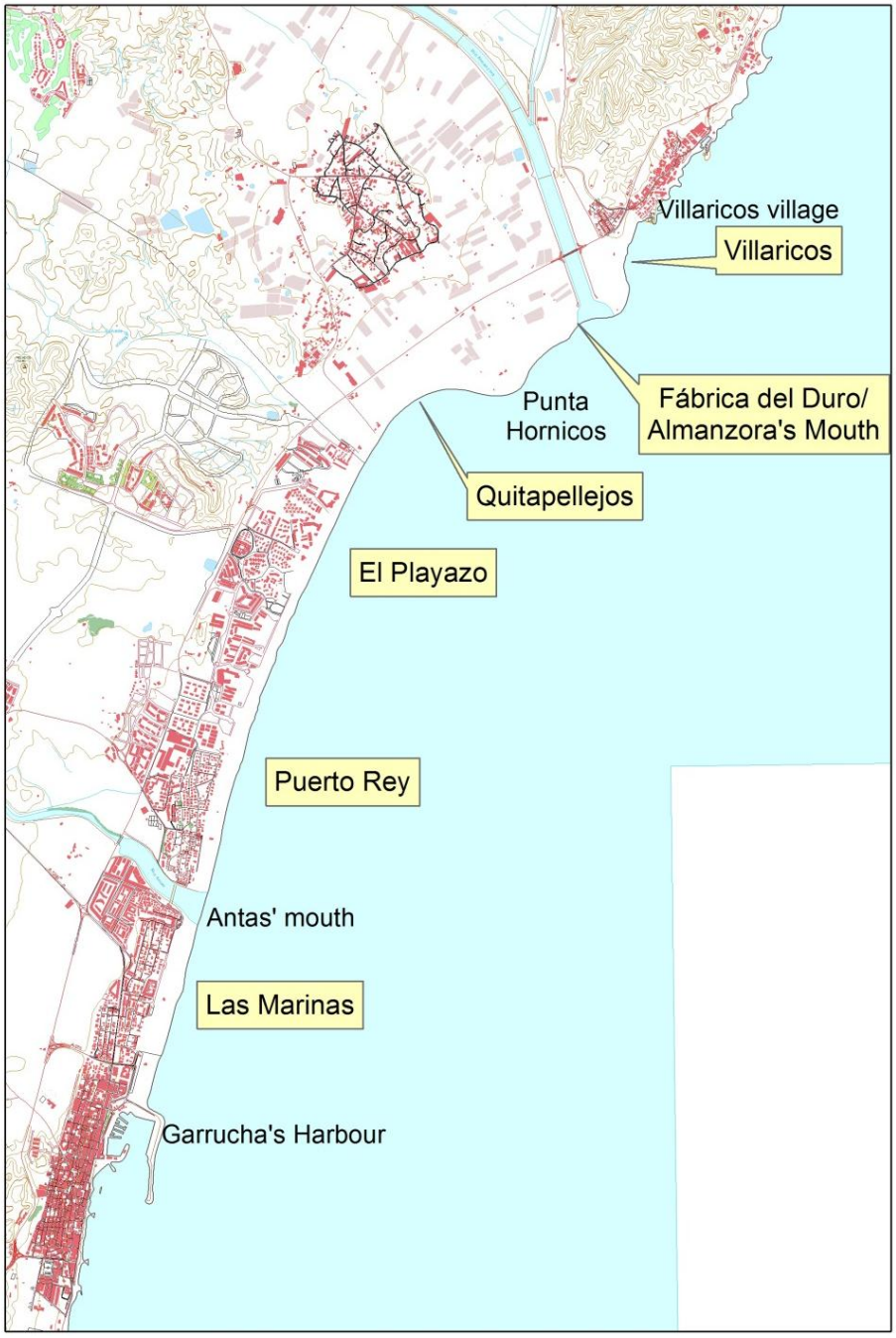

Figure 4.3. Location map. The beaches are represented in boxes.

Figure 4.4. Front of erosion located at Quitapellejos beach. Note that coarse grain size instead of sand beach is nowadays presented in this area.

Natural features

Some of the natural factors causing coastal erosion are winds, storm events, near-shore currents, vertical land movements (e.g. land subsidence), slope processes (i.e. landslides) and relative Sea Level Rise or SLR (European-Commission 2004). Regarding the time and space patterns of that processes, hydrodynamic scale (tides, winds, storms, waves), engineering scale (near-shore current, slope processes), and geological scale (SLR, land subsidence) can be considered. In this study, although geological scale represents the general framework to work, hydrodynamic and engineering scale processes will be especially considered. Therefore, the climate features of this area will be highly important in order to better understand the coastal evolution results.

Oceanographic features

Since this study site is located in a Mediterranean area, the tidal regime can be considered as microtidal, presenting about 50 cm of water level variation. According to the oceanographic and meteorology information supplied by the Official Department of Spanish Harbours (Puertos del Estado, www.puertos.es), the most frequent wind directions in the study area are from northeast (NE) to southwest (SW) and vice versa (Figure 4.5).

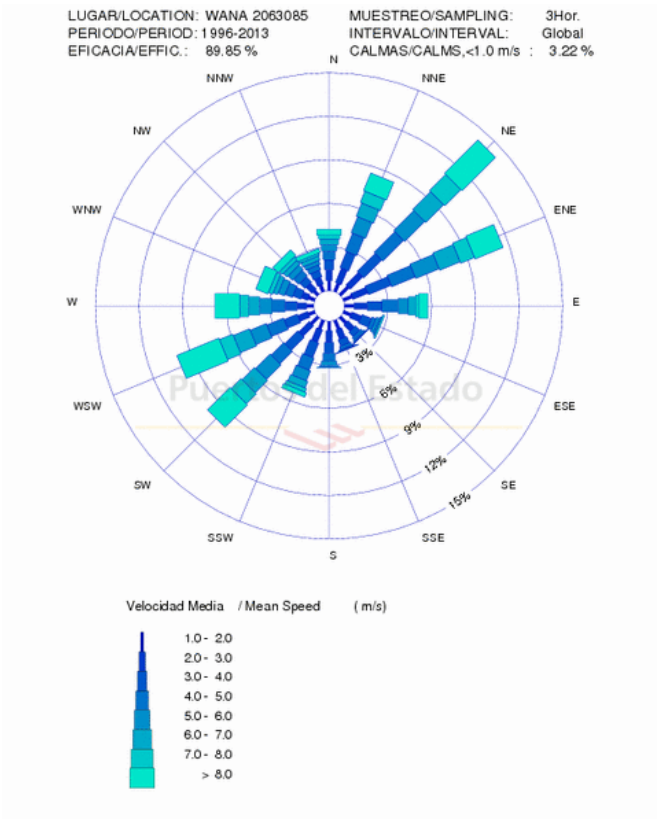

Figure 4.5. Compass card supplied from the nearest information node available at www.puertos.es

Additionally, the strongest wind episodes also occurred along those directions. Regarding the dominant wave direction, it is important to highlight that waves usually reach this coast coming from the East, being the significant wave height usually less than 2 meters. Finally, the currents direction should be taken into account. Unfortunately, there is not a near coast buoy to allow obtaining information with respect to this important variable. However, the nearest one (*Cabo de Palos*, about 200 km in NE direction) is expected to provided suitable information. As expected, the currents direction almost coincided with the winds

direction, being NE and SW the most frequent. The oceanographic data presented here have to be taken into account in order to determine the alongshore sediment transport. That is dominated by the flows induced by waves approaching the shoreline at an angle, although this current can be enhanced or reduced by wind-driven or tidal currents. The magnitude of alongshore transport is directly related to the incident wave energy as well as the angle of wave incidence (Schwartz 2005).

Climatic considerations

Since the weather conditions are a key factor not only for oceanographic features but also for the sediment supply, it is important to describe the general climate in the study site. Generally, the area is under a semi-arid Mediterranean climate characterized by a low level of rain episodes. However, some extreme storm episodes coupled with important floods events can happen, constituting both the main source of natural sediment supply and, at the same time, a huge source of sand beaches erosion. In fact, some parts within this area have been classified by the Regional Government as potentially flood zones (*Antas*' mouth, *Puerto Rey* and *Quitapellejos* beaches).

A list of the main historical floods events is shown in Table 4.1, in which a lack of flooding episodes can be observed between 1943 and 1968. Moreover, three different temporal variations can be made out: first, from 1870 to 1901, eleven events occurred which implies a rate of 3.5 events per decade; secondly, only 0.4 events per decade happened from 1901 to 1968; and finally, in the time span from 1968 to 2012 more than 3 great floods per decade was again reached. Taking it into account, this kind of climatic factor constitutes the main sediment supply agent in this coastal cell (Viciana 1996), indicating that the shoreline evolution could have been deeply affected by the overflowing irregularity.

The effects of a very recent flooding could be tested on the 28th of September 2012 when the urbanized area next to the *Antas*' mouth was flooded and the surrounded beaches suffered a very significant erosion (for instance, the sand barrier located in the *Antas'* mouth was totally removed, Figure 4.7). Additionally, some extreme water level events have occurred mainly coupled with extreme winds from East or Northeast (the so-called *"Levante"* in Spanish). Those events can lead to overwash and washover (sediment deposited inland of a beach) processes but also to beach erosion since the wave energy is considerably increased (Figure 4.6).

Table 4.1. Flooding events documented in the study site since nineteenth century. Source: "Spanish National Catalogue of Historic Floods. Area South. Updated until 2011" (Catálogo Nacional de Inundaciones Históricas. Zona Sur. Actualización año 2011)

Affected river	Date	Comments
Almanzora	1830	
Almanzora	October 1871	
Almanzora	June 1877	
Almanzora and ravines	October 1879	3000 m3/s
Almanzora	November 1884	
Almanzora	June 1886	
Almanzora	September 1888	
Albox ravine	September 1891	
Almanzora	March 1894	
Almanzora	November 1894	
Almanzora	Julio 1899	
Almanzora	June 1900	
Almanzora	October 1915	205 litres in 8 hours
Almanzora	October 1924	Water flow of 2000 m3/s
Almanzora	October 1943	
Almanzora	November 1969	
Almanzora	November 1972	Several overflowing events in the same month
Almanzora	June 1973	
Almanzora, Antas, and Aguas	October 1973	Water flow of 3500 m3/s. The largest one in 100 years
Almanzora	August 1974	
Almanzora	October 1977	Water flow of 1000 m3/s
Antas, Aguas	September 1980	
Almanzora	September 1989	
Almanzora and Antas	September 1996	
Almanzora	September 1997	
Antas	November 2001	
Almanzora	July 2002	
Almanzora	July 2006	

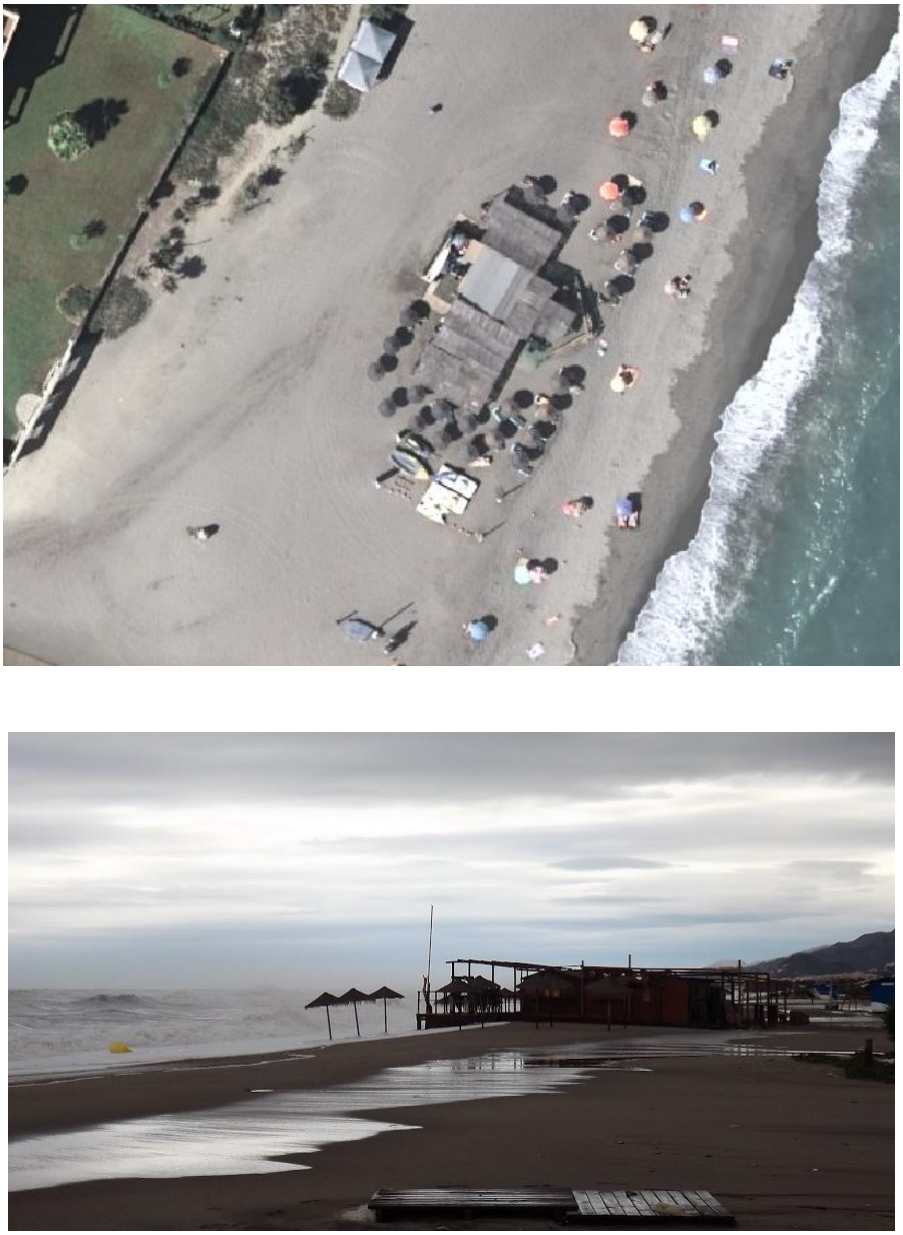

Figure 4.6. The beach bar depicted in the top image (2009 orthoimage) was surpassed by the maximum runup of a storm surge happened in April 2013, producing a huge damage and a significant erosion along the beach (own picture).

Figure 4.7. Example of damage caused in the Puerto Rey beach by the overflowing of the Antas river (own photography taken 9th October 2012)

Important human induced factors

The human interaction with coastal system has been increased mainly during the twentieth century. In general, urbanization of the coast has turned coastal erosion from a natural phenomenon into a problem of growing intensity. The so called 'coastal squeeze' because of the encroaching of artificially stabilized seafronts on sedimentary coastlines and cliffs do not enable the natural behaviour of coastal environments. Coastal engineering elements such as seawalls or breakwaters are one of the most important factors. These constructions modify the alongshore sediment transport (creating a deficit downdrift), hamper energy dissipation and augments turbulence resulting in increased cross-shore erosion, and alter the wave crest (wave diffraction) resulting in a wave energy diluted in some place and concentrated in others. Furthermore, river basin regulation works constitute one of the most visible impacts on sediment budget, directly influencing the shoreline equilibrium. Any activity which results in a reduction of the water flow or prevents river flooding (such as channelling) is expected to reduce the volume of sediments reaching the coast. For instance, the annual volume of sediment discharge for the southern European rivers is considered less than 10% of their level in 1950. Other important human induced factors are dredging for navigational purposes (including sand mining for some areas), vegetation clearing, and gas mining or water extraction which can provoke land subsidence which effects result irreversible (European-Commission 2004). The previously mentioned time and space patterns can be considered for this kind of factors as well. Thus, while dredging can affect the shoreline evolution yearly, both river damming and coastal artificialization are expected to influence over a century scale.

Human factors affecting the study site area

Similarly to others Spanish Mediterranean coasts, the human factors constitute a key factor for understanding coastal evolution and, therefore, the influence of those factors should be evaluated. Here, a set of human factors is listed as possible influential components of the coastal evolution of the study site area.

a. Urbanization process

The previously mentioned 'coastal squeeze' effect can be clearly seen in the study area from the 50s to nowadays by only checking the historical aerial images. While only *Villaricos* and *Garrucha* villages existed in the first half of the twentieth century, a wide stripe of urbanized area can be seen nowadays mainly dedicated to touristic activities. The most affected areas are those located close to the beaches of *El Playazo*, *Puerto Rey*, and *Las Marinas* (Figure 4.8). This process has restricted the natural processes on the coastal area by influencing the sediment exchange between the beach and the inland area. Moreover, some natural environments have been degraded. This is the case of some wetlands which have been confined and currently have virtually disappeared (Figure 4.9). Finally, this urbanization process has not only affected the sediment exchange but it has provoked a high risk of flooding in some areas such as the *Antas*' mouth, a circumstance which could be checked in the last flood event registered in September 2012. In conclusion, the urbanization process developed in the study site can have affected the natural sediment exchange in most of the coastal fringe under study.

Figure 4.8. Urbanization process carried out in Puerto Rey beach from 1957 (left) to 2009 (right)

Figure 4.9. Degradation of the wetland known as 'Charca del Gato' by the urbanization process from 1977 (left) to 2009 (right)

b. Sand mining

The Almeria province has undergone a huge increase in its agricultural sector since the 70s. One of the main developed areas was the greenhouse based agriculture (intensive agriculture) which required a great amount of sand which was extracted from the coastal environments all over the Almeria coast. A summary of that sand mining is presented in the Table 4.2 (some illegal sand mining activities have been documented but not accounted). Additionally, sand mining was also done from the fluvial channels between 1957 and 1995, being approximately 248.000 m^3 and 1.103.000 m^3 for *Antas* and *Almanzora* rivers respectively (Dr. Alfonso Viciana, personal communication). Here it is hypothesized that those mining activities have somehow affected the sediment supply within the studied coastal cell, so significantly altering the natural shoreline evolution.

c. Sand nourishment

When the sand mining stopped, just a process of sand nourishment was started. That was clearly due to the increase of the touristic sector in the Almeria province economy. As can be checked in Tables 4.2 and 4.3, the sand nourishment has been much more intensive than the sand mining (almost 3 times larger without including the sand mining carried out on the river channels). These sand nourishments processes have been mainly undertaken in the *Quitapellejos* and *El*

Playazo beaches, which correspond to the significantly more eroded beaches over the years.

Table 4.2. Evolution of sand volume extracted in the study area from 1974 to 1986. It is known that illegal sand extractions were done but they could not be documented. Source: Dr. Alfonso Viciana, personal communication.

Year	Sand volume extracted (m^3)
1974	30600
1975	33000
1976	42800
1977	38000
1978	37400
1979	34500
1980	43700
1981	0
1982	100
1983	5000
1984	102000
1985	0
1986	11100
TOTAL	343700

*Table 4.3. Evolution of sand nourishment during the period of 1988-2009. *2009 data corresponds to the nourishment carried out from the Garrucha's harbour dredging. Source: General Coastal Division (Dirección General de Costas) through Dr. Alfonso Viciana.*

Year	Sand nourishment volume (m3)
1988	52402
1991	46000
1993	24000
1997	56998
1998	56000
2001	33380
2002	48600
2008	400000
2009*	100000
TOTAL	817380

d. External mining activities

The mining sector played an important role in the economy of the study area from the nineteenth century to the beginning of the twentieth one. According to the Spanish Mining Statistics of 1911 (*'Estadística Minera de España. Año 1911'*) belonging to the Spanish Geologic and Mining Institute (*'Instituto Geológico y Minero de España'*), the water volume flown into the study site coastal area during the 1906-1910 period was 3,303,417 m^3 in 1910 and about 2,523,000 m^3 per year from 1906 to 1909. It is expected that these huge water flows have influenced the sediment supply in the coastal cell although an accurate evaluation of that results constitute a really difficult task. However, it can be a key factor to explain previous accretion in the shoreline position since an extra sediment supply was done in a relatively short period of time.

e. River basins regulation

Both sand mining and nourishment activities have directly affected the sediment budget in the study coastal cell. Another important key factor affecting the sediment budget corresponds to the regulation carried out on the river basins. The main regulation works applied to the rivers *Almanzora* and *Antas* turn out to be the '*Cuevas del Almanzora*' dam and the channelling of the rivers *Almanzora* and *Antas*. The '*Cuevas del Almanzora*' dam was built in 1982 15.5 km upstream from the coastline and affects to 81.6% of the total basin surface so only downstream basin portion remains active for coast sediment supply. In this sense, the beaches along this area highly depend on the sediment supply coming from only the 18.4% of the river basin. This dam is expected to reduce the sediment supply of the river basin up to 7.5% based on the estimated erosion rate (400 Tm/km^2), the sediment yield rate (between 32% and 42%) and the previously indicated active area of the river basin (Viciana 1996). In the same study, the sediment supply available for beach formation is evaluated to be between 83,069 and 154,233 m^3/year based on a previous work which calculated a percentage of between 14 and 23% of the sediment provided by a river into a delta in Mediterranean areas (Carau 1981). Furthermore, the net sediment transport towards South from the *Quitapellejos* and *Puerto Rey* beaches vary from 131,000 and 175,000 m^3/year (Viciana 1996).

Therefore, the averaged sediment supply and the estimated sediment transport are almost coincident and the sediment budget can be balanced under this conditions. However, since the dam was installed, only a sediment quantity of between 6,069 and 11,633 m^3/year is available for the beaches upkeep, so the deficit of sediment due to the '*Cuevas del Almanzora*' dam (an estimated value of between 126000 and 13300 m^3/year) have clearly affected the shoreline evolution of the coastal cell studied in this work.

f. Coastal engineering

The coastal engineering carried out in the study site corresponds to the construction of harbour structures and jetties. The most influent harbour structure was built in *Garrucha* village. This construction finished in 1947 and the main cross-shore dyke modified the coastal sediment transport since it acts as a barrier for sediment transport (from the North-South drift) but also drives the sediment into the *Palomares* canyon, performing as a perfect sediment sink. In fact, the *Garrucha*'s harbour divided the physiographic unit and reducing the influence of *Almanzora* and *Antas* rivers from 43 km alongshore to no more than 9 km along the entire study site of this work (Viciana 1996).

Two jetties were installed between July 2007 and March 2008 in the beaches of *Quitapellejos* and *El Playazo* in order to mitigate and correct the high erosive process observed in those areas. These jetties were built along the cross-shore direction in order two retain the sediment perpendicularly to the main alongshore sediment transport direction. This action was coupled with an important sand nourishment action (2008 nourishment in the Table 4.3). The installation of those two jetties, and the subsequent nourishment, clearly influenced the short-term shoreline evolution since it originated an accretion process just located at the North of the jetties and a more intensive erosion process immediately localized at the South of them.

The emplacement of those jetties makes the shoreline evolution study to be divided in two temporal spans since the influence of these engineering structures marks a turning point in the most eroded areas at the coastal cell (Figure 4.10). Although these jetties seem to keep the sediment in the North face, a concomitant erosive process occurred in the South face, so the short-term and medium-term effects of these constructions should be adequately evaluated.

g. Others human impacts

Firstly, some hydrological and forestry measures were undergone in the *Almanzora* river basin trying to somehow stop the high erosive processes that happened in this area. These interventions, such as coniferous repopulation processes, measures against soil erosion (e.g. terracing) and river banks defence structures, likely reduced the capability of the river basin to supply sediment to the coastal system, but it is very difficult to quantify and, moreover, it is out of the scope of this Thesis. Furthermore, the channelling of several stretches of the *Almanzora* (1980-1981) and *Antas* (1986-1989) rivers have notably reduced the erosion of their river banks. In the same way, the enlargement of agricultural areas near to the river channel should have also influenced the contribution of river sediment deposition in the delta area.

Figure 4.10. Coastal evolution according to the jetties emplacement. In the left, activities regarding the construction (2007, official web map service source) are shown. In the right, first year stages of the construction and the sand nourishment is presented (2008, official web map service source).

DATASETS

Two kinds of datasets were used for shoreline extraction: DEMs and orthoimages. DEMs were consequently differenced regarding their original data source from which they were extracted. Thus, LiDAR and photogrammetrically derived DEMs were separately considered since their nature and accuracies are highly different. Furthermore, orthoimages were employed in order to extract shoreline through manually digitizing the position by means of the HWL, assuming to be the line between the wet and dry sands and representing the maximum altitude of the water for each dataset. The orthoimages were also divided according to the source. Therefore, own-oriented photogrammetric data and official orthoimages taken from different Web Map Services (WMS) were jointly used as data source. These datasets have been previously included in the general *Datasets* section of this Thesis so only more relevant information was included here just to clarify their use for the shoreline extraction.

Digital Elevation Models

LiDAR-derived DEMs

This kind of data was used from the so-called first and second digital flights taken in 2009 and 2011. Their high accuracy and point density allowed a suitable use for shoreline extraction.

Stereomatching-derived DEMs

Photogrammetric flights which allowed own-produced georreferenced data were used to generate stereomatching-derived coastal elevation models (CEMs) in order to extract datum-based shorelines. Thus, CEMs from *American flight* (1956), *Agriculture flight* (1977), and *Coastal flights I* and *II* (1988 and 2001) were produced mainly by means of an intense stereo editing process since sand beaches did not usually allow an appropriate image matching due to their lack in texture. The use of these CEMs will depend on the comparison between the accuracies estimated from datum-based CEMs-derived shorelines and orthoimage-derived ones in which HWL was used as a proxy for shorelines extraction.

Orthoimages

Own-produced orthoimages

These data sources were widely described in *Dataset* section of this Thesis (*Photogrammetric Flights* subsection). The orthoimages production was carried out following usual digital photogrammetric processes. Summing up, six own-produced orthoimages (1956, 1977, 1989, 2001, 2009, and 2011), ranging from archival aerial panchromatic images (1956 and 1977 images) to new digital aerial multi-channel (2009 and 2011 datasets), were compiled. The 1988 and 2001 orthoimages were extracted from colour aerial frames and they required a previous scanning process similar to the one applied to the 1956 and 1977 aerial images. These data sources are listed in Table 4.4.

Web Map Services orthoimages

Although the previous set of images covers the time span under study (1956-2011), it was clear that some relevant information could be lost. For instance, the placement of the jetties in *El Playazo* was carried out in 2007 while the own-produced orthoimages were compiled from 2001 and 2009 data. Therefore, the evolution between 2001 and 2007 could keep unknown if a previous shoreline dataset was not included. Furthermore, some of the available WMS orthoimages can enable to fill some gaps in the own-produce data if the time span between two consecutive images was too large.

Orthoimages from Web Map Services (WMS) can contribute to provide suitable information without an extra effort (i.e., scanning the original

photographs, carrying on the photogrammetric interior and exterior process, and deriving the final orthoimages) but their use should be carefully undergone because of accuracy and information issues. Moreover, and in order to compute erosion rates for shoreline evolution, the more observations (shorelines) are included, the lower will be the final uncertainty of the estimated rate. All the image data sources were obtained from the Spatial Data Infrastructure (SDI) provided by the regional government of Andalusia (www.ideandalucia.es). The WMS used are listed in Table 4.4. It is clear that the number of datasets have been increased from the beginning of the twenty first century.

Table 4.4. Orthoimages used as source for digitizing shorelines.

Year	Source	Date	GSD (m)	Comments
1956	Own-produced	30/09/1956	1.00	
1977	Own-produced	15/07/1977	0.50	
1984-85	SDI	31/12/1984	1.00	Information do not specify if the year was 1984 or 1985
1988	Own-produced	15/09/1989	0.30	
1998-99	SDI	31/12/1998	1.00	Information does not specify whether the year was 1998 or 1999
2001	Own-produced	09/04/2001	0.20	
2001	SDI	31/12/2001	0.50	Images taken after the other 2001 flight
2004	SDI	Unknown	0.50	
2006	SDI	Unknown	0.50	
2007	SDI	Unknown	1.00	
2008	SDI	Unknown	0.50	
2009	Own-produced	28/08/2009	0.15	
2011	Own-produced	30/08/2011	0.10	

SHORELINE INDICATORS

In order to evaluate what shoreline proxy was more appropriate for shoreline rate change assessment, a comparison was carried out between three proxies for the 2009-2011 period, where shorelines extracted from LiDAR-derived DEMs were expected to be a good reference. First, the HWL was used to estimate the Net Shoreline Movement (NSM) and End Point Rate (EPR) between 2009 and 2011 shorelines. It is convenient to explain that the NSM reports a distance between the oldest and youngest shorelines for each transect, not a rate. If this distance is divided by the number of years elapsed between the two shoreline positions, the result is the EPR. Secondly, the 0 m contour estimated by EGTP method (see Chapter 3) was utilized as a proxy of shoreline for the same calculation. Finally, a non-extrapolated contour was used in order to check the differences between the mentioned proxies so that the disadvantages of using extrapolated contours could be tested. These differences were evaluated in six different sand beaches environments: (1) *Fábrica del Duro*, (2) the *Quitapejellos* beach part northern the jetties, (3) the beach enclosed between both jetties, (4) the *El Playazo* beach part southern the jetties, (5) a part of *Puerto Rey* beach, (6) and the nearest part from *Las Marinas* beach to the *Garrucha's* harbour. A set of 5 m spaced transects was used for this analysis so that the intersection of the three types of shoreline with this transects set was performed, resulting between 83 and 196 the number of transects for every group.

Comparing DEM-derived contours with HWL

The comparisons made to check the differences between every proxy used were performed for the same year. As shown in Tables 4.5 to 4.7, it was clear that the computed differences highly depended on the concrete tidal features of each dataset, being the 2011 HWL much more close to the 0 m contour than 2009 HWL, and even showing a seaward location in the case of 0.75 m contour level (negative differences). It should be noted that the group in which differences were assessed had also an important incidence on the results. For instance, the results on group 1 are significantly different to the others, especially for the 2009 dataset and 0 m contour level. It is also clear that the standard deviation was always smaller when HWL was compared with the 0.75 m contour level, indicating that this shoreline proxy was more robust than the 0 m contour, which resulted obvious since the latter was estimated by means of an extrapolation process while the former was interpolated. A previous work demonstrated that the HWL – datum-based offset highly depends on the foreshore beach slope which induces variations in wave runup (Moore, Ruggiero & List 2006). The same authors estimated that the beach slope and offset are inversely proportional (the steeper the slope, the smaller the offset), concluding that the use of HWL as a shoreline indicator can be really complex. The relationship between slope and offset can be seen in groups 5 and 6.

According with Table 4.7 they are the only ones in which the differences between 0 m and 0.75 m contours were larger for 2009 than for 2011, which completely matched with the fact that the slope got steeper for those groups. Additionally, the largest difference (group 4) coincided with the largest increase in slope.

Table 4.5. Estimated offsets (in meters) between 0 m contour and HWL positions for the six tested locations along the working coastal area (see text for more details)

	2009		2011	
Group	Average	Std. dev.	Average	Std. dev.
1	5.15	1.18	4.58	2.30
2	11.57	3.48	5.69	2.30
3	13.80	2.54	6.43	2.11
4	10.52	1.42	7.73	2.41
5	15.02	2.82	5.64	1.70
6	15.02	3.69	6.23	2.83

Table 4.6. Estimated offsets (in meters) between 0.75 m contour and HWL positions for the six tested locations along the working coastal area (see text for more details)

	2009		2011	
Group	Average	Std. dev.	Average	Std. dev.
1	0.14	0.82	-2.06	1.12
2	2.73	1.63	-4.06	1.11
3	4.92	0.96	-3.05	1.33
4	4.08	1.04	-3.94	1.61
5	4.85	1.04	-3.02	1.13
6	3.64	3.03	-3.96	2.55

Table 4.7. Estimated offsets between 0 m and 0.75 m contours (estimated as the difference between the offsets yielded with HWL for both contours) for the six tested locations along the working coastal area (see text for more details)

Group	2009	2011	Offset difference (2009-2011)	Slope difference in degrees (2009-2011)
1	5.02	6.64	-1.63	0.9971°
2	8.84	9.75	-0.91	0.4279°
3	8.88	9.48	-0.60	0.2718°
4	6.44	11.67	-5.23	2.5303°
5	10.17	8.66	1.51	-0.5023°
6	11.37	10.19	1.18	-0.6891°

The offset between DEM-derived contours and HWL has been previously parameterized, and its effects on shoreline accuracy and change rates have been studied (Ruggiero, Kaminsky & Gelfenbaum 2003, Moore, Ruggiero & List 2006, Ruggiero, List 2009). That offset or proxy-datum bias was formulated based on the fact that it is due to wave driven water level variations on beaches including wave setup and runup, and therefore that offset is predictable. By means of the formulation of total water level (TWL), which is a combination of the tidal level and a statistical representation of the wave runup elevation (Stockdon et al. 2006), and the datum utilized (MHW for the previously mentioned studies), the bias formula is expressed as in eq. 4.1.

$$Bias = (X_{HWL} - X_{datum}) = \frac{\left(\left[Z_T + 1.1\left(0.35\, tan\beta \sqrt{H_0 L_0} + \frac{\sqrt{H_0 L_0 (0.563\, tan\beta^2 + 0.004)}}{2}\right)\right] - Z_{datum}\right)}{tan\beta} \quad (4.1)$$

where X_{HWL} and X_{datum} are the shoreline positions for both shoreline proxies, Z_T and Z_{datum} are the elevation of both proxies, β is the foreshore beach slope, H_0 is the offshore wave height, and L_0 is the offshore wave period, given by linear theory as $(g/2\pi)T^2$, being g the acceleration of gravity and T is the wave period (in seconds). Therefore, according to eq. 4.1, the bias depends on the local beach morphology (slope) and the natural oceanographic features. Of course, HWL digitization errors are not accounted here.

In order to estimate the bias between both datum-based proxies and HWL, H_0 and T values were extracted from the WANA dataset (wave data estimated by modelling in the point 2063087; see Puertos del Estado, 2013) since no direct measurement are available in this area (Puertos del Estado 2013) Regarding the temporal series in 2009, 0.90 m and 6.0 s values were used for H_0 and T respectively, while no available data existed for the data collection period in 2011, so the approximate median values of 0.50 m and 5 s were employed. The Z_T values for 2009 and 2011 shorelines, both estimated through tidal data and LiDAR elevations, were 0.21 m and 0.12 m respectively.

Some of the results are depicted in Tables 4.8 and 4.9, showing that the empirical way to determine the bias resulted in the same order of magnitude than the actual one for both shorelines, although the bias estimated for 2009 was generally larger than for 2011. If the parameterization was considered completely correct, then the remaining error or offset could be considered as the digitizing error. For instance, up to 4 m offset due to different digitizing strategies was reported in other work (Moore, Ruggiero & List 2006), so the differences found here can be deemed as usual. Therefore, it is recommended that the same analyst performs the digitization of all shorelines as far as possible. Otherwise, a test to determine the differences between analysts should be carried out. Furthermore, more precise data about simultaneous oceanographic features are needed in order

to refine this assessment and the adjustment of the model expressed in eq. 4.1 should be adapted and validated for this kind of coastal areas as well.

Table 4.8. Offset measured and estimated bias for 2009 shoreline and 0 m contour. Similar results were found for 2009 shoreline and 0.75 m contour.

Group	Mean slope	Mean offset measured (m)	Estimated bias (m)	Offset – bias (m)
1	0.130	5.155	7.86	-2.70
2	0.075	11.566	9.95	1.62
3	0.071	13.804	10.28	3.52
4	0.099	10.519	8.73	1.79
5	0.062	15.020	11.05	3.97
6	0.058	15.018	11.57	3.45

Table 4.9. Offset measured and estimated bias for 2011 shoreline and 0.75 m contour. Similar results were found for 2011 shoreline and 0 m contour

Group	Mean slope	Mean offset measured (m)	Estimated bias (m)	Offset – bias (m)
1	0.129	-2.065	-1.01	-1.06
2	0.113	-4.057	-1.58	-2.48
3	0.087	-3.048	-2.99	-0.06
4	0.075	-3.936	-3.96	0.02
5	0.111	-3.017	-1.67	-1.35
6	0.085	-3.959	-3.16	-0.80

Summing up, it was proved that the offsets between the HWL and the datum-based shorelines depended on the foreshore beach slope and, furthermore, no HWL identification gross errors affecting shoreline morphology were appreciated, what was checked by comparing the estimated bias with the observed offset. Contrary to other studies which considered the shoreline proxies bias as negligible for microtidal areas (Virdis, Oggiano & Disperati 2012), this offset has been demonstrated as significant in this work. Moreover, the standard deviation figures showed that an interpolated contour level can be more suitable for shoreline definition since the extrapolated 0 m contour level yielded more variable differences with respect to HWL than the interpolated 0.75 m one.

Shoreline change estimation regarding the proxy used

In order to test how differences between HWL and both datum-based shorelines affect the shoreline rate of change, NSM and EPR were estimated between 2009 and 2011 dataset for the same six previously mentioned groups by

using the three proxies. The results are shown in Table 4.10 pointing out some important differences regarding the tested group and mainly the proxy used for extracting the shoreline. As can be seen, results are highly variable. For instance, regarding groups 3 and 6, the average offset was similar between both contours but HWL yielded significant different results. For groups 2 and 5, both contours were not so similar, but again HWL achieved different results being even on the contrary direction for group 5 (accretion estimated by HWL instead of erosion yield by both datum-based proxies). For the remaining groups 1 and 4, the 0 m contour level results were more similar to HWL ones than to 0.75 m. Therefore, it is important to discuss what shoreline proxy can be more appropriate by taking into account these results. Note that here, a short-term shoreline evolution was performed (only 2 years gone by) and the EPR results presented significant differences. However, if medium-term evolution was calculated, the EPR differences would be significantly smaller.

Table 4.10. NSM (m) and EPR (m/yr) results for every group and shoreline proxy.

	Group	1	**2**	**3**	4	**5**	**6**
Mean NSM (m)	HWL	2.79	-10.49	17.99	13.51	3.21	24.78
	0 m	2.21	-16.46	10.55	10.85	-6.50	16.43
	0.75 m	0.66	-18.16	10.12	5.46	-4.64	16.84
Std. dev. NSM (m)	HWL	2.55	17.87	3.34	5.87	3.30	10.65
	0 m	3.23	16.95	3.57	7.18	5.77	13.76
	0.75 m	1.79	16.96	2.47	6.47	3.15	11.76
EPR	HWL	1.39	-5.23	8.97	6.74	1.60	12.36
	0 m	1.10	-8.21	5.26	5.41	-3.24	8.19
	0.75 m	0.33	-9.05	5.04	2.72	-2.31	8.40

First, the large differences between both datum-based shorelines will be explored in groups 1 and 4. Figure 4.11 shows the differences in NSM distribution for both proxies. It can be seen that 0.75 m contour seems to be less variable than 0 m contour. While up to 1620 transect both proxies behave similarly, 0 m contour yielded larger NSMs values from that transect to the last one. Furthermore, if cross shore profiles of both years are checked (Figure 4.12), a clear change on the profile can be seen. While for 2009 the profile had a clear reflexive slope, a more dissipative beach profile appeared in 2011. According with the Figure 4.12 the 0.75 contour offset will be significantly different than the 0 m contour offset since the change on the profile was yielded in smaller elevations. The latter means that the 0.75 m contour did not reflect the actual shoreline movement since erosion actually occurred. Therefore, the contour-derived NSM was also related to the local slope as well as the HWL-derived.

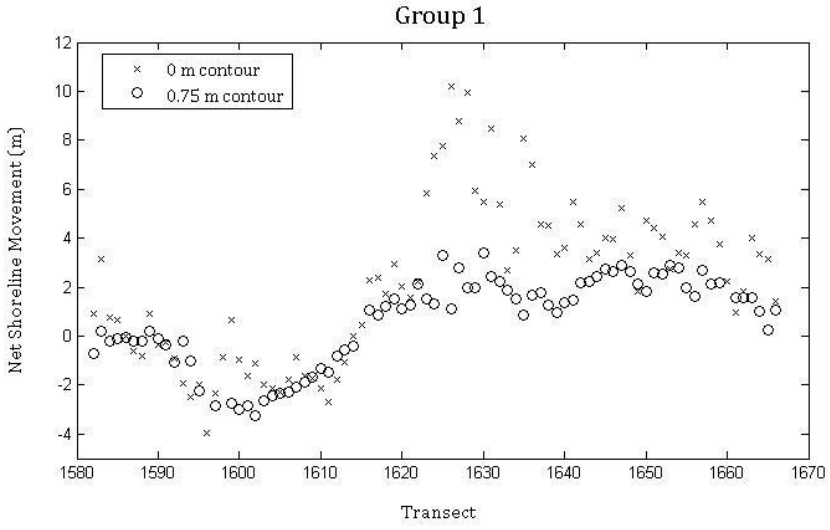

Figure 4.11. NSM distribution between 2009 and 2011 for 0 m and 0.75 m contours in the case of group 1.

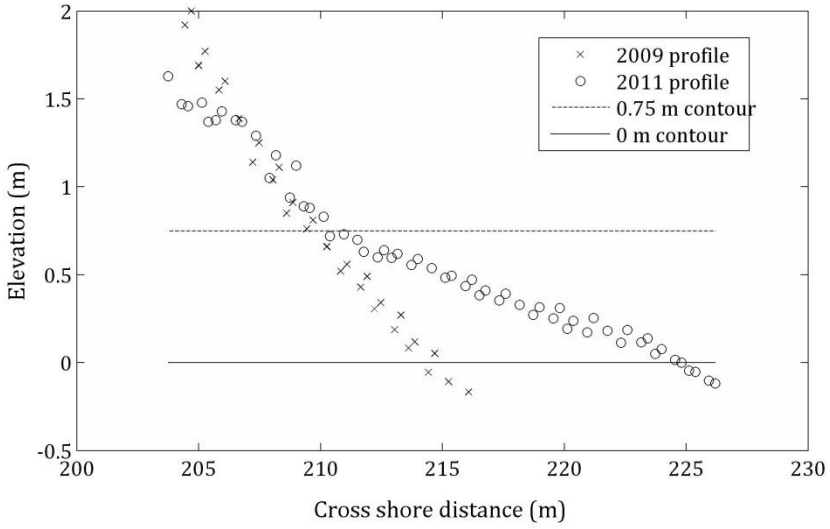

Figure 4.12. 2009 and 2011 cross shore profile corresponding to the transect number 1626 (Group 1).

On the other hand, for Group 4, in which the sand beach was much wider than for Group 1 and profile equilibrium dynamic played an important role, NSM in 0 m contour was much more pronounced and variable than those for 0.75 m. The same

problem than Group 1 appeared (different slope in 2009 and 2011 provoked more differences when 0 m contour was used) but some errors due to extrapolation came up. For instance, in Figure 4.13 the extrapolation carried out in 2011 seems to be exaggerated and then, the NSM for 0 m contour was much larger than for 0.75 m contour. Therefore, the 0.75 m contour was evaluated as more appropriate for Group 4, unlike than for Group 1.

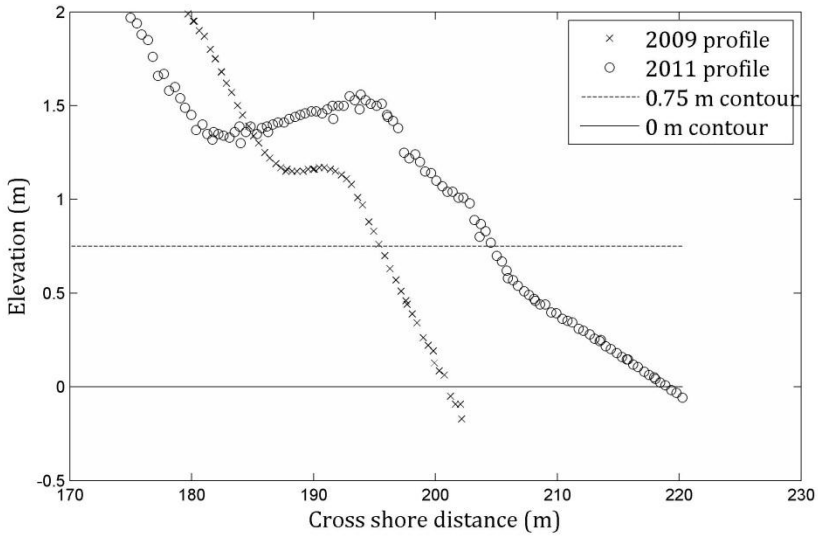

Figure 4.13. 2009 and 2011 cross shore profile corresponding to the transect number 1160 (Group 4).

Once the groups in which the observed differences between using 0 m contour level and 0.75 one were excessively large have been explored, the groups in which both proxies yielded similar results will be discussed (groups 3 and 6). As shown in Figure 4.14, although the mean NSM was similar, the 0 m contour NSM results were more variable than the 0.75 m contour ones for group 3. Furthermore, some areas of important differences are shown (profiles around 1230 and from 1290 to 1310). If elevation profiles of this group are checked (Figure 4.15) the parallelism of the foreshore slope for both years can be tested and therefore, the use of different datum-based shorelines was less influent for these groups. Generally, the steeper the slope, the smaller the differences between both proxies, because of a little error on gradient extrapolation means a great error on horizontal shoreline position when slope is gentle. Regarding the differences between NSM by means of HWL and datum-based shorelines in the groups 3 and 6, it is highlighted that the NSM differences were practically constant (Figure 4.16), which meant that the offset between both proxies were related to a constant error, probably due to the combination of HWL digitizing and the different shoreline proxy bias (remember that the tide level was different between 2009 and 2011).

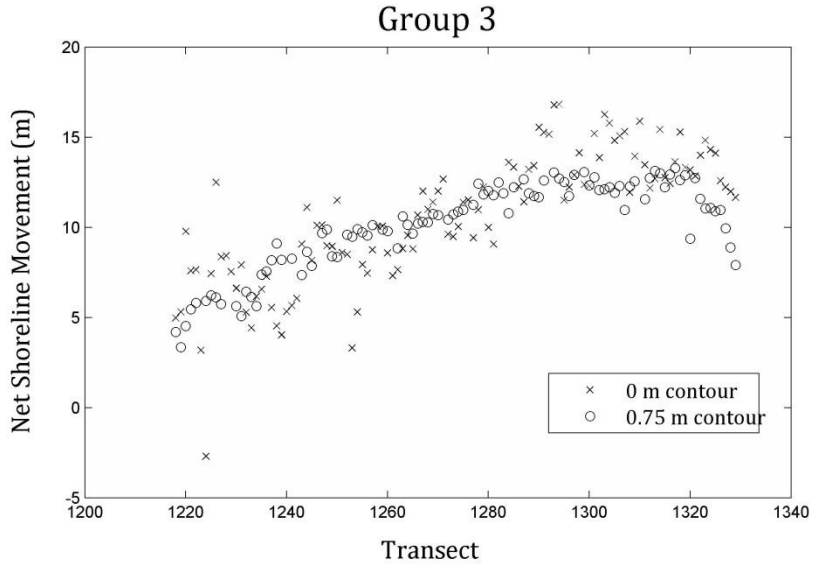

Figure 4.14. NSM distribution between 2009 and 2011 for 0 m and 0.75 m contours in the case of group 3.

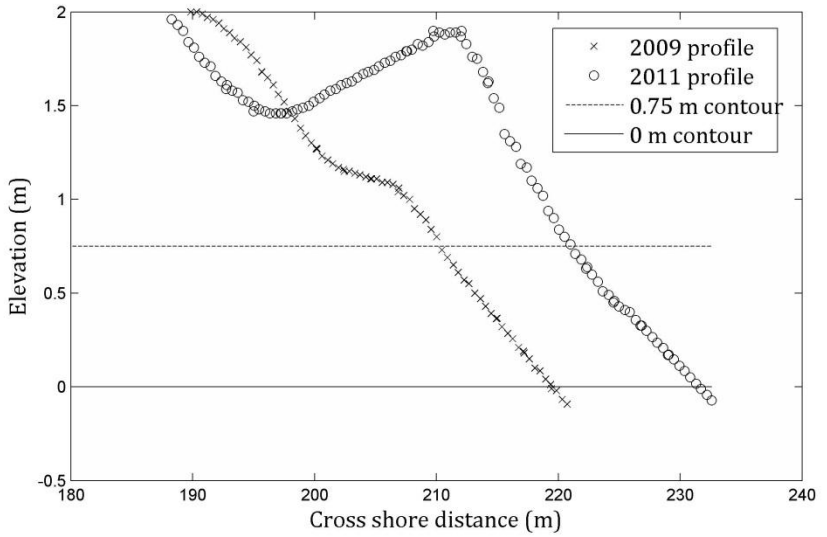

Figure 4.15. 2009 and 2011 cross shore profile corresponding to the transect number 1160 (Group 3).

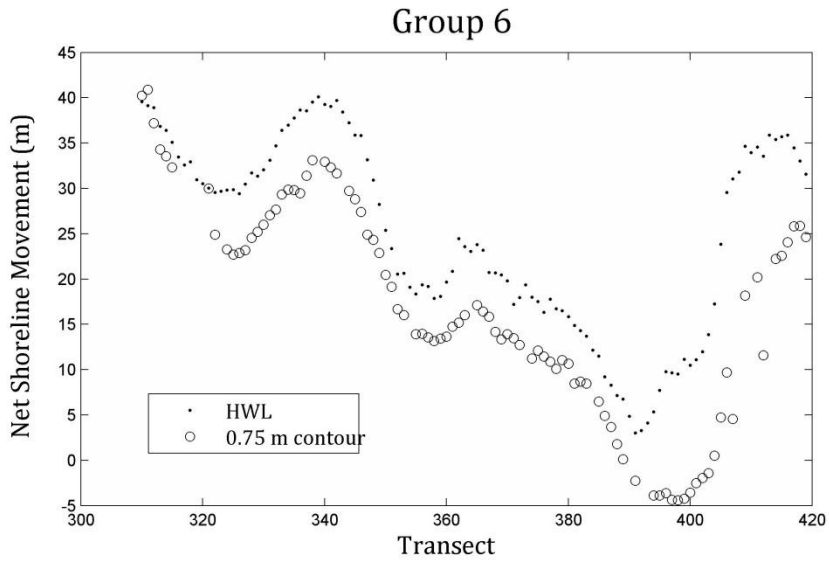

Figure 4.16. NSM distribution between 2009 and 2011 for HWL and 0.75 m contours in the case of group 6. Both NSMs were almost parallel, indicating a systematic offset induced.

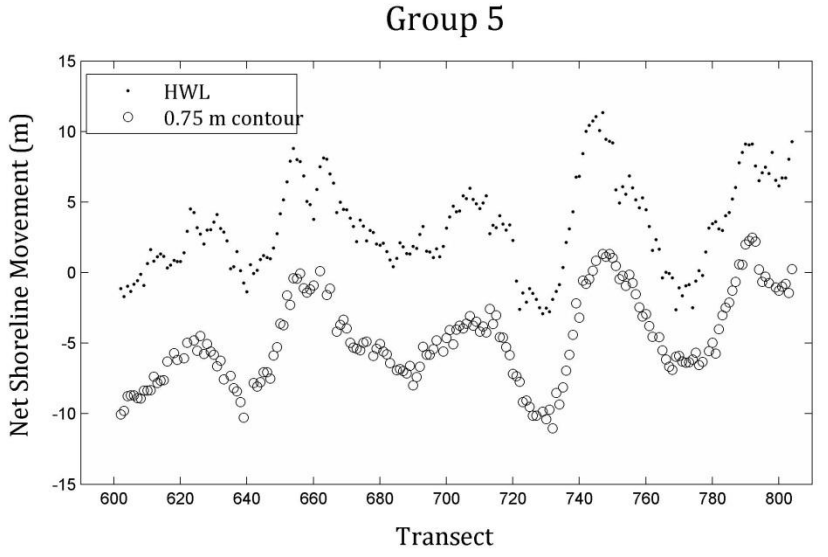

Figure 4.17. NSM distribution between 2009 and 2011 for HWL and 0.75 m contours in group 5. Both NSMs were almost parallel, indicating a systematic offset induced.

Finally, the groups 2 and 5 in which the three proxies used were highly different will be explored. For group 5, HWL indicated that accretion occur while both datum-based shoreline indicators pointed out to an erosion process (Table

4.10). It is important to determine what could be the error since those different results could lead to misunderstand the actual shoreline evolution. Regarding the NSM results shown in Figure 4.17, it was clear that those were constantly parallel and so, some systematic error was committed. Again, there were two main possibilities: either a constant HWL interpretation error or a tidal and runup-induced offset. Regarding the differences between both datum-based shorelines, the 0 m contour results depicted a high variability regarding some difference in the extrapolated gradient (similar to Figure 4.13). Both the fact that the HWL showed the similar distribution than 0.75 m contour, but with an added offset, and the fact that the 0 m contour was too variable because of extrapolation errors, leaded to the conclusion that 0.75 m contour was the most stable proxy datum for shoreline representation. Similar conclusions could be extracted from the results on Group 2, although more coincidences were found between both datum-derived shorelines mainly due to steeper slopes which implied less extrapolation errors.

How to apply the shoreline proxies bias

Two different ways of including bias can be considered. First, transforming the datum-based shorelines by moving the shoreline the same quantity that the estimated offset (Moore, Ruggiero & List 2006), and, secondly, incorporating bias into the HWL shorelines (Ruggiero, List 2009) and its uncertainty as runup uncertainty and bias. Here, the HWL has been corrected according to the bias estimated between that HWL and the 0.75 m contour. Thus, if $Bias = X_{0.75m} - X_{HWL}$, then the corrected HWL position is $X_{HWLcorrected} = X_{HWL} + Bias$. Then, once the corrected position was calculated, both NSM and EPR values were again estimated and compared with the previous datum-based shorelines (Table 4.11).

Table 4.11. NSM (m) and EPR (m/yr) results for every group including bias-corrected HWL.

	Group	1	2	3	4	5	6
Mean NSM	$HWL_{corrected}$	0.67	-18.20	10.11	5.45	-4.65	17.07
	0 m	2.21	-16.46	10.55	10.85	-6.50	16.43
	0.75 m	0.66	-18.16	10.12	5.46	-4.64	16.84
Std. dev. NSM	$HWL_{corrected}$	2.54	17.94	3.25	5.92	3.28	10.42
	0 m	3.23	16.95	3.57	7.18	5.77	13.76
	0.75 m	1.79	16.96	2.47	6.47	3.15	11.76
EPR	$HWL_{corrected}$	0.34	-9.08	5.04	2.72	-2.32	8.51
	0 m	1.10	-8.21	5.26	5.41	-3.24	8.19
	0.75 m	0.33	-9.05	5.04	2.72	-2.31	8.40

The results demonstrated that the bias correction should be taken into account if both shoreline proxies are used together. When bias was included, the NSM and EPR results were similar for 0.75 m contour and $HWL_{corrected}$. If compared

with Table 4.10, it is clear that the effect provoked by the different relative position between both proxies was removed. For instance, for Group 5, in which accretion process was estimated for non-corrected HWL, the results were practically similar when correction was applied and both shoreline proxies showed erosion. If Figure 4.18 is compared with Figure 4.17, it is also highlighted that the offset have been removed and similar shoreline change rates were estimated. Of course, it still remained some differences regarding the shoreline extraction methods but the results were completely comparable.

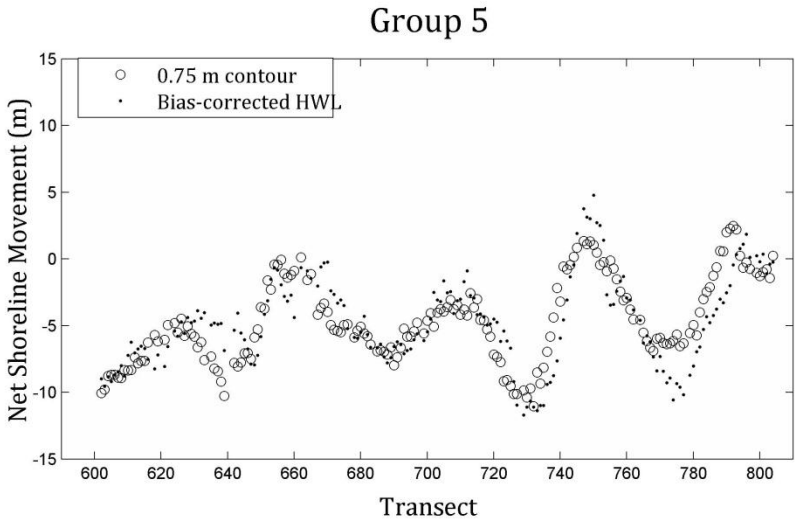

Figure 4.18. NSM between 2009 and 2011 distribution for $HWL_{corrected}$ and 0.75 m contour in group 5.

According to the previous results, the datum-based proxies will be always preferred instead of HWL for change rate estimation. According to Ruggiero, List (2009), "datum-based shorelines provide a more repeatable alternative to visual shoreline proxies, eliminating not only the effect of varying hydrodynamic conditions but also variations in shoreline interpretation". However, the time span used for that rate assessment should be taken into account. That has been previously defined as "endpoint rate shift" (Moore, Ruggiero & List 2006) and it corresponds with the estimated offset divided by the time span. In cases when linear regression is used, the same authors recommended to assess both regressions (with and without including bias), evaluate both cases at the most recent shoreline, and estimate the difference divided by the time span.

As an example, if the both shorelines used would be more time-spaced (e.g. 50 instead of 2 years), with a 50 m of accretion in the studied transect, and the constant offset between 0.75 m contour and HWL would be the same magnitude but opposite sign (e.g. +7 m for one year and -7 m for the other), the EPR in 50

years would be 1.28 m/yr using HWL instead of 1 m/yr by using datum-derived shoreline, while the EPR in 2 years would be 32 m/yr instead of 25 m/yr. Furthermore, if HWL and contour shoreline were put together to estimate EPR, 1.14 m/yr would be yield for a span of 50 years. Therefore, the combination of both kinds of proxies for medium-term shoreline evolution assessment can be considered. In fact, regarding the poor accuracy in height determination by means of stereo-photogrammetry using old and low scale photographs, HWL should be considered for shoreline definition.

Finally, and from the estimation of the shorelines offset, it was clear that there was a shoreline position uncertainty due to water level variations. In this study, the effect of the bias can be removed by estimating the differences between the estimated offsets in 2009 and 2011 and, therefore, the results represent the difference due to water level variations (no digitizing error was supposed here). Apart from the Group 1, with a difference of 2.2 m between both shorelines, the average difference estimated for the remaining groups was 7.6 m. That meant that, only due to different natural features, the digitized shorelines were highly inaccurate as compared with datum-based ones.

Therefore, the uncertainty due to water level variations or wave runup error (Virdis, Oggiano & Disperati 2012) should be evaluated. In a previous research the bias uncertainty was used as an estimation for water level variations uncertainty, being assessed through applying error propagation law on the eq. 4.1, taking into account the tidal height, beach slope, H_0, and L_0 uncertainties (Ruggiero, List 2009). Although the natural features were not the same than for this study area, a bias uncertainty of 9 m was estimated in that study. Unfortunately, accurate H_0 and L_0 data were not available for this study and therefore, further research should be carried out. As an approximation, mean and standard deviation of H_0, L_0 (estimated through the wave period T), tidal height (Z_t), and slope were estimated. While for the latter the DEM data were used, information extracted from histograms were used for the rest, so the results should be taken as approximate. The difference between the maximum and the minimum values was about 10 m, which is slightly probable. Taking into account the previous estimated difference, the previous research, and the maximum values, a wave runup uncertainty of ±7 m for digitized shorelines seemed to be a conservative value for this kind of coastal areas. As a consequence, more effort should be done in order to estimate this uncertainty more accurately.

SHORELINE ACCURACY

When the shoreline used for coast evolution rate estimation is based on the aerial image digitizing of a specific feature such as the high water line (HWL) - defined as the “markings left on the beach by the last high tide” (Pajak, Leatherman 2002)- some uncertainties influences the accuracy of the extracted shoreline.

Generally, three kinds of error sources can be taken into account: (i) the positional uncertainty due to natural phenomena such as tide stage, seasonal, and runup uncertainties, which reduce the exactitude of the shoreline (Fletcher et al. 2003, Romine et al. 2009, Virdis, Oggiano & Disperati 2012); (ii) the planimetric uncertainty due to data source (in this case, the orthorectification error should be included); and (iii) the spatial uncertainty regarding the measurement method such as pixel or digitizing errors (Moore 2000, Fletcher et al. 2003). Taking into account the previous considerations, the next error sources were considered for this study:

Natural phenomena uncertainty sources

Tidal fluctuation error

Tidal fluctuation error (Genz et al. 2007, Romine et al. 2009, Virdis, Oggiano & Disperati 2012), also called tide stage uncertainty (Fletcher et al. 2003), is the horizontal shift due to the variation of the tide in a tidal cycle. Therefore, this uncertainty depends on the oceanographic features of the study site but also on the grain size of the considered beaches (Bowman, Pranzini 2008). In the Mediterranean areas, a microtidal regime exists which implies that this uncertainty will be less influent than that from macrotidal coasts. There is not a tide gauge located close to the study site area, but some approximation can be carried out by using the nearest gauge called 'Almeria', 85 km far away the study site, which has been available from 2006. The tidal range in the period of 2006-2010 of that gauge was 0.23 m and 0.59 m for the mean and the maximum respectively. Furthermore, the differences between the maximum and minimum sea level was only 1.17 m (-0.20 m in 2007 and 0.97 m in 2010). The MSL corrected by using the Spanish datum offset in the tide gauge (-0.23 m) was 0.16 m. The evaluation of this error was estimated by a randomly generated uniform distribution since it has been considered as a conservative estimate of the probability distribution of HWL positions due to tidal fluctuation (Romine et al. 2009). A deviation standard of ±1.48 m was estimated, which can be comparable to previous studies where the tidal regime is similar. For example, ±1.5 m was estimated for a Mediterranean Italian beach (Virdis, Oggiano & Disperati 2012). Otherwise, a range from ±2.5 to ±3.4 m was estimated for microtidal beaches with a wider tide fluctuation of 1 m (Romine et al. 2009). It is important to note that this kind of error affects to all the shorelines in the same way since tide regime is supposed to be similar during the time span considered in this work.

Seasonal uncertainty

It is defined as the difference between the HWL position in winter and in summer. It pretends to describe weather effects such as storms and tries not to remove any observation but include this uncertainty in the analysis. In other

microtidal environments, some estimates have been performed based on field campaigns measures. For instance, in microtidal Hawaiian areas of the Pacific Ocean a seasonal variability of ±8.6 m was found using two years observation (Fletcher et al. 2003) while a range from ±3.6 to ±6.2 m were estimated in a set of beaches of Oahu (Hawaii) through a more reliable study during 8 years (Romine et al. 2009). However, some authors assumed this uncertainty as negligible since their data were collected in spring and summer (Virdis, Oggiano & Disperati 2012). In this work, no data have been collected in order to evaluate this uncertainty. However, since the data were collected from April (2001 photographs) to September (1957 dataset), this seasonal error can be considered as negligible as well. Nevertheless, further work should be carried out in order to estimate this kind of error for this study site. Similarly to the tidal fluctuation error, the seasonal uncertainty would reach the same value for all the datasets independently on time.

Wave runup uncertainty

It is a short-term effect that should be taken into account when HWL is used as a proxy datum (Ruggiero et al. 2001, Virdis, Oggiano & Disperati 2012). It is possible to estimate extreme runup elevation $R_{2\%}$ from empirical equations based on the deep-water significant height H_0, the wave period T, and the beach slope (Stockdon et al. 2006). In a similar microtidal beach this uncertainty was evaluated to be ±0.7 m for a $R_{2\%}$ ranging from 0.24 to 0.43 m (Virdis, Oggiano & Disperati 2012), although only the uncertainty for LiDAR-derived slopes was taken into account, not being included H_0 and T variations. However, as explored in the section '*Comparing shoreline proxies*', the influence of this uncertainty must be considered. Although a rigorous approach could not be applied here, the wave runup uncertainty was conservatively estimated in ±7 m for the entire area. It is highlighted that some previous research did not include this uncertainty despite it may be considered one of the most important part of the final uncertainty for digitized shorelines. In '*Comparing shoreline proxies*' section, the influence of the proxy datum shoreline bias for shoreline change rate was proved. However, since bias was not able to be estimated for all datasets, the wave runup uncertainty was expected to reflect the inaccuracy produced by this variable.

Data source uncertainty

As the shorelines have been digitized from aerial orthoimages, the main error that could be attributed to the data source is the *orthorectification uncertainty*. Although some authors have considered this error together with the pixel error (Fletcher et al. 2003), orthorectification error is commonly put aside (Moore 2000, Romine et al. 2009, Virdis, Oggiano & Disperati 2012). This uncertainty is usually given by the corresponding planimetric orthoimage RMSE and should be below the GSD of the image.

Uncertainty sources related to measurement methods

Pixel uncertainty

It is the minimum visible unit for digitizing and limits the ability to resolve the position of a feature (Romine et al. 2009), although some authors assume this error within the orthorectification uncertainty (Fletcher et al. 2003). Therefore, pixel error constitutes the uncertainty due to the size of the pixel on the ground (GSD).

Digitizing uncertainty

Also called onscreen delineation, digitizing uncertainty depends on the digitizer and it is measured by repeating the digitization of the shoreline following diverse strategies. For this study, an experiment was done by using three different areas on the aerial orthoimages from 1956 to 2011. Those areas were named A, B, and C, and were placed in the beaches of *Quitapellejos*, *El Playazo*, y *Las Marinas*, respectively. WMS data sources were not included. 20 shorelines were digitized in every area for each year so a total amount of 60 shorelines were available for each data source. Then, a set of 20 cross-shore transects were placed in each area and the variability of the shoreline position for each transect was evaluated. The results are shown in Table 4.12 and depict a low level of variation than it could be expected.

Table 4.12. Standard deviation (SD) for digitized shoreline position. Note that ± symbol for SD values has not been included.

Data	Overall SD	Group 1 SD	Group 2 SD	Group 3 SD	GSD	Flight scale
1956	1.00	0.83	1.14	1.03	1.00	1/33.000
1977	0.56	0.58	0.59	0.52	0.50	1/18.000
1988*	1.23	0.53	1.73	1.18	0.30	1/10.000
2001	0.52	0.58	0.35	0.59	0.20	1/5.000
2009	0.18	0.09	0.20	0.23	0.15	Digital flight
2011	0.23	0.18	0.17	0.31	0.10	Digital flight

A direct relation seems to exist between the GSD and the overall standard deviation (OSD) being both figures similar for 1956, 1977, and 2009 data. However, significantly higher OSD than GSD could be found for 2001, 2011, and especially for 1988. In the cases of 1988 and 2001, several tide levels can be seen and some confusion existed apart from the poor visualization, especially for 1988 data (Figure 4.19). Otherwise, in cases of 2009 and 2011 it is supposed that the main factor for a larger OSD was the operator skill.

Figure 4.19. Digitalization uncertainty for 1988 image due to previous runup level and poor visualization of the image.

Regarding this kind of error, which depends on the data source but also on the operator, other studies undertaken on similar conditions have reported very variable results. For example, for a flight scale of 1:19,500 localized in Hawaii it was found an uncertainty of ±3.0 m by means of a test of reproducibility (Fletcher et al. 2003), while a range from ±0.5 to ±5.7 m was estimated for larger scale images in the same islands through the interpretation of several expert analyst (Romine et al. 2009). In a Mediterranean beach, digitizing uncertainties from ±0.6 to 7.0 m were calculated by delineating the same feature several times and calculating its standard deviation (Virdis, Oggiano & Disperati 2012). In the latter work, it was also proved that the flight scale did not have a key role for this kind of error since for three images with similar scales (near to 1:33,000) three different uncertainties were estimated depending on the dataset and tide conditions (±5.0, ±1.6, and ±2.0 m). Here, it can be concluded that the natural regime of beach and tides and the quality of image have a key role for the digitizing uncertainty. Therefore, one only expert should be recommended in order to digitize all shorelines included in the same study or instead, a clear criterion should be established for using shorelines from different operators. For instance, a mean

offset of up to 4 m was found in other research when an entire regional coast was digitized by 3 different operators (Moore, Ruggiero & List 2006).

Overall uncertainty of digitizing shorelines

The overall uncertainty was evaluated for the 1956-2011 orthoimages datasets (WMS not included) by means of the square root of all previously described variances (squared standard deviations). The results are shown in Table 4.13 and yielded an overall uncertainty range from ±7.15 m for the most recent 2009 and 2011 orthoimages to ±7.45 for the oldest 1957 orthoimage. If variances are taken into account, the percentage of every single variable variance on the overall one is able to be calculated. It is worth noting that wave runup uncertainty was the most influent uncertainty since it is constituted of 88.3% up to 95.8% of the total variance. Therefore, an additional effort should be done in order to accurately estimate this source of uncertainty.

Finally, it is important to note that the entire coastal study site has been considered as one homogeneous unit instead of determining different uncertainties depending on the particular subarea or beaches.

Table 4.13. Components of overall uncertainty results expressed in meters for own-produced orthoimages.

Data	Natural phenomena uncertainties		Data source and measurement method uncertainties			Overall uncertainty
	Tidal fluctuation	Wave runup	Orthorect.	Pixel	Digitizing	
1957	1.43	7.00	1.56	1.00	1.00	7.45
1977	1.43	7.00	0.30	0.50	0.56	7.19
1988	1.43	7.00	0.32	0.30	1.23	7.26
2001	1.43	7.00	0.17	0.20	0.52	7.17
2009	1.43	7.00	0.18	0.15	0.18	7.15
2011	1.43	7.00	0.15	0.10	0.23	7.15

Including shoreline accuracy for WMS-derived shorelines

Similarly to the previous digitizing shorelines which were extracted from own-produced orthoimages, accuracy estimation should be undertaken for WMS-derived shorelines. Here, since the image orientation process was not controlled and other error sources were not known, only an approximation could be performed. For instance, while the seasonal uncertainty was not included in

previous own-orthoimages digitized shorelines, this error was included for WMS orthoimages of 1984-85 and 1998-99 since the actual date of the images was not known. A conservative uncertainty of ±5 m was estimated according to other works (Fletcher et al. 2003, Romine et al. 2009). Furthermore, the natural sources of uncertainty were considered identical to the previous ones (tidal fluctuation and wave runup) and the digitizing uncertainty was not evaluated but estimated by means of the relation between the GSD and the digitizing uncertainty on the previously calculated own-derived orthoimages (R^2=0.83). Finally, the pixel accuracy was obviously the GSD for every image while the orthorectification accuracy was conservatively estimated to be the double of the GSD since no information about it was found. Thus, the accuracy results were those shown in Table 4.14. As can be checked, the seasonal uncertainty made the 1984-85 and 1998-99 datasets more inaccurate than the others. Again, the effect of wave runup uncertainty was clear for this kind of shorelines. Finally, it is highlighted that both own-produced and WMS orthoimages yielded shorelines with comparable accuracies.

Table 4.14. Overall accuracy estimated for WMS orthoimages digitized shorelines

WMS orthoimages date	Overall accuracy (m)
1984-85	9.10
1998-99	9.10
2001	7.27
2004	7.27
2006	7.27
2007	7.61
2008	7.27

Digitized shoreline accuracy vs. DEM-extracted shoreline accuracy

Once the accuracies of both ways to extract shorelines have been established, the comparison between them can be afforded. The accuracy of DEM-derived shorelines (DDS) strongly depends on the local beach slope (Stockdon et al. 2002, White et al. 2011). On one hand, the local slope of the beaches along the working area was estimated to be between 0.05 and 0.15. On the other hand, the vertical accuracy for photogrammetric DEMs (photo-DEM) was estimated by means of the comparison between every photo-DEM and the high accurate 2009 LiDAR-derived DEM in areas with no apparent changes and after applying outliers removal. The provided accuracy for every photo-DEM was estimated as the standard deviation of the differences between DEMs with an estimation error, used as an uncertainty measure of the final accuracy estimated (Aguilar, Agüera & Aguilar 2007), close to

3% for all DEMs since the comparisons between DEMs were done by means of a high number of check points.

If a simple relationship between DEM accuracy and slope is used ($\sigma_{xy} = \sigma_z/slope$), it could be found that only 1956 image digitized shoreline (IDS) would be more accurate than 1956 DDS if a mean 0.10 slope was considered (Table 4.15). For the rest of datasets, DDSs were more accurate, especially when steeper slopes were considered. The great effort to extract photogrammetric DDSs should be taken into account, since the automatic stereo matching gets usually poor results in sandy areas and a huge manual DEM-editing may be required. However, photo-DEMs can be really useful for volumetric changes (e.g. in sand environments) and their production may be highly interesting.

If DDS and IDS are directly compared (Table 4.16), it is noted that for the most accurate DEM (i.e. LiDAR-derived DEM), the horizontal accuracy of DDS was almost 9 times higher than the one corresponding to IDS. For 2001 and 1988 shorelines, the DDS accuracy was more than 2 times higher while for 1977 both accuracies can be considered quite similar. On the contrary, the 1956 DDS accuracy was three times less accurate than the IDS one.

Table 4.15. Horizontal accuracy (expressed in meters) according to the type of DEM used and the local.

Data	Type of DEM	Std dev DEM	Accuracy 0.15 slope	Accuracy 0.10 slope	Accuracy 0.05 slope
1956	Photogrammetric	2.20	14.67	22.00	44.00
1977	Photogrammetric	0.50	3.33	5.00	10.00
1988	Photogrammetric	0.28	1.87	2.80	5.60
2001	Photogrammetric	0.27	1.80	2.70	5.40
2009	Lidar-derived	0.089	0.59	0.89	1.78
2011	Lidar-derived	0.082	0.55	0.82	1.64

Table 4.16. Horizontal accuracy for DDS and IDS for each dataset and relation between them. An overall slope of 0.10 was used for estimating accuracy of DDS.

Data	Accuracy DDS (m)	Accuracy IDS (m)	Acc IDS/ Ac DDS
1956	22.00	7.45	0.34
1977	5.00	7.19	1.44
1988	2.80	7.26	2.59
2001	2.70	7.17	2.66
2009	0.89	7.15	8.03
2011	0.82	7.15	8.72

SHORELINE CHANGE RATES METHODS

For most of the shoreline change rates methods, linear change is assumed. However, shoreline erosion or accretion may not be uniform. For instance, a second or more polynomial can fit a short-term change properly, although non-linear fits may not improve predictions of shoreline trends (Dolan, Fenster & Holme 1991). Moreover, Minimum Description Length (MDL) was developed in order to describe non-linear shoreline behaviour and to be compared with linear methods (Fenster, Dolan & Elder 1993), although some authors found no differences (Crowell, Douglas & Leatherman 1997, Douglas, Crowell 2000). Linear methods have been considered appropriate for shorelines unaffected by inlets or engineering changes but they should be used carefully otherwise (Galgano, Douglas 2000). Other main discussion about change rates methods has corresponded to the huge storm treatment since it can be considered as an outlier for the general rate (Douglas, Crowell 2000, Honeycutt, Krantz 2003) or as a key data for non-linear long-term shoreline movement (Fenster, Dolan & Morton 2001)

The shoreline data used for rates estimation also plays a key role since different sources of data are subject to varying degrees of error and the availability of data dictates the temporal limits of the study (Crowell, Leatherman & Buckley 1993). Thus, to estimate historical shoreline change rate with some degree of confidence, the assessed movement must be larger than the shoreline mapping error (Anders, Byrnes 1991). As a consequence, the confidence interval computed from the linear regression analysis should be used for the shoreline position forecast (Douglas, Crowell 2000).

Finally, other main factors are constituted by the time span in which change rates are estimated and the shoreline distribution during time, preferring evenly distributed sequence of shoreline (Dolan, Fenster & Holme 1991). For long-term studies, it should be considered more than several decades, and also considered the recovery from storms in more than 1 year, and more than 100 years was recommended (Galgano, Douglas & Leatherman 1998). It is important not to consider intervals of a few decades as adequate to characterize shoreline behaviour in a specific area except for few years into the future (Crowell, Douglas & Leatherman 1997). Therefore, the time span available for this study (1956 to 2011) can be considered as medium-term shoreline evolution and the results should be taken carefully for forecasting purposes. Moreover, the great amount of human interventions in the study area made difficult to consider the shoreline evolution as natural. However, it was expected that a suitable description about the shoreline changes can be performed.

Bearing in mind the latter, the shoreline change rates methods historically developed are subsequently listed according to previous works (Genz et al. 2007).

End Point Rate (EPR)

Only two shorelines are used to compute a change rate by means of the net shoreline movement in meters (NSM) divided by the time span. It is very simple and easy to carry out but the EPR will be inaccurate if one of the reference shorelines is wrong.

Average of Rates (AOR)

Using a minimum time criterion regarding the shoreline accuracies, all the possible EPRs which passes that criterion are estimated and finally averaged. It is not very useful since short periods can be estimated and, then, the estimated EPR may result inaccurate.

Minimum Description Length (MDL)

MDL tries to describe influential short-term changes by estimating the best model to fit (line, quadratic, etc.). In general, if the resulting model is quadratic or more, two lines are fitted: first, the MDL ZERO by means of the most recent data and, second, the MDL LOW which assigns low weights to the oldest data. The reader is referred to Fenster, Dolan & Elder (1993) for further information.

Ordinary Least Squares (OLS)

A linear regression is estimated by taking into account all the shorelines available and assuming independent Gaussian errors. However, some outliers produced by storms, sediment supply and transport, presence of coastal structures, and so on, may not result in Gaussian variations in the data so the method is sensitive to outliers. Furthermore, non-well-spaced shorelines can greatly affect the results and the future shoreline position accuracy is not known since the shoreline uncertainties are not included.

Jackknifing (JK)

This method uses several OLS fits by means of removing one point for each iteration. Finally, the slope estimated is averaged. It can decrease the effect of clustering points but it could result inefficient (Genz et al. 2007).

Reweighted Least Squares (RLS)

It is based on identifying outliers through least median of squares (LMS). Those outliers are weighted as zero and the rest of points are assigned a weight of

one. Then, an OLS is fitted using the data with weight equal to one. Therefore, RLS is more robust than OLS since it is not sensitive to outliers. However, this method could lead to an undesirable risk, since points are removed without any previous knowledge.

Weighted Least Squares (WLS)

The uncertainties for every shoreline are included in the co-variance matrix when least squares are applied. The weight is set to be the inverse of the variance ($1/\sigma^2$) and so points presenting less variance will have large influence on the final results and vice versa. This method could be sensitive to outliers even if their weights are small, so a priori knowledge could be necessary.

Reweighted Weighted Least Squares (RWLS)

RWLS is similar to RLS but different weights for every point are considered. Then, LMS is also used for identifying and removing outliers and WLS is utilized to estimate the rate.

Least Absolute Deviation (LAD)

LAD was developed to minimize the sum of the absolute value residuals instead of the sum of the squared residuals. It is more robust than OLS because outliers have less influence on the adjustment since residual are not squared. Moreover, LAD is preferable to least squares methods when outliers are in the *y* direction, e.g. shoreline positions (Rousseeuw, Leroy 1987).

Weighted Least Absolute Deviation (WLAD)

Similarly to WLS, weights can be incorporated for LAD and then, the fewer the variance, the lager the influence on the fitting process.

For this study, the MATLAB® function *fit* was utilized for all the regression methods. The general option utilized for this function was *'poly1'*, indicating that linear regression is performed. When weights were required (RLS, WLS, RWLS, and WLAD) the function *fit* was set with the option *'Weight'*. Finally, for LAD and WLAD, the function *fit* was set with the options *'Robust'* and *'LAR'* (Least Absolute Residual) to indicate a different method to achieve the linear regression (LAD instead of OLS).

EVOLUTION OF CHANGES OVER TIME

Here, a general description of changes occurring from 1956 to 2011 in the study site is done. For that reason, an explanation of every two consecutives shorelines is performed trying to identify the keys on the shoreline evolution occurred in this area. In order to carry out this analysis, the own-orthoimage-derived shorelines were used and a high resolution set of 5 m spacing transects was created by means of the DSAS software tool, running into ArcMap GIS software (Thieler et al. 2008). Thus, the EPR and NSM were estimated for each couple of consecutive (in time) shorelines.

1956-1977

This is the period where shoreline changes were more evident. The alongshore distribution of the differences depicts a clear erosive area at North and an accrete area at South, following the general alongshore sediment transport previously described. The main affected areas by erosion were the surrounding areas of the *Almanzora*'s mouth (where the typical convex shape of the delta became to an erosive concave shape), *Punta de Hornicos*, and especially *Quitapellejos* beach, which reached a net shoreline movement of -154.4 m (-7.43 m/yr of erosion rate). However, the accreted areas did not reach that intensity and a maximum NSM of 53.7 m (2.58 m/yr) was observed.

During this period, there were some episodes of sand mining since 1974, although no documented sand nourishment has been found (Tables 4.2 and 4.3). However, the main reason of shoreline erosion seems to be related to the lack of powerful rain or floods episodes from 1943 to 1969, according to Table 4.1. In fact, and according to the study carried out by Viciana (1996), between 1957 and 1965 the erosion affected mainly at the South (-20 m), *Punta de Hornicos* (-40 m), *Fábrica del Duro* beach (-45 m), being the *Quitapellejos* beach the most affected area with an estimated erosion of up to -120 m, yielding an incredibly high erosion rate close to 15 m/yr, which was the double of the rate estimated between 1956 and 1977. That huge erosion rate was clearly related to the lack of sediment supply during the 1957-1965 time span since the erosion rate was later mitigated up to about -3 m/yr between 1965 and 1977 when some floods episodes occurred (e.g., 1969, 1973, and 1974, see Table 4.1). Viciana (1996) found some accreted areas between 1965 and 1973 around the *Antas* and *Almanzora* mouths (20 and 30 m approximately in some points) but the entire area still reflected a general erosion process (43,421 m^2 of beaches were estimated to be lost in this period by Viciana (1996)).

Summing up, the 1956-1977 period clearly explained that the coastal cell defined by the study site was highly dependent on the sediment supply as well as the general alongshore sediment transport was proved. Also, the area between

Almanzora's delta and *Quitapellejos* beach appeared as the most vulnerable to erosion mainly due to the initial coastal orientation regarding the main wave approaching angle. It was also clear that the *Garrucha*'s harbour main dock acted as a limit for the sediment making this area to have the main accretion processes. Finally, the existence of a sediment sink (i.e. the *Palomares* canyon) was proved since the erosive processes acting at North were not compensated or balanced by the accreted ones at South. This coastal evolution was highly important since showed its natural behaviour because of no clear human intervention was performed other than previously mentioned sand mining during the 1974-1977 period.

1977-1988

The main characteristic of this period is the construction of the *Cuevas del Almanzora* dam in 1982, what drastically reduced the natural sediment supply towards the coastal cell. Furthermore, sand mining activities could play a key role since almost the 80% of the complete sand mining was carried out in this period and a total of 271,800 m^3 were extracted from the coastal cell. This quantity was equivalent to two or three times the sediment supply yielded by the *Almanzora* river mouth per year which was expected to contribute to the sand beach formation (Viciana 1996).

The erosion still dominated from North to the *Puerto Rey* beach from which some accretion and erosion areas were consecutively located. The main erosive process took place in the *Almanzora*'s mouth, where the concave shape was more pronounced, clearly related to the dam construction. Here, a maximum of -94.43 m NSM was calculated which leaded to a high erosive rate of -7.76 m/yr. An intensive erosion rate was estimated in *Quitapellejos* beach as well (about -4.5 m/yr). The erosion was declining from *Quitapellejos* to *El Playazo* beaches, indicating that the intensity of the erosion process was related to the relative position between the coast angle (given by the normal to the shoreline) and the dominant waves direction (a climate variable) (Roelvink, Reniers 2012). In this sense, the sediment balance during this period was clearly negative.

1988-2001

During this period of time, the sand nourishment activities became a key role for the coastal evolution, since the greatly erosive process which affected the coastal cell had to be stopped. In total, about 215,000 m^3 of sand were poured into the study site area which was equivalent to 1.5 times the average of the available natural sediment supply in normal conditions per year. Additionally, although some flood events occurred in 1989, 1996, and 1997, the *Cuevas del Almanzora* dam dramatically reduced its sediment supply. Furthermore, even if sand

nourishment and flood events were taken into account, the erosion was expected to affect this area during the 1988-2001 period.

On one hand, the erosion was clear between *Quitapellejos* and *El Playazo* beaches (up to -39 m or -3.4 m/yr) and in the *Villaricos* (-32 m) and *Fábrica del Duro* (-31 m or -2.7 m/yr) beaches. However, and towards South of *El Playazo*, erosive processes were only estimated in the North face of the *Garrucha*'s harbour. On the other hand, accretion processes were observed in the *Almanzora*'s mouth due to the reconfiguration of that environment because of the lack of sediment supply and the natural sediment migration. This mouth constitutes a highly dynamic sedimentary unit in which the finest sediment rapidly evolved forming some curious sandy shapes (Figure 4.20).

Southern the *El Playazo* beach, the accretion was generalized being the maximum in *Las Marinas* beach (South face of the *Antas*' river mouth reached an accretion of about 46 m or 4 m/yr). This local high accretion rate could be related to the sand nourishment and the flood events since the *Antas River* still allowed some natural sediment supply. Furthermore, an important accretion was observed in the *Quitapellejos* beach part located next the *Punta de Hornicos* (in which the wave incident angle clearly differs from the general shoreline orientation). However, this accretion was clearly related to a specific nourishment carried out on this area (even the sand colour was different, see Figure 4.21). It is important to note that this accretion was quickly lost according to the 2001 WMS orthoimage indicating that this area constituted a natural erosive area mainly due to the dominant wave approaching angle.

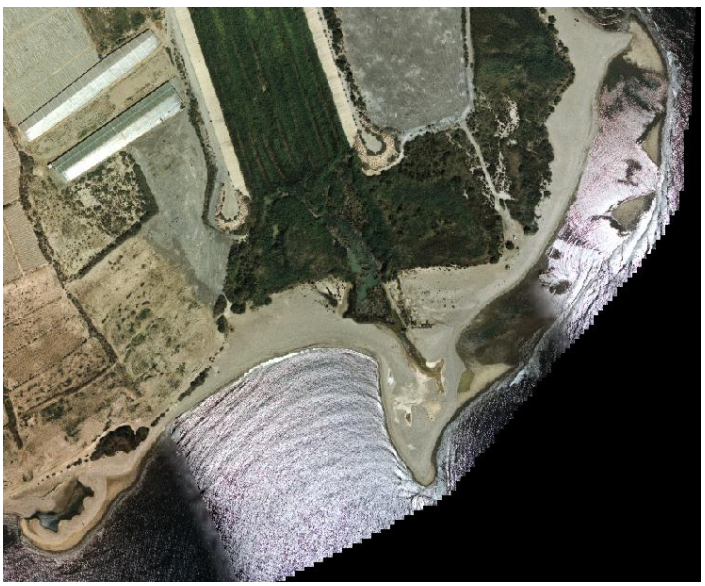

Figure 4.20. Examples of sand migration and reconfiguration in the Almanzora's mouth. Own-produced 2001 orthoimage.

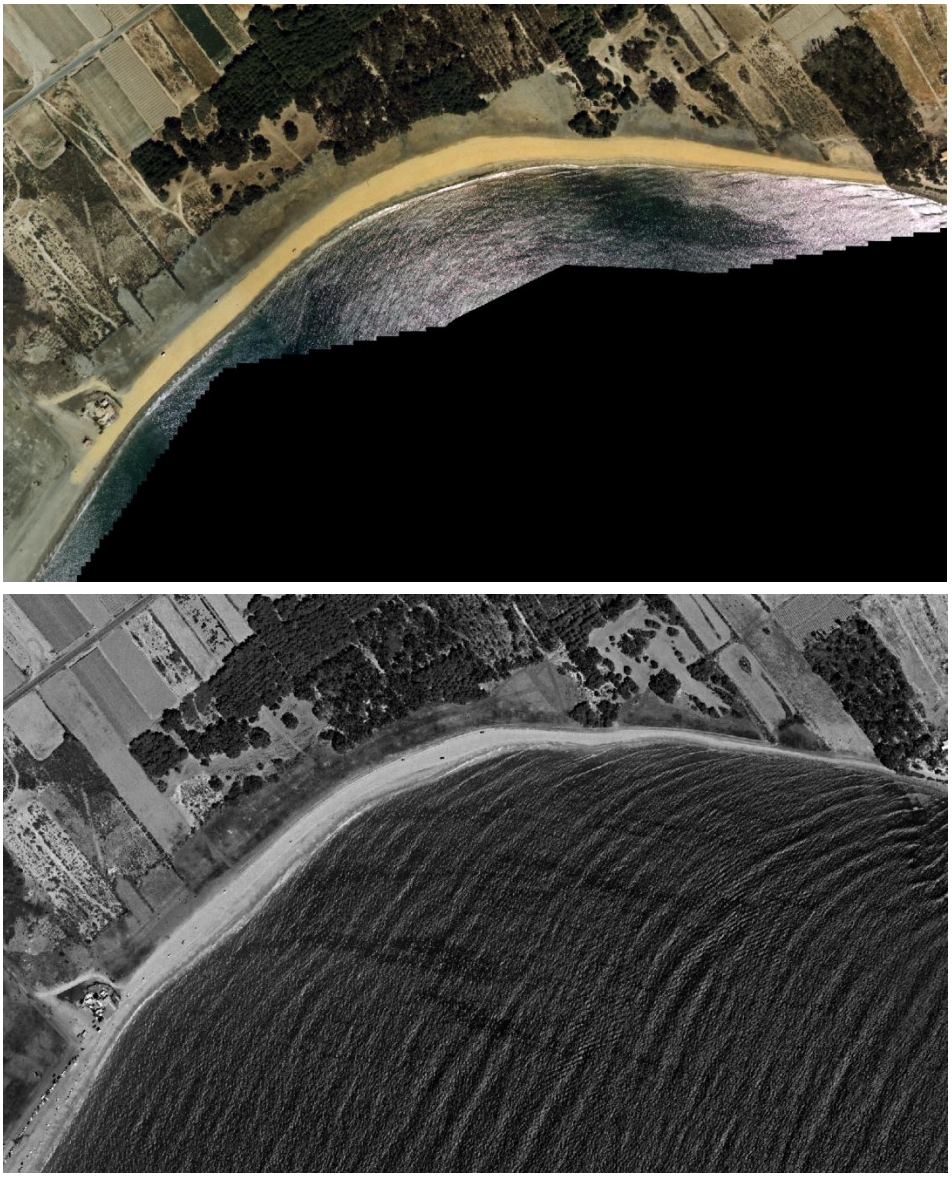

Figure 4.21. Top image represents the Quitapellejos beach on the 2001 own-produced image. Bottom image shows the same beach on the 2001 WMS image. It is clear that external sand nourishment was performed and a rapid erosive process took place and the old 1988 shoreline position was reached or even eroded.

Summing up, the time span from 1988 to 2001 showed an average accretion scenario (the mean NSM was 7.68 m) which was mainly attributed to the sand nourishment carried out in the coastal cell. The main evolution was observed in the *Almanzora*'s mouth and surrounding areas, and also in the *Quitapellejos* beach where a sand nourishment was rapidly removed because of the general wave

approaching angle and the alongshore sediment transport. The nourishment activities, but also the flood events, were related to the general accretion on the beaches located at the South of the coastal cell.

2001-2009

In this period some important human-induced changes were carried on. A clear and great effort to stop the erosive processes was performed mainly in the *Quitapellejos* and *El Playazo* beaches. Here, two cross shore jetties were installed between 2007 and 2008, and a high volume nourishment was performed in order to stop the high erosion rates borne by these areas. In total, 548,600 m^3 were deposited during this period which was equivalent to 3.5 times the maximum annual sediment supply by the *Almanzora* River in natural conditions, but a half of the total sediment that was supposed to be provided by the delta in that time span. It is important to note that the flood events occurred in 2002 and 2006 are supposed to not significantly contribute to the sediment supply because of the *Cuevas del Almanzora* dam.

When erosive and accreted areas were analysed, some stretches of eroded and accreted areas were found. The *Quitapellejos* and *El Playazo* beaches were highly accreted because of the joint effect of nourishment and jetties, while *Puerto Rey* beach reached a NSM up to about 30 m (3.8 m/yr of accretion rate). A part of *Puerto Rey* beach accreted also up to 21 m probably as a consequence of sand nourishment or alongshore sediment transport. The eroded areas were the *Almanzora*'s mouth surrounding areas up to *Punta de Hornicos*, the South part of *El Playazo* (maximum erosion of -40 m), located towards South the jetty, and a large eroded shoreline appeared from *Puerto Rey* to *Las Marinas* beaches (maximum erosion of -37 m), likely influences by the lack of a local nourishment. The *Almanzora's* mouth was still on a reconfiguration process (general erosion occurred and sand migration still continued) and a jetty was installed here in order to provide sea water to a local desalination plant.

Generally, erosive processes were still presented and an average NSM of -3.8 m was estimated for the entire coastal cell even when a great nourishment effort and jetties installation took place. However, since such important human interventions were performed between 2001 and 2009, a more detailed explanation was needed and the WMS images were highly helpful in this regard (2004, 2006, 2007, and 2008 WMS images were available). As previously mentioned, the 2001 WMS orthoimage enabled a more suitable description of the *Quitapellejos* beach evolution since it demonstrated that the accretion shown in the 2001 own-produced image was greatly temporary. Because of that, the great accretion estimated in this area between 2001 and 2009 was supposed to be even larger. The erosion was clear for the periods 2001-2004 and 2004-2006 in *Quitapellejos* beach, mainly affected by the lack of sediment supply and the wave

approaching incident angle, and a slight accretion stage occurred between 2006 and 2007, when the northern jetty was being installed. Regarding the *Almanzora*'s mouth, the sand migration continued from 2001 and 2007 and the trend was clearly towards the equilibrium. Moreover, an accretion process seemed to turn up at *Las Marinas* and *Puerto Rey* beaches, confirming the alongshore sediment transport. Finally, if 2007 and 2008 WMS-derived shorelines are analysed (both jetties are visible in 2008 image), a large accretion can be seen in *Quitapellejos* beach in between both jetties and surrounding northern areas (a huge sand nourishment was performed) while some important erosion can be proved southern the jetty located more southern. Likewise, important erosion was seen at *Las Marinas* beach between both images and it could be related to the *Garrucha*'s harbour main dock extension carried out during this period.

Summing up, the period between 2001 and 2009 was not easy to analyse since many human interventions were carried out and the natural shoreline evolution was partially masked by them. However, important information could be extracted from WMS orthoimage and some conclusions could be extracted.

2009-2011

During this short time span, a general accretion occurred at *Las Marinas*, *Puerto Rey*, and *El Playazo* beaches, while the erosive processes were concentrated at the *Quitapellejos* beach. The previous sand nourishment done during 2009 and the jetties installation seems to maintain a significant impact. The area under erosion in *Quitapellejos* beach got significantly reduced by the jetties although that had a high intensity, reaching up to -43 m (-21.6 m/yr). Similar to what happened in 2001, the rapid erosion carried out in this area is clearly dissuading new sand nourishment on it, at least in those parts which the wave approaching angle is far to be perpendicular. However, the alongshore sediment transport turned out to have an accretion effect on the southern areas, especially due to the jetties installation and the *Garrucha*'s harbour. Thus, the jetties acted as a wall for sediments in their North face, reaching 25 m of accretion between both of them. Moreover, once the capability of retaining sediments of the southern jetty was exceeded, the sediment started to follow towards alongshore direction through the South, and the beaches beyond the jetties started to accrete up to 22 m cross shore. However, the main accretion occurred in *Las Marinas* beach in which a NSM of up to 44 m was calculated (a rate of 21.9 m/yr). Here, it is estimated that the new *Garrucha*'s harbour dock played a key role by acting as a wall for sediment.

Some conclusions from the evolution of changes

The previously discussed results showed that the study site coastal cell evolution was really variable. Too many factors were proved to play highly

important roles. Firstly, natural features on the study site were very influent. On one hand, the lack of sediment supply derived from the few number of flood events between 1943 and 1969 leaded to point it out as the main factor explaining the generalized huge erosion observed in the North part of the area during the 1956-1977 coast evolution. On the other hand, the seaward positions of the shoreline in 1977 for the South part clearly indicated the general alongshore transport, the important role played by the unbalanced orientation of the shoreline regarding the wave approaching incident angle, and the importance of the *Garrucha*'s harbour as a cross shore limit for sediment transport. Therefore, this coastal cell can be classified as a highly dynamic coastal area regarding its morphology because of the sediment supply was not provided regularly due to the local climate features (sediment supply highly depends on the flood events), but also because of the initial orientation of the shoreline which made some areas, such as *Quitapellejos* beach, potentially erodible due to the coastline angle with respect to the dominant wave approaching.

In this sense, a modified model of alongshore transport of sediment adapted from the model proposed by (Roelvink, Reniers 2012) has been run in the study area to compute the erosion/accretion balance (sediment transport in m^3/yr) for every point along the coastline as a function of different variables such as bathymetric data, climate data (wave direction and associated probability, significant wave height and wave peak period) and coast angle (given by the normal to the shoreline). The results, which should be interpreted as qualitative more than quantitative data due to the fact that the model has not been validated against experimental data, are depicted in Figure 4.22. It is worth noting that the negative net sediment transport (red line) is situated approximately between the coast angles from 165º to 205º with respect to the North, clearly coinciding with the area corresponding to the *Quitapellejos* beach, i.e., the coastal area which has been experimentally pointed out as the more vulnerable in the presented shoreline evolution analysis. The estimated volume of sediment lost in the worse point of this zone would reach a value close to 170000-180000 m^3/yr along an active cross-shore profile of about 2193 m length and up to a depth of 30 m below the sea surface.

The dependence of the sediment supply can be proved if the results reported by Viciana (1996) are taken into account. The erosion rate decelerated in *Quitapellejos* beach if 1957-1965 and 1965-1973 are compared, being the latter the half of the former. That reduction was probably due to the flood episodes of 1969 and 1972. Finally, the fact that the erosion was always more evident than accretion could demonstrate the existence of a sediment sink located at the *Palomares* canyon. Therefore, sediment budget (supply, sources, and sinks) and oceanographic conditions were revealed as important factors for shoreline evolution of the study area. Here, it is important to note that the geology framework, the grain size, and the nearshore can play a significant role (Honeycutt,

Krantz 2003). That means that the changes occurred over the years in the study area could make the evolution to be different in the future. For instance, the *Almanzora's* delta became formed by coarse grain size while it was formed by finer sizes in 1956. Thus, the potential erosion is nowadays less than it was before and the erosion rate will be surely changed. The same could occur in *Quitapellejos* beaches where the erosive front is clearly formed by stones or clays instead of sand beaches. Therefore, the shoreline evolution cannot be linear in those areas since the material to be eroded has been changed over time.

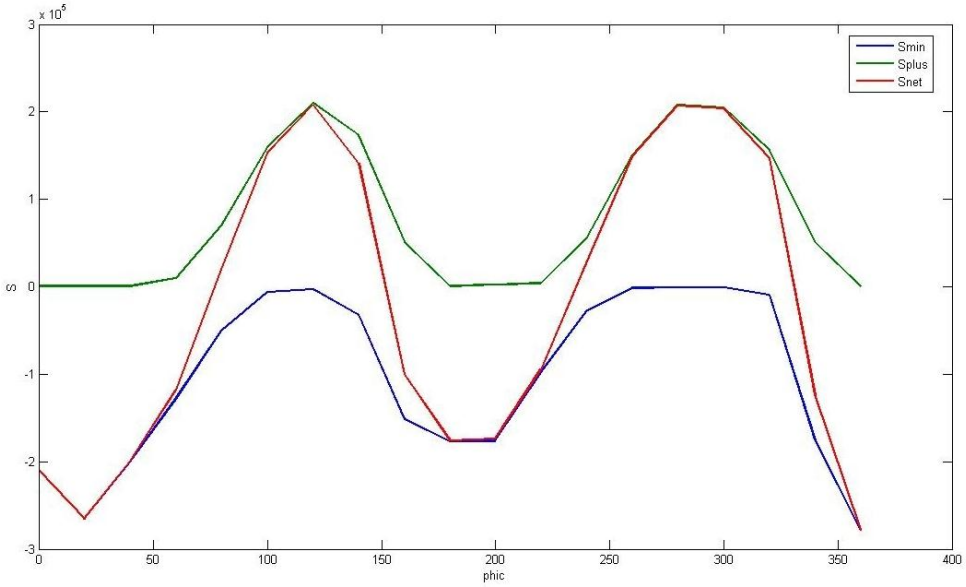

Figure 4.22. Sediment transport (S) expressed in m³/yr according to the coast angle Phic (given by the normal to the shoreline with respect to the North). Green and Blue lines indicate sediment inputs and outputs, respectively, for a particular coastline point (finite element for computation). Red line represents the net balance (input-output) for every coastline point.

Secondly, regarding the human-induced factors, the influence was more difficult to estimate. The main anthropic factor was the *Cuevas del Almanzora* dam construction (between 1982 and 1984) which was proved to be the main reason of the dramatic sediment supply reduction. Additionally, sand mining until 1986 could play an important role for the large erosion found in 1989, and the *Almanzora*'s mouth channelling apparently affected the shape of the delta since the way the water flow reach the sea changed deeply. The sand nourishment activities, although temporary made the beaches accrete, seemed to have exceptional effects and the beaches recovered the previous state rapidly. However, the installation of the jetties could fix the sediment supply in the northern areas and once the effect of wave incidence was corrected by means of making a seaward shoreline. Therefore, the remaining factors would only be the power of some events to provoke erosion (storms and so on) and the main alongshore transport direction

which leads the sediment towards the *Garrucha*'s harbour and the *Palomares* canyon. Therefore, if no additional sediment is provided in the coastal cell, the general evolution would trend to the erosion since the alongshore sediment transport has a clear main direction and a sediment sink on the south border or the cell exists.

MEDIUM-TERM SHORELINE CHANGE RATE ASSESSMENT

According with the previous sections of this chapter, the shorelines to be used for medium-term shoreline evolution assessment in the study area were obtained from orthoimages digitizing (i.e. HWL was used as a proxy for shorelines from own-produced or Spatial Data Infrastructure –SDI- images) or DEM-derived (0.75 m contour level). The finally extracted shorelines are shown in Table 4.17. In order to simplify the process of change rate accuracy assessment, an average slope value of 0.10 was used to evaluate the planimetric accuracy for DEM-derived shorelines, thus the computed accuracy was independent on the alongshore position.

Table 4.17. Shorelines used for medium-term changes rate

Year	Source	Date	Shoreline estimated accuracy (m)
1956	Own-produced ortho.	30/09/1956	7.45
1977	DEM	15/07/1977	5.00
1984-85	SDI ortho.	31/12/1984	9.10
1988	DEM	15/09/1989	2.80
1998-99	SDI ortho.	31/12/1998	9.10
2001	DEM	09/04/2001	2.70
2001	SDI ortho.	31/12/2001	7.27
2004	SDI ortho.	15/06/2004	7.27
2006	SDI ortho.	15/06/2006	7.27
2007	SDI ortho.	15/06/2007	7.61
2008	SDI ortho.	15/06/2008	7.27
2009	DEM	28/08/2009	0.89
2011	DEM	30/08/2011	0.82

Note that, for this study, the longest term evolution is considered in cases which the first available data is included (1956) since it constitutes the maximum time span available in the study area, although the time span used for this study have been considered as medium-term (several decades) for some authors (Crowell, Douglas & Leatherman 1997, Galgano, Douglas & Leatherman 1998).

Thus, although all datasets would correspond with the longest term evolution as possible, medium-term was used in order to be as rigorous as possible.

In order to check the influence of the data used for medium-term shoreline evolution, four different configurations have been taken into account. First, A1 configuration only considered the 6 own-produced shoreline data (no SDI data were included) for the entire time span. Secondly, all the available data (13 shorelines) were included for the entire time span for A2 configuration. Then, the time span was divided in two parts in order to determine the possible influence of the installation of the two jetties and the large sand nourishment carried out in 2007. Thus, the two considered periods were 1956-2007 and 2008-2011, including the SDI extracted shorelines in order to count on enough number of data for rate regression estimation. Therefore, 10 shorelines for 1956-2007 and 3 shorelines for 2008-2011 time spans were utilized. The last configurations were called B1 and B2, respectively, representing a medium- and short-term shoreline evolution.

Table 4.18. Different homogeneous areas used for shoreline evolution results.

Zone	Alias	N° transects	Group
Fábrica del Duro I	FD1	52	3
Fábrica del Duro II	FD2	56	4
Punta Hornicos	PH	43	5
Quitapellejos I	QP1	64	6
Quitapellejos II	QP2	66	7
North jetties	NJ	111	8
Between jetties	BJ	114	9
South jetties	SJ	164	10
Puerto Rey	PR	578	12
Las Marinas	LM	155	13

Furthermore, and for the sake of helping to understand the results, homogeneous coastal areas were established and the transects included in those areas were used for averaging the final results. The selection of these areas was based on geomorphic and evolution features (Table 4.18). For instance, the jetties installed between the beaches *El Playazo* and *Quitapellejos* made up 3 different groups: north part, south part, and the beach located just between both jetties.

The shoreline change rate estimation methods applied in this study were EPR, MDL, OLS, JK, RLS, WLS, RWLS, LAD, and WLAD (see *Shoreline change rates methods* section). However, JK and MDL methods were not included in the final analysis since those results were highly dependent on the number of shorelines

used and they were not applicable for every configuration, especially for the B2 (only 3 shorelines).

Influence of adding SDI-derived shorelines

Although shorelines digitized from SDI orthoimages were the less accurate, they increase the number of observations and, then, their influence on the results should be estimated. Therefore, the results obtained from configurations A1 and A2 must be compared. The largest differences between both configurations occurred for RLS method while RWLS, LAD, and WLAD presented some significant differences for some groups, OLS and WLS being considered similar for every group and both configurations. The differences for RLS method are shown in Table 4.19. It is highlighted that the differences for groups FD1, FD2, QP1, QP2, NJ, and BJ cannot be considered appropriate, indicating that the number of shorelines involved in the calculation played a key role.

Table 4.19. Difference between A1 and A2 configurations for RLS method (expressed in m/yr)

Area	A1	A2	Difference (A2-A1)
FD1	-0.32	-1.12	-0.80
FD2	-1.70	-1.25	0.45
PH	-1.36	-1.41	-0.05
QP1	0.67	-0.02	-0.70
QP2	-0.35	-1.26	-0.91
NJ	-0.95	-2.35	-1.40
BJ	-1.51	-2.26	-0.75
SJ	-0.94	-0.97	-0.04
PR	0.37	0.38	0.01
LM	0.51	0.73	0.21

As previously detailed, RLS is based on removing outliers before fitting the regression line, not including the corresponding shoreline uncertainty. When the group in which the largest difference is analysed and the removed shorelines were accounted, it was found that 1956 shoreline (the oldest) was removed 109 times for both A1 and A2 configurations. However, while for A1 no more shorelines were generally removed, for A2 configuration (with SDI shorelines) 2008, 2009, and 2011 shorelines were eliminated in 77, 109, and 98 transects respectively. Those observations perfectly matched with the period after jetties installation (2007). Therefore, RLS method treated those shorelines as outliers (Figure 4.23). It was proved that the influence jetties area (QP2, NJ and BJ groups) had the largest

difference between both configurations. For FD1 area, A2 configuration trended to remove the oldest shoreline since the concentration of the newest ones had a large influence. That implied that the equally time spaced data was preferable for shoreline change rate estimation.

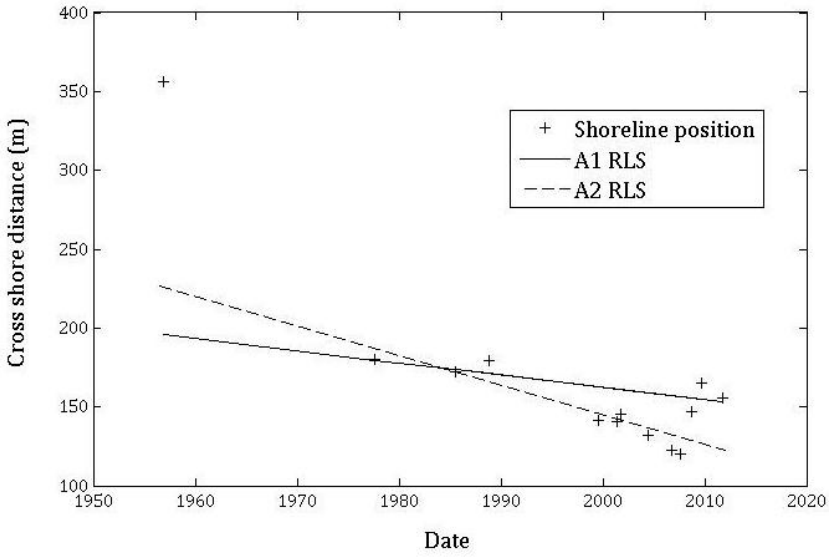

Figure 4.23. RLS results for A1 and A2 comparison in one transect of the group NJ. Note that 1956 shoreline has not been included for both regressions while 2008, 2009, and 2011 shorelines were not included for A2 configuration.

Influence of including shoreline uncertainty

Some of the estimated rates were proved to significantly vary regarding whether the data were weighted or not. When homologous methods were compared larger differences were found in the case of the A2 configuration for RLS-RWLS and LAD-WLAD comparisons, while both configurations yielded similar differences when OLS-WLS were compared (Figure 4.24). The areas affected by those differences were FD1, QP1, QP2, NJ, and BJ. Therefore, the effect of the jetties installation was clear. Regarding those results, an overweighting effect was found mainly due to two reasons: first, the last shorelines had a much higher accuracy than the others and this made the erosion rate smaller (e.g. the erosion rates computed from WLS and RWLS were much smaller than those obtained from OLS and RLS respectively, as can be seen in Table 4.20); and second, most of the shorelines were acquired from 2000 so those data provoked that the influence of the oldest shoreline was very little (e.g., that effect provoked that RLS rates were smaller than OLS when 1956 was considered as outlier).

Table 4.20. OLS and WLS methods comparison for A2 configuration (expressed in m/yr)

Area	OLS A2	WLS A2	Difference (WLS-OLS)
FD1	-1.45	-0.73	0.72
FD2	-1.78	-1.55	0.23
PH	-1.61	-1.39	0.22
QP1	-0.92	0.02	0.93
QP2	-2.73	-1.23	1.50
NJ	-3.10	-1.30	1.80
BJ	-1.75	-0.52	1.23
SJ	-0.82	-1.13	-0.31
PR	0.46	0.36	-0.10
LM	0.55	0.53	-0.03

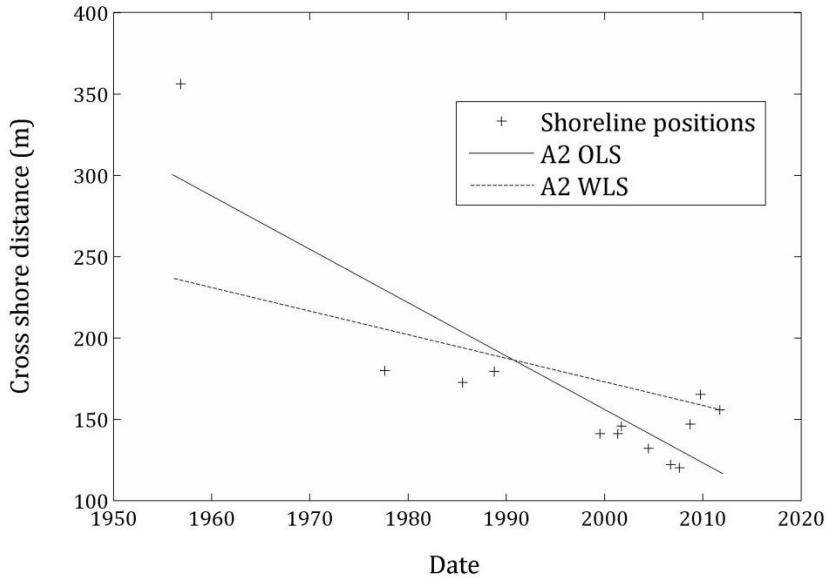

Figure 4.24. OLS-WLS for the same profile (group NJ). Note that when weights were considered, the most accurate shorelines (2009 and 2011) had a large influence while 1956 shoreline largely influences the OLS result.

Beach areas with stable change rates

Those areas in which the jetties installation had less effect showed similar shoreline change rates regardless the method applied. For instance, the areas PH, SJ, PR, and LM yielded no differences when configurations A1 or A2 were applied for every regression method, so the linearity was maintained after the jetties installation (Table 4.21). Moreover, the aforementioned areas (and also FD2) did not present large differences when unweighted methods were compared against

the homologous weighted ones (OLS-WLS, RLS-RWLS, and LAD-WLAD, see Figure 4.25). Finally, reweighted methods (i.e. outliers are removed) performed similar to their homologous non-reweighted methods (OLS-RLS and WLS-RWLS) for these areas as well.

Table 4.21. Regression methods results for areas with stable change rates for configuration A1 (expressed in m/yr).

Area	OLS	WLS	RLS	RWLS	LAD	WLAD
FD2	-1.74	-1.56	-1.70	-1.61	-1.64	-1.69
PH	-1.59	-1.38	-1.36	-1.38	-1.43	-1.42
SJ	-0.80	-1.12	-0.94	-1.15	-0.91	-1.02
PR	0.56	0.36	0.37	0.29	0.43	0.40
LM	0.62	0.59	0.51	0.53	0.80	0.64

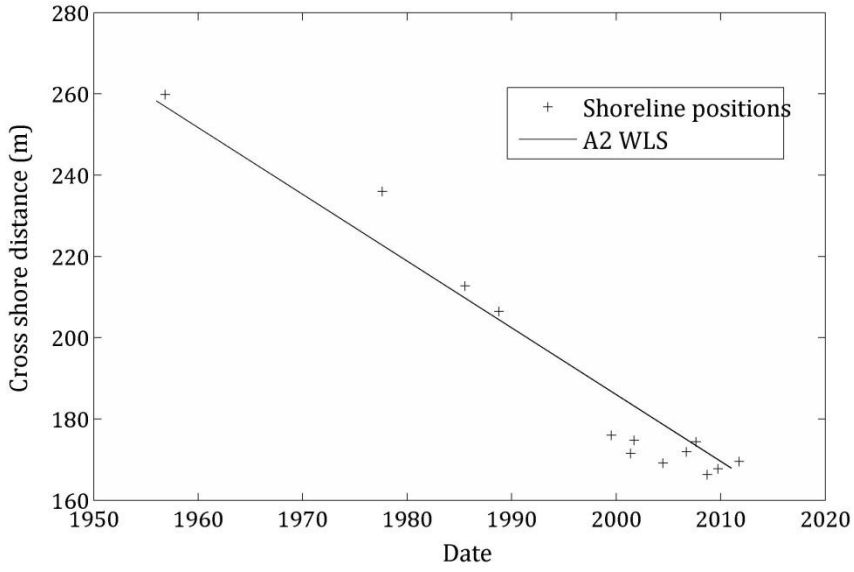

Figure 4.25. Linear trend estimated in FD2 group by means of WLS and A2 configuration. Note that the noise in shoreline positions for the last years did not significantly modify the general trend.

Divided time span

Previously, the entire time span configurations, A1 and A2, have been considered. Here, the results obtained by means of the configurations B1 and B2 will be presented and discussed. As previously mentioned, both configurations were set taking into account all shorelines (SDI data included) but the time span was divided into two parts regarding the jetties installation: 1956-2007 (B1) and

2008-2011 (B2), meaning 10 and 3 shorelines respectively. Therefore, B1 configuration was supposed to describe non-human influenced shorelines (although that was not completely true) and the results should be comparable with those estimated by A1 and A2 configurations. Moreover, these comparisons could help to explain the influence of including the newest shorelines.

First of all, the influence of the regression method should be determined for configuration B1 (Table 4.22). Thus, the influence of using weighted and reweighted methods was determined. When weighted methods were applied, the estimated rates were similar except for areas QP1 and QP2 for OLS-WLS and RLS-RWLS comparisons, and for areas FD2 and QP1 for LAD-WLAD comparison. The largest differences occurred in the case of OLS-WLS comparison. Again, the concentration of the newest shorelines and their higher accuracy seem to make the change rates smaller (Figure 4.26). Furthermore, the influence of 1956 shoreline for OLS could be also too high since rates computed from OLS were always higher than those obtained from WLS. However, the differences between both reweighted methods were quite smaller since 1956 shoreline positions were estimated as outliers in most of the transects.

Table 4.22. Absolute differences (m/yr) between weighted and non-weighted regression methods and between reweighted and non-reweighted methods for B1 configuration. Bolded figures represent the highest differences.

Area	OLS-WLS	RLS-RWLS	LAD-WLAD	OLS-RLS	WLS-RWLS
FD1	0.15	0.03	0.11	**1.04**	**1.22**
FD2	0.16	0.03	**0.32**	0.02	0.16
PH	0.10	0.03	0.08	0.01	0.08
QP1	**0.47**	**0.22**	**0.23**	**1.29**	**1.05**
QP2	**0.69**	**0.32**	0.09	**1.96**	**1.59**
NJ	**0.28**	0.17	0.01	**1.25**	**0.80**
BJ	0.16	0.05	0.17	**0.43**	0.33
SJ	0.05	0.05	0.03	0.28	0.19
PR	0.01	0.02	0.01	0.16	0.13
LM	0.02	0.05	0.15	**0.43**	**0.40**

The influence of removing some shorelines (especially the 1956 shoreline) can be tested in OLS-RLS and WLS-RWLS comparisons (Table 4.22). The results varied deeply when reweighted regression was applied, being the estimated rates much smaller when outliers were removed. In fact, reweighted methods trended to perform erosion rates much smaller and even accretion was estimated for the QP1 area when RWLS was applied (+0.08 m/yr). This effect was due to the fact that the 1956 shoreline was always removed and 2009 and 2011 high accurate shorelines contributed with a high weight on the rate estimation. In the case of QP1 area, the

sand nourishment performed in 2001 (DEM-derived shoreline) had also a significant effect since produced an artificial and temporal accretion but the shoreline was also high accurate.

The areas in which differences among regression methods were smaller were FD2, PH, SJ, BJ, PR, and LM. The rest of the areas, that is FD1, QP1, QP2, and NJ, were affected by estimating 1956 shoreline as outlier (reweighted methods) or overweighting the more recent shorelines. Moreover, natural morphological behaviour had an important effect for FD1, where sediment migration from the near delta shaped up a more curved coastline (change observed between 1988 and 1998). Thus, non-linear but natural behaviour also affected the estimated rates.

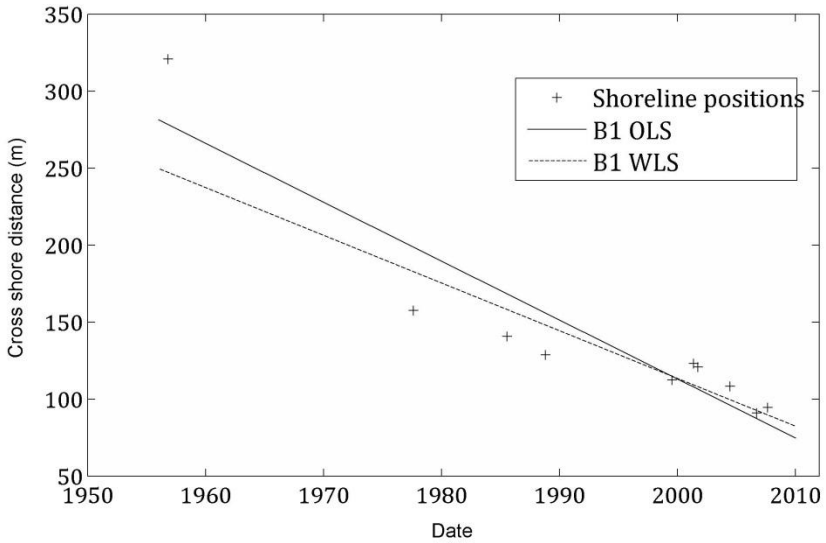

Figure 4.26. OLS and WLS comparison for the area QP2. Note the slight shoreline change rate reduction when weights were applied.

Regarding the B2 configuration, it should be noted that a very short-term shoreline evolution was assessed and some of the methods tested were not able to be estimated since only three shorelines were available (2008, 2009, and 2011). For instance, reweighted methods were not applicable to areas FD1, FD2, and NJ because of regression cannot be computed when one shoreline had to be removed. Moreover, the time span was too little to estimate a change in the estimated rates as compared to B1 configuration. However, this short-term changes could help to understand the shoreline adaptation to the new situation derived from the jetties installation. For instance, it seems to set out an accretion process for the FD1 and FD2 areas due to the previously mentioned sand migration process. Furthermore, the PH area was confirmed as a no-change zone while for B1 configuration a clear

medium-term erosion rate was estimated. In this way, the erosion trend observed in *Quitapellejos* beach (QP1 and QP2) was confirmed despite the large sand volume poured on this area in 2008. However, a subtle change on trend was found in NJ, BJ, and SJ areas in which erosive process turned to be accretion from 2008. That fact highlighted the main alongshore sediment transport direction and the effect of retaining the sediment by means of both jetties. Finally, an important accretion process was detected in LM area, probably due to the effect of the *Garrucha*'s harbour main dock which worked as a true barrier with respect to the natural alongshore flow, therefore accumulating the sediment at the South edge of the coastal cell.

Reducing the number of shorelines

It has been proved that one of the main problems when linear regression is applied for shoreline change rates estimation is related to the overweighting due to the concentration of highly accurate shorelines in the last years of the analysed period. Then, a test based on two additional configurations C1 and C2 involving seven (1956, 1977, 1984, 1988, 1998, own-produced 2001, and 2007) and eight (C1+2011) shorelines, respectively, has been carried out. Those configurations were supposed to be analogous to B1 (all possible shorelines until 2007) and A2 (all possible shorelines) configurations.

Regarding the influence of the weighted and reweighted based methods, it should be highlighted that the results for C1 were similar to the B1 ones and also between C2 and A2. Therefore, weighted methods still made the rates smaller (except for RWLS if compared with RLS) and reweighted methods also had the same effect.

It was also interesting to know about the differences between C1 and C2, determining the influence of the last shoreline (2011). Firstly, it should be noted that those differences were smaller than the differences between A2 and B1 configurations, especially for RLS and WRLS methods, indicating that the overweighting effect could be solved by means of these methods. Secondly, important differences between C1 and C2 existed when WLS and WLAD were considered (Table 4.23). Those results were due to the high accuracy of the 2011 shoreline which trended to reduce the computed erosion rate. Otherwise, RLS and LAD yielded the most similar results although some areas presented important differences yet.

When C1 and C2 configurations were faced against their respective homologous B1 and A2 configurations, some interesting results came up. Firstly, differences between C1 and B1 reflected a good agreement between both configurations (Table 4.24) except for FD1 and FD2 areas, in which reweighted methods resulted highly sensitive to those shorelines considered as outliers.

Table 4.23. Absolute differences between configurations C1 and C2 in m/yr. Bold figures indicates the highest differences.

Area	OLS	WLS	RLS	RWLS	LAD	WLAD
FD1	0.20	**1.29**	0.21	**0.43**	0.00	**1.76**
FD2	0.09	**0.53**	**0.35**	**0.40**	0.09	**0.79**
PH	0.04	0.16	0.03	0.13	0.05	0.12
QP1	0.24	**0.61**	0.07	0.06	0.26	0.17
QP2	**0.43**	**1.19**	0.24	0.26	0.11	**0.67**
NJ	**0.58**	**2.05**	0.28	**0.52**	0.28	**2.18**
BJ	**0.43**	**1.78**	0.03	0.07	**0.38**	**2.21**
SJ	0.11	**0.40**	0.04	0.07	0.07	**0.40**
PR	0.05	0.23	0.10	0.14	0.01	0.23
LM	0.09	0.09	**0.43**	**0.42**	0.11	0.10

Table 4.24. Absolute differences between configurations C1 and B1 in m/yr. Bold figures indicates the highest differences.

Area	OLS	WLS	RLS	RWLS	LAD	WLAD
FD1	0.19	0.28	**0.40**	**0.47**	0.12	**0.37**
FD2	0.01	0.03	**0.44**	**0.51**	0.01	0.25
PH	0.02	0.00	0.21	0.11	0.00	0.03
QP1	0.13	0.03	0.09	0.12	0.12	0.07
QP2	0.23	0.08	0.08	0.14	0.08	0.01
NJ	0.17	0.08	0.09	0.13	0.05	0.05
BJ	0.07	0.03	0.20	0.21	0.17	0.01
SJ	0.08	0.05	0.09	0.04	0.10	0.06
PR	0.06	0.05	0.16	0.14	0.08	0.03
LM	0.01	0.07	0.24	0.20	0.00	0.10

If differences between those configurations which included the entire time span are considered (C2 and A2, see Table 4.25), it is worth noting that larger differences than the previous C1-B1 comparison were attained. However, those differences were generally lower than those yielded between B1 and A2 configurations, both thought to determine medium-term shoreline change rates. The main differences were observed in the case of RWLS method since only one high accurate shoreline (2011) and less number of recent shorelines were included. That fact contributed to the oldest shoreline position (1956) was

estimated as outlier much less frequently, leading to computed erosion rates much more intense.

Table 4.25. Absolute differences between configurations C2 and A2 in m/yr. Bold figures indicates important differences.

Area	OLS	WLS	RLS	RWLS	LAD	WLAD
FD1	0.12	0.01	**0.38**	0.09	0.23	0.16
FD2	0.03	0.02	**0.68**	**0.99**	0.01	0.19
PH	0.02	0.01	0.01	0.03	0.02	0.06
QP1	**0.40**	**0.41**	0.04	**0.42**	0.06	0.25
QP2	**0.62**	**0.52**	0.01	**0.51**	0.26	**0.64**
NJ	0.33	0.27	0.14	**1.72**	0.35	0.14
BJ	0.01	0.08	0.19	**2.05**	0.10	**0.31**
SJ	0.15	0.10	0.10	0.28	0.18	0.00
PR	0.03	0.07	0.13	0.02	0.11	0.09
LM	0.30	0.21	0.05	0.28	0.19	0.22

Discussion on the rates variability

In the results previously presented, a high variability on the estimated rates was found and four variables were discussed: (i) the time span used for medium-term change rate estimation (1956-2007 vs. 1957-2011 based on the highly influence human intervention in 2007), (ii) the number of shorelines used (all the available shorelines vs. a better time-spaced shorelines), (iii) the influence of using weighted data based on the corresponding shoreline accuracy, and (iv) the influence of considering some shorelines as outliers (therefore not all the shorelines are included in the change rate assessment).

The main goal of this study was to develop an efficient method to determine the underlying medium-term shoreline movement trend in order to estimate future shoreline position or determine erosion hazard vulnerability along the coastal area under study. The high variation on estimated shoreline change rates gave a clear idea about how difficult was the determination of the most appropriate regression method. Regression methods generally suppose linear behaviour regarding shoreline change, but this fact may not match quite well the actual data. For instance, the high grade of human intervention in this coastal cell (see *Human factors affecting the study site area section*) clearly indicated that the natural erosion/accretion processes were probably masked.

With regard to the time span used for shoreline evolution assessment, complete time-span configurations (A1, A2, and C2) generally yielded similar results except when applying reweighted methods. Otherwise, if non-complete time-span is considered (B1 and C1), results were highly similar except for some areas when using RWLS and RLS methods since different shorelines were considered as outliers. In general, previous research has proved that, because of the variability in the data, the longer the temporal span of the data, the lower the uncertainty of the long-term trend (Honeycutt, Crowell & Douglas 2001, Douglas, Crowell & Leatherman 1998). In this sense, a minimum time span of 100 years has been recommended to estimate long-term rates (Crowell, Douglas & Leatherman 1997). Therefore, and owing to no older data were available for our coastal area, medium-term rates had to be considered in this work (Jiménez, Sánchez-Arcilla 1993).

Focus on the number of shorelines, RWLS and RLS methods were especially affected by the overweighting effect since too many shorelines were concentrated into the most recent decades. Having available evenly distributed shorelines has been previously recommended for long-term shoreline rate estimation (Dolan, Fenster & Holme 1991, Genz et al. 2007, Bowman, Pranzini 2008). However, the number of shorelines used for carrying out the calculation affected the shoreline change rate estimation. In fact, it has been proved that making predictions of future shoreline position based on small number of temporal samples cannot be expected to yield accurate results (Douglas, Crowell & Leatherman 1998). The number of shorelines actually involved in the calculation was affected when applying the RLS and RWLS methods since they can remove some observations. One of the most frequently removed shoreline was the 1956 one due to the fact that the 1956-1977 time span did not follow the general linear-trend because more intensive erosion was registered during this period. However, some researchers have found that the oldest data can play a key role for long-term shoreline rate estimation, especially when few old shorelines are included and that oldest position also helps to constrain estimates of shoreline location into the future (Douglas, Crowell & Leatherman 1998, Honeycutt, Crowell & Douglas 2001).

Regarding considering some positions as outliers, it emerges the question about whether shorelines should be considered as anomalous or not since significant differences can appear when using reweighted methods. For areas FD1 and FD2, the historical sand migration made the shoreline position to move differently over the years and the shoreline positions should not be targeted as outliers but highly noise data from which a larger time span could reflect better the general trend. However, outliers removal was positive for finding the underlying trend for A2 and C2 configurations in which most recent shorelines were removed in the human-influenced areas since they did not follow that trend. Therefore, the need of outlier detection depended on the study area. In previous studies, some discussion have been done about including this kind of observations

or not, mainly referred to storm events. Some researchers stated that those shorelines should be removed from the regression by having a prior knowledge about storm events (Douglas, Crowell & Leatherman 1998, Douglas, Crowell 2000) and even removal of storm-specific shorelines has been considered one of the most important factor in improving erosion forecasts (Honeycutt, Crowell & Douglas 2001). Thus, these events are considered as inconsistent for long-term evolution which is supposed to be dependent on SLR or variation in sediment supply. Furthermore, beaches are usually recovered over the next years to decades (Douglas, Crowell 2000, Bowman, Pranzini 2008). Otherwise, other authors have determined that some coastal areas can be considered as storm-influenced and those shoreline positions should not be removed because they are part of the entire signal (Fenster, Dolan & Morton 2001).

In this study two types of outliers can be found. First, natural outliers occurred when a natural shoreline position did not match the estimated medium-term trend. That was the case for 1956 shoreline in many transects since the 1956-1977 erosion was much higher than the erosion observed from then on. In other works, oldest positions were only inconsistent with the general trend where beach nourishment or different geologic or sedimentary processes appear (Honeycutt, Crowell & Douglas 2001). This matched with different factors affecting this study area such as a drastic reduction of sediment supply (see *Climatic considerations* subsection within *Study site* section) and a significant sand nourishment undertaken in 2007. Both facts were supposed to influence for pointing out the 1956 shoreline as an outlier. Second, artificial outliers turned up when the shoreline position was influenced by human interventions. Here, the jetties installation and the sand nourishment done in 2007 made that newer shorelines did not follow the general trend in some areas afterwards that intervention (at least in a short-time period). For some authors, artificial physical changes can make data at prior epochs to be misleading (Crowell, Douglas & Leatherman 1997) and then, quasiperiodic nature must be considered in evaluating the forecast (Douglas, Crowell & Leatherman 1998). In fact, simple linear regression has been considered appropriate only for shorelines unaffected by inlets or engineering changes (Galgano, Douglas & Leatherman 1998). However, it is understood that the medium-term erosion trend affecting the area prior to the 2007 human intervention can still determine the general erosive trend existing on the study area and the effect of the artificial influence should be performed in the future based on that previous medium-term trend.

Determining the most suitable shoreline change rate method

The confidence interval (CI) was estimated for the estimated change rate in every transect ($p<0.05$) and the mean value for every group was also assessed by using every shoreline configuration. CIs were directly estimated as a secondary

result of the regression applied by means of the same software (MATLAB®). In other works, error in prediction (EIP) has been used in other works to determine the most suitable shoreline change rate method by means of comparing an extrapolated shoreline (based on the estimated rates) with an actual shoreline (Honeycutt, Crowell & Douglas 2001, Genz et al. 2007). Here, the time span utilized, the fact that most of the shorelines were recent, and the high degree of human intervention made difficult to use one of the available shorelines as a reference for EIP assessment. Therefore, CI was carefully used to determine the most suitable shoreline change rate method (Table 4.26). Results showed that configuration and, especially, the applied change rate estimation method had an important effect on CIs. It was highlighted that reweighted methods (RLS and RWLS) achieved the lowest CIs for B1, C1, and C2 configurations, while RLS yielded significantly lower CIs for A1 and A2. The reduction of the CI when outliers are removed was also demonstrated by Douglas, Crowell (2000). Again, the effects of overweighting came up for RWLS when high accurate and recent-time gathered shorelines were used (A1 and A2), while the results between RLS and RWLS were similar when either not recent shorelines were included (B1 and C1) or just one high accurate shoreline was enclosed (C2). Regarding the configuration used, it was clear that B1 yielded the less CI for every regression method because it did not enclose recent shorelines (as compared to A1 and A2) and the number of shorelines involved in the calculation were larger (as compared to C1 and C2 configurations).

Table 4.26. Averaged IC results (± m/yr) for the different regression methods tested and every configuration. Results from LAS and WLAS were not included since they were similar to OLS and WLS.

	A1	A2	B1	C1	C2
IC_OLS	1.19	0.68	0.65	0.98	0.93
IC_WLS	1.73	0.91	0.76	1.09	0.84
IC_RLS	0.57	0.35	0.31	0.37	0.37
IC_RWLS	1.45	0.85	0.31	0.36	0.32

According to these results, RLS or RWLS could be the shoreline change rate estimation method to choose. In this way, the outlier removal seemed to be a key stage to improve shoreline change rates accuracy. Moreover, B1, C1, and C2 configurations yielded similar results for both methods (A2 was also similar by using RLS but not RWLS). In general, and bearing in mind that shoreline accuracy must be included in the analysis, the largest time span should be also taking into account, shorelines should be evenly distributed, and anomalous shoreline position (outliers) could exist, RWLS method over C2 configuration should be finally chosen (results shown in Table 4.27). In fact, this combination embraced

the entire 1956-2011 period with less-gathered and weighted shoreline positions. Human-altered positions of 2011 (jetties and *Quitapellejos* areas) and non-linear trend estimated for 1956 (high intense erosion occurred in 1956-1977 period was later apparently mitigated) were treated as outlier for most of the transects in QP1, QP2, NJ, and BJ areas.

Table 4.27. Shoreline change rates results for RWLS and C2 configuration (i.e. from 1956 to 2011). Rates are expressed in m/yr, while the standard deviation and CI are in ±m/yr. R^2 represent the coefficient of determination.

Area	Mean rate	Std. dev. rate	Mean CI	Std. dev. CI	Mean R^2
FD1	-0.56	0.87	0.42	0.22	0.61
FD2	-1.98	0.50	0.15	0.13	0.99
PH	-1.38	0.83	0.15	0.06	0.92
QP1	0.14	0.18	0.24	0.11	0.40
QP2	-0.87	0.27	0.48	0.16	0.74
NJ	-2.10	1.05	0.71	0.13	0.78
BJ	-2.60	0.36	0.44	0.14	0.97
SJ	-0.91	0.61	0.16	0.09	0.88
PR	0.34	0.39	0.20	0.12	0.69
LM	0.68	0.77	0.30	0.12	0.65

Previous results contrasted with those found by Genz et al. (2007) from which OLS, RLS, WLS, RWLS, LAD, and WLAD evaluated by EIP were not different each other when synthetic data were used. However, they stated that weighted method were preferred when major uncertainties are known, underlining that reweighted methods should be used when storms effects (outlier positions) are hard to identify. The determination of the most suitable method and configuration combination through the CI can have some limitations and further research should be carried out to estimate EIP for some future shoreline in order to validate the estimated rates. Moreover, some results could be inconsistent if linear shoreline migration was considered. For instance, the area QP1 yielded a mean R^2 too small, indicating that linear trend did not exist in this area. Here, two errors can be committed: first, the evolution trend is supposed to be linear although some shorelines have been proved not to change uniformly (Bowman, Pranzini 2008); and second, the reweighted methods were not capable to eliminate the outliers positions and large errors were introduced into the long-term determination (Honeycutt, Crowell & Douglas 2001). In fact, the previous knowledge of climatology and engineering history was recommended to be taken into account since non-linear components are likely to be critical factors controlling short-term

shoreline change (Galgano, Douglas & Leatherman 1998, Honeycutt, Crowell & Douglas 2001, Bowman, Pranzini 2008). Additionally, some transects could lead to irrelevant change rate since the CI can be even larger than RWLS rate. However, that occurred much more frequently when OLS or WLS were applied since outliers significantly increased the yielded CI.

CONCLUSIONS

In this Chapter, the long as possible term for shoreline change rate was assessed in a Mediterranean coastal area by means of a set of shorelines from multitemporal/multisource georeferenced data. Thus, digitized shorelines from orthoimages have been used together with automatically-derived shorelines from CEMs (both extrapolated 0 m contour level and a stable contour level of 0.75 m). Therefore, two different kinds of shoreline indicators were used: HWL and datum-based shorelines. Comparison between both kinds of indicators proved that HWL can lead to more inaccurate erosion/accretion rates since it can be highly variable because of natural hydrodynamic. Moreover, non-extrapolated datum based indicators (e.g. 0.75 m contour level) was found more suitable than the extrapolated one for shoreline extraction due to the frequent mismatching between the gradient used for extrapolation and the actual one.

Regarding the shoreline accuracy assessment, natural phenomena was found as the most influent source of uncertainty mainly because of the difficulties to precisely estimate the wave runup previously detected by the comparison between HWL and 0.75 m contour level shoreline indicators. Therefore every digitized shoreline was assigned similar uncertainty regardless its spatial resolution or positional accuracy. The estimation of shoreline accuracy for both indicators allowed to evaluate what indicator to be used, either HWL or 0.75 m contour level. HWL was only used for the oldest photogrammetric dataset and all the non-own-produced orthoimages (taken from an official spatial data infrastructure), while contour-based shoreline was chosen for all the others photogrammetric and LiDAR derived-CEMs, demonstrating that digitized shorelines are more accurate than CEMs-derived ones only for very old and small scale images (usually archival aerial flights).

When evolution of shoreline changes over the time span used in the calculation was studied, it was found that the changes were highly variable. It was also clear that the coastal evolution in this cell was controlled by the sediment-supply and the wave action along. Thus, it was proved that alongshore sediment transport played a key role in sediment migration towards the South. Additionally, the most eroded areas match with those that were more angled with respect to the incident dominant wave approaching direction (a local climate variable). Finally, the estimation of changes was highly difficult to assess since several human

impacts (different sand extractions and sand nourishments, jetties installation, and so on) have been done over the years.

In order to analyse the underlying medium-term shoreline change rate, the most common regression methods were used to adapt a linear trend for every transect. Non-weighted, weighted and reweighted methods were tested regarding whether shorelines accuracy was included or not and whether outliers detection was performed or not. Six different sets of shorelines were used to test the influence of some parameters in shoreline change rate assessment. Thus, it was tried to find out the effect of the major human intervention (jetties installation), whether SDI shorelines are used or not, how evenly the shorelines would have to be, and how the time span used affects the estimated shoreline rates.

When all shorelines were included, overweighting effect turned up due to most of the extracted shorelines acquired from recent years and rates became smaller than when the shorelines were more regularly distributed over time. In general, reweighted methods (RLS and RWLS) trended to work quite well when the entire time span was considered and the shorelines were more evenly distributed since human-induced outlier shoreline positions, but also natural outliers, were able to be removed from the analysis. Moreover, reweighted methods yielded the lowest CIs for estimated rates. Finally, RWLS was recommended for medium-term shoreline change rate assessment together with an evenly distributed set of shorelines that includes the entire time span for some reasons: RWLS method seemed to be able to remove out of trend shoreline points, overweighting effects are avoided, and no artificial division of the time span has to be done.

Finally, the medium-term shoreline change rate results matched with those observed in the evolution over time. Net erosion was estimated for northern areas (*Villaricos, Fábrica del Duro, Punta Hornicos, Quitapellejos,* and *El Playazo*), while stable and accretion areas were observed at middle (*Puerto Rey*) and southern areas (*Las Marinas*) respectively. According to Bowman, Pranzini (2008), erosion can be classified as extreme (>1 m/yr) for many of the tested coastal areas, reaching up to a rate of -2.60 m/yr in an area of *El Playazo*.

FURTHER WORK

Although a general erosive trend has been stated in the study area, some tasks remain and deserve to be carried out for a complete understanding of its shoreline behaviour. First, it is recommended to perform a complete sediment budget study to take into account all the possible sources, sinks and reservoirs. That would enable to take the necessary medium-term measures by coupling this sediment budget and the estimated shoreline trend. Additionally, the *Palomares* canyon should be proved as the sediment sink that it is supposed to be by means of, for example, a bathymetric monitoring of sedimentary processes around the sea bed

of the canyon. This could complete the sediment budget by identifying it as the main sediment sink of the coastal cell.

Regarding the shoreline change rate assessment, binning methods should be tested in order to remove the intrinsic alongshore variability of the rates. Thus, groups of transects should be automatically done and even the CIs of those rates will be improved by means of using much more shoreline positions (Genz et al. 2007, Frazer, Genz & Fletcher 2009). Additionally, polynomial methods which include some non-linear shoreline behaviour and acceleration in the evolution could be also tested in order to be able to predict short-term shoreline evolution (Romine et al. 2009, Romine, Fletcher 2013).

The digitized shorelines accuracy must be refined by calculating more in detail seasonal, tidal, and especially runup uncertainties, since they constituted the main source of uncertainty for this kind of shoreline. Additionally, it is recommended to develop a method to describe digitizing uncertainty by means of more than just one operator.

Finally, the results presented here should be confirmed in the future through the extraction of newest shoreline positions for coping with a reliable medium-term shoreline evolution forecasting. To do that, error in prediction (EIP) should be achieved by comparing forecast shoreline positions and actual ones. Lastly, the erosive patterns should be carefully assessed in the defensive structures installed to stop those processes in order to check their influence on the shoreline stability.

REFERENCES

Aguilar, F.J., Agüera, F. & Aguilar, M.A. 2007, "A theoretical approach to modeling the accuracy assessment of digital elevation models", *Photogrammetric Engineering and Remote Sensing,* vol. 73, no. 12, pp. 1367-1379.

Alberico, I., Amato, V., Aucelli, P.P.C., D'argenio, B., Di Paola, G. & Pappone, G. 2012, "Historical shoreline change of the Sele Plain (Southern Italy): The 1870-2009 time window", *Journal of Coastal Research,* vol. 28, no. 6, pp. 1638-1647.

Anders, F.J. & Byrnes, M.R. 1991, "Accuracy of shorelines change rates as determined from maps and aerial photographs.", *Shore & Beach,* vol. 59, no. 1, pp. 17-26.

Boak, E.H. & Turner, I.L. 2005, "Shoreline definition and detection: A review", *Journal of Coastal Research,* vol. 21, no. 4, pp. 688-703.

Bowman, D. & Pranzini, E. 2008, "Shoreline monitoring: review and recommendations", *Beach erosion monitoring. Results from BEACHED-e / OpTIMAL Project,* , pp. 15-24.

Brommer, M.B. & Bochev-Van Der Burgh, L.M. 2009, "Sustainable coastal zone management: A concept for forecasting long-term and large-scale coastal evolution", *Journal of Coastal Research,* vol. 25, no. 1, pp. 181-188.

Carau, C. 1981, "Hacia una valoración del papel que juegan los condicionantes de caudales sólidos en la estabilidad de una playa.", *Revista de obras Públicas,* vol. 3192, pp. 343-360.

Cowell, P.J., Stive, M.J.F., Niedoroda, A.W., De Vriend, H.J., Swift, D.J.P., Kaminsky, G.M. & Capobianco, M. 2003, "The Coastal-Tract (Part 1): A Conceptual Approach to Aggregated Modeling of Low-Order Coastal Change", *Journal of Coastal Research,* vol. 19, no. 4, pp. 812-827.

Crowell, M., Douglas, B.C. & Leatherman, S.P. 1997, "On forecasting future U.S. Shoreline positions: A test of algorithms", *Journal of Coastal Research,* vol. 13, no. 4, pp. 1245-1255.

Crowell, M., Leatherman, S.P. & Buckley, M.K. 1993, "Shoreline change rate analysis: Long-term vs. short-term data.", *Shore and Beach,* , no. April, pp. 13-20.

Dolan, R., Fenster, M.S. & Holme, S.J. 1991, "Temporal Analysis of Shoreline Recession and Accretion", *Journal of Coastal Research,* vol. 7, no. 3, pp. pp. 723-744.

Douglas, B.C. & Crowell, M. 2000, "Long-term shoreline position prediction and error propagation", *Journal of Coastal Research,* vol. 16, no. 1, pp. 145-152.

Douglas, B.C., Crowell, M. & Leatherman, S.P. 1998, "Considerations for shoreline position prediction", *Journal of Coastal Research,* vol. 14, no. 3, pp. 1025-1033.

Espinosa, V. & Rodríguez, I. 2009, "Evolución costera del tramo comprendido entre San Juan de los Terreros y playas de Vera (Almería)", *Revista de la Sociedad Geológica de España,* vol. 22, no. 1-2, pp. 3-12.

European-Commission, E. 2009, *The economics of climate change adaptation in EU coastal areas. Final report.*, Directorate-General for Maritime Affarirs and Fisheries, Brussels.

European-Commission, E. 2004, *Living with coastal erosion in Europe - Sediment and Space for sustainability. Part I - Major findings and policy recommendations of the EUROSION project.*, Office of official publications of the European communities, Luxembourg.

Fenster, M.S., Dolan, R. & Elder, J.F. 1993, "A new method for predicting shoreline positions from historical data", *Journal of Coastal Research,* vol. 9, no. 1, pp. 147-171.

Fenster, M.S., Dolan, R. & Morton, R.A. 2001, "Coastal storms and shoreline change: Signal or noise?", *Journal of Coastal Research,* vol. 17, no. 3, pp. 714-720.

Fletcher, C., Rooney, J., Barbee, M., Lim, S.-. & Richmond, B. 2003, "Mapping Shoreline Change Using Digital Orthophotogrammetry on Maui, Hawaii", *Journal of Coastal Research,* , no. SPEC. ISS. 38, pp. 106-124.

Frazer, L.N., Genz, A.S. & Fletcher, C.H. 2009, "Toward parsimony in shoreline change prediction (i): basis function methods", *Journal of Coastal Research,* vol. 25, no. 2, pp. 366-379.

Galgano, F.A. & Douglas, B.C. 2000, "Shoreline position prediction: Methods and errors", *Environmental Geosciences,* vol. 7, no. 1, pp. 23-31.

Galgano, F.A., Douglas, B.C. & Leatherman, S.P. 1998, "Trends and variability of shoreline position", *Journal of Coastal Research,* vol. S.I., no. 26, pp. 282-291.

Genz, A.S., Fletcher, C.H., Dunn, R.A., Frazer, L.N. & Rooney, J.J. 2007, "The predictive accuracy of shoreline change rate methods and alongshore beach variation on Maui, Hawaii", *Journal of Coastal Research,* vol. 23, no. 1, pp. 87-105.

Hapke, C.J., Reid, D., Richmond, B., Ruggiero, P. & List, J. 2006, *National assessment of shoreline change: Part 3: Historical shoreline changes and associated land loss along the sandy shorelines of the California coast*, U.S. Geological Survey Open-File Report.

Honeycutt, M.G., Crowell, M. & Douglas, B.C. 2001, "Shoreline-position forecasting: Impact of storms, rate-calculation methodologies, and temporal scales", *Journal of Coastal Research,* vol. 17, no. 3, pp. 721-730.

Honeycutt, M.G. & Krantz, D.E. 2003, "Influence of the Geologic Framework on Spatial Variability in Long-Term Shoreline Change, Cape Henlopen to Rehoboth Beach, Delaware", *Journal of Coastal Research,* , no. SPEC. ISS. 38, pp. 147-167.

Jiménez, J.A. & Sánchez-Arcilla, A. 1993, "Medium-term coastal response at the Ebro delta, Spain", *Marine Geology,* vol. 114, no. 1-2, pp. 105-118.

Maiti, S. & Bhattacharya, A.K. 2009, "Shoreline change analysis and its application to prediction: A remote sensing and statistics based approach", *Marine Geology,* vol. 257, no. 1-4, pp. 11-23.

Marchand, M., Sanchez-Arcilla, A., Ferreira, M., Gault, J., Jiménez, J.A., Markovic, M., Mulder, J., van Rijn, L., Stânicâ, A., Sulisz, W. & Sutherland, J. 2011, "Concepts and science for coastal erosion management - An introduction to the Conscience framework", *Ocean and Coastal Management,* vol. 54, no. 12, pp. 859-866.

Meikle, C. 2008, *The Pleistocene drainage evolution of the Río Almanzora, Vera Basin, SE Spain*, Newcastle University.

Meikle, C., Stokes, M. & Maddy, D. 2010, "Field mapping and GIS visualisation of quaternary river terrace landforms: An example from the rí o almanzora, SE Spain", *Journal of Maps,* vol. 2010, pp. 531-542.

Moore, L.J. 2000, "Shoreline mapping techniques", *Journal of Coastal Research,* vol. 16, no. 1, pp. 111-124.

Moore, L.J., Ruggiero, P. & List, J.H. 2006, "Comparing mean high water and high water line shorelines: Should prosy-datum offsets be incorporated into shoreline change analysis?", *Journal of Coastal Research,* vol. 22, no. 4, pp. 894-905.

Morton, R.A. & Miller, T.L. 2005, *National assessment of shoreline change: Part 2: Historical shoreline changes and associated coastal land loss along the U.S. Southeast Atlantic Coast.*, U.S. Geological Survey Open-file Report.

Morton, R.A., Miller, T.L. & Moore, L.J. 2004, *National assessment of shoreline change: Part 1: Historical shoreline changes and associated coastal land loss along the U.S. Gulf of Mexico.*, U.S. Geological Survey Open-file Report.

Ojeda, J., Vallejo, I., Hernández, L. & Álvarez, J. 2007, "Fotogrametría y LIDAR como fuentes de información en geomorfología litoral (marismas mareales y sistemas dunares): El potencial de su análisis espacial a través de SIG", *Boletín de la A.G.E.,* vol. 44, pp. 215-233.

Pajak, M.J. & Leatherman, S. 2002, "The high water line as shoreline indicator", *Journal of Coastal Research,* vol. 18, no. 2, pp. 329-337.

Pranzini, E. & Daniela, S. 2008, "Beach evolution monitoring: Surface variation analysis vs Transept based analysis", *Beach erosion monitoring. Results from BEACHED-e / OpTIMAL Project,* , pp. 25-31.

Puertos del Estado. Available: http://www.puertos.es/ [2013, 03/13].

Roelvink, D. & Reniers, A. 2012, *Advances in coastal and ocean engineering (vol. 12). A guide to modeling coastal morphology.* World Scientific Publishing, Singapore.

Romine, B.M. & Fletcher, C.H. 2013, "A summary of historical shoreline changes on Beaches of Kauai, Oahu, and Maui, Hawaii", *Journal of Coastal Research,* vol. 29, no. 3, pp. 605-614.

Romine, B.M., Fletcher, C.H., Frazer, L.N., Genz, A.S., Barbee, M.M. & Lim, S.-. 2009, "Historical shoreline change, southeast oahu, Hawaii; Applying polynomial models to calculate shoreline change rates", *Journal of Coastal Research,* vol. 25, no. 6, pp. 1236-1253.

Rosati, J.D. 2005, "Concepts in sediment budgets", *Journal of Coastal Research,* vol. 21, no. 2, pp. 307-322.

Rousseeuw, P.J. & Leroy, A.M. 1987, *Robust Regression and Outlier Detection,* John Wiley and Sons, New Jersey.

Ruggiero, P., Kaminsky, G.M. & Gelfenbaum, G. 2003, "Linking Proxy-Based and Datum-Based Shorelines on a High-Energy Coastline: Implications for Shoreline Change Analyses", *Journal of Coastal Research,* , no. SPEC. ISS. 38, pp. 57-82.

Ruggiero, P., Komar, P.D., McDougal, W.G., Marra, J.J. & Beach, R.A. 2001, "Wave Runup, Extreme Water Levels and the Erosion of Properties Backing Beaches", *Journal of Coastal Research,* vol. 17, no. 2, pp. pp. 407-419.

Ruggiero, P. & List, J.H. 2009, "Improving Accuracy and Statistical Reliability of Shoreline Position and Change Rate Estimates", *Journal of Coastal Research,* vol. 25, no. 5, pp. 1069-1081.

Sánchez-Arcilla, A., Jiménez, J.A. & Marchand, M. 2011, "Managing coastal evolution in a more sustainable manner. The Conscience approach", *Ocean and Coastal Management,* vol. 54, no. 12, pp. 951-955.

Sanò, M., Jiménez, J.A., Medina, R., Stanica, A., Sanchez-Arcilla, A. & Trumbic, I. 2011, "The role of coastal setbacks in the context of coastal erosion and climate change", *Ocean and Coastal Management,* vol. 54, no. 12, pp. 943-950.

Schwartz, M.L. 2005, *Encyclopedia of Coastal Science*, Springer, Dordrecht, The Netherlands.

Senciales, J.M. & Malvárez, G. 2003, "La desembocadura del Río Vélez (Provincia de Málaga, España). Evolución reciente de un delta de comportamiento

mediterráneo.", *Revista cuaternario y geomorfología,* vol. 17, no. 1-2, pp. 47-61.

Stockdon, H.F., Holman, R.A., Howd, P.A. & Sallenger Jr., A.H. 2006, "Empirical parameterization of setup, swash, and runup", *Coastal Engineering,* vol. 53, no. 7, pp. 573-588.

Stockdon, H.F., Sallenger Jr., A.H., List, J.H. & Holman, R.A. 2002, "Estimation of shoreline position and change using airborne topographic lidar data", *Journal of Coastal Research,* vol. 18, no. 3, pp. 502-513.

Stokes, M. 2008, "Plio-Pleistocene drainage development in an inverted sedimentary basin: Vera basin, Betic Cordillera, SE Spain", *Geomorphology,* vol. 100, no. 1-2, pp. 193-211.

Stokes, M. & Mather, A.E. 2003, "Tectonic origin and evolution of a transverse drainage: The Río Almanzora, Betic Cordillera, Southeast Spain", *Geomorphology,* vol. 50, no. 1-3, pp. 59-81.

Thieler, E.R., Himmelstoss, E.A., Zichichi, J.L. & Ergul, A. 2008, *Digital Shoreline Analysis System (DSAS) version 4.0—An ArcGIS extension for calculating shoreline change.*, U.S. Geological Survey Open-File Report.

Uceda, A.C., Sánchez-Arcilla, A. & Cardeña, Z. 2005, "Chapter 11. Impacts on coastal areas" in *Impacts of climate change in Spain*, ed. J.M. Moreno-Rodríguez, Centro de Publicaciones. Ministerio Medio Ambiente, Madrid, pp. 451-504.

Viciana, A. 1996, "Problemática litoral derivada de la regulación hidrológica del Río Almanzora: El caso de la presa de Cuevas.", *Paralelo 37º,* vol. 17, pp. 31-47.

Virdis, S.G.P., Oggiano, G. & Disperati, L. 2012, "A geomatics approach to multitemporal shoreline analysis in western mediterranean: The case of platamona-maritza beach (Northwest Sardinia, Italy)", *Journal of Coastal Research,* vol. 28, no. 3, pp. 624-640.

White, S.A., Parrish, C.E., Calder, B.R., Pe'Eri, S. & Rzhanov, Y. 2011, "LIDAR-derived national shoreline: Empirical and stochastic uncertainty analyses", *Journal of Coastal Research, ,* no. SPEC. ISSUE 62, pp. 62-74.

CHAPTER 5

Non-parametric object-based approaches to carry out impervious surface areas classification from archival aerial orthoimage and very high resolution satellite imagery

ABSTRACT

In order to map the impervious surfaces for a coastal area, three non-parametric approaches -Classification and Regression Trees, Nearest Neighbour (NN), and Support Vector Machines (SVM)- were applied to a dataset of very high resolution archival orthoimages which had poor radiometry, with only red, green and blue spectral information. An object-based image analysis was carried out and four feature vectors were defined as input data for the classifier: 1) red, green and blue spectral information plus four relative spectral indices; 2) Dataset 1 plus texture indices based on the grey level co-occurrence matrix (GLCM); 3) Dataset 1 plus texture indices based on the local variance; and 4) the vector defined by 1), 2) and 3). Two classification strategies were developed in order to identify the pervious/impervious target classes (aggregation of all the subclasses and binary classification). The separability matrix was used to present the statistical comparative results clearly and concisely. SVM achieved the highest accuracy through binary classification as well as it was the most efficient method. Then, this method was applied on two very high resolution orthoimages from GeoEye-1 and WorldView-2 satellites using similar feature sets than those applied to the archival orthoimage. The entire study area was independently classified by three subsets (using a pilot area training and an *ad hoc* training) and by means of the total training samples. All of the data sources were compared and an estimation of the appropriate number of samples was performed. Results showed that texture based on local variance was a valuable feature to improve classification accuracy. Furthermore, the influence of data source, training size, and training distribution was also proved.

Keywords: Archival orthoimages, GeoEye-1, WorldView-2, very high resolution (VHR), impervious surface area (ISA), nearest neighbour (NN), non-parametric classifiers, object based image analysis (OBIA), support vector machines (SVMs), texture features, training size, accuracy assessment

INTRODUCTION

Impervious areas are defined as anthropogenic features through which water cannot infiltrate into the soil (Thomas, Hendrix & Congalton 2003, Weng 2012) such as rooftops, pavements, roads, sidewalks, thus being a good indicator of the degree of urbanization in an area. The impervious surface areas (ISAs) influence the hydrology of a watershed and have an impact on the potential volume increase, duration, and intensity of runoff and also affect the quantity of groundwater and increase stormflow (Weng 2001). An often overlooked environmental problem which is caused by ISAs is the increase in runoff volume and discharge rate, in conjunction with non-point source pollution, which alter in-stream and riparian habitats (Gillies et al. 2003). Additionally, it increases the risk of erosion and habitat degradation. Those are the reasons why the percentage of ISA in a watershed is considered to be a basic indicator for the evaluation of non-point runoff and an estimate of the future available water quality (Gillies et al. 2003). Moreover, ISAs show different thermal properties compared to pervious ones (Slonecker, Jennings & Garofalo 2001, Weng 2012) since they retain more heat than natural surfaces and therefore the stream temperature could potentially increase up to 6.5 degrees Celsius (Schueler 1994). The percentage of impervious surface area in a watershed is frequently correlated with the health of the ecosystem which the stream flows through (Schueler 1994, Arnold Jr., Gibbons 1996). In this sense the ecosystem can be classified as stressed (up to 10% of the total surface area is impervious), impacted (between 11 and 25%) and degraded (more than 25%).

Taking into account all the aforementioned reasons, efficient techniques to accurately determine and map ISAs should be developed. In this context, a remote sensing approach offers an appropriate and efficient alternative to identify impervious/pervious surfaces instead of using other labour-intensive approaches such as manually digitising digital orthoimages (Slonecker, Jennings & Garofalo 2001, Brabec, Schulte & Richards 2002) or land surveying using GPS receivers. During the first decade of the 21st century, there has been an increase in studies related to both very high spatial resolution imagery and classification methods based on texture. According to Weng (2012), the considerations to keep in mind when implementing an ISAs classification using digital images are: 1) spatial resolution; 2) geometric characteristics of urban features; 3) spectral resolution; and 4) temporal resolution.

The very high spatial resolution of images from satellites such as IKONOS, QuickBird, GeoEye-1 or WorldView-2 have enabled the accurate classification of relatively small size elements and the suitable extraction of ISAs (Goetz et al. 2003, Zhou, Wang 2008, Lu, Weng 2009). Furthermore, the orthoimages acquired from airborne platforms are regularly produced by government programmes (e.g.,

National Plan of Aerial Orthoimage, Spain, or National Digital Orthophoto Program, USA) and constitute an archival data source which enables multitemporal land-use change studies and/or ISA detection (Miller, Nelson & Hess 2009) without the need for new data acquisition. While the current orthoimages usually include additional information such as the near infrared band (Thomas, Hendrix & Congalton 2003) or ancillary data (e.g., LiDAR data (Hodgson et al. 2003)), most of the archival orthoimages offered by the administration provide only information for the three regions of the visible spectrum red, green and blue (RGB). Additionally, archival images can have some artefacts, sometimes due to them not being carefully preserved. Therefore, since little spectral information is available, the identification of ISAs from archival orthoimages is challenging. In order to obtain accurate results, the use of additional or ancillary information from GIS databases or image data fusion is needed (Weng 2012). Moreover, contextual information and image texture analysis (Laliberte, Rango 2009) have been considered helpful. The development of an efficient and accurate ISAs classification method from very high spatial resolution RGB imagery would add value to the available archival data as a source of information for land-use change detection, coastal areas evolution, or urban monitoring. The comparison with the results obtained from very high resolution (VHR) satellite orthoimages by means of similar approaches can be essential to test the capability of these images to carry out this kind of tasks.

Since the spatial resolution of the orthoimagery derived from photogrammetric flights is usually very high (0.20 – 1 m), it is appropriate to use an OBIA (object-based image analysis) approach. Similarly, the VHR-satellite imagery from GeoEye-1 or WorldView-2 (0.5 m for PAN band) would lead to apply the same analysis, especially if both data sources are going to be compared. In fact, a higher local variance of urban land cover classes is found when the resolution of the input image is increased (Myint et al. 2011), and therefore, the accuracy of the traditional pixel-based classification approaches is reduced and the results could show a “salt and pepper” effect (Treitz, Howarth 2000, Pu, Landry & Yu 2011). Classification accuracy is particularly problematic in urban environments, which typically consist of mosaics of small features made up of materials with different physical properties. To overcome this problem, OBIA has been recognised as an approach that can help improve the performance of supervised classifiers (Carleer, Wolff 2006, Im, Jensen & Tullis 2008, Blaschke 2010, Lu, Hetrick & Moran 2010, Myint et al. 2011). In fact, OBIA is a new paradigm in the field of geographic information science in which images are segmented into meaningful segments (or objects) according to different criteria before classification is carried out. The OBIA methodology is based on aggregating similar pixels in order to obtain homogenous objects, which are then assigned to a target class. Using objects instead of pixels as a minimum unit of information minimizes the “salt-pepper” effect due to the spectral heterogeneity of individual pixels. Furthermore, and unlike traditional pixel-based methods which only use spectral information, object-based approach

can use shape, texture and context information associated with the objects and thus it has the potential to efficiently handle more difficult image analysis tasks. Moreover, this object-oriented approach enables the use of hierarchical classifications at different scales (Benz et al. 2004). In this way, the amount of available OBIA works is increasing rapidly and there are numerous empirical studies published in peer-reviewed journals which have provided sufficient evidence of the advantages of object-based classification over traditional pixel-based classification (Blaschke, Strobl 2001, Yan et al. 2006, Cleve et al. 2008, Im, Jensen & Tullis 2008, Lu, Hetrick & Moran 2010, Myint et al. 2011, Whiteside, Boggs & Maier 2011). A comprehensive review of the advantages and the disadvantages of using OBIA approach for image classification as well as the state of the art of these methods can be found in Blaschke (2010).

Taking into account all the aforementioned explanations regarding the application of OBIA methodology on high resolution images, the main goal of this work was to identify and map impervious and pervious surfaces of a coastal area using an OBIA approach and two types of very high resolution images: RGB archival orthoimages from a photogrammetric flight and two different VHR-satellite images such as GeoEye-1 and WorldView-2. All the data sources were used without any other ancillary information. Three non-parametric classification methods -Classification and Regression Trees (CART), Nearest Neighbour (NN) and Support Vector Machines (SVM)- were tested on the archival orthoimage in order to avoid assumptions about the distribution of the data. The three methods, which will be described in the following section, are widely known and used for image classification in remote sensing (Pal, Mather 2003, Lu, Weng 2007, Samaniego, Bárdossy & Schulz 2008, Mountrakis, Im & Ogole 2011). Furthermore, different features sets were used in the classification in order to determine the most suitable feature space. Then, and as a relevant contribution from this work, these non-parametric classifiers were tested for the classification of impervious surfaces on the archival orthoimage using two strategies: 1) a binary classification where pervious/impervious objects were directly classified; and 2) by defining and classifying subclasses (roads, rooftops, etc.) which were later on aggregated into the corresponding final pervious/impervious classes. Summing up, this study tried to find out the most appropriate combination of non-parametric classification method, feature set, and strategy in order to target pervious and impervious areas from VHR orthoimages, both RGB archival aerial orthoimages (which had poor radiometry and many artefacts due to poorly-preserved positives) and GeoEye-1 and WorldView-2 satellite imagery. Additionally, the influence of the training samples set was tested for every data source in terms of distribution, size, and the capability to expand local training to wider areas.

STUDY AREA AND DATASETS

Archival Orthoimage (ArO)

The classification approaches tested in this work were firstly applied to the archival RGB aerial orthoimages obtained from a photogrammetric flight carried out on April 9, 2001. The original photographs were acquired by the Coastal Board (Spanish Government) by using a RC30 (focal distance = 152.92 mm) analogical camera at an approximate scale of 1:5000. The relatively poorly-preserved positives which had poor radiometry and many artefacts (scratches, fingerprints, etc.) were digitised by a photogrammetric scanner resulting in a Ground Sample Distance (GSD) close to 0.10 m, with a resolution of 20 μm in the RGB channels (8 bits). The final RGB orthoimages were obtained through a standard digital photogrammetry process carried out with the software SOCET SET©, and the final spatial resolution, or GSD, was 0.20 m.

A high spatial variability in the radiometric values was detected. In fact, atmospheric haze variations, poor conservation of the original positives and, mainly, the so-called "hot-spot" effect, which makes most landscapes appear brighter when the viewing direction in the image gets closer to the lighting direction of the sun, are well-known sources of radiometric heterogeneities in aerial images (Chandelier, Martinoty 2009). Thus, since the orthoimagery was obtained from different aerial images which were radiometrically heterogeneous, the resulting orthoimages showed areas with different radiometry. It should be noted that a radiometric correction was not carried out on the images. This was not done so that the original digital numbers were preserved and because the input data required to perform an atmospheric correction were not available, which happens for most of the aerial archival data (Chandelier, Martinoty 2009). Moreover, relative or absolute atmospheric corrections were not required (Song et al. 2001), since the main goal of this work was not to estimate biophysical variables (where radiance and reflectance are needed), but to classify pervious and impervious areas using the digital numbers from the RGB bands as input. In order to take into account the radiometric heterogeneity, two radiometrically different areas (North and South) were identified in the study area, as shown in Figure 5.1. This kind of radiometrical irregularity is a common drawback of mosaicked archival or historical images, and suggests that the introduction of radiometrically independent features, (e.g. RGB ratios and texture indices) can be suitable for image classification (Pacirici, Solimini 2007, Chini et al. 2008). In order to overcome the radiometric artifact, the classification process should be independently applied to each of the radiometrically homogeneous areas, thus the study area was divided into two datasets.

Figure 5.7. Orthoimage corresponding to the central area of the study site.

Very High Resolution Satellite imagery

In order to classify ISAs in the study site, GeoEye-1 and WorldView-2 VHR-satellite images were tested apart from the previously described archival orthoimage (henceforth, both experiments will be referred to GE1 and WV2 for GeoEye-1 and WorldView-2 respectively). Therefore, three different data sources could be compared and the differences among them could be tested. The original ground sample distance (GSD) for GeoEye-1 imagery at nadir is 0.41 m for panchromatic band (PAN), while the GSD for multispectral (MS) product is 1.65 m. Otherwise, WorldView-2 has the ability to collect PAN and MS images with pixel size of 0.46 and 1.84 m, respectively. However, the final products from both satellites have to be down-sampled to 0.5 and 2 m for PAN and MS respectively for commercial sales, as a requirement levied by the U.S. Government. The main difference between those satellites is the number of bands available. While GeoEye-1 counts on the Near infrared (Nir) band in addition to the three color bands Red, Green and Blue (R, G, and B), WorldView-2 comprises all the previous ones and four additional bands which are Coastal Blue (CB), Yellow (Y), Red Edge (RE), and Near infrared-2 (Nir-2). Both images were acquired in August, 2011, with only nine days of difference such that no significance land-cover change can be supposed between both collections. Both satellites acquired the images under a similar off-nadir angle, being 8.5^0 for GeoEye-1 and 10.0^0 for WorldView-2. So no differences were expected for that reason either. One PAN orthoimage was performed using the rational polynomial coefficients (RPCs), refined with 7

accurate ground control points (GCPs) by means of a simple translation at the image space, and a high accurate LIDAR-derived DEM for both satellite images. The final $RMSE_{2D}$, evaluated on 48 independent check points (ICPs), was 0.41 m for GeoEye-1 and 0.46 m for WorldView-2. Therefore no differences in classification accuracies were expected due to image misallocation. A second orthoimage was generated for both satellites based on the pan-sharpened images with 0.5 m GSD and containing the spectral information gathered from the MS image (four or eight bands for GeoEye-1 or WorldView-2 respectively). The pan-sharpened orthoimage was obtained with the same resolution and accuracy as for the PAN one. For further and detailed information about the orientation of the sensor, orthoimage generation and quality assessment, the reader is referred to the previous works (Aguilar et al. 2012, Aguilar, Saldaña & Aguilar 2013a).

Study Area Subsets

Although the main goal was to find a suitable approach for the entire study area, a pilot area was first selected in order to carry out the initial tests. The chosen pilot area was located in the northern part of the image since it had a good representation of most of the land uses that were in the whole study area (e.g. sea, urban, agricultural, forest). The size of the pilot area was 162.5 ha, covering around 25% of the total area. The final workflow obtained from the pilot area for each data source was eventually tested on the entire image. The rest of the study area was divided into two additional regions because of the previously mentioned radiometric discontinuity in the Archival Orthoimage. Thus, the northern part of the study area (pilot area was not included) was identified as area A, and the southern part as area B (Figure 5.2). In order to validate the classification method, the spatial distribution of the target classes had to be taken into account. In this sense, the pilot area had a class distribution similar to the class distribution in area B (large percentage of urban area), while the non-urban class was the predominate class in area A. The entire study area was then equally separated into the same three subsets for both VHR-satellite images so that exactly the same areas were classified. Thus, the pilot area will be used for selecting the most suitable feature set while the other two areas will be utilized for testing the capability to achieve accurate results when the pilot area training (local training) is used. Finally, an *ad hoc* training samples set was extracted for both areas and for the three data sources in order to compare the accuracy results in this areas with respect to the pilot area training samples accuracy results.

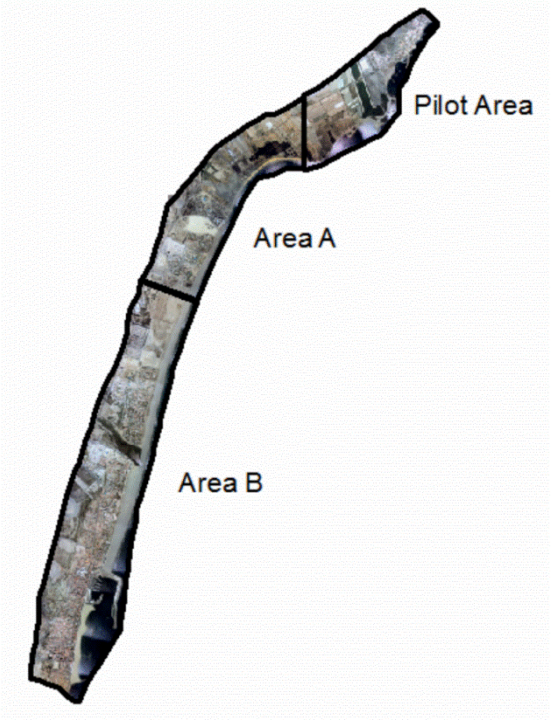

Figure 5.8. Distribution of the three study areas.

METHODS

Minimum Classification Unit

The analysis carried out in this study was based on the OBIA approach, so the object (a set of pixels which are homogeneous regarding certain features) constitutes the minimum classification unit and also the unit used for validation purposes. The segmentation algorithm used was the multiresolution segmentation (Benz et al. 2004) implemented in eCognition 8. This approach requires the following input data: 1) quantitative information (e.g. spectral bands) used for the segmentation and its weight on the process; and 2) scale, shape and compactness parameters. For a comprehensive explanation of the algorithm and parameters see Benz et al. (2004).

In the case of the Archival Orthoimage, the segmentation was carried out using the RGB digital numbers as inputs (same weight), a scale parameter of 50, and shape and compactness parameters of 0.3 and 0.7, respectively. The final values of the parameters were fixed after several tests, in order to select the combination of final segments which fits the actual field plots the best.

In the case of the VHR-satellite images, the segmentation was carried out on the pan-sharpened orthoimage (GSD = 0.5 m) by equally-weighting the corresponding multispectral bands, using the same shape and compactness parameters applied to the Archival Orthoimage and selecting the scale parameter to approximately maintain the same number of objects segmented in the ArO study. Thus, scales of 50 and 40 were used for GeoEye-1 and WorldView-2 experiments respectively. Both the same parameters and number of objects may assure that the possible accuracy differences due to the segmentation stage were minimised.

Classes to extract and classification strategies

The aim of this work was to classify pervious and impervious areas, which were identified as *target classes*. These two classes were not defined by their own spectral characteristics, so they were defined by spectrally homogenous land cover (*subclasses*), which were classified and added to the target classes according to their perviousness/imperviousness. A classification method which tried to identify each visually recognisable class was proposed and those classes were additionally aggregated according to their perviousness as a pervious or an impervious class. The description of the subclasses and the target class that they belong to are shown in Table 5.1.

Table 5.21. Target classes and corresponding subclasses. Number of training and validation samples used for the classification and accuracy assessment of the Pilot Area for ArO experiment.

Subclass	Target class	No. Training samples	No. Validation samples	No. Validation samples	No. Training samples
Dark sea	Pervious	23	35	455	143
Bright sea		23	31		
Individual trees		16	29		
Bare soil		20	72		
Scrubland		18	71		
Beach		20	68		
Cultivated agricultural field		9	67		
Non-cultivated agricultural field		4	31		
Forest		10	51		
Red building	Impervious	20	41	284	71
White building		6	28		
Gray building		4	19		
Road		13	51		
Path		8	24		
Harbour dam		2	22		
Sports court		1	5		
Swimming Pool		2	9		
Greenhouse		10	61		
Sidewalk		5	24		
Total sample size		214	739	739	214

Regarding the classification strategies workflow, two main approaches were carried out. The first one, which was called *Aggregation*, involved two steps: 1) classification of each subclass (land cover) using the different classification approaches; and 2) aggregation of each subclass to its corresponding target class, so the final classes were *Pervious* and *Impervious.* The second classification method was called *Direct Classification,* since the subclasses were not identified separately, and the two target classes were directly obtained by using the training samples corresponding to the land cover that was assigned to each target class. The aims of testing different classification strategies were to find out if there was any impact in the accuracy of the classification and if the impact depended on the considered algorithm. The strategies comparison was only performed for the ArO experiment since the results were supposed to be similar regardless of the data source used. Thus, if the accuracy results were dependent on the applied strategy, the most accurate one will be finally used for both VHR-satellite orthoimages. Finally, it is worth noting that choosing the most suitable strategy could result in minimising the effort to identify the training data required for the classification.

Features Tested for Image Classification

ArO experiment

Since the classification was based on image objects, the applied features were calculated for each object according to the pixels that formed the object. Each object was therefore characterised by using the RGB information. Unfortunately, valuable information commonly used in this sort of studies such as LiDAR data, GIS ancillary data, or vegetation indices which use the infrared part of the spectrum (e.g. Normalized Digital Vegetation Index (NDVI) or Soil-Adjusted Vegetation Index (SAVI)) were not available for their application. Nevertheless, additional features were calculated and used in the analysis. First, a simple set of ratios were derived from the original RGB bands in order to evaluate their potential as input features for the classification process. The computed features were: the green ratio (G/(R+G+B)), the red ratio (R/(R+G+B)), the blue ratio (B/(R+G+B)) and the green-red ratio (G/R). The green, red and blue ratios are three chromaticity colour transformations which provide additional spectral information. These transformations are useful for images where data are strongly correlated (e.g. RGB images, since correlations between blue, green and red digital numbers are often larger than 0.9), because they decorrelate the image so that the weakly correlated components of the data (i.e. the chromatic information) can be enhanced independent of the correlated intensity component (Gillespie, Kahle & Walker 1987). The use of the green-red ratio is based on the three groups of spectral patterns for major components of land cover which can be found by using the information provided by the green and red regions of the spectrum (Motohka et al. 2010). Thus, in the case of green vegetation, green reflectance is higher than red

reflectance (i.e. G/R > 1, expressed in digital numbers for archival aerial photographs), while for roofs or concrete, green reflectance is lower than red reflectance (i.e. G/R < 1). Regarding water or snow, green and red reflectance are similar (i.e. G/R = 1). Therefore the G/R index can be used as a surrogate of red-infrared ratio (R/IR) to distinguish vegetation from other land cover, and to differentiate types of vegetation (Gamon, Surfus 1999). Moreover, the use of band ratio images that include short wavelength bands has been proved to be effective for lithological mapping (Gad, Kusky 2006), since they contribute to suppress the topographic variation and the brightness difference related to grain size variation.

Moreover, texture features (e.g. variance) have been found to be essential in order to provide better results when very high spatial resolution orthoimages are used (Chen, Stow & Gong 2004). Texture features are considered to be more suitable than absolute radiometric values which can vary artificially along the entire data set, particularly when working with archival imagery (see Figure 5.1). Finding the most suitable texture indicator was beyond the scope of this work (for more information about finding the most suitable texture indicator, please refer to Agüera, Aguilar & Aguilar (2008) and Pacifici, Chini & Emery (2009)), so only two widely used texture measurements were tested. The first one was the local variance (Nagao, Matsuyama 1979), which was computed using a 7x7 window size using the formula:

$$Variance = \sum_{i=1}^{n} \frac{(DN_{x,y} - \overline{DN})^2}{n-1} \quad (5.1)$$

where $DN_{x,y}$ represents the digital number of the pixel located at row x and column y and $\overline{DN}$ being the mean digital number for the n=49 pixels that belong to the mobile window.

The window size was considered large enough to satisfactorily capture the textural patterns of the objects according to the land-use class that needed to be identified. The local variance was computed for each RGB band as a raster image and added to the feature space, so that the mean and the standard deviation could be calculated for each object.

The second type of texture feature was based on the Gray Level Co-occurrence Matrix (GLCM) descriptors available in eCognition, i.e., an object-based version of the original features proposed (Haralick, Shanmugam & Dinstein 1973). Among all of the available features, homogeneity and correlation were chosen since they have been tested and recommended by different authors. Homogeneity is considered one of the most suitable texture measurement that can be used to differentiate urban land uses (Clausi 2002, Herold, Liu & Clarke 2003), while correlation was suggested as one of the most suitable GLCM statistics (Clausi 2002, Yu et al. 2006). Furthermore, homogeneity and correlation are not linear dependent features (Baraldi, Parmiggiani 1995).

The computed features were grouped into different subsets or feature vectors (Table 5.2) in order to know the impact of the different features on the classifiers, as well as their performance for the whole classification process. Thus, the feature vector called Basic grouped the RBG bands into derived features including the mean value of each band and the four band ratios as previously described. The Basic feature vector including the band ratios was preferred over the simple RGB feature vector after comparing the results of using each one as input data, although RGB feature set was later used for comparison purposes regarding the satellite image classification accuracy. It was found that using the Basic feature provided a significantly better classification than that coming from only applying RGB bands (overall accuracy and Kappa) for two of the three classification methods that were tested (i.e. CART, NN), while for the other classifier (SVM) the differences were not statistically significant at a 95% confidence level.

Table 5.22. Feature vectors for ArO experiment.

Basic	Variance	GLCM	Total
Mean Red Mean Green Mean Blue Green Ratio Red Ratio Blue Ratio Green-Red Ratio	Basic +	Basic +	Basic +
7 features	Mean Variance Red Mean Variance Green Mean Variance Blue Std. dev. Var. Red Std. dev. Var. Green Std. dev. Var. Blue	Homogeneity Red Homogeneity Green Homogeneity Blue Correlation Red Correlation Green Correlation Blue	Mean Variance Red Mean Variance Green Mean Variance Blue Std. dev. Var. Red Std. dev. Var. Green Std. dev. Var. Blue
	13 features	13 features	Homogeneity Red Homogeneity Green Homogeneity Blue Correlation Red Correlation Green Correlation Blue
			19 features

The group Variance was comprised of all the Basic features plus the mean and standard deviation of the local variance texture, which was estimated according to eq. 5.1. The GLCM group had the Basic features plus the GLCM texture features used in this work. All the previously mentioned features were included in the feature vector called Total, which resulted in a vector which was defined by 19 features.

Satellite images experiment

Since one of the main goals was to compare each satellite image with the ArO results and both satellites each other, the feature sets should be selected such that the comparisons among different sources are meaningful and the feature set should be the same for the three sources when that is possible (e.g. the basic information of R, G and B bands). Additionally, the feature sets design for both satellites should be similar to that performed for ArO experiment. However, GLCM texture was not included in the case of VHR satellite images since both irrelevant information for improving classification accuracy and a decrease in efficiency could be demonstrated from the ArO experiment (see following sections). Otherwise the chromatic ratios (red, green and blue ratios), the Green-Red ratio, and the local variance used as texture indicator were used for this study. Furthermore, since not only RGB information is contained in the satellite images, the additional bands have to be included and, thus, three different kind of feature sets were designed following an addition scheme in which some features are added to the previous feature set (Table 5.3).

First, the basic feature sets including the average of all the available bands as well as some reduction of those for comparison purposes were performed. Secondly, the feature sets which include the rates that can be either the same rates than those used in the ArO experiment or the Normalized Difference Indexes (NDI) were included. NDIs are one of the most common features used in remote sensing classification (e.g. Normalized Difference Vegetation Index, NDVI) and they are based on the difference between one band and Nir band divided by the sum of the same band and Nir band. Therefore, three NDIs for GeoEye-1 (R, G, and B) and six for WorldView-2 (R, G, B, CB, Y, and RE) were estimated (Nir-2 band was not utilized since a high correlation between Nir-1 and Nir-2 bands was expected).

The third type of feature sets corresponded with the texture estimated through the local variance. Here a key difference with the ArO experiment can be noticed since the GSD was largely different (0.20 m for ArO and 0.50 m for VHR satellite orthoimages) and the proper window size to determine that variance could be different. For instance, while a 7x7 window size was used for the ArO experiment, which equals an area of 1.4x1.4 m to estimate the variance, the same window size in the case of VHR satellite images represents an area of 3.5x3.5 m, i.e. six times larger than the former. For that reason, different window sizes such as 3x3, 5x5 and 7x7 were tested for both satellite studies (T3, T5, and T7, respectively). Thus, the influence of the window size could be tested as well as the combination of every of them in terms of classification accuracy. Another difference between the ArO and the satellite data experiments was the availability of the PAN band which allowed the calculation of variance from it in the case of the satellite images whereas the variance was estimated for each band of the visible spectrum (RGB) in the case of the ArO experiment. The last difference between both feature sets based on variance texture was the use of standard deviation of

the variance for the ArO experiment. Those features were not included since no improvement in the accuracy results was found for both WV2 and GE1 when standard deviation of variance was included. Although the window size and the bands from which variance was estimated could somehow affect the classification accuracy results, both feature sets were considered similar and directly comparable with the feature set called Variance in the ArO experiment.

*Table 5.23. Feature sets used for GE1 and WV2 experiments. * indicates that datasets are directly comparable with the ArO study. The number of features used for each feature set is indicated in brackets.*

Feature set name	GeoEye-1	WorldView-2
RGB*	R, G, B (3)	R, G, B (3)
Basic1	RGB set + PAN + Nir (5)	RGB set + PAN + Nir (5)
Basic2	-	Basic1 set + CB + Y + RE + Nir2 (9)
Rates1*	Basic1 set + Chromatic ratios (R, G, B) + G/R ratio (9)	Basic2 set + Chromatic ratios (R, G, B) + G/R ratio (13)
Rates2	Rates1 set + NDBI + NDGI + NDVI (12)	Rates1 set + NDBI + NDGI + NDVI + NDYI + NDREI + NDCBI (19)
Texture3	Rates2 + T3 (13)	Rates2 + T3 (20)
Texture5	Rates2 + T5 (13)	Rates2 + T5 (20)
Texture7	Rates2 + T7 (13)	Rates2 + T7 (20)
TextureAll*	Rates2 + T3 + T5 + T7 (15)	Rates2 + T3 + T5 + T7 (22)
TextureOnly	Basic1 set + T3 + T5 + T7 (8)	Basic2 set + T3 + T5 + T7 (12)

Non-parametric Classification Methods Tested

Similarly to the variable strategy applied for the ISAs classification, the different non-parametric classifiers considered in this work were only tested for the ArO experiment, since the results were supposed to be similar regardless of the data source used. Therefore, the classifiers described along this section were tested and compared for the ArO experiment over the pilot area and, then, the best combination of strategy and classifier was applied on the areas A and B and also on the VHR-satellite imagery.

Classification and Regression Tree (CART) analysis was the first tested method. CART is a non-parametric method widely used in remote sensing for image classification (Friedl, Brodley & Strahler 1999, Yu et al. 2006, Mallinis et al. 2008). The most explanatory variables are detected by this kind of analysis and a prediction of response values can be carried out. CARTs use a sequential method for class assignment issues in which tree construction requires a recursive partitioning of the training dataset, which is divided into subsets, increasing their internal homogeneity according to one or more features (Brodley, Friedl 1997). The decision tree model that was used in this work corresponded to the univariate

CART (Breiman et al. 1984), with no pruning algorithm being applied (Esposito, Malerba & Semeraro 1997).

The Nearest Neighbour (NN) method was the second tested method. NN is a non-parametric supervised classification approach which stands out because of its simplicity and flexibility (Cover, Hart 1967, Samaniego, Bárdossy & Schulz 2008). It is characterised by achieving suitable results when the number of required training samples is not very high (Keller, Gray & Givens 1985). The k nearest neighbours in the feature space are searched for in order to determine which class the element being classified belongs to. Although k-NN methods benefit the outlier effect removal, they also involve a large computational effort (Zhu, Basir 2005). However, OBIA approaches enable k-NN methods to be applied in a more efficient way, since the use of objects can significantly reduce the number of elements that need to be classified, when compared to using pixels as minimum classification unit (Yu et al. 2006). In this work, the 1-NN approach was used (Duda, Hart 1973) as implemented in the eCognition software. This approach allows the membership probability value of every object belonging to each target class to be computed (Keller, Gray & Givens 1985, Mallinis et al. 2008) according to the description provided by the software (Definiens 2010).

The third method that was tested was Support Vector Machine (SVM), which is a non-parametric supervised learning technique used for classification and regression analysis. The application of SVM on remote sensing image classifications has increased extraordinary recently mainly because: 1) it does not rely on the assumption that the data are drawn from a given probability distribution; and 2) it requires a relative small number of training samples (Huang, Davis & Townshend 2002, Mountrakis, Im & Ogole 2011), which is an advantage due to the difficulty in obtaining ground truth samples. SVM has been previously used for impervious surface mapping or urban area classification (Zhu, Blumberg 2002, Huang, Zhang 2009) using hyperspectral data (Melgani, Bruzzone 2004) or high resolution satellite imagery (Inglada 2007). However, few applications have been carried out on archival aerial RGB photography (Trinder, Salah 2011). Therefore the successful application of an object-based classification using SVM on the dataset used in this work could boost the use of these techniques for long-term land-use evolution studies.

In short, SVM methods try to find a hyperplane which splits a dataset into two subsets during the training phase, using a set of samples where the classification is previously known (Vapnik 1995). The training phase tries to find the optimum boundary decision solution that minimises misclassifications (Mountrakis, Im & Ogole 2011). A crucial aspect of SVM is that not all samples are used to define the final hyperplane. Only those samples which are in the margin between classes are used to define the hyperplane and they are called Support Vectors (Zhu, Blumberg 2002). To obtain that hyperplane, a kernel function needs to be used. The radial basic function (RBF) is the most commonly used approach and therefore it was

used, following the formula expressed in the eq. 5.2 (Foody et al. 2006, Chang, Lin 2011):

$$K(x_i, x_j) = e^{-\gamma \|(x_i - x_j)\|^2};\ \gamma > 0 \qquad (5.2)$$

where the kernel parameter γ, together with the penalty parameter of the error term (usually denoted by C, with C>0) are estimated from the training data set through cross validation (Chang, Lin 2011).

In the present work, the free-distribution library LIBSVM (Chang, Lin 2011) was used for the application of SVM classifier. The general methodology proposed by the authors was also applied. This methodology consists of the following steps: 1) a simple scaling is applied to the training data (in order to avoid the over-weighting due to the features presenting the highest absolute values); 2) the applied kernel is RBF. The determination of parameters C and γ is solved by cross validation and grid search on the training data set. Then, 3) the estimated parameters are applied to the dataset used for testing (previously scaled), and the error matrix is computed. Finally, 4) the computed SVM parameters are used to classify the scene.

Each non-parametric classifier previously described (CART, NN and SVM) was applied on ArO, using as an input each of the four feature vectors (Basic, Variance, GLCM and Total). Both classification strategies (i.e. *Aggregation* and *Direct Classification)* were carried out for each combination of classifier and feature vector, which led to 24 different classifications being undertaken (3 classifiers x 4 feature vectors x 2 strategies). However, taking into account the description of NN approach, it has to be clarified that both strategies have been proved to achieve the same classification results since the nearest sample in the feature space will be the same for both strategies, e.g. if the nearest sample corresponds to 'Forest' for the *Aggregation* strategy, it will necessarily correspond to 'Pervious' for the *Direct Classification*. Thus, the number of combinations is reduced to 20 final classifications.

Validation and Comparison

The sampling design, both for the training stage and the accuracy assessment, is a crucial task in the image classification process. Since the homogeneous object was established as the minimum classification unit in this work, they were also chosen as the unit used for the training and testing samples, instead of using single pixels. A randomly stratified sampling method was followed, so that well distributed random samples were identified for each subclass. The samples were located on the orthoimages and each sample was assigned to the corresponding subclass (Table 5.1). The high spatial resolution of the aerial orthoimages and the VHR-satellite images enabled each class to be identified visually with no detectable

errors. Once the sampling design was performed for the ArO experiment, approximately the same samples were used for both VHR-satellite images, obviously changing the class labeled when a change in land use from 2001 to 2011 was detected.

It has been widely proven in previous works that classification accuracy can be affected by training sample size (Zhuang et al. 1994, Foody, Mathur 2004b, Foody et al. 2006). It is also known that the number of required samples depends on both the classifier (Foody, Mathur 2004b) and the number of classes to be labelled (Foody et al. 2006). On the other hand, the number of validation samples that are needed to carry out the accuracy assessment needs to be larger than the training dataset in order to achieve narrow confidence intervals for the accuracy estimation. It was suggested that 50 could be a proper number of samples per class when the scene is not too extensive, while a number from 75 to 100 would be advisable for vast areas or predominant classes (Congalton 1991). Otherwise, some statistically-based formulas such as binomial distribution (Jensen 1996) or multinomial distribution (Congalton, Green 2009) are suggested. These methods utilise the expected precision per cent and the toleration error in order to estimate the testing sample size. According to Congalton, Green (2009), the validation sample size for the pilot area (739, see Table 5.1) can be considered suitable, and slightly higher than necessary to achieve an overall accuracy of 85% ($p<0.05$).

Error matrices were calculated for each classification and overall accuracy (OA), user's accuracy (UA), producer's accuracy (PA) and KHAT statistic were derived (Congalton 1991). Additionally, in order to offer significance to the given results, intervals of confidence by Exact method (Sauro, Lewis 2005) were calculated ($p<0.05$), because it corresponds to the maximum likelihood estimate (i.e. the actual value of the estimated accuracy OA, UA or PA) even when it is not symmetrical (the values above and below are reported). The result of performing a Kappa analysis is a KHAT statistic ($\hat{K}$), an estimate of Kappa. Additionally, the variance of $\hat{K}$, $\widehat{var}(\hat{K})$ and the Z statistic can be calculated to test the significance of a single error matrix (Congalton, Green 2009). The Kappa test was applied at a statistical level of significance $p<0.05$, in order to estimate whether the error matrix was statistically different from another one (Congalton, Green 2009). In order to compare two independent error matrices (i.e. 1 and 2), the following statistic is calculated:

$$Z_{12} = \frac{\left|\hat{K}_1 - \hat{K}_2\right|}{\sqrt{\widehat{var}(\hat{K}_1) + \widehat{var}(\hat{K}_2)}} \tag{5.3}$$

This statistic is also standardised and normally distributed. Thus, the null hypothesis (K1 - K2 = 0) will be rejected if $Z \geq 1.96$ ($p<0.05$). That rejection would mean that the error matrices 1 and 2 are considered significantly different at a 95% confidence level.

190 different comparisons between methods were made by applying the Kappa test. In order to help understand the results, a separability matrix (SM) was computed (see the next section). The matrix was defined by the statistics used to compare the different classification approaches, so the statistics given by eq. 5.3 were calculated for each approach versus the other 19 approaches.

RESULTS AND DISCUSSION

As previously mentioned, the main goal of this chapter was to address three issues: (i) what non-parametric classifier yielded the most accurate output; (ii) what feature set led to the most accurate classification and; (iii) if the application of *Aggregation* or *Direct Classification* strategies affected the accuracy. On one hand, this section shows and discusses the accuracy values obtained by each approach and the statistical comparison between the different approaches, to determine if they were statistically different. On the other hand, once the most accurate method was selected, this section establishes a protocol and tests it in an operational context.

Accuracy Assessment and Comparisons

Archival Orthoimage study

As previously exposed, the ArO study included the determination of the most suitable strategy and classifier to be later used for both VHR-satellite experiments since they are inherent to the approach and no-dependence on the data source was expected. A summary of the results of the accuracy assessment for ArO study, showed as the 95% confidence intervals, are presented in Table 5.4 for each target class. The highest overall accuracy was achieved with the SVM and NN approaches in those cases in which Total or Variance feature vectors were used, i.e., when the local variance texture feature was included. Those results were considered to be suitable since the OA was higher than 85%, which has been established as the minimum acceptable value for the classification results (Congalton, Green 2009). That minimum seemed to be a reasonable reference for the required accuracy in this work, since there was a large variability within the classes that were labelled and the radiometric quality of the archival dataset was relatively poor. The results obtained from ArO could be considered more accurate than those in previous work with basic comparative information (no near infrared band and high spatial resolution) which achieved an OA of around 80% for ISAs detection (Cleve et al. 2008). Another comparable study achieved an OA of 90% with a high spatial resolution Quickbird image, which included the near infrared band (Myint et al. 2011). Finally, an OA of 81% for urban classification with digital 1-m spatial resolution orthoimagery was obtained in other study (Thomas, Hendrix & Congalton 2003). On the other hand, the CART approaches provided the lowest classification accuracies.

Table 5.24. Confidence interval of accuracy assessment results for the ArO experiment from the corresponding error matrices. The feature vectors are denoted as Basic (B), GLCM (G), Variance (V) and Total (T), while the classification strategies are coded as Aggregation (1) and Direct Classification (2).

	Overall accuracy	Producer's Accuracy		User's Accuracy	
		Pervious	Impervious	Pervious	Impervious
CART_B_1	77.8 - 83.6	87.5 - 93.1	59.3 - 70.7	76.9 - 84.0	75.5 - 86.0
CART_B_2	69.2 - 75.7	79.6 - 86.6	49.3 - 61.2	70.9 - 78.6	61.0 - 73.4
CART_G_1	75.6 - 81.7	91.7 - 96.2	47.9 - 59.8	72.9 - 80.1	79.5 - 90.3
CART_G_2	69.0 - 75.6	82.9 - 89.4	44.0 - 56.0	69.5 - 77.2	62.8 - 75.8
CART_V_1	78.2 - 84.0	78.6 - 85.8	74.0 - 83.8	82.8 - 89.5	68.5 - 78.6
CART_V_2	72.9 - 79.2	89.2 - 94.4	44.7 - 56.7	71.2 - 78.5	73.4 - 85.6
CART_T_1	78.2 - 84.0	80.5 - 87.4	71.0 - 81.2	81.5 - 88.3	69.7 - 80.0
CART_T_2	71.4 - 77.8	76.3 - 83.8	60.0 - 71.4	75.0 - 82.6	61.7 - 73.0
NN_B	82.8 - 88.0	85.0 - 91.2	75.9 - 85.4	84.8 - 91.0	76.2 - 85.7
NN_G	78.9 - 84.6	82.4 - 89.0	69.9 - 80.3	81.4 - 88.1	71.6 - 81.8
NN_V	83.6 - 88.7	84.6 - 90.8	79.0 - 87.9	86.5 - 92.4	76.3 - 85.5
NN_T	85.2 - 90.1	87.7 - 93.3	78.2 - 87.3	86.4 - 92.2	80.1 - 88.9
SVM_B_1	77.9 - 83.7	87.0 - 92.7	60.4 - 71.7	77.3 - 84.4	75.0 - 85.6
SVM_B_2	76.9 - 82.8	89.5 - 94.6	54.3 - 66.0	75.1 - 82.2	77.2 - 87.9
SVM_G_1	78.8 - 84.5	83.1 - 89.6	68.4 - 79.0	80.6 - 87.4	72.1 - 82.3
SVM_G_2	78.2 - 84.0	84.6 - 90.8	64.7 - 75.7	79.0 - 85.9	72.9 - 83.3
SVM_V_1	85.1 - 90.0	85.0 - 91.2	82.1 - 90.4	88.3 - 93.8	77.5 - 86.4
SVM_V_2	87.0 - 91.6	89.5 - 94.6	80.2 - 88.8	87.7 - 93.2	82.8 - 91.0
SVM_T_1	86.1 - 90.8	87.2 - 92.9	81.3 - 89.7	88.1 - 93.6	80.0 - 88.7
SVM_T_2	86.9 - 91.4	89.0 - 94.2	80.5 - 89.1	87.9 - 93.3	82.2 - 90.5

Regarding the PA, it was systematically higher for the pervious class than for the impervious class, which meant that the impervious objects had a larger omission error than the pervious objects, especially for the CART approaches. Generally, the same occurred for the UA. As a result, it can be said that the pervious class was better classified than the impervious class, being more noticeable in the case of the PA results. Taking into account that the sample design was balanced (33% of classified objects were impervious while the 37% of validation and training samples were from the same target class), the differences between the results of impervious and pervious classes happened because objects in impervious class were made by different kinds of construction materials, which leads to a spectrally heterogeneous class (Lu, Hetrick & Moran 2011). In order to prove the latter, the error matrix corresponding to the subclasses was computed (not shown). As an example, the classification of impervious subclasses such as roads, paths and harbour dam yielded, respectively, an omission error of 23.53%, 33.33% and 59.09% with the pervious subclasses. Note that SVM with the feature

sets Variance and Total and NN with all feature sets, presented very similar values of PA and UA for both target classes, while SVM with the feature sets Basic and GLCM and especially CART with all the feature sets, yielded larger differences between PA and UA.

As a measure of agreement or accuracy, KHAT is considered to show strong agreement when it is greater than 0.75 (Jones, Vaughan 2010), while values lower than 0.40 indicate poor agreement (Congalton, Green 2009).

Table 5.25. KHAT statistic for each combination of classifier, feature vectors and classification strategy and Z statistic corresponding to the differences between the two classification strategies tested for ArO experiment. Bold letters highlight significant differences (p<0.05).

Approach	KHAT (overall accuracy)	Z statistic for the two different classification strategies
CART_B_1	0.5783	**3.8268**
CART_B_2	0.3993	
CART_G_1	0.5175	**2.8617**
CART_G_2	0.3841	
CART_V_1	0.6080	**2.6774**
CART_V_2	0.4816	
CART_T_1	0.6038	**3.2650**
CART_T_2	0.4628	
SVM_B_1	0.5827	0.7736
SVM_B_2	0.5538	
SVM_G_1	0.6106	0.4405
SVM_G_2	0.5948	
SVM_V_1	0.7423	0.7656
SVM_V_2	0.7758	
SVM_T_1	0.7604	0.2919
SVM_T_2	0.7734	
NN_B	0.6938	N/A
NN_G	0.6190	N/A
NN_V	0.7129	N/A
NN_T	0.7416	N/A

According to Table 5.5, the SVM approach with the Variance and Total feature vectors and NN with Total could be considered results that have strong agreement. However, the CART approaches were showed to be the least accurate, especially when the direct classification approach was applied, since the internal heterogeneity made it difficult to achieve a suitable separation using regression trees (Lu, Hetrick & Moran 2011). Thus, the CART classifier was capable of identifying the most explanatory variables that were needed to classify the most abundant subclasses, increasing the internal homogeneity and improving the final overall accuracy when the *Aggregation* strategy was applied. Noticeably, those subclasses (i.e. dark sea, bright sea or individual trees as pervious classes, and red

buildings or greenhouses as impervious surfaces) had the largest weights over the entire scene. On the contrary, when only two highly heterogeneous subclasses were considered, i.e. pervious and impervious, the variables which improved the homogeneity were not as easy to obtain and consequently, the accuracy achieved was significantly lower for *Direct Classification* strategy.

In order to determine the influence of the two different classification strategies for the ArO study (*Aggregation* and *Direct Classification*) as well as to carry out a statistical comparison between the two methods, KHAT values were computed both for all the error matrices and for each target class, pervious and impervious. The results shown in Table 5.5, pointed out that only the CART approaches with all feature vectors were significantly affected ($p<0.05$) by the classification strategy. Otherwise, from the results of SVM approaches can be inferred that the classification agreement was not statistically sensitive to the use of subclass aggregation or the application of a direct binary classification. It should be noted that only when pervious subclasses were confused with impervious ones (and vice versa), e.g. bare soil was misclassified as roads or paths, and roads were misclassified as scrubland, the accuracy results were affected. Therefore, although some subclasses were difficult to classify, the most common misclassifications were commonly with other subclasses of the same target class (e.g. scrubland was misclassified mostly with agricultural fields) so the final accuracy was not affected. It is relevant to highlight that, since the training samples were acquired through a balanced random stratified sampling for each subclass, most of the spectral variability of the final target classes were successfully captured from the subclass-based training. Only when this kind of sampling is carried out (extracting samples from every significant subclass), a successful classification of the target classes can be expected. Otherwise, the expected results when using the direct classification approach could be different.

In order to determine the most adequate combination of classifier, feature set and strategy, several separability matrices (SMs) were used (see Tables 5.6-5.9). A SM depicts every approach to be compared in columns and rows from the highest KHAT to the lowest one so that the same order is followed. Every cell of the matrix represents the Z statistics (eq. 5.3) between each pair of approaches so the diagonal cells correspond to the same method and therefore the Z statistic for those cells is zero. Therefore, the SM is a valuable tool that can easily identify which methods are significantly different from the others. In this work, since the total size of the SM for all the approaches (20 x 20 dimension) did not allow a proper display, the results are shown in order to independently analyse the influence of every studied variable, i.e. classification strategy, classifier and feature vector. Table 5.6 shows the separability for all the approaches which used the *Direct Classification*. The SVM and NN classifiers in combination with the feature sets Variance and Total yielded the best accuracy results and they were significantly different from the other approaches (although NN with the feature set

Basic was not separable from the NN Total and Variance). Similar results were found in the SM of *Aggregation* strategy approaches. Those results implied that the GLCM feature set was not able to achieve any similar results regarding the accuracy of the classification and did not add any relevant information for the classification of ISAs in this study area. This was probably due to the fact that the GLCM matrices were computed within each object and homogeneity and correlation were estimated for each independent object (OBIA approach). Instead, the texture obtained as local variance has been proved to have a large influence on the improvement of accuracy, probably due to the independence of the object limits and the window size which is large enough to extract a suitable spectral variability (Chen, Stow & Gong 2004). Moreover, the CART approaches were clearly pointed out as the least accurate classifiers.

In order to clarify the impact of the different approaches on each classifier, a SM comprising of all the approaches that used the same classifier was computed. Table 5.7 shows the SM for the SVM classifier and highlights two aspects: first, non-significant differences existed between the feature sets Variance and Total and second, no differences were detected among approaches which used GLCM and Basic feature sets either. However, both blocks (i.e. Variance and Total vs. GLCM and Basic) were clearly distinguished, highlighting that Variance and Total feature sets yielded the most accurate results for the SVM classifier. Similar results were found for NN but the Basic feature set did not achieve significant differences from Variance or Total showing that NN was less dependent on the chosen feature set (Table 5.8). Regarding CART, the strategy used was the main factor that affected its accuracy, the *Aggregation* strategy being the most accurate. The feature sets played a less important role for the CART classifier. Finally, a SM of all the approaches that used the same feature set was displayed. Table 5.9 shows all the combinations with the Total feature set. It can be pointed out that only CART can be considered as the least accurate classifier, since its KHAT statistics were significantly different from all of the other approaches (the highest KHAT for CART was 0.6038, while for the other approaches the KHAT values were between 0.7416 and 0.7733). Additionally, the type of strategy employed had no influence on the approach except for the CART classifier. Similar behaviour was observed for the Variance and GLCM feature sets. However, when the Basic feature set was applied, the NN resulted to be significantly more accurate than the other classifiers and SVM and CART were similar when CART was applied to the *Aggregation* strategy. Therefore, according to the results previously discussed it can be proved that: (i) the most accurate classifiers were NN and SVM, (ii) NN was the least dependent classifier on the feature set employed, (iii) only CART was dependent on the strategy that was followed; and (iv), the feature sets which allowed the most accurate results to be obtained were Total and Variance. As a result, the CART classifier could have been rejected as an accurate classifier for this study while it has been proved that the incorporation of the texture variance was significant in order to increase the accuracy of the ISAs classification using archival RGB images.

Table 5.26. Separability matrix for classification strategy 2 (Direct Classification). Bold type indicates significant differences (p<0.05).

	SVM_V_2	SVM_T_2	NN_T	NN_V	NN_B	NN_G	SVM_G_2	SVM_B_2	CART_V_2	CART_T_2	CART_B_2	CART_G_2
SVM_V_2	0	0.071	0.956	1.644	**2.069**	**4.400**	**4.653**	**5.601**	**7.643**	**7.904**	**9.420**	**10.244**
SVM_T_2	0.071	0	0.887	1.578	**2.005**	**4.326**	**4.584**	**5.532**	**7.568**	**7.832**	**9.347**	**10.165**
NN_T	0.956	0.887	0	0.720	1.161	**3.304**	**3.627**	**4.559**	**6.484**	**6.774**	**8.245**	**8.971**
NN_V	1.644	1.578	0.720	0	0.440	**2.398**	**2.764**	**3.665**	**5.459**	**5.765**	**7.173**	**7.802**
NN_B	**2.069**	**2.005**	1.161	0.440	0	1.867	**2.254**	**3.140**	**4.868**	**5.183**	**6.559**	**7.142**
NN_G	**4.400**	**4.326**	**3.304**	**2.398**	1.867	0	0.517	1.491	**3.307**	**3.674**	**5.154**	**5.740**
SVM_G_2	**4.653**	**4.584**	**3.627**	**2.764**	**2.254**	0.517	0	0.932	**2.634**	**3.002**	**4.413**	**4.929**
SVM_B_2	**5.601**	**5.532**	**4.559**	**3.665**	**3.140**	1.491	0.932	0	1.655	**2.039**	**3.438**	**3.909**
CART_V_2	**7.643**	**7.568**	**6.484**	**5.459**	**4.868**	**3.307**	**2.634**	1.655	0	0.431	1.873	**2.301**
CART_T_2	**7.904**	**7.832**	**6.774**	**5.765**	**5.183**	**3.674**	**3.002**	**2.039**	0.431	0	1.415	1.815
CART_B_2	**9.420**	**9.347**	**8.245**	**7.173**	**6.559**	**5.154**	**4.413**	**3.438**	1.873	1.415	0	0.347
CART_G_2	**10.244**	**10.165**	**8.971**	**7.802**	**7.142**	**5.740**	**4.929**	**3.909**	**2.301**	1.815	0.347	0

Table 5.27. Separability matrix for SVM classifier. Bold type indicates significant differences (p<0.05).

	SVM_V_2	SVM_T_2	SVM_T_1	SVM_V_1	SVM_G_1	SVM_G_2	SVM_B_1	SVM_B_2
SVM_V_2	0	0.071	0.447	0.961	**4.292**	**4.653**	**4.927**	**5.601**
SVM_T_2	0.071	0	0.376	0.889	**4.223**	**4.584**	**4.859**	**5.532**
SVM_T_1	0.447	0.376	0	0.514	**3.856**	**4.218**	**4.493**	**5.167**
SVM_V_1	0.961	0.889	0.514	0	**3.354**	**3.718**	**3.994**	**4.666**
SVM_G_1	**4.292**	**4.223**	**3.856**	**3.354**	0	0.369	0.645	1.303
SVM_G_2	**4.653**	**4.584**	**4.218**	**3.718**	0.369	0	0.276	0.932
SVM_B_1	**4.927**	**4.859**	**4.493**	**3.994**	0.645	0.276	0	0.655
SVM_B_2	**5.601**	**5.532**	**5.167**	**4.666**	1.303	0.932	0.655	0

Table 5.28. Separability matrix for NN classifier. Bold type indicates significant differences (p<0.05).

	NN_T	NN_V	NN_B	NN_G
NN_T	0	0.720	1.161	**3.304**
NN_V	0.720	0	0.440	**2.398**
NN_B	1.161	0.440	0	1.867
NN_G	**3.304**	**2.398**	1.867	0

Table 5.29. Separability matrix for the approaches using the Total feature vector. Bold type indicates significant differences (p<0.05).

	SVM_T_2	SVM_T_1	NN_T	CART_T_1	CART_T_2
SVM_T_2	0	0.376	0.887	**4.105**	**7.832**
SVM_T_1	0.376	0	0.521	**3.765**	**7.448**
NN_T	0.887	0.521	0	**3.223**	**6.774**
CART_T_1	**4.105**	**3.765**	**3.223**	0	**3.063**
CART_T_2	**7.832**	**7.448**	**6.774**	**3.063**	0

Establishment of an Operational Protocol

From both operational and mapping production standpoints, the efficiency of the classification process is crucial for the selection of the final approach. In that sense, the SVM classifier was highlighted as being clearly more efficient than the NN classifier. Table 5.10 shows a comparison of the computational budget (measured as running time) needed in order to carry out the ISAs classification from ArO for the pilot area. The measured time was exclusively referred to as the classification task, excluding the previous segmentation phase. When using the NN classifier both the number of classes to be classified and, especially the feature vector, had an influence on the running time for computing the classification results. The computational cost of processing the feature vectors including the texture indices based on GLCM (homogeneity and correlation) turned out to be actually unaffordable under real operational conditions for current mapping production, as it has been previously indicated by other authors (Soh, Tsatsoulis 1999, Maillard 2003, Wang et al. 2004). Comparatively, the texture index, based on local variance previously computed for a 7 x 7 window size, took less than five minutes of additional running time than when the Basic feature vector was used. As a result, the use of the GLCM texture was not efficient, especially taking into account that the pilot area comprised of only around 25% of the entire working area. Furthermore, the number of target subclasses was a key factor according to the processing time, particularly when the local variance texture was used, since the required time was fifteen times longer for the aggregation strategy than for the direct classification (17 minutes and 1 minute respectively). This fact can be explained because each object is compared to each subclass in order to be assigned

to the nearest subclass. If only two classes were being compared (pervious/impervious), the process required less computational effort. The number of training samples would be another significant factor related to computational time since each element has to be compared against each object and then finally labelled according to the corresponding object. Eventually, if a NN classifier is employed, the use of a previously computed local variance texture index is suggested. In the same direction, the use of the direct classification (pervious/impervious classes) is also recommended. In that case, an exhaustive training sample is required in order to feed the classifier the whole spectral variability of the subclasses composing of the final target classes.

Table 5.30. Running time to carry out the pilot area classification from ArO using the NN classifier (eCognition8®, SVM and CART). Results have been obtained by using a 3.20 GHz dual core processor with 8 Gb. RAM and 64 bits.

Classifier	Feature vectors	Aggregation Classification Strategy (Running Time)	Direct Classification Strategy (Running Time)
NN	Basic	15 min 11 sec	1 min 08 sec
	GLCM	5 h 21 min 15 sec	4 h 22 min 21 sec
	Variance	16 min 50 sec	1 min 20 sec
	Total	6 h 50 min 02 sec	5 h 18 min 19 sec
SVM	All cases	< 1 min.	< 1 min.
CART	All cases	< 1 min.	< 1min.

Summing up, and taking into account the previous results, SVM classifier was chosen since the accuracy results did not depend on the strategy used and, moreover, the efficiency was higher than in the case of NN, which anyway achieved similar classification accuracy results. Therefore, SVM classifier using *Direct Classification* strategy was used for GE1 and WV2 experiments.

Results from GE1 experiment

The OA, PA, UA and KHAT results obtained through the error matrices for every feature set applied are shown in Table 5.11. Those results highlighted that all feature sets yielded accurate classification results ranging from 86.1% to 90.0%. However, more differences were found for both UA and especially for impervious PA (up to 14.7% difference between the maximum and minimum classification accuracy figures). On one hand, the results implied that whereas the PA for the pervious class was very high, the PA for the impervious class was significantly lower (the average of that difference was close to 22%). On the other hand, the UA differences were much smaller (differences about 5%). This means that pervious class was classified more accurately, especially if omission error (related to PA) was considered. It is worth noting that PA was always higher than UA (about 9%) for pervious class, while UA was more accurate in all cases for impervious class (about 17%). In general, those results highlighted that

impervious class was more difficult to classify than pervious class. This fact can be perfectly understandable since the impervious class is composed of a higher number of spectrally different subclasses and materials, such as roads, buildings or paths.

Table 5.31. General accuracy results for GE1 study. OA, PA, and UA values are expressed in %. 1 and 2 indicate pervious and impervious class, respectively.

Feature set	Alias	OA	PA1	PA2	UA1	UA2	KHAT
RGB	RGB	86.1	95.9	69.2	84.4	90.6	0.685
Basic1	B1	87.8	95.9	73.7	86.4	91.2	0.725
Rates1	R1	86.8	97.2	68.8	84.4	93.4	0.699
Rates2	R2	86.3	95.5	70.3	84.8	89.9	0.689
TextureOnly	TOnly	87.4	93.5	76.7	87.4	87.2	0.720
Texture3	T3	88.6	96.5	74.8	86.9	92.6	0.744
Texture5	T5	88.9	97.2	74.4	86.8	93.8	0.749
Texture7	T7	87.5	94.6	75.2	86.9	88.9	0.721
TextureAll	TAll	90.0	93.7	83.5	90.8	88.4	0.781

The previous results shown that OA was not the most appropriate parameter to determine what feature set had to be chosen. In fact, all OA values seemed to be quite accurate and they were not very different (from 86.1% to 90.0%). Otherwise, although the OA can be similar, the differences between the PA and UA for each class can also indicate the goodness of the accuracy results. For instance, whereas the Texture5 feature set has a similar OA than the TextureAll set, the latter yielded much smaller differences regarding to PA and UA.

Regarding KHAT results, it is highlighted that every feature set yielded a good agreement and some of them were close to obtain strong agreement (>0.80 according to Congalton, Green (2009)). Those KHAT results were used to check the potential significant differences between the tested approaches through different Kappa tests which were grouped by means of a separability matrix presented in Table 5.12.

The separability matrix depicted in Table 5.12 clearly highlight that only TextureAll feature set made the classification approach statistically different from others (i.e. RGB, Rates1, and Rates2). These results were different to a previous study for a more reduced urban zone in the same area, in which the NDIs ratios achieved more accurate results than the basic feature set (Aguilar, Saldaña & Aguilar 2013b), although the classified area was not comparable since the classes to be targeted were significantly different. Summing up, only the use of all the available features tested in this work achieved a significant improvement on the classification accuracy assessment. Additionally, according with the low

differences between PA and UA, TextureAll feature set was chosen as the most suitable for ISAs classification by SVM approach.

Table 5.32. Separability matrix of KHAT values for GE1 feature sets. Values above 1.96 (bold figures) indicates significant differences for KHAT statistics (p<0.05).

	TAll	T5	T3	B1	T7	TOnly	R1	R2	RGB
TAll	0	0.91	1.05	1.55	1.65	1.68	**2.23**	**2.57**	**2.58**
T5	0.91	0	0.15	0.64	0.74	0.77	1.32	1.56	1.67
T3	1.05	0.15	0	0.49	0.60	0.62	1.18	1.41	1.52
B1	1.55	0.64	0.49	0	0.10	0.13	0.68	0.92	1.03
T7	1.65	0.74	0.60	0.10	0	0.03	0.58	0.82	0.93
TOnly	1.68	0.77	0.62	0.13	0.03	0	0.55	0.79	0.90
R1	**2.23**	1.32	1.18	0.68	0.58	0.55	0	0.24	0.35
R2	**2.47**	1.56	1.41	0.92	0.82	0.79	0.24	0	0.11
RGB	**2.58**	1.67	1.52	1.03	0.93	0.90	0.35	0.11	0

WV2 experiment results

The Table 5.13 shows the general accuracy results for WorldView-2 data classification. Similarly to the GE1 study, it is clear that the differences between the PA values for the pervious and impervious target classes are significantly different, being for the former up to 27% better than the latter. Again, UAs yielded fewer differences than PAs. In this sense, OA can be also viewed as not the most suitable parameter to be considered in order to choose the best feature set. Instead of simply OA, the best balance between OA, PA and UA figures should be considered and so the feature set TextureOnly should be chosen. When taking into account statistical separability (Table 5.14), a higher level of separability can be appreciated for WV2 than for GE1. For WorldView-2 data, texture information seems to yield a relevant improvement as compared to rates and basic feature sets, although no differences could be established among different texture combinations. Thus, the feature set TextureAll was chosen in order to be compared with the GE1.

Summing up, the feature set TextureAll was applied to both VHR-satellite orthoimages in order to obtain the corresponding ISAs classification over the previously described areas A and B.

Table 5.33. General accuracy results for WV2 study. OA, PA, and UA values are expressed in %. 1 and 2 indicate pervious and impervious class, respectively.

Feature set	Alias	OA	PA1	PA2	UA1	UA2	KHAT
RGB	RGB	85.4	95.2	68.4	84.0	89.2	0.670
Basic1	B1	86.4	96.5	68.8	84.3	92.0	0.690
Basic2	B2	87.4	95.5	73.3	86.1	90.3	0.716
Rates1	R1	86.4	95.5	70.7	85.0	90.0	0.693
Rates2	R2	88.0	89.6	85.3	91.4	82.5	0.744
TextureOnly	TOnly	90.8	93.5	86.1	92.1	88.4	0.800
Texture3	T3	89.0	94.2	80.1	89.1	88.8	0.758
Texture5	T5	90.8	96.3	81.2	89.9	92.7	0.796
Texture7	T7	91.5	96.1	83.5	91.0	92.5	0.812
TextureAll	TAll	90.8	95.0	83.5	90.9	90.6	0.798

Table 5.34. Separability matrix of KHAT values forWV2 feature sets. Values above 1.96 (bold figures) indicates significant differences for KHAT statistics (p<0.05).

	T7	TOnly	TAll	T5	T3	R2	B2	R1	B1	RGB
T7	0	0.37	0.44	0.50	1.60	**1.99**	**2.72**	**3.31**	**3.38**	**3.88**
TOnly	0.37	0	0.07	0.13	1.23	1.63	**2.36**	**2.95**	**3.02**	**3.53**
TAll	0.44	0.07	0	0.06	1.16	1.56	**2.28**	**2.88**	**2.95**	**3.45**
T5	0.50	0.13	0.06	0	1.10	1.49	**2.22**	**2.82**	**2.88**	**3.39**
T3	1.60	1.23	1.16	1.10	0	0.38	1.12	1.72	1.79	**2.29**
R2	**1.99**	1.63	1.56	1.49	0.38	0	0.75	1.35	1.41	1.92
B2	**2.72**	**2.36**	**2.28**	**2.22**	1.12	0.75	0	0.60	0.66	1.17
R1	**3.31**	**2.95**	**2.88**	**2.82**	1.72	1.35	0.60	0	0.06	0.57
B1	**3.38**	**3.02**	**2.95**	**2.88**	1.79	1.41	0.66	0.06	0	0.51
RGB	**3.88**	**3.53**	**3.45**	**3.39**	**2.29**	1.92	1.17	0.57	0.51	0

VHR-satellite imagery vs. Archival Orthoimage comparison

The feature sets to be compared, which can be considered as quite similar for both satellite and archival orthoimage studies, would be RGB, Rates1, and TextureAll (Table 5.3). Although TextureAll was similar for GE1 and VW2 (estimated from panchromatic band and comprising of 3 different window sizes), this feature set was slightly different for ArO since panchromatic band was not available and only one window size was tested. However, the texture was calculated for each colour band (Red, Green, and Blue) and the effect on accuracy results was greatly relevant. The comparison between VHR-satellites and ArO classification accuracy results according to the application of different feature sets was performed only for the pilot area. It should be noted that the classifier (SVM) and the strategy (binary classification) were both fixed along these tests.

GE1 vs ArO

The comparison results, based on the Kappa test, can be observed in the Table 5.15. It is shown that RGB and Rates1 feature sets for ArO were much more inaccurate than for GE1 experiment. They also indicated that texture features had an improvement effect for both studies but it was quantitatively more important in the case of ArO. Furthermore, the results for both experiments by applying texture feature sets yielded similar accuracy results. Therefore, a more reliable data source (e.g. VHR GeoEye-1 imagery) did not imply significant improvement as compared to the results achieved from higher spatial resolution archival orthoimage, which included some artefacts and had poor radiometry, when texture features were applied. However, regarding basic information and ratios, the GeoEye-1 imagery yielded significantly higher classification accuracy, which could mean that this kind of images may have better radiometric conditions for image classification due to the absence of irregularities or artefacts that can be common in archival orthoimages.

Table 5.35. Separability results between ArO and GE1 experiments. Values above 1.96 (bold figures) indicates significant differences for KHAT statistics between both accuracy figures (p<0.05).

	KHAT	Z statistic
GE_RGB	0.685	**4.11**
ArO_RGB	0.507	
GE_Rates1	0.699	**3.45**
ArO_Rates1	0.554	
GE_TextureAll	0.781	0.16
ArO_Variance	0.776	

WV2 vs. ArO

The classification accuracy results for WorldView-2 imagery, depicted in Table 5.16, were similar to those shown in the GE1-ArO comparison. Again, larger differences were found were RGB or rates feature sets were used. However, the results were not statistically different when the classification was carried out by means of the texture-based feature set.

Summing up, the results for both satellites underlined the importance of using invariable features for image classification, such as local variance texture. Moreover, it seems to be some limit on the classification accuracy around 90% of OA (close to 0.80 of KHAT) inherent to the used approach. That could be related to the known shortcomings of object-based analysis. For example, under-segmentation errors could occur if the applied scale parameter was not the most appropriate for these images (Liu, Xia 2010). In fact, other experiment carried out through SVM classifier and OBIA approach over a QuickBird image obtained a maximum overall accuracy of about 90% for the most suitable scale parameter

(Liu, Xia 2010). In other work that used OBIA approach and a true-color aerial photography, a value of 92% OA was achieved (Kampouraki, Wood & Brewer 2008). However, the determination of the scale parameter which would lead to the most accurate classification (optimal segmentation) was beyond the scope of this work and, thus, a certain point of error due to image segmentation has to be taken into account.

Table 5.36. Separability results between ArO and WV2 experiments. Values above 1.96 (bold figures) indicates significant differences for KHAT statistics between both accuracy figures (p<0.05).

	KHAT	Z statistic
WV2_RGB	0.670	**3.729**
ArO_RGB	0.507	
WV2_Rates1	0.693	**3.288**
ArO_Rates1	0.554	
WV2_TextureAll	0.798	0.669
ArO_Variance	0.776	

GE1 vs. WV2 comparison

In order to check the influence of the satellite imagery source for ISAs classification, the classification accuracy results achieved in the pilot area from GE1 and WV2 experiments were compared (Table 5.17). Those results showed that the differences between both image sources were very small. Actually, they were statistically significant only for the feature sets Texture7 and TextureOnly, being more accurate for WorldView-2 image. Although the differences were no significant, WV2 achieved more accurate classification accuracy results when additional bands (Yellow, Coastal Blue, Red Edge and Nir-2), and the ratios derived from those bands (Rates2), were used. Leaving aside these additional bands, GE1 yielded slightly more accurate classification results than WV2. Note that difference between using additional bands or not (Basic 1 and Basic 2 feature sets) was not significant for WV2 so the effect of adding those bands was not clear, at least until texture indices were included (Texture7 and TextureOnly).

It is worth noting that these results are slightly different from those achieved in a previous study carried out in a smaller urban area of the same study site (Aguilar, Saldaña & Aguilar 2013b) in which GeoEye-1 image leaded to more accurate results than WorldView-2. Although not exactly the same feature set was used (e.g. variance texture was not considered for the previous study), and also a different classifier was tested, it seems to be clear that the classes to be targeted and the use of a larger and more heterogeneous area may affect the satellite images comparison.

Table 5.37. Separability results between GE1 and WV2 experiment. Note that Basic1 and Basic2 feature sets for WV2 were compared with Basic 1 set for GE1. Values above 1.96 (bold figures) indicates significant differences for KHAT statistics between both accuracy figures (p<0.05).

	KHAT	Z statistic
GE_RGB	0.685	0.38
WV2_RBG	0.670	
GE_Basic1	0.725	0.90
WV2_Basic1	0.690	
WV2_Basic2	0.716	0.24
GE_Rates1	0.699	0.15
WV2_Rates1	0.693	
GE_Rates2	0.689	1.43
WV2_Rates2	0.744	
GE_Texture3	0.744	0.39
WV2_Texture3	0.758	
GE_Texture5	0.749	1.35
WV2_Texture5	0.796	
GE_Texture7	0.721	**2.58**
WV2_Texture7	0.812	
GE_TextureOnly	0.720	**2.25**
WV2_TextureOnly	0.800	
GE_TextureAll	0.781	0.51
WV2_TextureAll	0.798	

Classification of the areas A and B

Once the most suitable combination of classifier, strategy, and feature set was chosen for each experiment, i.e., using Variance feature vector for ArO and TextureAll for GE1 and WV2, and by applying SVM classifier and *Direct Classification* strategy, the areas A and B were classified through two different training sets: (1) the previously validated pilot area training, and (2) an *ad hoc* training set for each area and image source referred to a new training set extracted just from the same area to be classified (A or B) by using the feature set which yielded the best results in the pilot area training set (Variance or TextureAll depending on the kind of orthoimage). Thus, the ability to extrapolate a local training to the entire area will be tested through this experiment by comparing if the training of the classifier limited on a localized subset within the entire image is capable to achieve accurate classification results beyond the area of training.

Therefore, the influence of the area to be classified and the training samples will be estimated.

ArO experiment

The results for ArO study are shown in Table 5.18. When the areas A and B were classified using the training samples extracted from the pilot area (Pilot area training in Table 5.18), the accuracy of the results was statistically poorer than when the training samples were collected from a specific area to be classified (*ad hoc* training in Table 5.18). According to the Z statistic, the accuracy significantly increased when *ad hoc* training was applied. Furthermore, the Z statistic between both *ad hoc* classifications showed that they were statistically similar (Z = 0.033) and, therefore, the feasibility of the method was proved. These results highlighted the importance of the training dataset, especially when images presenting radiometric artefacts (such as archival aerial orthoimages) are employed. Moreover, the subclass distribution can vary from one scene to another, which implies a different spectral variability for each specific area. It was also found that although it improved the accuracy of the classification results, the use of variance-based features did not seem to contribute to the mitigation of the radiometric artefacts, since an *ad hoc* training set was needed for each area. Finally, it should be pointed out that the final classification results obtained from subsets A and B for the ArO study led to an appropriate KHAT statistic and an overall accuracy value above the minimum value of 85% recommended by some authors (Congalton, Green 2009).

Table 5.38. Classification accuracy assessment results for ArO experiment in the entire area by using the SVM classifier, Variance feature vector and Direct Classification strategy.

Area	Training set	Overall Accuracy	KHAT	Z statistic	Class	Producer's Accuracy	User's Accuracy
A	Pilot area training	73.14%	0.4705	5.286	Pervious	89.16%	66.07%
					Impervious	58.70%	85.71%
	Ad hoc training	86.10%	0.7195		Pervious	79.12%	90.37%
					Impervious	92.39%	83.06%
B	Pilot area training	77.63%	0.5539	3.591	Pervious	90.49%	71.69%
					Impervious	65.06%	87.50%
	Ad hoc training	85.90%	0.7181		Pervious	86.69%	85.07%
					Impervious	85.13%	86.74%

VHR-satellite images (GE1 and WV2 experiments)

Similarly to the ArO experiment, the most appropriate feature set chosen for GE1 and WV2 experiments (TextureAll) was used in order to classify the A and B areas by means of the pilot area training and the *ad hoc* training sets. As shown in Table 5.19, some important variations in KHAT values exist when GeoEye-1 image was used. Whereas the KHAT statistic yielded a good agreement for *ad hoc* training

in both areas, the pilot area training led to inaccurate results close to a poor agreement. Regarding the training samples, two different sections can be differentiated. First, both *ad hoc* classification results are not statistically different each other, and second, the classification results from the pilot area training in areas A and B are also statistically similar each other. However, it is worth noting that the differences between *ad hoc* training and the pilot area training were strongly important and highlighted that a suitable design of the sampling method constitutes a key factor for image classification through this approach. It is also important to note that, although not statistically relevant, both *ad hoc* trainings yielded important differences and some additional tests about the sampling method or the feature sets could be taken into account.

Table 5.39. Separability matrix for areas A and B in GE1 and WV2 experiments. The training sample sets are denoted as P and AH for Pilot Area and ad hoc training sets, respectively. Values above 1.96 (bold figures) indicates significant differences for KHAT statistics (p<0.05).

GE1 experiment

		B_AH	A_AH	B_P	A_P
	KHAT	0.804	0.732	0.515	0.505
B_AH	0.804	0	1.84	**6.55**	**6.66**
A_AH	0.732	1.84	0	**4.67**	**4.81**
B_P	0.515	**6.55**	**4.67**	0	0.20
A_P	0.505	**6.66**	**4.81**	0.20	0

WV2 experiment

	B_AH	A_AH	B_P	A_P
KHAT	0.725	0.713	0.689	0.670
0.725	0	0.28	0.83	1.24
0.713	0.28	0	0.55	0.96
0.689	0.83	0.55	0	0.41
0.670	1.24	0.96	0.41	0

The classification results for the WV2 experiment are also shown in Table 5.19. Although *ad hoc* results were more accurate than those from pilot area training, it is worth noting that no significant differences between both training sets were found for this study in any of the considered areas. Thus, WV2 data set seemed to be more consistent since a local training set of that image was able to accurately classify the separated areas A and B. However, less classification accuracy was achieved for *ad hoc* training, mainly in the case of the area B. In fact, if the separability matrices of the three experiments were merged (table not shown), three groups of results could be distinguished: (1) the pilot area training in both areas performed significantly inaccurate results for ArO and GE1 experiment; (2) the *ad hoc* training for ArO and WV2 are not significantly different with respect to the pilot area training for WV2; and (3) only the area B classified on GE1 by means of *ad hoc* training was statistically more accurate than the WV2 and ArO experiments.

Those results strengthen the importance of a suitable sampling method for both training and validation phases according to the data set used, showing that it may not be appropriate the use of training samples of a relatively small area for classifying external areas. Of course, that will depend on the variability of the

classes to be targeted as well as the radiometric conditions of the images used. In this case, WorldView-2 imagery has been proved as more appropriate for extrapolating training samples from a subset of the total area, maybe due to its additional information content (Yellow, Red Edge, Coastal Blue, and Nir-2 additional bands).

This experiment was carried out in order to check the capability of extrapolate training samples to classify external areas. It has been proved that this ability depends on the image to be classified and also the training and testing set designed. However, a general classification approach would take into account the entire area for both, training and testing phases. The next section was performed in order to check the capability of classifying ISAs using all the available testing and training samples from the three areas. Additionally, since a large number of samples were used to train the classification algorithm, a reduction of training samples approach was carried out in order to determine the most suitable training sample size.

Classification of the entire area

Once the influence of the training area has been proven, the classification accuracy results by using all the training and testing samples was tested. The general results are shown in Table 5.20. Notice that all the data sources achieved very accurate results. For instance, the OA was close to 90% for every image. Furthermore, PA and UA figures were balanced for both classes since the differences between them were lesser than 1.1%.

Table 5.40. General accuracy results for ArO, GE1 and WV2 experiment when all training and testing samples were included. OA, PA, and UA expressed in %. Significant differences ($p<0.05$) between KHAT values are indicated by different letters.

	Archival Orthoimage	GeoEye-1	WorldView-2
OA	88.1	90.4	89.7
PA1	88.6	90.5	90.9
PA2	87.5	90.1	88.3
UA1	89.2	91.5	90.1
UA2	86.8	89.0	89.2
KHAT	0.760^{b}	0.806^{a}	0.792^{ab}
Training size (no. objects)	576	583	583
Testing size (no. objects)	1796	1783	1783

Those results proved that a well-distributed and large training set could reach a suitable classification for every type of image used. In fact, when statistical significance was performed by means on Kappa test, only GE1 classification accuracy can be considered as more accurate than that estimated for the ArO study. Therefore, WV2 classification accuracy was not statistically different than that yielded from the other image sources. In fact, the high number of validation samples enabled the statistical separability to be much more powered. In this sense, some of these complete area classifications were statistically more accurate than some separated parts. For instance, the complete area classification was more accurate than the areas A and B for WV2, and it was also more accurate than area A for GE1. Regarding the classifications performed over the pilot area, only ArO classification accuracy was statistically different with respect to the one coming from GE1 entire area. Therefore, the entire area classification accuracies for both satellite images were statistically similar to those achieved in the pilot area. Since a relatively large training size was used, which is not a common feature for this kind of experiments, in the next section it is tried to reveal how the accuracy results for the entire area varies when training size is reduced.

Estimation of the appropriate training size

It is clear that the number of training samples used in this work could be unaffordable for a practical classification approach. Furthermore, it would be interesting to find out how reducing the number of training samples affects the final classification accuracy results. However, the classification method should be taken into account. According to Foody et al. (2006), the classifier used in this study, Support Vector Machines (SVM), "seeks to find the optimal separating hyperplane between classes by focusing on the training cases that lie at the edge of the class distributions, the support vectors". That means that the accuracy will be affected when the most appropriate support vectors or samples to differentiate pervious and impervious classes are to be included in the training phase. That is different as compared to usual parametric methods such as Maximum Likelihood Classifier (MLC), which is based on the mean and variance of the population. If the number of samples was the appropriate, those parameters may not vary and the population would be well represented. For instance, if the 10% of the samples are removed from the total set, and key support vectors were also removed, the final classification accuracy would be significantly lower while the mean and variance could not significantly vary and so the results of using MLC would not differ. Additionally, and taking into account the sample design of this study (pervious and impervious class are targeted from several heterogeneous subclasses), a poor representation of the actual land cover could be performed if the number of samples was too small and some subclasses were poorly represented on the remaining training set.

In order to check the influence of the training sample size on SVM performance, a training sample reduction was undertaken. Nine different levels of training sets were produced by randomly reducing the total samples in discrete steps of 10% ranging from 10% to 90% of the total samples. Additionally, four repetitions for every sampling level were performed also through random methods so the final number of different samples sets was 36. Therefore, the relationship between the classification accuracy and the training size, the variability for every training size, and the suitable number of samples could be estimated.

h. ArO study

The results can be checked in Figure 5.3. It is important to note that the OA average increased when more training samples were used. The OA average seemed to stabilize when 50% of the available samples were used. It is also worth noting that the estimated variability of the OA values for the same training size was reduced when higher training sizes were employed. That variability was clearly lower when the 60% of the available samples were reached. For PA and UA values, the results were similar regarding OA average trend, although the estimated variability was even higher than for OA.

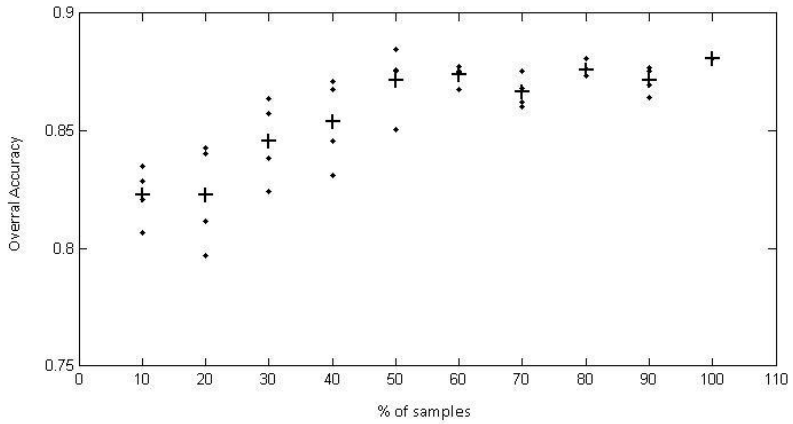

Figure 5.9. Overall accuracy (so much per one expressed) for each repetition and the average value, symbolized as a cross, for each training size. Archival Orthoimage experiment.

When separability matrix was statistically performed by means of Kappa test, it was proved that a value of 50% meant the higher percentage of training samples in which there was significant differences between consecutive training sizes (data not presented). Furthermore, the OA averages from 50% training size and higher were not statistically less accurate than the classification based on the whole samples. In conclusion, a training size around the 60% of the total samples (346 out of 576) could be recommended in the case of the Archival Orthoimage to

extract ISAs through SVM approach without any significant affection on the final accuracy.

i. GeoEye-1 study

The classification accuracy results for GE1 experiment are presented in Figure 5.4 Similarly to the ArO study, the OA increased and the variability of the results decreased when more samples were included. In this case the OA seemed to achieve accurate results when only the 30% of the available samples were included, although the OA keeps a growing trend when the number of samples was increased. In this case the OA variability for every training size was not statistically significant for the 70, 80, and 90% training sizes, so more training samples than for ArO study were needed to achieve that. Again, the variability for the PA and UA values was significantly larger than that for OA up to the 70% of the available samples were included. Anyway, the averages for those per-class accuracies followed a similar trend than OA.

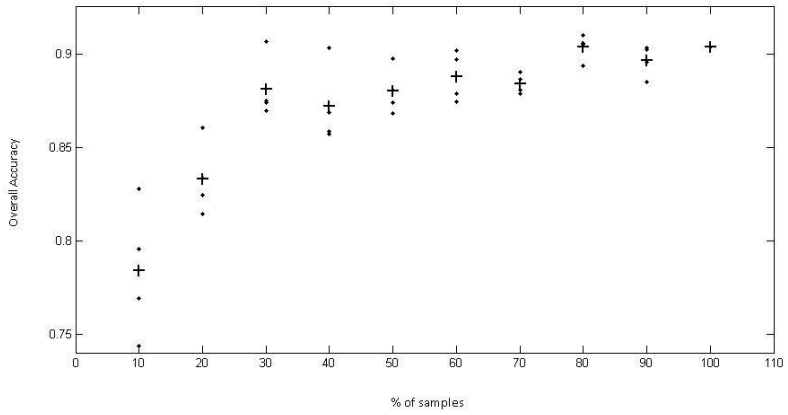

Figure 5.10. Overall accuracy (so much per one expressed) for each repetition and the average value, symbolized as a cross, for each training size. GE1 experiment.

The estimation of the statistical separability between the different training sizes leaded to consider that using 60% or more samples had no significant influence. Thus, the less number of samples that should be considered in order to maintain the classification accuracy figures was the 70% of the total samples (408 out of 583) since the accuracy results were not statistically different of those obtained from applying the total sampling set and, moreover, the variability among the repetitions was not significant either. This fact involved that GeoEye-1 study required over 60 additional samples as compared to ArO study.

j. WorldView-2 study

Figure 5.5 depicts the results for the WV2 sampling reduction study. It is shown again the progressive increase of the OA when more samples were used to train the classifier. Similarly to previous experiments, it is also clear that the variability for every training size generally decreased when more training samples were added. In this case, the variability in the estimated accuracy figures did not present significant differences for the 60% training size and the statistical separability of the OA averages indicated that a training size ranging from 40% to 90% was not separable ($p<0.05$) from the total training classification accuracy results, except for the case of 50% training size. Those results leaded to choose the 60% of available samples as the most appropriate training size for ISAs classification over the WorldView-2 image (i.e. 350 out of 583).

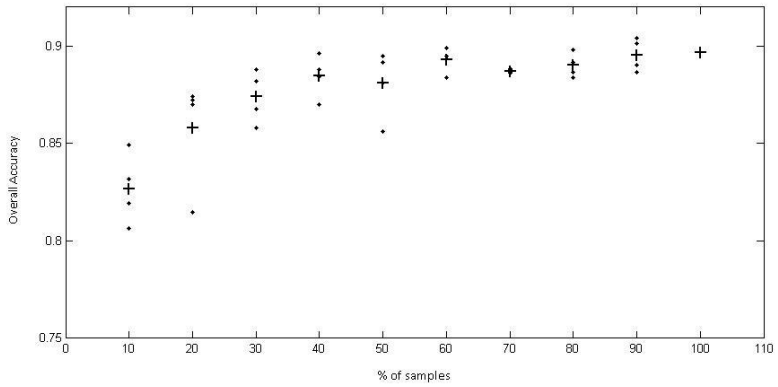

Figure 5.11. Overall accuracy (so much per one expressed) for each repetition and the average value, symbolized as a cross, for each training size. WV2 experiment.

Data source comparison

In order to compare the effect of applying each different data source, the average of the overall accuracy for each tested training size was calculated. Then, the statistical separability ($p<0.05$) was estimated through the differences between both proportions following the eq. 5.4 (Foody 2009), where P represents an averaged proportion for every percentage level (averaged overall accuracy for the data source 1 or 2), $\bar{p}$ is the average of both proportions to compare, and n is the number of validation samples used (also for data source 1 or 2). In this case the comparison was performed by means of this approach instead of the Kappa test since the use of the averaged KHAT and its variance could be problematic. Similarly to the Kappa test, a difference is taken to be statistically significant ($p<0.05$) if $z > |1.96|$

$$z = \frac{P_1 - P_2}{\sqrt{\bar{p}(1-\bar{p})\left(\frac{1}{n_1}+\frac{1}{n_2}\right)}} \tag{5.4}$$

According to the Figure 5.6, the ArO experiment was clearly the less accurate as compared to both satellite images when the 20% of available samples or more was utilized. Using the hypothesis test explained previously, the ArO experiment was only significantly more accurate for the 10% training size. However, that training size did not yield accurate enough results for any data source since the minimum required 85% was not achieved. For all the other training sizes, ArO yielded statistically less accurate results than those achieved from both satellite images (except for the 70% case in which ArO could not be separated from WV2 results). Furthermore, GE1 results were significantly more accurate for the training sizes 30, 70 and 90%, while the WV2 results were more accurate than GE1 only for the case of 40% training size.

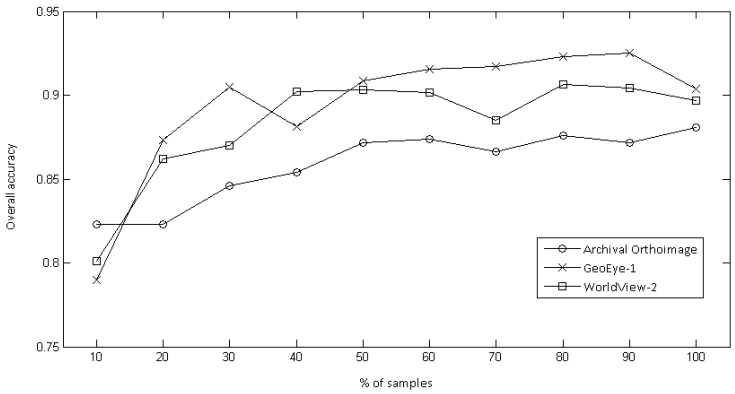

Figure 5.12. OA average for each data source and every training size tested.

According to the previous results, the SVM classifier used to classify impervious areas has been proved as a suitable approach for all the image sources tested. The relationship between the number of training samples employed to train the classifier and the final accuracy results was clearly positive although it was not a perfect linear relation because of the basis of the SVM classifier. It was also found an inherent relationship between the accuracy results and the sample size for SVM approach (Foody, Mathur 2004a); although it was reported that SVM achieved better accuracies with a smaller number of samples than other methods. In the present study, all the data sources achieved an accurate classification when the 60 or 70% of the total samples were taken into account. It was also proved that the sampling design or distribution can have a large affection on the accuracy. For instance, using a half of samples for WV2 (292 samples) and having two different samples distribution, a difference of up to 5% in OA was estimated. Thus, if this

kind of study was not performed the same approach with the same number of training samples could yielded, for instance, an accuracy result from 80 to 85% if the distribution of samples was different. This fact would be critical whether a minimum acceptable accuracy was previously established (e.g. the most common 85% OA considered) and the lowest results were achieved, leading to the analyst to reject the applied approach. However, the approach would have been perfectly suitable if more samples had been collected or a different distribution had been chosen.

Regarding the specific approach used in this work, it is worth noting that the classifier and the strategy of sampling can play a key role. Concretely, the sampling of this approach was based on the direct classification of pervious and impervious areas. However, these superclasses were composed of several subclasses and, therefore, they can be considered as highly heterogeneous. The original sampling (the 100 per cent set) was carried out through a stratified strategy and so a significant number of samples for each subclass was considered. Otherwise, the reduction on the number of samples was performed with no stratified consideration and only the superclasses were considered for removing samples. That means that when few samples were considered (10 to 30%) the probability of removing key samples for some subclasses was probably high and, therefore, the final accuracy would be negatively affected. Furthermore, since non-special training selection was carried out (Foody, Mathur 2004b), the less number of samples, the higher likelihood of removing meaningful support vectors to effectively separate pervious and impervious classes. Thus, and similar to the findings of Foody, Mathur (2004a), although a small training set can be suitable for SVM classifier, a large sample size could be required in order to ensure that appropriate training data are included, especially if no classifier-oriented selection of sample sites was carried out (Mathur, Foody 2008). Since the comparison against different classifiers was an aim in a first stage, no differences in sampling design were estimated.

CONCLUSIONS

This work showed that RGB archival aerial orthoimagery can be used as a relevant data source for ISAs classification, even when ancillary data are not available. However, this kind of archival imagery is usually radiometrically deficient, due to it being not well preserved (degraded from being stored improperly), scanning errors and radiometric variations among the different aerial photographs covering the working area (which can be detected when the images are mosaicked). Therefore, an adapted workflow which takes into account those characteristics was presented and validated in this work.

A relevant methodological contribution presented in this work was the exhaustive statistical analysis undertaken in order to make sure that the results

that were obtained were reliable. The KHAT statistic was used to compare the error matrices corresponding to each combination (one-against-one), which indicated whether the accuracies were significantly different from one another. Because of the high number of combinations that were compared, the separability matrix (SM) was introduced as a tool to clarify the statistical analysis results. This matrix was proved to be a useful method in order to make the obtained results more intelligible and organised.

From the SMs results on ArO, some conclusions can be derived. First, SVM and NN were ranked as the most suitable classifiers, especially when the local variance texture descriptor was included in the feature vector. For those cases the OA was close to 90% and KHAT was about 0.75. Local variance represents a simple and easy way to extract texture, so its utilisation and adaptation to images that have different spatial resolutions should be tested in further works. The CART classifier, based on decision trees, performed the worst regarding overall accuracy, achieving a score not higher than 82%. The absence of significant improvement regarding classification results was remarkable when texture information based on object-based GLCM (homogeneity and correlation texture indices) was added to the basic spectral features (mean of the RGB channels and 4 different band ratios for each object). Additionally, GLCM-based texture indices are computationally expensive and, therefore, difficult to implement under operational conditions or mapping production.

Another notable conclusion that can be extracted from this work is the relative low influence of the classification strategy (aggregation of subclasses or direct classification) on the pervious/impervious classification accuracy results from ArO. Only the CART classifier was significantly affected by the classification strategy used, since the direct classification turned out to be less accurate than the aggregation strategy for one of the feature vectors that was tested. It is worth noting that, for the case of direct classification, the target classes, pervious and impervious, were labelled in a binary way so more errors could be expected because only two classes could correspond to a large spectral variability. As opposed to CART, the SVM and NN classifiers were not sensitive to the large heterogeneity attributed to the target classes in the case of direct classification since they work in a more localised feature space (nearest neighbour or support vectors). On the other hand, the NN classifier used a large computational budget which, in contrast to SVM, was highly depended on the number of classes that were to be labelled, the number of training samples, as well as the support feature vector. In fact, NN was proved to be a non-efficient method when it is supported by GLCM texture features, especially if large areas have to be classified.

When the most suitable classification approach was selected, it was proved that the selection of an *ad hoc* training set was needed to accurately classify the remaining study area (aside from the pilot area) and to achieve a constant level of accuracy for all of the study area. Then, when the entire area was classified by

means of all the training samples, accurate results were achieved for the entire area and all the data sources and, therefore, the distribution of the samples was proved as a key factor for the final classification accuracy. Additionally, the reduction of training samples showed that the training size and samples distribution plays a key role. In this sense, large uncertainty in the results could be obtained whether the number of samples was not appropriate.

Regarding the data source used, it was proved that VHR-satellite images (WV2 and GE1) yielded higher accurate results than ArO when feature set which did not include variance texture features were used (RGB, and Rates feature sets). However, when variance was included, the results obtained by all the orthoimages were not statistically different. Therefore, texture indices were highlighted as a highly useful feature for ISAs classification. Both satellite orthoimages had only significantly different accuracy for 2 out of 7 feature sets tested, being WV2 more accurate than GE1. The data source also affected the differences between both training sets used (from the pilot area and from *ad hoc* training). Thus, while ArO and GE1 showed high differences, yielding the *ad hoc* training set the most accurate results, WV2 results reflected that the pilot area was capable to achieve comparable results to those acquired from the *ad hoc* training set.

Finally, this work showed that the training sample selection should be carefully planned, because of the spectral variation, which is typical of archival aerial photographs. It has been proved that classification accuracy is notably affected by radiometric variation and also by an incorrect capture of the class variability for the entire area to be classified (poor spatial distribution of training samples). Therefore, an *ad hoc* training sample, which should be close to the area to be labelled, is recommended, including a good representation as well as enough samples for each subclass that constitute the pervious/impervious target classes.

REFERENCES

Agüera, F., Aguilar, F.J. & Aguilar, M.A. 2008, "Using texture analysis to improve per-pixel classification of very high resolution images for mapping plastic greenhouses", *ISPRS Journal of Photogrammetry and Remote Sensing,* vol. 63, no. 6, pp. 635-646.

Aguilar, M.A., Aguilar, F.J., Saldaña, M.M. & Fernández, I. 2012, "Geopositioning accuracy assessment of GeoEye-1 panchromatic and multispectral imagery", *Photogrammetric Engineering and Remote Sensing,* vol. 78, no. 3, pp. 247-257.

Aguilar, M.A., Saldaña, M.D.M. & Aguilar, F.J. 2013a, "Assessing geometric accuracy of the orthorectification process from GeoEye-1 and WorldView-2 panchromatic images", *International Journal of Applied Earth Observation and Geoinformation,* vol. 21, no. 1, pp. 427-435.

Aguilar, M.A., Saldaña, M.M. & Aguilar, F.J. 2013b, "GeoEye-1 and WorldView-2 pan-sharpened imagery for object-based classification in urban environments", *International Journal of Remote Sensing,* vol. 34, no. 7, pp. 2583-2606.

Arnold Jr., C.L. & Gibbons, C.J. 1996, "Impervious surface coverage: The emergence of a key environmental indicator", *Journal of the American Planning Association,* vol. 62, no. 2, pp. 243-258.

Baraldi, A. & Parmiggiani, F. 1995, "Investigation of the textural characteristics associated with gray level cooccurrence matrix statistical parameters", *IEEE Transactions on Geoscience and Remote Sensing,* vol. 33, no. 2, pp. 293-304.

Benz, U.C., Hofmann, P., Willhauck, G., Lingenfelder, I. & Heynen, M. 2004, "Multi-resolution, object-oriented fuzzy analysis of remote sensing data for GIS-ready information", *ISPRS Journal of Photogrammetry and Remote Sensing,* vol. 58, no. 3-4, pp. 239-258.

Blaschke, T. 2010, "Object based image analysis for remote sensing", *ISPRS Journal of Photogrammetry and Remote Sensing,* vol. 65, no. 1, pp. 2-16.

Blaschke, T. & Strobl, J. 2001, "What's wrong with pixels? Some recent developments interfacing remote sensing and GIS", *Geo-Informations-Systeme,* vol. 14, no. 6, pp. 12-17.

Brabec, E., Schulte, S. & Richards, P.L. 2002, "Impervious surfaces and water quality: A review of current literature and its implications for watershed planning", *Journal of Planning Literature,* vol. 16, no. 4, pp. 499-514.

Breiman, L., Friedman, J.H., Olshen, R.A. & Stone, C.J. 1984, *Classification and Regression Trees,* Chapman & Hall/CRC, Monterey, California.

Brodley, C.E. & Friedl, M.A. 1997, "Decision tree classification of land cover from remotely sensed data", *Remote Sensing of Environment,* vol. 61, no. 3, pp. 399-409.

Carleer, A.P. & Wolff, E. 2006, "Urban land cover multi-level region-based classification of VHR data by selecting relevant features", *International Journal of Remote Sensing,* vol. 27, no. 6, pp. 1035-1051.

Chandelier, L. & Martinoty, G. 2009, "A radiometric aerial triangulation for the equalization of digital aerial images and orthoimages", *Photogrammetric Engineering and Remote Sensing,* vol. 75, no. 2, pp. 193-200.

Chang, C.C. & Lin, C.J. 2011, "LIBSVM: A Library for support vector machines", *ACM Transactions on Intelligent Systems and Technology,* vol. 2, no. 3.

Chen, D., Stow, D.A. & Gong, P. 2004, "Examining the effect of spatial resolution and texture window size on classification accuracy: An urban environment case", *International Journal of Remote Sensing,* vol. 25, no. 11, pp. 2177-2192.

Chini, M., Pacifici, F., Emery, W.J., Pierdicca, N. & Del Frate, F. 2008, "Comparing statistical and neural network methods applied to very high resolution satellite images showing changes in man-made structures at rocky flats", *IEEE Transactions on Geoscience and Remote Sensing,* vol. 46, no. 6, pp. 1812-1821.

Clausi, D.A. 2002, "An analysis of co-occurrence texture statistics as a function of grey level quantization", *Canadian Journal of Remote Sensing,* vol. 28, no. 1, pp. 45-62.

Cleve, C., Kelly, M., Kearns, F.R. & Moritz, M. 2008, "Classification of the wildland-urban interface: A comparison of pixel- and object-based classifications using high-resolution aerial photography", *Computers, Environment and Urban Systems,* vol. 32, no. 4, pp. 317-326.

Congalton, R.G. 1991, "A review of assessing the accuracy of classifications of remotely sensed data", *Remote Sensing of Environment,* vol. 37, no. 1, pp. 35-46.

Congalton, R.G. & Green, K. 2009, *Assessing the accuracy of remotely sensed data,* 2th edition, CRC Press, Boca Raton.

Cover, T. & Hart, P. 1967, "Nearest neighbor pattern classification", *IEEE Transactions on Information Theory,* vol. 13, no. 1, pp. 21-27.

Definiens, I. 2010, *eCognition Document Version 1.2.1*, Munich, Germany.

Duda, R.O. & Hart, P.E. 1973, *Pattern Classification and Scene Analysis,* Wiley and Sons, New York.

Esposito, F., Malerba, D. & Semeraro, G. 1997, "A comparative analysis of methods for pruning decision trees", *IEEE Transactions on Pattern Analysis and Machine Intelligence,* vol. 19, no. 5, pp. 476-491.

Foody, G.M. 2009, "Sample size determination for image classification accuracy assessment and comparison", *International Journal of Remote Sensing,* vol. 30, no. 20, pp. 5273-5291.

Foody, G.M. & Mathur, A. 2004a, "A relative evaluation of multiclass image classification by support vector machines", *IEEE Transactions on Geoscience and Remote Sensing,* vol. 42, no. 6, pp. 1335-1343.

Foody, G.M. & Mathur, A. 2004b, "Toward intelligent training of supervised image classifications: Directing training data acquisition for SVM classification", *Remote Sensing of Environment,* vol. 93, no. 1-2, pp. 107-117.

Foody, G.M., Mathur, A., Sanchez-Hernandez, C. & Boyd, D.S. 2006, "Training set size requirements for the classification of a specific class", *Remote Sensing of Environment,* vol. 104, no. 1, pp. 1-14.

Friedl, M.A., Brodley, C.E. & Strahler, A.H. 1999, "Maximizing land cover classification accuracies produced by decision trees at continental to global scales", *IEEE Transactions on Geoscience and Remote Sensing,* vol. 37, no. 2 II, pp. 969-977.

Gad, S. & Kusky, T. 2006, "Lithological mapping in the Eastern Desert of Egypt, the Barramiya area, using Landsat thematic mapper (TM)", *Journal of African Earth Sciences,* vol. 44, no. 2, pp. 196-202.

Gamon, J.A. & Surfus, J.S. 1999, "Assessing leaf pigment content and activity with a reflectometer", *New Phytologist,* vol. 143, no. 1, pp. 105-117.

Gillespie, A.R., Kahle, A.B. & Walker, R.E. 1987, "Color enhancement of highly correlated images. II. Channel ratio and "chromaticity" transformation techniques", *Remote Sensing of Environment,* vol. 22, no. 3, pp. 343-365.

Gillies, R.R., Brim Box, J., Symanzik, J. & Rodemaker, E.J. 2003, "Effects of urbanization on the aquatic fauna of the Line Creek watershed, Atlanta - A satellite perspective", *Remote Sensing of Environment,* vol. 86, no. 3, pp. 411-422.

Goetz, S.J., Wright, R.K., Smith, A.J., Zinecker, E. & Schaub, E. 2003, "IKONOS imagery for resource management: Tree cover, impervious surfaces, and riparian buffer analyses in the mid-Atlantic region", *Remote Sensing of Environment,* vol. 88, no. 1-2, pp. 195-208.

Haralick, R.M., Shanmugam, K. & Dinstein, I. 1973, "Textural features for image classification", *IEEE Transactions on Systems, Man and Cybernetics,* vol. smc 3, no. 6, pp. 610-621.

Herold, M., Liu, X.H. & Clarke, K.C. 2003, "Spatial metrics and image texture for mapping urban land use", *Photogrammetric Engineering and Remote Sensing,* vol. 69, no. 9, pp. 991-1001.

Hodgson, M.E., Jensen, J.R., Tullis, J.A., Riordan, K.D. & Archer, C.M. 2003, "Synergistic use of lidar and color aerial photography for mapping urban parcel imperviousness", *Photogrammetric Engineering and Remote Sensing,* vol. 69, no. 9, pp. 973-980.

Huang, C., Davis, L.S. & Townshend, J.R.G. 2002, "An assessment of support vector machines for land cover classification", *International Journal of Remote Sensing,* vol. 23, no. 4, pp. 725-749.

Huang, X. & Zhang, L. 2009, "Road centreline extraction from high-resolution imagery based on multiscale structural features and support vector machines", *International Journal of Remote Sensing,* vol. 30, no. 8, pp. 1977-1987.

Im, J., Jensen, J.R. & Tullis, J.A. 2008, "Object-based change detection using correlation image analysis and image segmentation", *International Journal of Remote Sensing,* vol. 29, no. 2, pp. 399-423.

Inglada, J. 2007, "Automatic recognition of man-made objects in high resolution optical remote sensing images by SVM classification of geometric image features", *ISPRS Journal of Photogrammetry and Remote Sensing,* vol. 62, no. 3, pp. 236-248.

Jensen, J.R. 1996, *Introductory digital image processing: a remote sensing perspective. Second edition*. Prentice Hall, New Jersey.

Jones, H.G. & Vaughan, R.A. 2010, *Remote Sensing of Vegetation: Principles, techniques, and applications,* Oxford University Press, Oxford.

Kampouraki, M., Wood, G.A. & Brewer, T.K. 2008, "Opportunities and limitations of object based image analysis for detecting urban impervious and vegetated surfaces using true-color aerial photography" in *Object-based image analysis: spatial concepts for knowledge-driven remote sensing*, eds. T. Blaschke, S. Lang & G. Hay, Springer-Verlag, London, pp. 555-569.

Keller, J.M., Gray, M.R. & Givens, J.A. 1985, "Fuzzy k-nearest neighbor algorithm.", *IEEE Transactions on Systems, Man and Cybernetics,* vol. SMC-15, no. 4, pp. 580-585.

Laliberte, A.S. & Rango, A. 2009, "Texture and scale in object-based analysis of subdecimeter resolution unmanned aerial vehicle (UAV) imagery", *IEEE Transactions on Geoscience and Remote Sensing,* vol. 47, no. 3, pp. 1-10.

Liu, D. & Xia, F. 2010, "Assessing object-based classification: Advantages and limitations", *Remote Sensing Letters,* vol. 1, no. 4, pp. 187-194.

Lu, D., Hetrick, S. & Moran, E. 2011, "Impervious surface mapping with quickbird imagery", *International Journal of Remote Sensing,* vol. 32, no. 9, pp. 2519-2533.

Lu, D., Hetrick, S. & Moran, E. 2010, "Land cover classification in a complex urban-rural landscape with QuickBird imagery", *Photogrammetric Engineering and Remote Sensing,* vol. 76, no. 10, pp. 1159-1168.

Lu, D. & Weng, Q. 2009, "Extraction of urban impervious surfaces from an IKONOS image", *International Journal of Remote Sensing,* vol. 30, no. 5, pp. 1297-1311.

Lu, D. & Weng, Q. 2007, "A survey of image classification methods and techniques for improving classification performance", *International Journal of Remote Sensing,* vol. 28, no. 5, pp. 823-870.

Maillard, P. 2003, "Comparing texture analysis methods through classification", *Photogrammetric Engineering and Remote Sensing,* vol. 69, no. 4, pp. 357-367.

Mallinis, G., Koutsias, N., Tsakiri-Strati, M. & Karteris, M. 2008, "Object-based classification using Quickbird imagery for delineating forest vegetation polygons in a Mediterranean test site", *ISPRS Journal of Photogrammetry and Remote Sensing,* vol. 63, no. 2, pp. 237-250.

Mathur, A. & Foody, G.M. 2008, "Crop classification by support vector machine with intelligently selected training data for an operational application", *International Journal of Remote Sensing,* vol. 29, no. 8, pp. 2227-2240.

Melgani, F. & Bruzzone, L. 2004, "Classification of hyperspectral remote sensing images with support vector machines", *IEEE Transactions on Geoscience and Remote Sensing,* vol. 42, no. 8, pp. 1778-1790.

Miller, J.E., Nelson, S.A.C. & Hess, G.R. 2009, "An object extraction approach for impervious surface classification with very-high-resolution imagery", *Professional Geographer,* vol. 61, no. 2, pp. 250-264.

Motohka, T., Nasahara, K.N., Oguma, H. & Tsuchida, S. 2010, "Applicability of Green-Red Vegetation Index for remote sensing of vegetation phenology", *Remote Sensing,* vol. 2, no. 10, pp. 2369-2387.

Mountrakis, G., Im, J. & Ogole, C. 2011, "Support vector machines in remote sensing: A review", *ISPRS Journal of Photogrammetry and Remote Sensing,* vol. 66, no. 3, pp. 247-259.

Myint, S.W., Gober, P., Brazel, A., Grossman-Clarke, S. & Weng, Q. 2011, "Per-pixel vs. object-based classification of urban land cover extraction using high spatial resolution imagery", *Remote Sensing of Environment,* vol. 115, no. 5, pp. 1145-1161.

Nagao, M. & Matsuyama, T. 1979, "Edge preserving smoothing", *Computer Graphics and Image Processing,* vol. 9, no. 4, pp. 394-407.

Pacifici, F., Chini, M. & Emery, W.J. 2009, "A neural network approach using multi-scale textural metrics from very high-resolution panchromatic imagery for urban land-use classification", *Remote Sensing of Environment,* vol. 113, no. 6, pp. 1276-1292.

Pacifici, F. & Solimini, C. 2007, "An innovative neural-net method to detect temporal changes in high-resolution optical satellite imagery", *IEEE Transactions on Geoscience and Remote Sensing,* vol. 45, no. 9, pp. 2940-2952.

Pal, M. & Mather, P.M. 2003, "An assessment of the effectiveness of decision tree methods for land cover classification", *Remote Sensing of Environment,* vol. 86, no. 4, pp. 554-565.

Pu, R., Landry, S. & Yu, Q. 2011, "Object-based urban detailed land cover classification with high spatial resolution IKONOS imagery", *International Journal of Remote Sensing,* vol. 32, no. 12, pp. 3285-3308.

Samaniego, L., Bárdossy, A. & Schulz, K. 2008, "Supervised classification of remotely sensed imagery using a modified k-NN technique", *IEEE Transactions on Geoscience and Remote Sensing,* vol. 46, no. 7, pp. 2112-2125.

Sauro, J. & Lewis, J.R. 2005, "Estimating completion rates from small samples using binomial confidence intervals: Comparisons and recommendations", *Proceedings of the Human Factors and Ergonomics Society*, pp. 2100.

Schueler, T.R. 1994, "The Importance of Imperviousness", *Watershed Protection Techniques,* vol. 1, no. 3, pp. 100-111.

Slonecker, E.T., Jennings, D.B. & Garofalo, D. 2001, "Remote sensing of impervious surfaces: A review", *Remote Sensing Reviews,* vol. 20, no. 3, pp. 227-225.

Soh, L.K. & Tsatsoulis, C. 1999, "Texture analysis of SAR sea ice imagery using gray level co-occurrence matrices", *IEEE Transactions on Geoscience and Remote Sensing,* vol. 37, no. 2, pp. 780-795.

Song, C., Woodcock, C.E., Seto, K.C., Lenney, M.P. & Macomber, S.A. 2001, "Classification and change detection using Landsat TM data: When and how to correct atmospheric effects?", *Remote Sensing of Environment,* vol. 75, no. 2, pp. 230-244.

Thomas, N., Hendrix, C. & Congalton, R.G. 2003, "A comparison of urban mapping methods using high-resolution digital imagery", *Photogrammetric Engineering and Remote Sensing,* vol. 69, no. 9, pp. 963-972.

Treitz, P. & Howarth, P. 2000, "High spatial resolution remote sensing data for forest ecosystem classification: An examination of spatial scale", *Remote Sensing of Environment,* vol. 72, no. 3, pp. 268-289.

Trinder, J.C. & Salah, M. 2011, "Support Vector Machines: Optimization and validation for land cover mapping using aerial images and lidar data", *34th International Symposium on Remote Sensing of Environment*, April.

Vapnik, V. 1995, *The Nature of Statistical Learning Theory,* Springer-Verlag, New York.

Wang, L., Sousa, W.P., Gong, P. & Biging, G.S. 2004, "Comparison of IKONOS and QuickBird images for mapping mangrove species on the Caribbean coast of Panama", *Remote Sensing of Environment,* vol. 91, no. 3–4, pp. 432-440.

Weng, Q. 2012, "Remote sensing of impervious surfaces in the urban areas: Requirements, methods, and trends", *Remote Sensing of Environment,* vol. 117, pp. 34-49.

Weng, Q. 2001, "Modeling urban growth effects on surface runoff with the integration of remote sensing and GIS", *Environmental management,* vol. 28, no. 6, pp. 737-748.

Whiteside, T.G., Boggs, G.S. & Maier, S.W. 2011, "Comparing object-based and pixel-based classifications for mapping savannas", *International Journal of Applied Earth Observation and Geoinformation,* vol. 13, no. 6, pp. 884-893.

Yan, G., Mas, J.F., Maathuis, B.H.P., Xiangmin, Z. & Van Dijk, P.M. 2006, "Comparison of pixel-based and object-oriented image classification approaches - A case study in a coal fire area, Wuda, Inner Mongolia, China", *International Journal of Remote Sensing,* vol. 27, no. 18, pp. 4039-4055.

Yu, Q., Gong, P., Clinton, N., Biging, G., Kelly, M. & Schirokauer, D. 2006, "Object-based detailed vegetation classification with airborne high spatial resolution remote sensing imagery", *Photogrammetric Engineering and Remote Sensing,* vol. 72, no. 7, pp. 799-811.

Zhou, Y. & Wang, Y.Q. 2008, "Extraction of impervious surface areas from high spatial resolution imagery by multiple agent segmentation and classification", *Photogrammetric Engineering and Remote Sensing,* vol. 74, no. 7, pp. 857-868.

Zhu, G. & Blumberg, D.G. 2002, "Classification using ASTER data and SVM algorithms: The case study of Beer Sheva, Israel", *Remote Sensing of Environment,* vol. 80, no. 2, pp. 233-240.

Zhu, H. & Basir, O. 2005, "An adaptive fuzzy evidential nearest neighbor formulation for classifying remote sensing images", *IEEE Transactions on Geoscience and Remote Sensing,* vol. 43, no. 8, pp. 1874-1889.

Zhuang, X., Engel, B.A., Lozano-Garcia, D.F., Fernandez, R.N. & Johannsen, C.J. 1994, "Optimization of training data required for neuro-classification", *International Journal of Remote Sensing,* vol. 15, no. 16, pp. 3271-3277.

GENERAL CONCLUSIONS AND FURTHER WORK

CONCLUSIONS

In this Thesis, several geomatics techniques have been applied to both produce suitable and accurate georeferenced primary data and extract valuable information for coastal monitoring purposes from those primary data. Those approaches have been studied, developed, and tested in a high vulnerable coastal area of the Spanish Mediterranean located at Almeria province. This coastal area or coastal cell has proved to be highly prone to erosive processes which bring out the necessity for developing an appropriate and complete monitoring system. It has been also demonstrated that, in order to carry out that monitoring, the need of knowing what happened in the past in order to understand what may occur in the future came up.

In this Thesis, two kinds of georeferenced data in order to obtain valuable information for coastal monitoring purposes have been utilized: images and digital elevation models (DEMs). On one hand, a range of image data, from old aerial images to the newest very high resolution satellite images or pre-existing data available through Spatial Data Infrastructure (SDI), have been employed. The range of image features such as scale, accuracy, state of conservation, spectral resolution, or scanning resolution, was quite large and, therefore, different geomatics approaches were implemented. On the other hand, DEMs were acquired by means of stereo-photogrammetric processes or LiDAR data classification. Thus the variability both in vertical accuracy or spatial resolution was also quite high.

Regarding the georeferenced primary data production, the first two chapters of this Thesis have been dedicated to discuss the metric accuracy of archival aerial flights by exploring their photogrammetric orientation by means of self-calibrating bundle adjustment routines, and to develop a new robust surface matching technique for georeferencing historical DEMs based on the availability of a more recent reference DEM. Therefore, those chapters tried to develop and implement suitable geomatics techniques to obtain the most accurate as possible georeferenced data for helping in coastal monitoring tasks (e.g. multitemporal shoreline change monitoring).

In Chapter 1, at least a range from six to nine GCPs per stereo pair was recommended to apply self-calibrating bundle adjustment routines. Furthermore, the self-calibrating model to apply for that should be estimated in every different case since each archival aerial flight can present systematic errors of a different nature. In this way, it was found that the scale and the particular features of each

flight could be the key factors affecting the choice of the more adequate self-calibration model. The final accuracy results were more heavily influenced by the number of GCPs used in the bundle adjustment than the self-calibration model employed due to the underlying masking effect coming from higher degree sources of error as compared to the sort of systematic errors that can be properly modelled by self-calibration. In other words, and focusing on poorly-conserved imagery, the magnitude of non-systematic errors could not be faced by self-calibration methods which have been thought to cope with systematic errors. In fact, no significant differences were found between self-calibrating bundle adjustment results when compared to no-self calibrated ones (NSC) mainly due to the aforementioned masking effect and the high number of GCPs used for NSC case.

Trying to achieve the same goal, but changing the point of view, some promising results were achieved in Chapter 2 since an accurate co-registration was obtained between reference and historical DEMs. Additionally, the proposed shaded-relief image matching algorithm was proved to accurately perform a suitable pre-orientation for the latter surface matching approach. Both approaches (image and surface matching) were found to work well together and the accuracy achieved was labelled as adequate. The accuracy yielded from robust matching approach was totally comparable to that photogrammetrically extracted from the NSC and, thus, it can be stated that a new and more efficient technique has been developed for historical DEMs orientation headed up to monitoring tasks.

Furthermore, regarding the extraction of secondary valuable information from the primary data, the remaining three chapters were dedicated to develop suitable geomatics approaches for shoreline extraction, shoreline rate change assessment, and impervious surface areas classification. In Chapter 3, a new method based on DEM extrapolation (Elevation Gradient Trend Propagation, EGTP) was built since the 0 m contour level was estimated as a desirable reference level. However, topographic LiDAR is not usually able to collect information at that height because of the microtidal regime of Mediterranean areas. The most widely utilized approach to obtain datum-based shoreline, the Cross Shore Profile (CSP) method, was also implemented in order to compare both approaches for extrapolation purposes. EGTP was found as more robust and less dependent on onshore data and the synthetic validation carried out revealed two main conclusions: first, the reference elevation from which extrapolation process is started had a great impact for CSP; and second, a systematic offset can appear for extrapolation methods when the estimated slope does not match with the actual one and therefore interpolation method would always be preferred.

The shoreline evolution assessment was studied in Chapter 4 in order to quantitatively determine the erosion or accretion over time as well as to estimate the underlying medium-term shoreline change rate. It was found that erosion generally occurred from 1956 to nowadays. Two main reasons for erosive processes were hypothesized: first, the lack of sediment supply caused for a

natural phenomenon by means of an irregularity on the flood events occurred in the twentieth century and, second, the human-induced factor represented by the installation of a dam in the main supplier river basin. Apart from the drastic reduction of sediment supply, the wave approaching incident angle related to the shoreline orientation was found as the main reason explaining the spatial variability on the intensity of the erosive processes, being the alongshore sediment transport quite clear and carrying those sediment to a sink represented by a close submarine canyon. In order to assess shoreline changes, datum-based shorelines extracted from DEMs were preferred if compared with high water line (HWL) digitized on orthoimages because of the natural variability of this proxy when medium- and high-accurate DEMs were used. Regarding the method to assess medium-term shoreline change rate, reweighted weighted least squares (RWLS) method was evaluated as the most appropriate since it was able to detect and remove some observations (outliers) which corresponded to human-induced artificial changes on shoreline behaviour or extreme but natural shoreline positions. Additionally, RWLS yielded the less confidence interval or uncertainty for the estimated rate. It was also found that the shoreline selection as data input for change rate assessment should be carefully performed since overweighting effects can appear because of the high accurate modern shorelines and the high number of shorelines available in the last decades. Finally, extreme erosion rates were found for some areas along the study site which strongly recommends the continuity of the monitoring in this coastal cell.

Finally, impervious surface areas (ISAs) classification by means of supervised non-parametric approaches and high resolution aerial and satellite images was explored in Chapter 5. It was determined that colour archival orthoimages were suitable for ISA classification by means of using a direct classification of the pervious and impervious areas through nearest neighbour (NN) or support vector machines (SVM), observing an improvement on the classification results when including simple texture features such as the local variance. Moreover, SVM was labelled as the most efficient classification method when using the strategy and the feature set which achieved the most accurate results. Other conclusions were: first, the need of having local training samples in those areas to be classified instead of samples from external areas; secondly, similar classification accuracy results were obtained from both satellite images (for almost every feature set used) and from the archival orthoimages (only when variance was included); and finally, the fact that the training sample selection should be carefully performed since it was affected by radiometric variations and the incorrect capture of the class variability in the entire area to be classified.

FURTHER WORK

Although it is estimated that the goals of this Thesis have been properly accomplished, it is however clear that some further work should be done in order to refine some of the methods or approaches developed.

For instance, and regarding the Chapter 2, it would be interesting to test the effectiveness and the accuracy of the shoreline extraction from the DEMs referenced by the robust surface matching approach developed. In this sense, it would be really helpful to define an automatic methodology for shoreline recreation of old DEMs. Moreover, the accuracy obtained should be compared to that extracted from non-automatically oriented DEMs.

Regarding the evaluated shoreline extraction methods from DEM extrapolation, some approaches for removing the apparently local offset effect should be explored. Especially for CSP, an automatic selection of the points included in the regression could be performed in order to avoid the so-called *berm effect*. Additionally, those extrapolation methods should be evaluated by means of more accurate data (e.g. a DGPS field campaign) instead of the synthetic data used in this Thesis.

Related also to the last issue, a most reliable datum for shoreline extraction and erosion rate assessment should be estimated for Spanish Mediterranean coasts in order to determine whether the reference height should be geodetic (altimetric datum) or may be related to the tidal regime, e.g. mean high water estimated over a large time period. In order to do that, it is worth to take into account that interpolation methods are usually preferred and, therefore, the datum height to be chosen should be included in topographic LiDAR measurements, which is actually the most used technique for DEM generation. That datum should be evaluated to be used at a regional scale so that it could be useful for the entire coast in the country or, at least, in the entire Mediterranean areas.

In the Chapter 4, some further work has been already pointed regarding to have a wider comprehension on shoreline evolution. Thus, a sediment supply study and the verification of the canyon influence would be interesting to carry out. With regard to the rate assessment approach, binning transects and non-linear shoreline trend methods should be tested in order to improve the change rate estimation. Additionally, future work should be done to validate the estimated rates in order to verify that the shoreline still follows the assessed underlying evolution.

Finally, an important work should be carried out in order to relate the historical increase of impervious surface areas along the study site with the shoreline erosion processes by means of spatial regression or geostatistic approaches. Focusing on the remote sensing approach, it could be interesting to test the developed method on every type of image data available: old panchromatic

images and very high resolution aerial images. In addition, DEMs or DSMs could be included in the classification approaches in order to improve the classification accuracy results.

APPENDIX 1

List of acronyms

ALS: airborne laser scanner

ANOVA: analysis of variance

AOR: average of rates

APs: additional parameters

ARO: automatic relative orientation

CART: classification and regression tree

CB: coastal blue

CEM: coastal elevation model

CI: confidence interval

CP: check point

CSP: cross shore profile

DDS: DEM-derived shoreline

DEM: digital elevation model

DF: decision factor

DGPS: differential global positioning system

DMC: digital mapping camera

DTM: digital terrain model

DSM: digital surface model

nDSM: normalized-digital surface model

EGTP: elevation gradient trend propagation

EIP: error in prediction

EPR: end point rate

ETRS89: European terrestrial reference system 1989

FOV: field of view

GAP: general adjustment program

GCP: ground control point

GLCM: grey level co-occurrence matrix

GPS: global positioning system

GSD: ground sample distance

HWL: high water line

ICP: independent check points

ICZM: integrated coastal zone management

IDS: image digitizing shoreline

INS: inertial navigation system

ISA: impervious surface area

ISAE: ImageStation automatic elevation

JK: Jackknifing

LAD: least absolute deviation

LAR: least absolute residual

LiDAR: light detection and ranging

LMS: least median of squares

LPS: Leica Photogrammetry Suite

LZD: least z-difference

MDL: minimum description length

MHW: mean high water

MLC: maximum likelihood classifier

MLLW: mean lower low water

MS: multispectral bands

MSL: mean sea level

MSA: mean separation analysis

NDI: normalized digital indexes

NDVI: normalized digital vegetation index

NN: nearest neighbor

NSC: no-self calibration

NSM: net shoreline movement

NTDE: national tidal datum epoch

OA: overall accuracy

OBIA: object-based image analysis

OLS: ordinary least square

OSD: overall standard deviation

PA: producer's accuracy

PAN: panchromatic band

RBF: radial basic function

RE: red edge

REDIAM: red de información ambiental de Andalucía

RGB: red, green, blue (referred to chromatic bands of images)

RLS: reweighted least squares

RMSE: root mean square error

$RMSE_p$: planimetric root mean square error

$RMSE_z$: vertical root mean square error

$RMSE_{3d}$: tridimensional root mean square error

RPC: rational polynomial coefficient

RSM: robust surface matching

RTK: real-time kinematic

RWLS: reweighted weighted least squares

SAVI: soil-adjusted vegetation index

SCI: site of community importance

SDI: spatial data infrastructure

SIFT: scale invariant feature transform

SLR: sea level rise

SM: separability matrix

SRIM: shaded-relief image matching

SVM: support vector machine

TB: Tukey's biweight

TWL: total water level

UA: user's accuracy

UTM: universal transverse mercator

VHR: very high resolution

WLS: weighted least squares

WLAD: weighted least absolute deviation

WMS: web map service

Y: yellow

APPENDIX 2

Scientific publications and awards derived from this Thesis

Papers published in international journals:

Aguilar, M.A., Aguilar, F.J., Fernández, I. & Mills, J.P. 2013, "Accuracy assessment of commercial self-calibrating bundle adjustment routines applied to archival aerial photography", *Photogrammetric Record*, vol. 28, no. 141, pp. 96-114.

Aguilar, F.J., Aguilar, M.A., Fernández, I., Negreiros, J.G., Delgado, J. & Pérez, J.L. 2012, "A new two-step robust surface matching approach for three-dimensional georeferencing of historical digital elevation", *IEEE Geoscience and Remote Sensing Letters*, vol. 9, no. 5, pp. 589-593.

Fernández, I., Aguilar, F.J., Aguilar, M.A., Pérez, J.L. & Arenas, A. 2012, "A new, robust, and accurate method to extract tide-coordinated shorelines from coastal elevation models", *Journal of Coastal Research*, vol. 28, no. 3, pp. 683.699.

Fernández, I., Aguilar, F.J., Álvarez, M.F., Aguilar, M.A. 2013, "Non-parametric object-based approaches to carry out ISA classification from archival aerial orthoimages", *IEEE Journal of Selected Topics in Applied Earth Observations and Remote Sensing*, Article in Press.

Congress and symposiums papers:

Aguilar, F.J., Fernández, I., Pérez, J.L., López, A., Aguilar, M.A., Mozas, A. & Cardenal, J. 2010, "Preliminary results on high accuracy estimation of shoreline change rate based on coastal elevation models", *International Archives of the Photogrammetry, Remote Sensing and Spatial Information Science,* Kyoto, Japan, 9-12 August 2010, pp. 986-991.

Aguilar, F.J., Fernández, I., Aguilar, M.A., Pérez, J.L., Delgado, J. & Negreiros, J.G. 2010, "Shaded-reliefs matching as an efficient technique for 3D geo-referencing of historical digital elevation models", *International Archives of the Photogrammetry, Remote Sensing and Spatial Information Science,* Kyoto, Japan, 9-12 August 2010, pp. 1002-1007.

Fernández, I., Aguilar, F.J., Pérez, J.L., Aguilar, M.A., Mozas, A. & López, A. 2011, "Improvements in the determination of extrapolated shorelines using Elevation Gradient Trend Propagation method", *Proceedings of the IMProVe*

2011, International Conference on Innovative Methods in Product Design, Venice, Italy, 15-17 June 2011, pp. 952-961.

Aguilar, F.J., Fernández, I., Aguilar, M.A., Delgado, J., Negreiros, J.G. & Pérez, J.L. 2011, "Robust surface matching as a rapid technique for terrain change detection", *Proceedings of the IMProVe 2011, International Conference on Innovative Methods in Product Design,* Venice, Italy, 15-17 June 2011, pp. 962-969.

Fernández, I., Aguilar, F.J., Aguilar, M.A., Álvarez, M.F. & Saldaña, M.M. 2013, "Impervious surface areas classification from GeoEye-1 satellite imagery using OBIA approach in a coastal area of Almería (Spain)", *XXIII International Conference on Graphic Engineering,* Madrid, Spain, 19-21 June 2013, *Accepted for publication.*

Fernández, I., Aguilar, F.J., Aguilar, M.A., Álvarez, M.F. & Saldaña, M.M. 2013, "Impervious surface areas classification from GeoEye-1 and WorldView-2 satellite imagery through OBIA approach in a coastal area of Almería (Spain)", *6th EARSeL Workshop on Remote Sensing of the Coastal Zone*, Matera, Italy, 5-7 June 2013, *Accepted for publication.*

Fernández, I., Aguilar, F.J., Aguilar, M.A., Álvarez, M.F. & Saldaña, M.M. 2013, "Clasificación de superficies impermeable mediante imágenes de satélite WorldView-2 en un área costera del levante almeriense usando técnicas de análisis de imágenes basado en objetos", *XV Congreso de la Asociación Española de Teledetección,* Madrid, Spain, 22-24 October 2013, *Accepted for publication.*

Awards received:

ISPRS Commission VIII Best Paper Award for the paper "*Preliminary results on high accuracy estimation of shoreline change rate based on coastal elevation models"*, presented at the ISPRS Commission VIII Symposium held from 9 to 12 August, 2010 in Kyoto, Japan.

Best Young Paper Award for the paper *"Improvements in the determination of extrapolated shorelines using Elevation Gradient Trend Propagation method"* in the International Conference on Innovative Methods in Product Design held from 15 to 17 June, 2011 in Venice, Italy (IMProVe 2011).